MULTIDISCIPLINARY CENTER FOR EARTHQUAKE ENGINEERING RESEARCH
A National Center of Excellence in Advanced Technology Applications

ISSN 1520-295X

Experimental Study of Bridge Elastomeric and Other Isolation and Energy Dissipation Systems with Emphasis on Uplift Prevention and High Velocity Near-Source Seismic Excitation

by

Amarnath Kasalanati and Michael C. Constantinou
University at Buffalo, State University of New York
Department of Civil, Structural and Environmental Engineering
Ketter Hall
Buffalo, New York 14260-4300

Technical Report MCEER-99-0004

February 26, 1999

This research was conducted at the University at Buffalo, State University of New York and was supported in whole or in part by the National Science Foundation under Grant No. BCS 90-25010.

NOTICE

This report was prepared by the University at Buffalo, State University of New York as a result of research sponsored by the Multidisciplinary Center for Earthquake Engineering Research (MCEER) through a grant from the National Science Foundation and other sponsors. Neither MCEER, associates of MCEER, its sponsors, University at Buffalo, State University of New York, nor any person acting on their behalf:

a. makes any warranty, express or implied, with respect to the use of any information, apparatus, method, or process disclosed in this report or that such use may not infringe upon privately owned rights; or

b. assumes any liabilities of whatsoever kind with respect to the use of, or the damage resulting from the use of, any information, apparatus, method, or process disclosed in this report.

Any opinions, findings, and conclusions or recommendations expressed in this publication are those of the author(s) and do not necessarily reflect the views of MCEER, the National Science Foundation, or other sponsors.

MULTIDISCIPLINARY CENTER FOR EARTHQUAKE ENGINEERING RESEARCH
A National Center of Excellence in Advanced Technology Applications

Experimental Study of Bridge Elastomeric and Other Isolation and Energy Dissipation Systems with Emphasis on Uplift Prevention and High Velocity Near-source Seismic Excitation

by

Amarnath Kasalanati[1] and Michael C. Constantinou[2]

Publication Date: February 26, 1999
Submittal Date: July 9, 1998

Technical Report MCEER-99-0004

Task Number 95-5104A

NSF Master Contract Number BCS 90-25010

1 Project Engineer, DIS, Inc., Lafayette, CA; former Research Assistant, Department of Civil, Structural and Environmental Engineering, University at Buffalo, State University of New York
2 Professor, Department of Civil, Structural and Environmental Engineering, University at Buffalo, State University of New York

MULTIDISCIPLINARY CENTER FOR EARTHQUAKE ENGINEERING RESEARCH
University at Buffalo, State University of New York
Red Jacket Quadrangle, Buffalo, NY 14261

Preface

The Multidisciplinary Center for Earthquake Engineering Research (MCEER) is a national center of excellence in advanced technology applications that is dedicated to the reduction of earthquake losses nationwide. Headquartered at the University at Buffalo, State University of New York, the Center was originally established by the National Science Foundation in 1986, as the National Center for Earthquake Engineering Research (NCEER).

Comprising a consortium of researchers from numerous disciplines and institutions throughout the United States, the Center's mission is to reduce earthquake losses through research and the application of advanced technologies that improve engineering, pre-earthquake planning and post-earthquake recovery strategies. Toward this end, the Center coordinates a nationwide program of multidisciplinary team research, education and outreach activities.

MCEER's research is conducted under the sponsorship of two major federal agencies: the National Science Foundation (NSF) and the Federal Highway Administration (FHWA), and the State of New York. Significant support is derived from the Federal Emergency Management Agency (FEMA), other state governments, academic institutions, foreign governments and private industry.

The Center's NSF-sponsored research is focused around four major thrusts, as shown in the figure below:

- quantifying building and lifeline performance in future earthquake through the estimation of expected losses;
- developing cost-effective, performance based, rehabilitation technologies for critical facilities;
- improving response and recovery through strategic planning and crisis management;
- establishing two user networks, one in experimental facilities and computing environments and the other in computational and analytical resources.

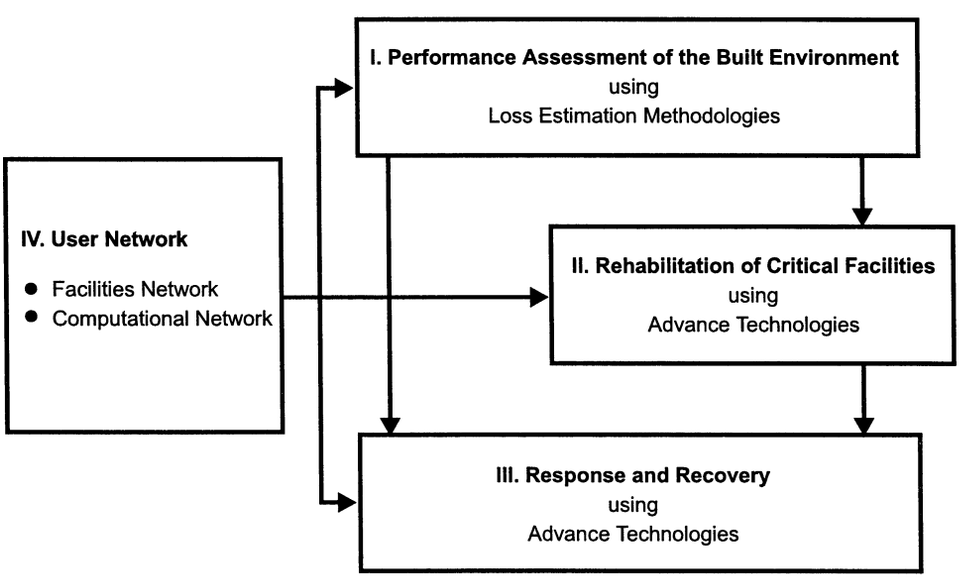

This report provides an assessment of the benefits offered by damping systems in near-source earthquakes and of the accuracy of currently available tools for analytical prediction of their seismic response. A two-span continuous deck bridge configuration was used in the test program. First, an isolator testing machine was designed and constructed that was capable of testing small bearings under controlled conditions. Next, three vastly different bearings (flat sliding, friction pendulum and elastomeric) were tested prestressed in the developed testing machine. Test results provided strong evidence for the capability of prestressing to prevent uplift or tension in isolation bearings. Finally, an experimental study of bridge elastomeric isolation systems with emphasis on near-source high velocity seismic excitation was performed. The addition of the damping devices caused a substantial reduction in displacement, provided relief to the vulnerable pier, caused a reduction in the total shear force transmitted to the bridge substructure, and provided for redistribution of the reduced inertia forces from the vulnerable pier to the presumed strong abutments.

The experimental results for the prestressed isolators, non-isolated configurations, and bridge model isolated with low damping elastomeric bearings, high damping elastomeric bearings, low damping elastomeric bearings combined with linear viscous dampers, and low damping elastomeric bearings combined with nonlinear viscous dampers are provided in postscript format in the publications section of MCEER's web site (http://mceer.buffalo.edu/pubs.html).

ABSTRACT

This report focussed on three parts: (a) the design and construction of an isolator testing machine, (b) the testing and modeling of prestressed isolators, and (c) an experimental study of bridge elastomeric isolation systems with an emphasis given to near source high velocity seismic excitation.

An isolator testing machine, that overcomes intrinsic difficulties encountered in such testing, was designed and constructed. The machine is capable of testing a variety of isolators under controlled conditions of axial load, lateral displacement and rotation.

The prestressing of isolators for preventing uplift or tension has been experimentally investigated for the purpose of demonstrating its effects on the behavior of isolators and for evaluating the validity and accuracy of theoretical predictions of the behavior of prestressed isolators. Flat sliding bearings, spherical FPS bearings and elastomeric bearings were tested prestressed within the developed testing machine under imposed combined horizontal displacement and variable axial load. A theory of prestressed isolators is presented and evaluated on the basis of the experimental results.

Earthquake simulator tests were performed on a quarter scale bridge model representing a two-span bridge. A total of four isolated configurations were studied. These consisted of a low damping elastomeric isolation system without and with linear and nonlinear viscous dampers, and a high damping elastomeric isolation system. In addition, three non-isolated configurations, without and with dampers, were investigated.
The testing of these systems had multiple objectives such as:

(a) Observation of the behavior of high damping elastomeric isolation systems under conditions of changing bearing properties due to the phenomena of scragging and related recovery.
(b) Comparative study of the effectiveness of elastomeric systems and elastomeric systems enhanced with viscous dampers.
(c) Observation of the behavior of elastomeric systems enhanced with linear and nonlinear viscous dampers in near-field source high velocity seismic excitation.
(d) Study of the behavior of non-isolated bridges with supplemental energy dissipation systems.
(e) Demonstration of the significance of enhanced damping in isolation systems for the reduction of displacement demand and the effective redistribution of the force transmitted to the substructure.
(f) Investigation of the validity and degree of accuracy of currently available analytical tools for the prediction of the dynamic response of bridges equipped with seismic isolation and energy dissipation systems.

ACKNOWLEDGMENTS

Financial support for this project was provided by the National Center for Earthquake Engineering Research (project No. 95 5104A) and Taylor Devices, Inc., North Tonawanda, NY. Scougal Rubber Corporation, Seattle, WA manufactured and donated the elastomeric bearings. Taylor Devices, Inc. manufactured and donated the fluid viscous dampers. SUSPA Spannbeton GmbH, Langenfeld, Germany manufactured and donated the fiberglass prestressing tendons used in the prestressed isolators. Special thanks are due to Dr. Ioannis S. E. Logiadis for his contribution in the testing and modeling of prestressed isolators.

This report is nearly identical to the doctoral dissertation of the first author. The dissertation committee consisted of the second author, Professors A. M. Reinhorn and T. T. Soong and Dr. Ronald L. Mayes.

TABLE OF CONTENTS

TABLE OF CONTENTS (CONTD.)

TABLE OF CONTENTS (CONTD.)

* The appendices are provided on MCEER's web site at *http://mceer.buffalo.edu*

LIST OF FIGURES

LIST OF FIGURES (CONTD.)

LIST OF FIGURES (CONTD.)

LIST OF FIGURES (CONTD.)

LIST OF FIGURES (CONTD.)

LIST OF FIGURES (CONTD.)

LIST OF FIGURES (CONTD.)

LIST OF FIGURES (CONTD.)

LIST OF TABLES

SECTION 1

INTRODUCTION

The increasing acceptance of seismic isolation and seismic energy dissipation technologies is evident in the number of structures constructed or retrofitted with these systems. Too many to attempt a detailed listing of these structures, it is sufficient to mention that just in North America there are as of 1998 about 120 bridges constructed or scheduled for construction with various forms of seismic isolation and energy dissipation systems. These bridges vary in size from small one-span bridges to monumental structures. The interested reader may find information on most, but not all, of these structures by visiting the web site of the Earthquake Engineering Research Center at www.eerc.berkeley.edu/prosys/applications.html.

A variety of seismic isolation systems have been used in bridge applications. They include lead-rubber bearings, lubricated sliding bearings with yielding steel devices, high damping elastomeric bearings, sliding bearings with restoring force and combined sliding and elastomeric systems. In the United States most applications employ lead-rubber bearings. Moreover, there is in the United States an increasing interest in the use of energy dissipation devices in bridges, either as elements of the isolation system or just as elements to reduce displacement demand and to provide for redistribution of inertia forces. A number of designs have been developed and a number of bridges in California are scheduled for installation of damping devices in 1998 and 1999. The devices of choice in these applications are fluid viscous dampers due primarily to the requirements for large stroke.

The acceptance of the technologies of seismic isolation and energy dissipation by the profession in the United States has been the result of a number of influencing factors, of which a significant one is the generation of experimental results and particularly results of shake table testing. Shake table testing, when performed with realistic models of sufficient size, allows for the observation of behavior under conditions of simulated extreme seismic loading and generates results that can be used to verify analytical methods for the prediction of the dynamic response. It is likely the best available tool for the observation of the seismic behavior of structural systems, which is surpassed only by field observations in actual earthquakes. Such observations have been made (Asher et al., 1997). While the observations have been so far for seismic motions which did not bring the isolation systems to the limits of their design, they provided convincing evidence of the validity of the technology.

Shake table testing of seismically isolated bridge models have been conducted at the University of California at Berkeley using low damping elastomeric and lead/rubber bearings (Kelly et al., 1986). These tests were conducted with a 427 kN rigid deck model. Despite the simplicity of this model, significant observations have been made including the instability of bearings during large deformations and the significance of damping (in this case provided by the lead core in the elastomeric bearings) for reducing the displacement response to acceptable limits.

Kawashima et al. (1992) reported on the shake table testing of high damping elastomeric and lead/

rubber bearing systems within a 392 kN bridge model at the Public Works Research Institute in Japan. The model featured flexible piers and testing was conducted at a time scale of unity. That is, the model was treated as a small size prototype. Due to limitations in the capability of the shake table, testing could not be conducted at large ground velocities which are representative of the Japanese bridge design motions of level 2. More recently, Feng and Okamoto (1994) conducted testing of a sliding isolation system using the same bridge model.

Bridge seismic isolation systems have been studied at the University at Buffalo starting in 1991 with the testing of a sliding isolation system using a 227 kN rigid deck model (Constantinou et al., 1991; 1992b). Work at Buffalo continued with the construction of a new 160 kN bridge which featured flexible and stiff piers. A variety of isolation systems have been tested including the Friction Pendulum System (Constantinou et al., 1993; Tsopelas et al., 1996a), sliding isolation systems with elastomeric restoring force devices and fluid dampers (Tsopelas et al., 1994b; 1996b), pressurized fluid devices (Tsopelas and Constantinou, 1994a) and lubricated sliding bearings with yielding steel devices (Tsopelas and Constantinou, 1994b; 1997). The testing included motions compatible with the level 2 Japanese bridge design spectra, motions compatible with the Caltrans 0.6g spectra and historic earthquakes with high peak acceleration (up to 1.0g) and peak velocity (up to 1.0 m/s in prototype scale). Several interesting observations were made including those of significant permanent displacements in systems with insufficient restoring force, and the significance of energy dissipation devices in reducing displacement demands to strict limits. These tests have been instrumental in the implementation of combined seismic isolation and energy dissipation systems in the United States and provided information for the modification of the criteria for sufficient restoring force in the 1997 AASHTO Guide Specifications for Seismic Isolation Design (American Association of State Highway and Transportation Officials, 1997).

The aforementioned testing programs were conducted prior to the 1994 Northridge and the 1995 Japanese Kobe earthquakes. These earthquakes generated a number of records with near-fault characteristics which had substantial peak ground accelerations and velocities. Near-source effects from strong earthquakes became an important consideration in earthquake engineering and cast doubt on the suitability of seismic isolation for near-fault locations (e.g., Hall et al., 1995).

The work described herein started as a continuation of the previous work at the University at Buffalo on bridge seismic isolation systems but with the concentration shifted to elastomeric systems and with emphasis given to near-source seismic effects. A particular two-span, continuous deck configuration was selected for testing and elastomeric bearings were designed to provide an isolation period in prototype scale of about 2 sec. While this and even larger values of period are entirely feasible, it was the limit at which testing could be conducted at the quarter length scale of the bridge model due to instability problems of the scaled bearings. It was presumed that the abutments of this bridge model represented strong elements to which the inertia forces could be directed, whereas the flexible pier was presumed to be the weak element in the system which needed relief from inertia forces. Inelastic action in the pier was not allowed based on the current philosophy in the 1997 AASHTO (American Association of State Highway Transportation Officials, 1997).

The elastomeric bearings (of low damping) provided a damping of about 7-percent of critical. The system was enhanced with linear viscous dampers which were located at the abutment locations. The enhanced system exhibited damping of about 35-percent of critical. In this configuration the bridge model was tested with a variety of seismic excitations including several with substantial near-source characteristics. The same system was also tested with nonlinear viscous dampers which were detailed to produce lesser damping force than the linear dampers beyond a specific velocity which was expected to be achieved in the near-source earthquakes. Accordingly, the nonlinear dampers were expected to be as effective as the linear dampers in reducing the displacement demand but with the benefit of lesser force transmitted to the abutments.

Moreover, high damping elastomeric bearings were used. These bearings were compounded to produce damping in the range of 15 to 20-percent and to have comparable stiffness characteristics to the low damping elastomeric bearings. This system was not tested with near-source excitations due to failure of one of the bearings. However, the testing provided valuable observations on the effects of the scragging and recovery processes of these bearings on the dynamic response. Moreover, data produced in the testing of this system provided a basis for comparison to the damping-enhanced systems and, once more, demonstrated the significance of damping in seismic isolation systems.

The two-span bridge model was also tested in its non-isolated configuration and then again in a non-isolated configuration but enhanced with linear and nonlinear dampers. The latter tests provided valuable information on the behavior of damping-enhanced conventional bridges.

The described work represented the bulk of the experimental effort in this report. The experimental data were utilized in a comparison of the behavior of isolated and non-isolated bridges, in the assessment of the benefits offered by damping systems in near-source earthquakes and in the assessment of the accuracy of currently available tools for the analytical prediction of seismic response.

As part of this work, elastomeric bearings required component testing prior to the shake table testing. This necessitated the design and construction of a bearing testing machine. This machine is now a permanent feature of the Structural Engineering and Earthquake Simulation Laboratory at the University at Buffalo. The design and capabilities of this machine are described herein.

Results obtained in the testing of a variety of seismic isolation bearings with this machine are presented. Particularly, sliding and elastomeric bearings were tested under conditions of variable axial load and lateral displacement in the presence of prestress for preventing uplift or tension. Due to the novelty of this approach and the complexities encountered in the design of a prestressing arrangement capable of accommodating large movements, this testing program is presented in detail. Moreover, analytical techniques for the prediction of the behavior of prestressed isolators are presented and evaluated on the basis of the experimental results.

This report ends with a number of appendices, totaling 158 pages, which contain selected graphs of experimental results. These appendices are provided on MCEER's web site at *http://mceer.buffalo.edu.*

SECTION 2

ISOLATOR TESTING MACHINE

2.1 Introduction

To understand the behavior of an isolation system, isolators need to undergo rigorous laboratory testing prior to their field installation. The conditions under which the testing should be done include a wide range of axial loads, displacements, velocities and temperatures. During moderate to large lateral displacements, isolators experience a change in height, thus requiring apparatus to accommodate this geometric change. Also, the isolator behavior may be sensitive to the rotation of its top and bottom parts. This chapter describes the design, construction and capabilities of an isolator testing machine that overcomes the intrinsic difficulties associated with such testing.

2.2 Factors Influencing the Isolator Testing Machine Design

Isolators exhibit changes in height when laterally displaced (e.g., FPS bearings have an increase in height with lateral displacement and elastomeric bearings experience a loss of vertical height during lateral displacement). Thus an isolator testing machine should be able to maintain the desired vertical load on the bearing during these movements.

The rotation of the top part of the isolator with respect to the bottom part has an influence on the isolator behavior. Therefore, the testing machine should have the capability to ensure that the top and bottom parts of the bearing are parallel and levelled during testing or should be able to impose a prescribed history of rotation.

The requirement for control of the isolator rotation precludes the possibility of load application through a concentric vertical actuator, for such an actuator would have no control over the rotation of the bearing. A rigid loading beam operated by symmetrically placed actuators can precisely control rotation. The actuators on the loading beam should be spaced as far apart as possible to minimize the difference between their forces during peak horizontal displacements of the bearing. Vertical actuators rotate about pivot points during the lateral movement of bearing. Hence, the actuators and their assemblage should be sufficiently long to keep the rotations and their secondary effects negligible.

It is important to measure the reaction forces, excluding inertia effects and losses due to friction. Thus, it is desirable to place a load cell directly under the bearing.

2.3 Designed Bearing Testing Machine

Figure 2-1 illustrates the designed testing machine. A total of three actuators are needed to ensure proper testing of the bearing: two vertical actuators to maintain the axial load on the bearing and one horizontal actuator to induce the lateral displacement. Also, three load cells are required to monitor the load on the bearing: one placed directly under the bearing (reaction load cell) which measures the axial and shear forces experienced by the bearing, and two load cells that are

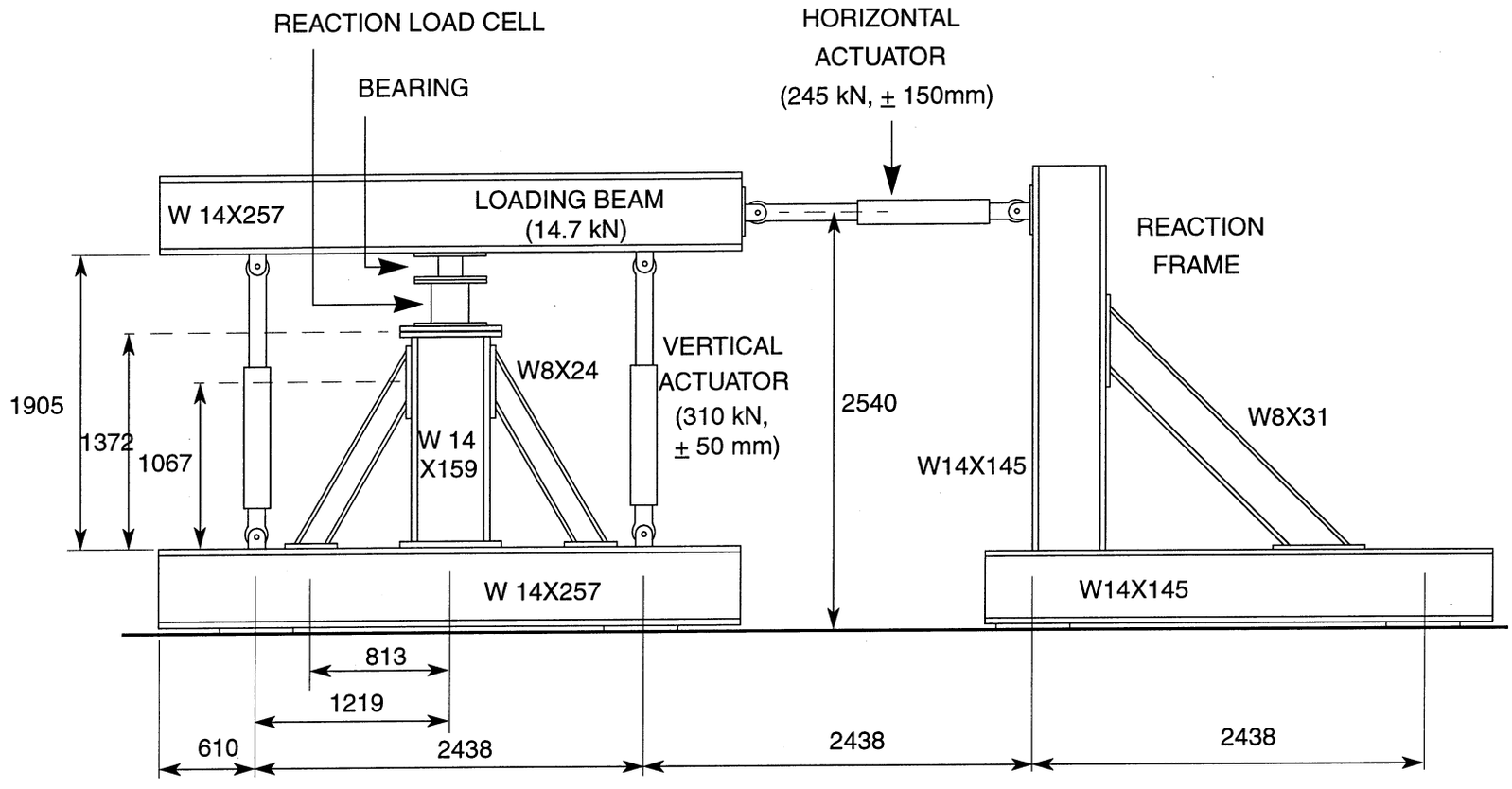

ALL DIMENSIONS IN mm

Figure 2-1: Isolator Testing Machine

connected to vertical actuators to control the vertical load.

The apparatus consists of two horizontal beams, a lower support beam that is fixed to the rigid floor and an upper loading beam that is moved by the horizontal actuator. The horizontal actuator is connected to a reaction frame, which in turn is fixed to the rigid floor. The lower beam supports a braced pedestal with the reaction load cell and the bearing mounted on the top of it. Two vertical actuators connect the top loading beam to the lower support beam at equal distances on either side of the pedestal. These vertical actuators support the loading beam as well as maintain the desired axial load on the bearing.

The displacement of one of the actuators was designed to be the master degree-of-freedom and that of the other was made to be the slave degree-of-freedom. This circuit arrangement ensures equal displacements by both the actuators, thus keeping the loading beam horizontal. The load cells of the two actuators and the load cell under bearing were connected by a feed back loop as illustrated in Figure 2-2.

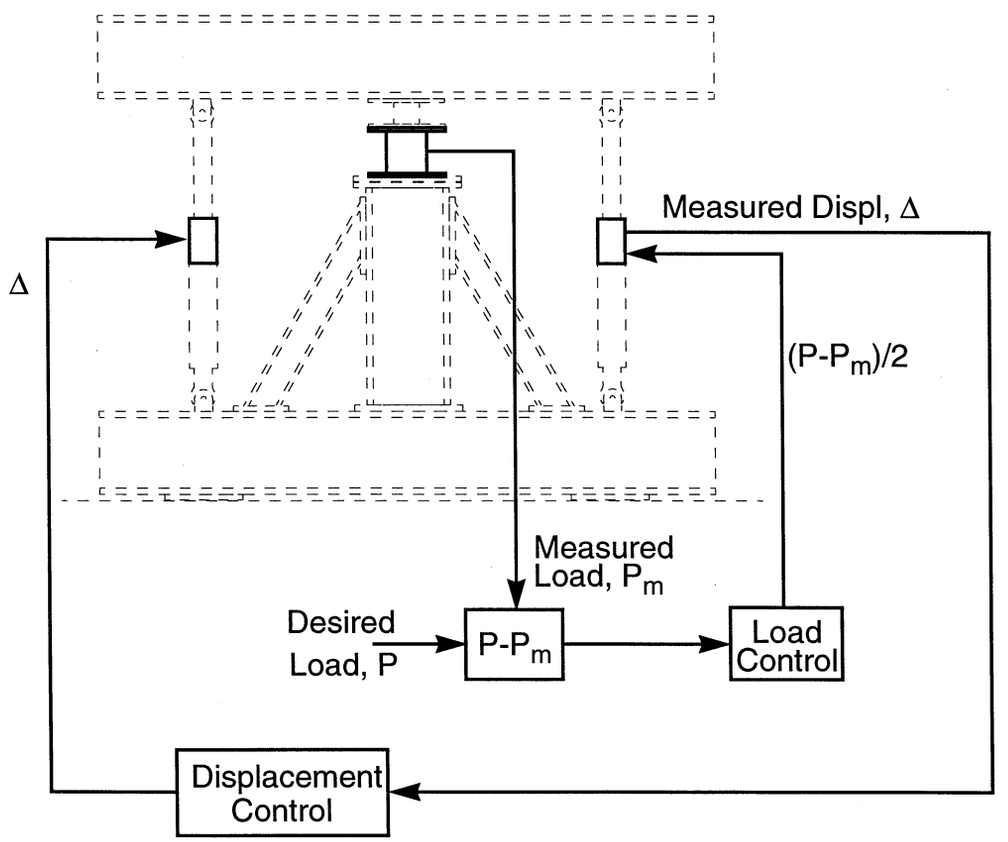

Figure 2-2: Load Control Using Reaction Load Cell (Control 1)

The control strategy is capable of maintaining the specified axial load on the bearing while imposing the specified lateral displacement, provided that sufficient hydraulic power is available. In the current configuration of the machine the horizontal actuator is furnished with a 90 GPM electrohydraulic servovalve and the vertical actuators with a 15 GPM servovalve each. There is a

mismatch in the flow capabilities of the vertical and horizontal actuators. Accordingly, the vertical load exhibited fluctuations during high speed lateral movement.

The load exerted by the vertical actuators and the weight of the loading beam would be referred to as "gravity load" hereafter. The control shown in Figure 2-2 was used when gravity load was the only vertical load experienced by the bearing. During the testing of prestressing bearings a second type of control as shown in Figure 2-3 was employed.

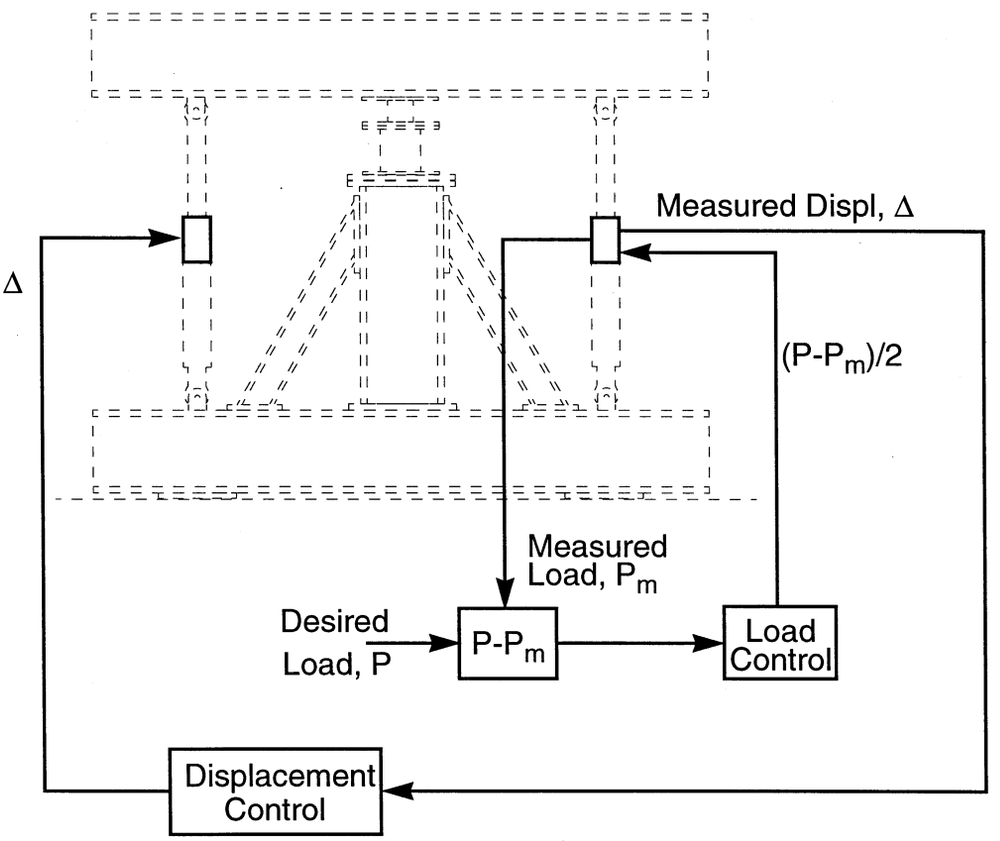

Figure 2-3: Load Control using Vertical Actuator Load Cells (Control 2)

In this case, the reaction load cell could not be utilized for the control of the gravity load on the bearing since it measures both the gravity load as well as the forces exerted on the bearing by the prestressing tendons. Accordingly, the vertical actuator load cells were utilized for this purpose. This control strategy was less accurate that the first one (control 1) due to errors introduced by the inclination of the vertical actuators and differences in the load applied by the vertical actuators.

The horizontal actuator used for applying lateral displacements on the bearing had a displacement range of ± 152 *mm* and force capacity of *245 kN*. The vertical actuators had a displacement range of ± 50 *mm* and a force limit of *356 kN* each. The upper and lower beams were spaced apart at a distance of $L=1905$ *mm* to reduce the angle of rotation of vertical actuators during extreme horizontal displacement of the bearing (less than 5^o at a displacement of *152 mm*). The top loading beam was supported for out-of-plane lateral stability.

The relative accuracy of the two control strategies can be assessed based on the free body diagrams of Figure 2-4. In control 1, when a load P is specified, it is achieved provided there is sufficient hydraulic power. In control 2, however, when a load P is specified, load $P/2$ is maintained by the master vertical actuator, whereas the slave actuator could have a variation in force from $\frac{P}{2}\times\frac{(L+d)}{(L-d)}$ to $\frac{P}{2}\times\frac{(L-d)}{(L+d)}$, where d=bearing displacement. Consequently, the load applied on the bearing varies from $\frac{PL}{(L+d)}$ to $\frac{PL}{(L-d)}$.

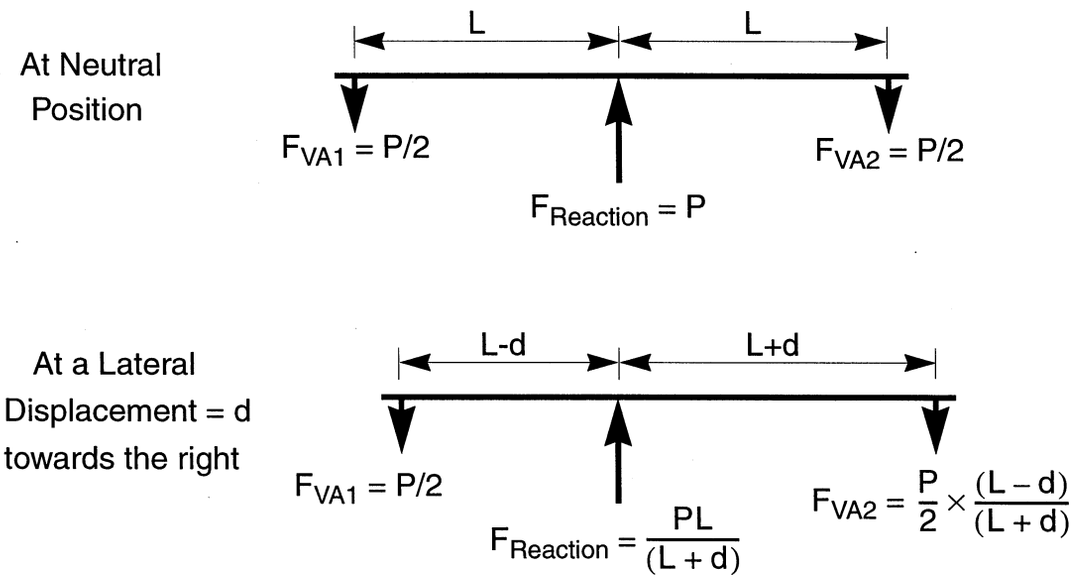

Figure 2-4: Variation of Vertical Load in Control 2

This variation occurs due to the requirements of equilibrium of the loading beam and is present even at low velocity quasi-static testing. That is, when *d=152 mm* (current capacity of the horizontal actuator), the variation in the axial force on the bearing is approximately minus *11*-percent to plus *14*-percent of the specified value. At *d=95 mm* (at which most of the testing was conducted), the variation is approximately $\pm$*8*-percent of the specified value.

2.4 Instrumentation

A total of 10 channels were monitored during the shear testing of bearings and 14 during compression tests. Figure 2-5 illustrates the instrumentation diagram. These include three measurements from the reaction load cell, the displacement (extension / contraction) and load in each vertical actuator (total of four), the displacement and load in the horizontal actuator (total of two) and the horizontal acceleration of the loading beam. During the compression-only tests, four additional displacements were monitored. These were the relative displacements of the top and bottom plates of the bearing at each of its four corners.

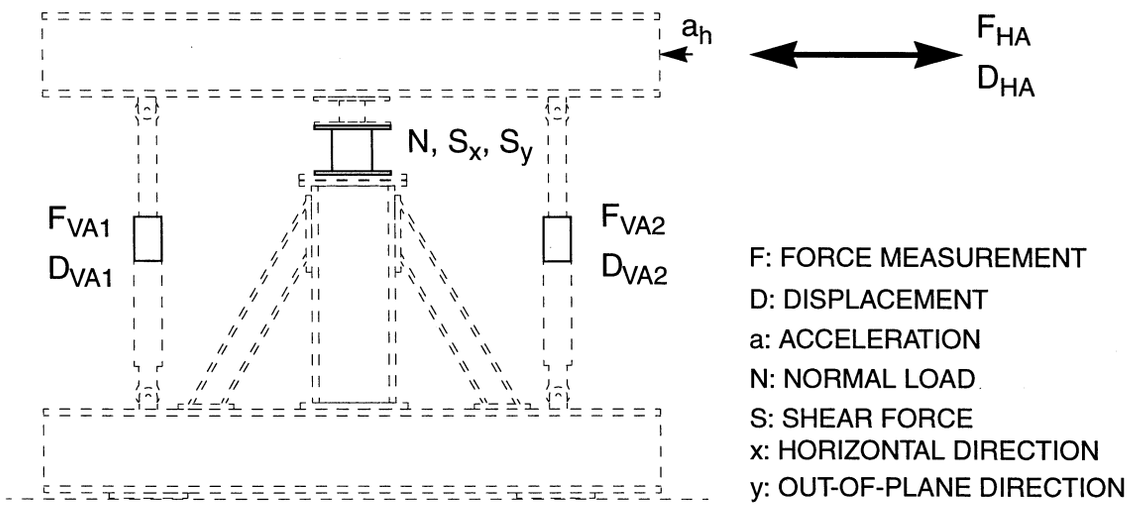

Figure 2-5: Instrumentation Diagram

2.5 Prestressing Tendon Capability

The machine has the capability for developing additional axial load on bearings by use of a prestressing tendon arrangement. Prestressing of bearings may be desirable for avoiding the occurrence of uplift conditions either because they may be catastrophic (e.g., rupture of rubber bearings or overturning of slender structures), detrimental (e.g., significant uplift in sliding bearings and impact on return), or simply undesirable by the responsible engineer. The prestressing of isolation bearings has been proposed by Logiadis (1996).

The testing machine has provisions to install two prestressing tendons on each side of the tested bearing. In its current configuration the arrangement features:

a. Spherical bushings for avoiding bending of the tendons. The bushings are at a distance of 1970 mm with a capability of adjustment of the distance by $\pm 50mm$.
b. Fiberglass tendons of *7.5 mm* diameter and *1100 mm* free length. The tendons have been supplied by SUSPA Spannbeton GmbH, Langenfeld, Germany. They have a low Young's modulus (*64,000 MPa*) and large ultimate strength (exceeding *1250 MPa*), which makes them ideal for bearing prestressing.
c. Load cells for direct measurement of the prestressing force.
d. Integrated capability for developing the initial prestress without the use of hydraulic jacks.

Figure 2-6 shows a view of the testing machine with installed prestressing tendons during the testing of a flat sliding bearing. Figure 2-7 shows a close-up view of the same arrangement, whereas Figures 2-8 and 2-9 show two views of the arrangement during the testing of a prestressed elastomeric bearing.

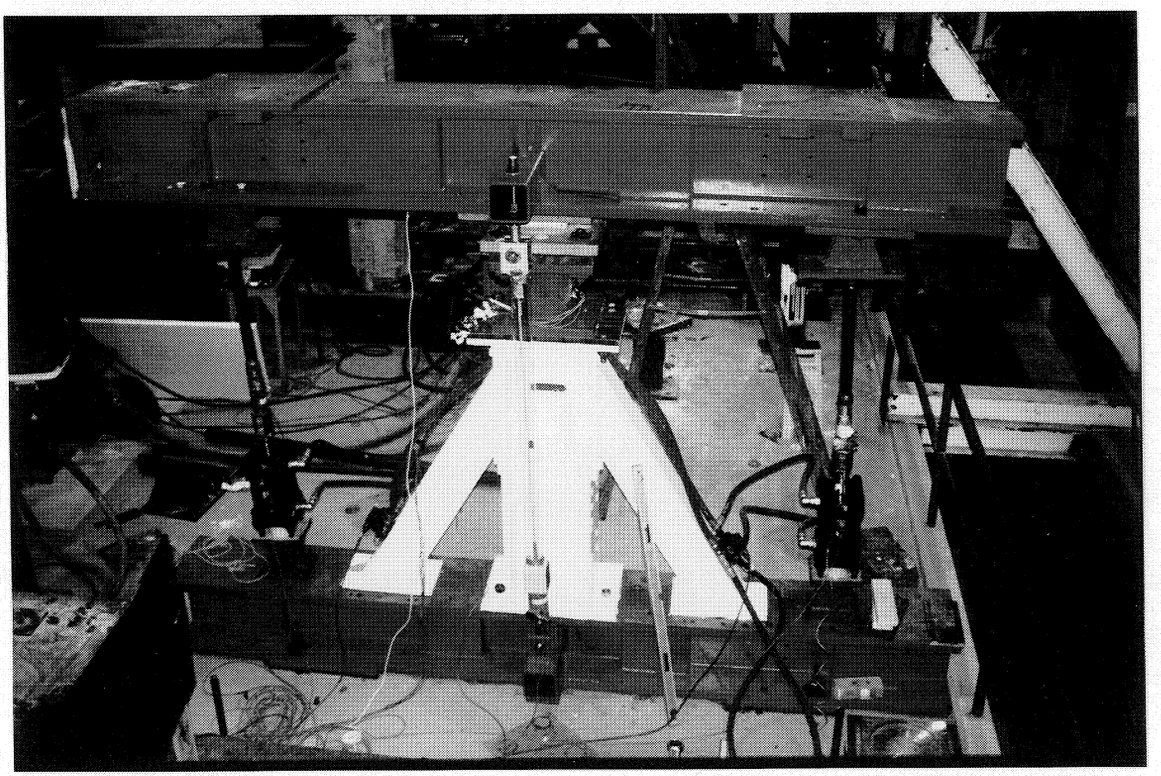

Figure 2-6: Testing Machine with Prestressing Tendons

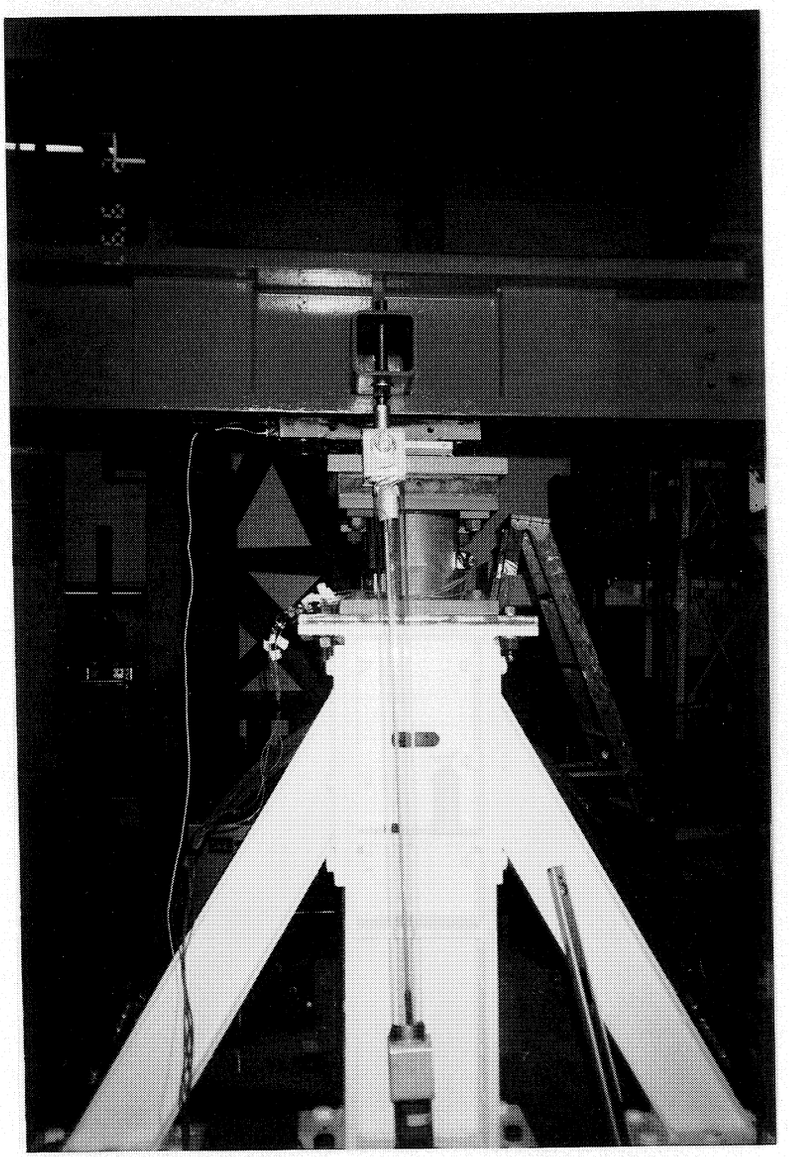

Figure 2-7: Close-up View of Prestressing Tendon Arrangement

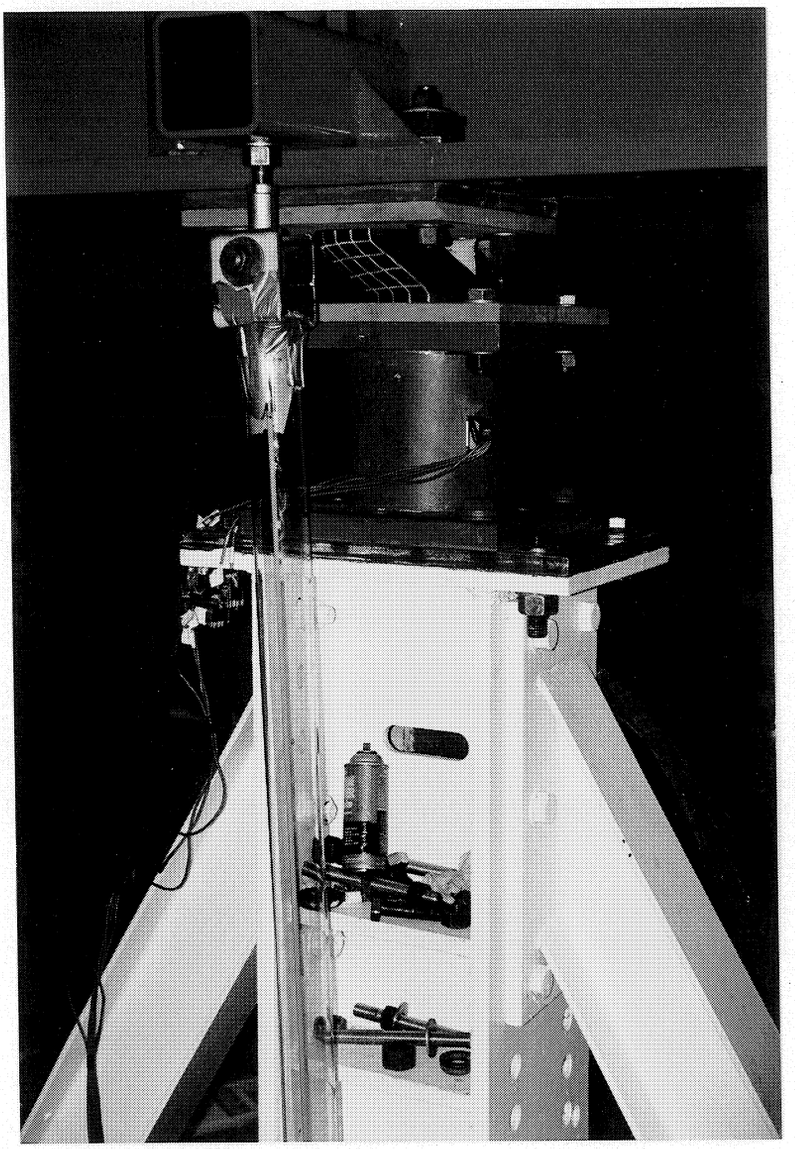

Figure 2-8: Prestressed Elastomeric Bearing Testing

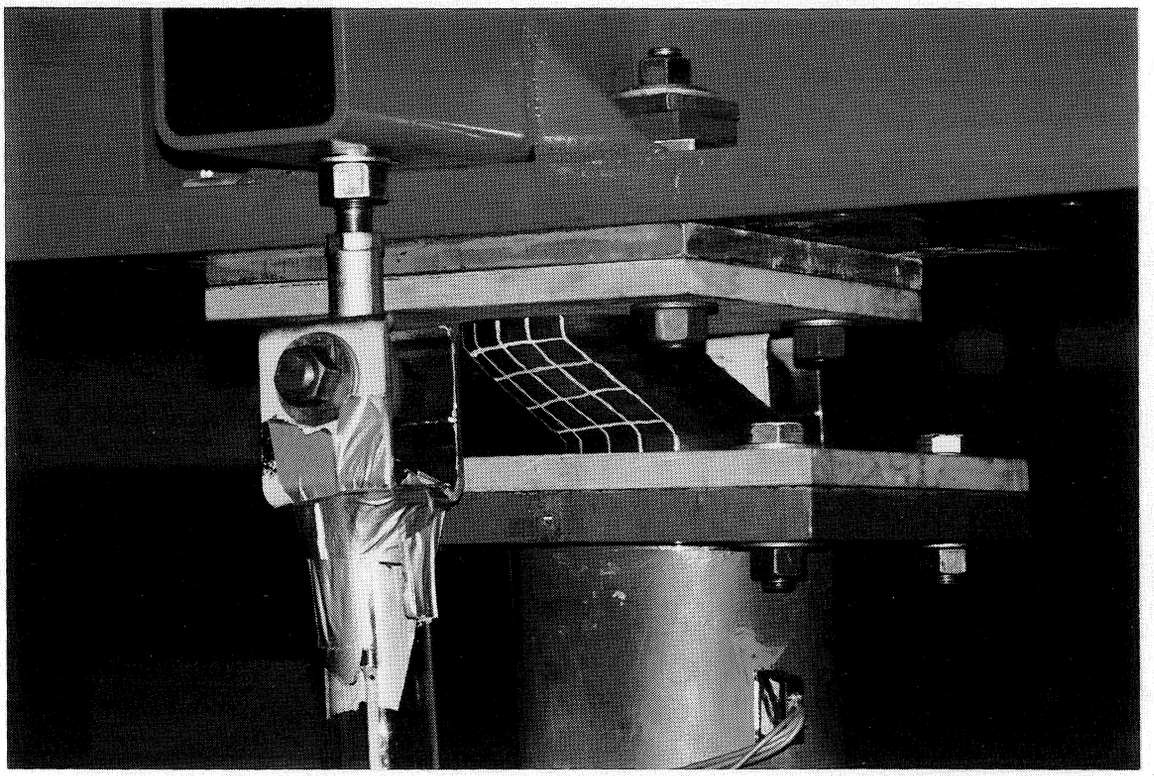

Figure 2-9: Close-up View of Elastomeric Bearing Testing

2.6 Examples of Test Results

2.6.1 Example of Results for Variable Axial Load

The testing machine is capable of exerting variable axial load on the bearing. This variation can be made a function of the horizontal displacement of the bearing or an independent programmable function. Figure 2-10 shows the results obtained in the variable axial load testing of an FPS bearing (Constantinou et al., 1993; Tsopelas et al., 1996a). Here, the axial load on the bearing is made a function of its lateral displacement: peak axial load at the neutral position and minimum load at either extreme lateral displacement. Testing was conducted using control strategy No. 1. The lateral force in the figure was measured by the reaction load cell. The axial load on the bearing was directly measured by the reaction load cell. The vertical actuator force is the sum of the forces monitored by the actuator load cells and the weight of the loading beam. Evidently, this measurement agrees with that of the reaction load cell.

The FPS bearing had a radius of curvature $R = 558.8\ mm$. The lateral force, F, needed to maintain a lateral displacement u is (Constantinou et al., 1993; Tsopelas et al., 1996a)

$$F = \frac{N}{R}u + \mu N sign(\dot{u}) \tag{2-1}$$

where N = axial load and μ = coefficient of friction. The recorded lateral force in Figure 2-10 shows a peculiar shape, however, this is entirely the result of the variable axial load. That is, if (2-1) is re-written as

$$\frac{F}{N} = \frac{u}{R} + \mu sign(\dot{u}) \tag{2-2}$$

we observe that the loop of the normalized lateral force versus displacement should be a perfect rigid-plastic loop with slope equal to $1/R$. Indeed, this is the behavior depicted in the bottom right figure except for a minor deviation due to the dependency of the coefficient of friction on apparent pressure.

Figure 2-11 shows test results from the testing of a flat sliding bearing under a different history of axial load. The load varies from *20 kN* at one peak lateral displacement to *130 kN* at the other peak displacement.

2.6.2 Importance of Direct Measurement of Lateral Force

The machine features a large and stiff loading beam having a mass of *1496 kg*. If measurements of the lateral force are made by using the load cell of the horizontal actuator, the inertia effects in dynamic testing may be significant. Correcting for these inertia effects by using measurements of the acceleration is not always successful and it may lead to erroneous results.

For example, consider the case of the tested flat PTFE sliding bearing of which the results are shown in Figure 2-11. Figure 2-12 shows again the recorded friction force (that is, the lateral force) versus displacement as obtained:

a. By the reaction load cell, which represents the most accurate measurement.

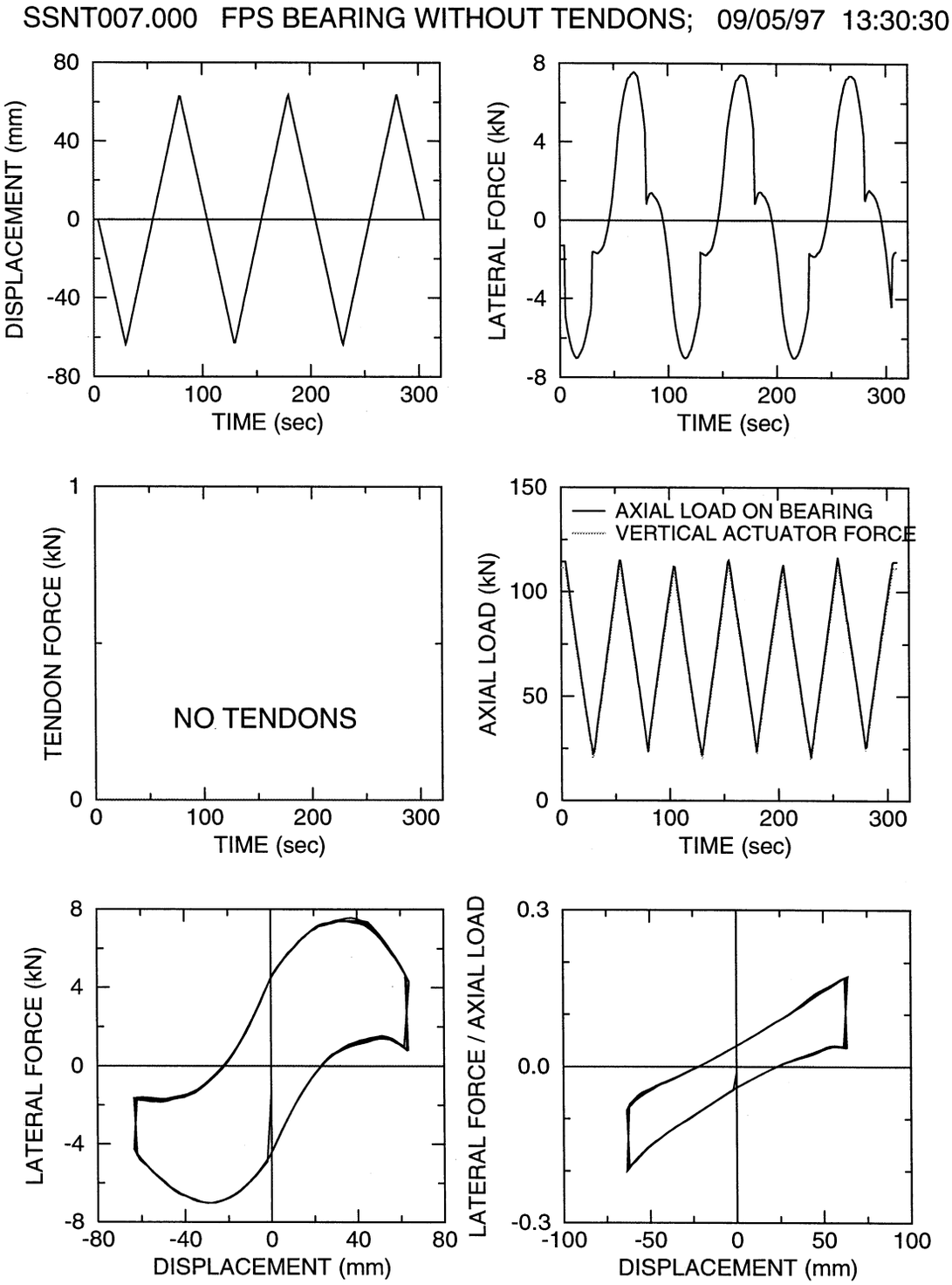

Figure 2-10: Example of Results in the Testing of an FPS Bearing under Variable Axial Load

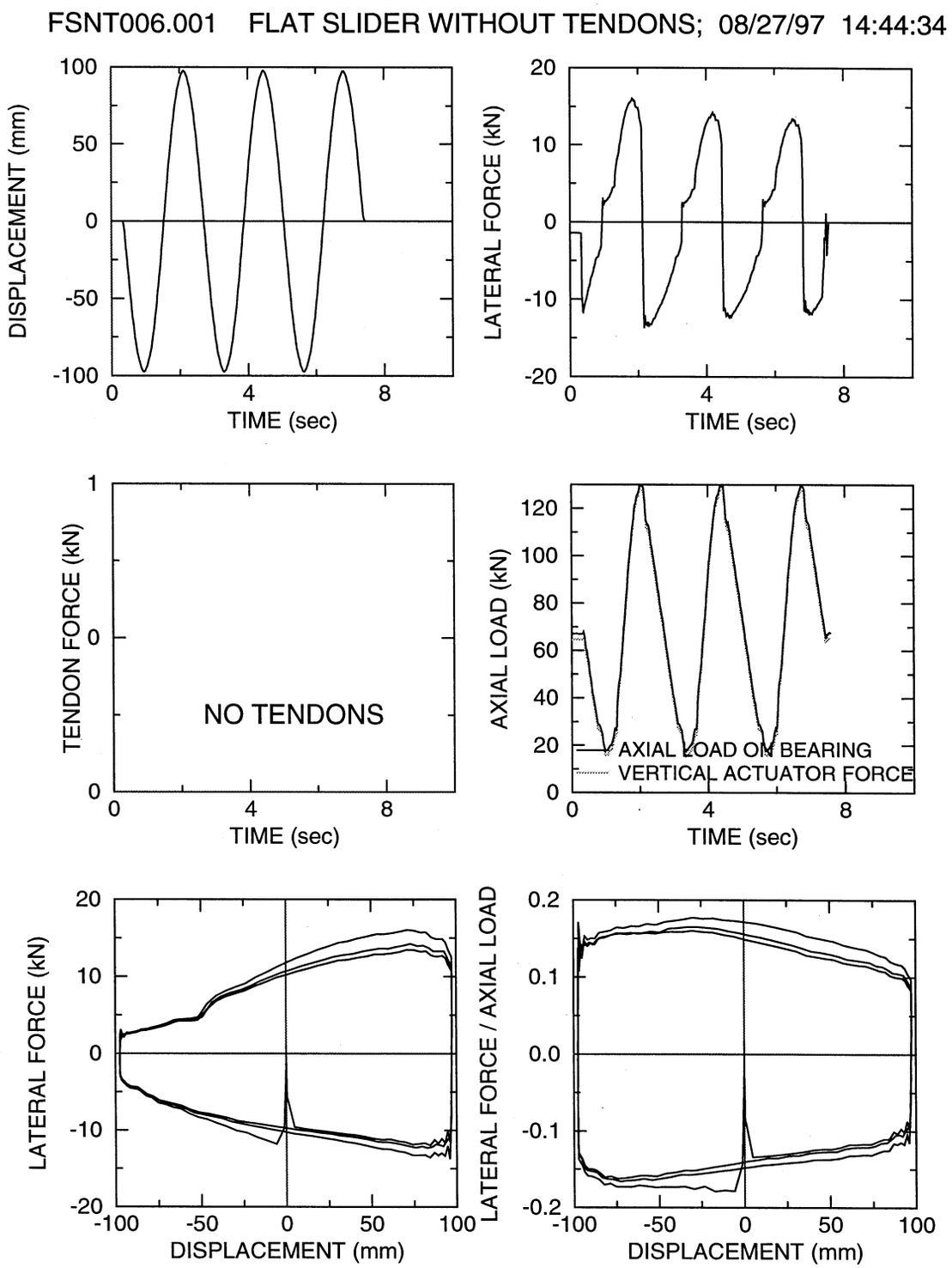

Figure 2-11: Example of Results in the Testing of a Flat PTFE Sliding Bearing under Variable Axial Load

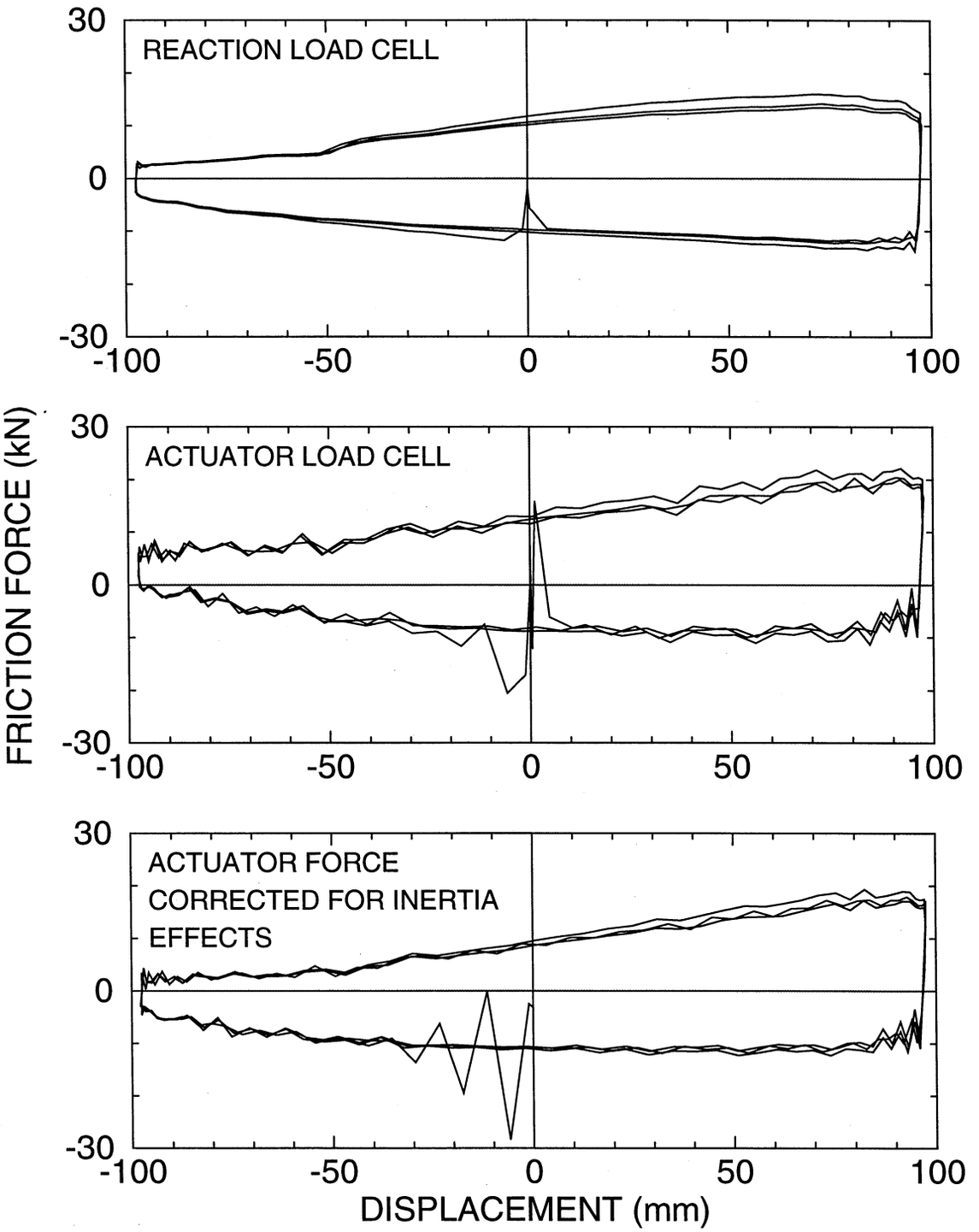

Figure 2-12: Loops of Friction Force versus Displacement in the Testing of a Flat Sliding Bearing as Measured by Various Mean

b. By the actuator load cell which includes the effects of the inertia force.
c. By the horizontal actuator load cell and correcting for the inertia effects by using records of the acceleration of the moving beam.

While the correction succeeded in removing much of the fluctuations measured by the actuator load cell, it did not so at the start of the experiment where the corrected friction force exhibits wild fluctuations. These fluctuations may be mistakenly interpreted as stick-slip.

2.6.3 Results of Testing of Prestressed Isolators

Figure 2-13 presents the results in the testing of a prestressed flat sliding bearing under constant gravity load. In this case an initial prestress of approximately *20*-percent of the gravity load was applied. As seen in Figure 2-13 the gravity load, as developed by the vertical actuators, exhibits fluctuations of about $\pm$*15*-percent around the specified value of *95 kN*. This error is the result of the utilized control strategy (see Section 2.3) and the inability of the vertical actuator servovalves to supply the required oil flow.

2.7 Summary of Capabilities of Testing Machine

Table 2-1 presents a summary of the capabilities of the testing machine. The machine has been designed for the load capabilities of the utilized actuators. However, the current load capabilities of the machine are limited by the rated capacity of the reaction load cell.

Table 2-1: Summary of Isolator Testing Machine Capabilities

Vertical Load Capacity (based on vertical actuator capacities)	635 kN compression 600 kN tension
Current Vertical Load Capacity (as limited by capacity of reaction load cell)	220 kN
Horizontal Load Capacity	245 kN
Current Horizontal Load Capacity (as limited by capacity of reaction load cell)	90 kN
Vertical Displacement Capacity	$\pm$50 mm
Horizontal Displacement Capacity	$\pm$ 150 mm
Bearing Top Rotation Capacity	$\pm$ 2 degrees
Specimen Plan Dimensions	within square of 300 mm x 300 mm
Specimen Height	adjustable within 6 mm to 230 mm

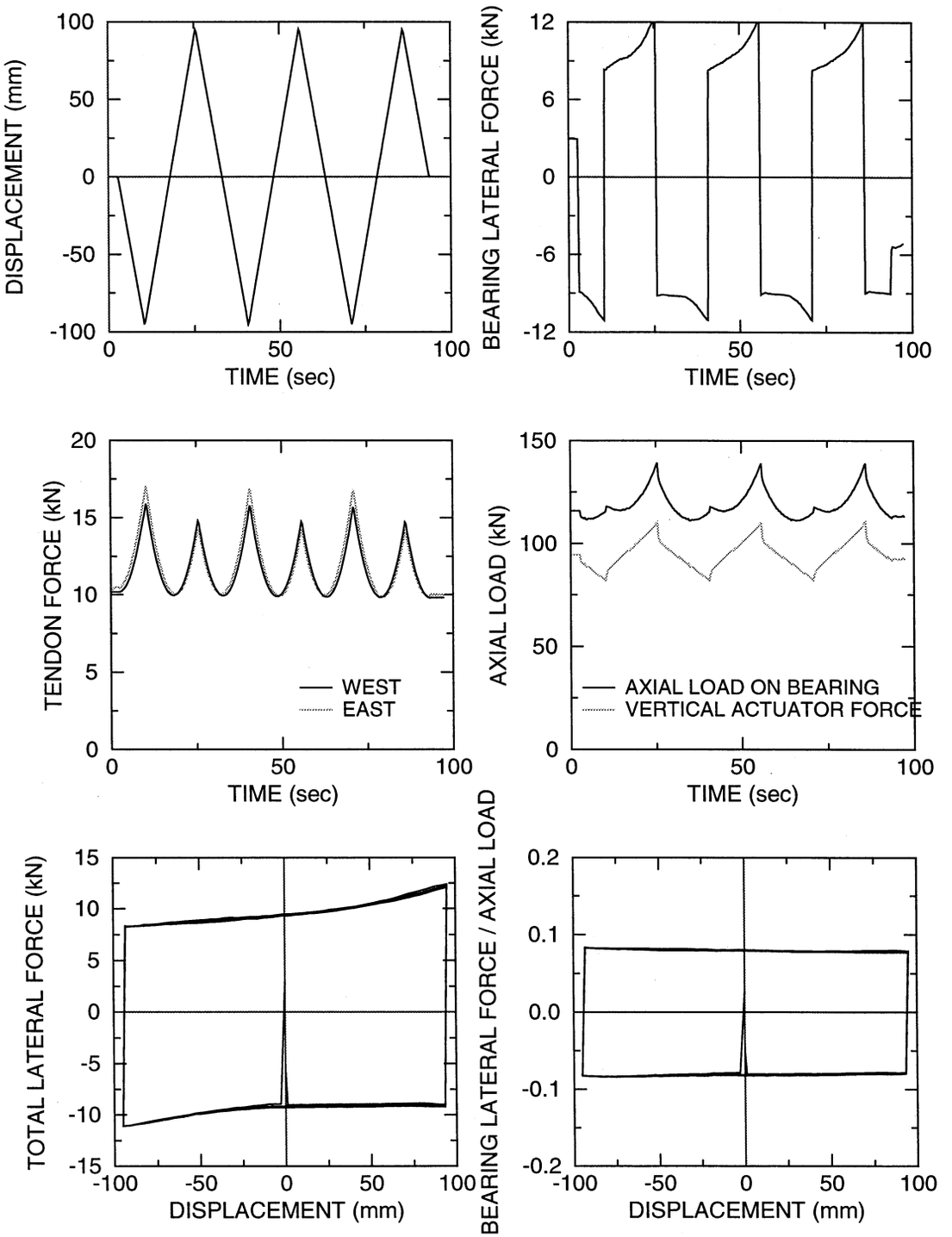

Figure 2-13: Results in the Testing of a Prestressed Flat PTFE Sliding Bearing under Specified Constant Gravity Load (FST2002.000)

SECTION 3

TESTING AND MODELING OF PRESTRESSED ISOLATORS

3.1 Introduction

Isolation bearings are typically subjected to varying axial load during seismic excitation. Under certain conditions bearings experience either tensile forces (e.g., bolted rubber bearings) or uplift (e.g., sliding bearings and doweled rubber bearings). A variety of conditions may result in either tensile forces or uplift in bearings. Examples are:

(a) Slender buildings with large height to width ratio. A notable example of such building is the Excel Minami-Koshigaya building in Koshigaya City, Japan. Completed in 1990 by Sumitomo Construction, this 10-story building is supported by 14 lead-rubber bearings in two rows of seven bearings at a distance of 9.3 m. To prevent uplift of the bearings, eight uplift restrainers were installed. Each consists of two massive steel beams at right angles and connected to the structure above and below the isolation bearings, respectively. They allow for some small vertical movement of 10 mm before engaging to prevent uplift.

Another uplift restraint mechanism has been described by Griffith et al. (1988, 1990). This mechanism is incorporated within a central hole in elastomeric bearings and can be activated only when the bearing undergoes either substantial uplift or substantial lateral deformation. Apart form this limitation, the mechanism is furthermore hidden within the bearing and can not be inspected (e.g., in case it has failed) without removal of the bearing and disassembly.

(b) Continuous concrete box girder bridges with large ratio of height of centroidal axis to the distance between the bearings. Often in this case the centroidal axis (and center of mass) of the girder above the piers is sufficiently high and the girder is supported by closely spaced bearings so that the combination of lateral earthquake force and unfavorable vertical excitation leads to bearing uplift.

(c) Bearings below braced columns. In such cases it has been the practice so far to create a massive and stiff basement above the isolators for altering the unfavorable load path and re-distributing the force to a large number of bearings, thus eliminating uplift.

The consequences of tensile forces or uplift in isolation bearings may be:

(a) Catastrophic when bearings rupture and can not anymore support the vertical load (unless the designer provides for an alternative load path) or the structure overturns. The latter case may appear an extreme situation. However, a simple calculation for the Excel Minami-Koshigaya building in Japan (height of 32 m above isolators, 9.3 m distance between isolators) shows that a lateral force of about 0.22 times the weight (or less when considering unfavorable vertical excitation) results in overturning.

(b) Problematic when significant uplift and impact on return cause damage to the bearings.

(c) Uneventful when the uplift is minor and measures have been taken in the design for the resulting axial and shear forces on the bearings and foundation. An example for such a case is the experiments reported in Al-Hussaini et al. (1994), in which a 7-story steel model structure supported by FPS isolators has been tested on the shake table. The bearings under the exterior columns in a moment frame configuration of the tested structure experienced uplift (this was monitored by load cells which measured a zero force transmitted to the column above the uplifted bearings). Nevertheless, the analysis of the structure with and without due account given for the uplift phenomenon resulted in nearly identical global responses of the structure in terms of story drifts, floor accelerations and story shear forces. However, the two analyses resulted in significantly different distribution of forces in the first story columns. Nevertheless, it is often the desire of the designer to avoid uplift or tensile forces out of concerns for the behavior of the bearings under conditions that are not well understood nor they are easily analyzed.

Apart from the aforementioned uplift restraint mechanism utilized in Japan and the mechanism of Griffith et al. (1988, 1990), Logiadis (1996) proposed the use of prestress for the prevention of tensile force and uplift in isolators. Prestressing tendons are used to develop, in a suitable arrangement, sufficient additional compressive force on the bearings so that tension or uplift are prevented. The arrangement contains tendons of suitable geometry and material properties in order to minimize the development of additional forces on the bearings and structure as a result of geometric changes in the tendons during the bearing horizontal movements.

In this section we describe tests conducted on prestressed isolation bearings under imposed combined horizontal movement and varying axial load. The tests were conducted with the isolator testing machine described in the previous section. Flat PTFE sliding bearings, spherical FPS sliding bearings and elastomeric bearings were tested. The objectives of these tests were to: (a) construct a practical prestressing arrangement, (b) generate experimental results that demonstrate the effect or prestress on the behavior of a variety of isolators, and (c) access the validity and accuracy of analytical methods to predict the behavior of prestressed isolators.

3.2 Theory of Prestressed Isolators

The prediction of the behavior of prestressed isolators depends entirely on the prediction of the additional forces developed in the tendons during lateral bearing displacement, provided that the bearing behavior without the effects of prestress is known. Logiadis (1996) presented a theory for prestressed isolators. Herein we revisit this theory for primarily the following reasons:

(a) to modify it for including a rigid portion within the prestressing arrangement,
(b) to simplify and present the theory in a concise manner, and
(c) to present a simpler theory for prestressed elastomeric bearings that can be carried out by hand calculations.

Figure 3-1 presents a schematic of a prestressing tendon in the initial and the deformed configurations. The tendon has a length of l_t and is connected to rigid parts for a total length of l of the moving part. Herein, we assume that length l is the distance between two pivoting points

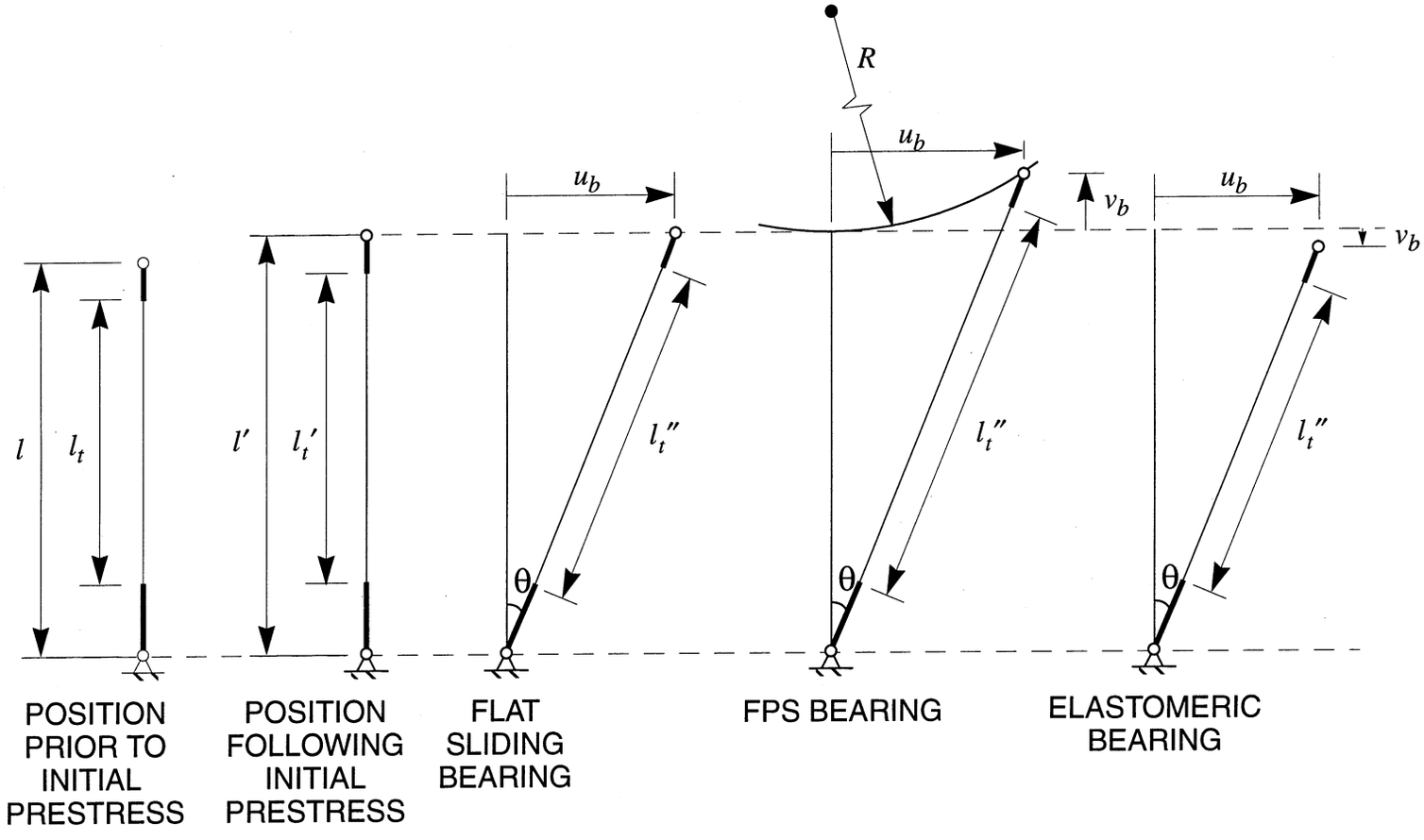

Figure 3-1: Schematic of Prestressing Tendon in Initial and Deformed Configurations

(hinges) in the tendon arrangement as it was the case in the tested configuration. Pivots, actually spherical bushings, were utilized in order to completely eliminate any bending action in the fiberglass tendons used. Note that the arrangement is shown to have a length l' following application of the initial prestress so that $l' > l$. For this, we have assumed that the prestressing equipment is located above the top hinge, as actually was the case in the tested arrangement. Had the prestressing equipment was between the two hinges, l' would have been equal to or less than l, however, the total length of the rigid parts of the tendon arrangement would have been reduced on initial prestress. In any case, the resulting strain and stress in the tendon are identical.

On lateral deformation, the top hinge moves laterally by an amount u_b (the horizontal bearing displacement) and vertically by an amount v_b (the vertical bearing displacement). Depending on the bearing used, the vertical displacement is either zero or nearly so (for flat sliding bearings), or nonzero and in the upward direction (for FPS bearings) or nonzero and in the downward direction (for elastomeric bearings). The case of elastomeric bearings is much more complex and will be discussed later in detail.

We will address each type of bearing separately. However, the state of strain and stress in the tendon depends on the extended length of the tendon due to the lateral and vertical displacement of the bearing. This length is denoted as l_t'', whereas the length following the initial prestress is denoted as l_t' as shown in Figure 3-1. Let the initial strain in the tendon (due to initial prestress) be ε_{in}, the added strain due to the lateral and vertical movement be ε and the total strain be $\varepsilon_t = \varepsilon_{in} + \varepsilon$. Note that the strain is herein defined as the change of length divided by the original length (l_t). The following relations may be easily derived by geometric considerations when assuming a vertically rigid bearing:

$$l_t' = l_t(1 + \varepsilon_{in}) \tag{3-1}$$

$$l_t'' = \{(l_t' + l_r + v_b)^2 + u_b^2\}^{1/2} - l_r \tag{3-2}$$

where $l_r = l - l_t$ is the length of the rigid parts of the tendon arrangement. In (3-2), v_b is the vertical bearing displacement which is taken positive when the movement is in the vertical upward direction. Since

$$\varepsilon = \frac{l_t'' - l_t'}{l_t} \tag{3-3}$$

it follows that the added strain is

$$\varepsilon = \left\{\left(\varepsilon_{in} + \frac{l}{l_t} + \frac{v_b}{l_t}\right)^2 + \left(\frac{u_b}{l_t}\right)^2\right\}^{\frac{1}{2}} - \frac{l}{l_t} - \varepsilon_{in} \tag{3-4}$$

and the total strain is

$$\varepsilon_t = \left\{\left(\varepsilon_{in} + \frac{l}{l_t} + \frac{v_b}{l_t}\right)^2 + \left(\frac{u_b}{l_t}\right)^2\right\}^{\frac{1}{2}} - \frac{l}{l_t} \tag{3-5}$$

The total force in the tendon arrangement is

$$P_t = \varepsilon_t EA \tag{3-6}$$

where E = modulus of elasticity of the tendon and A = area of the tendon. Herein, the assumption was made that the tendon exhibits linear elastic behavior which was indeed the case for the utilized fiberglass tendon. It is convenient to express

$$EA = \frac{P_{in}}{\varepsilon_{in}} \tag{3-7}$$

where P_{in} = initial prestress and ε_{in} = initial strain. Accordingly,

$$P_t = P_{in}\left(\frac{\varepsilon_t}{\varepsilon_{in}}\right) \tag{3-8}$$

Figure 3-2 illustrates the action of this force and its vertical and horizontal components. Note that the vertical component is added axial load on the bearing, whereas the horizontal component always opposes the direction of the lateral movement (thus, it is a restoring force). These forces are:

$$P_{tH} = P_t \sin\theta = P_t\left(\frac{u_b}{l_t'' + l_r}\right) \tag{3-9}$$

$$P_{tV} = P_t \cos\theta = P_t\left(\frac{l' + v_b}{l_t'' + l_r}\right) \tag{3-10}$$

where θ = angle of tendon inclination as shown in Figures 3-1 and 3-2. However, in most situations the horizontal and vertical displacements of the prestressed bearing are small by comparison to the length of the tendon arrangement (e.g., in our tests the maximum value of the ratio of u_b/l was *0.05*). Accordingly, angle θ is small and approximately $\cos\theta \approx 1$ and $\sin\theta \approx u_b/l \approx u_b/l'$. Thus,

$$P_{tH} \approx P_t\left(\frac{u_b}{l}\right) \approx P_t\left(\frac{u_b}{l'}\right), \qquad P_{tV} \approx P_t \tag{3-11}$$

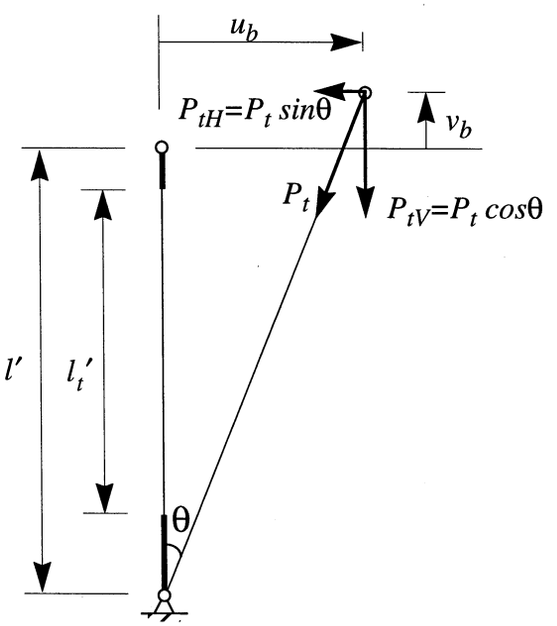

Figure 3-2: Total Force in Prestressing Arrangement and its Components

3.3 Behavior of Prestressed Flat Sliding Bearings

Flat sliding bearings are typically constructed with a supporting part capable of allowing for some limited rotation of the sliding interface. This part allows for some very small vertical displacement on application of axial load. We will neglect this very small vertical displacement and treat the bearing as having constant height. However, this will not be the case if the sliding interface is supported by an elastomeric bearing. In this case, the sliding interface will experience downward vertical movement on lateral bearing deformation as described in section 3.5.

We consider a flat (and vertically rigid) sliding bearing under a gravity load W which may be varying in time. In the absence of prestress the lateral force needed to maintain lateral motion u_b is (Constantinou et al., 1990)

$$F = \mu WZ \tag{3-12}$$

where Z = variable having values in the range $[-1,+1]$ and μ = coefficient of sliding friction. In general, the coefficient of friction depends on the velocity of sliding velocity $\dot{u}_b$ and apparent bearing pressure (normal load divided by apparent contact area) in approximately the following way:

$$\mu = f_{max} - (f_{max} - f_{min})\exp(-a|\dot{u}_b|) \tag{3-13}$$

where parameters f_{max}, f_{min} and a depend on the apparent pressure (Constantinou et al., 1990; Soong and Constantinou, 1994).

In the presence of prestress, (3-12) takes the following form:

$$F = \mu(W + P_{tV})Z + P_{tH} \tag{3-14}$$

in which P_{tV} and P_{tH} are given by (3-9) to (3-11) with $v_b=0$. Moreover and indirectly through the changing apparent pressure, the prestress affects the coefficient of friction.

For completeness, an equation for describing the variable Z is presented. It is based on the model of Wen (1976) as modified by Constantinou et al. (1990):

$$D_y\dot{Z} + 0.5|\dot{u}_b|Z|Z|^{\eta-1} + 0.5\dot{u}_b|Z|^{\eta} - \dot{u}_b = 0 \tag{3-15}$$

where $\dot{Z} = dZ/dt$, D_y = a "yield displacement" of the order of 0.5 mm and η = integer parameter (e.g., 3).

3.4 Behavior of Prestressed FPS Bearings

The behavior of FPS bearings has been documented in Constantinou et al. (1993) and Tsopelas et al. (1996a). In its simplest form this model takes the following form in the absence of prestress:

$$F = \frac{W}{R}u_b + \mu WZ \tag{3-16}$$

where R = radius of curvature of the spherical sliding surface, W = gravity load, μ is as described in (3-13), and Z is as described in the previous subsection.

In the presence of prestress, (3-16) takes the form:

$$F = \frac{(W + P_{tV})}{R} u_b + P_{tH} + \mu(W + P_{tV})Z \tag{3-17}$$

in which P_{tV} and P_{tH} are given by (3-9) to (3-11) with v_b (a positive quantity) given by

$$v_b = R - (R^2 - u_b^2)^{1/2} \tag{3-18}$$

This expression is easily derived from geometric considerations.

3.5 Behavior of Prestressed Elastomeric Bearings

The behavior of elastomeric bearings is much more complex than those of the sliding bearings for which the vertical movement is easily determined from geometric considerations. Moreover, the behavior of elastomeric bearings in shear is complex and is dependent on the compound used (particularly in the case of high damping rubber bearings), strain, axial load and frequency. However, it is generally acceptable to describe the shear behavior of elastomeric bearings by a smooth hysteretic model. That is, the lateral force needed to maintain the motion u_b may be described by

$$F = \alpha \frac{F_y}{D_y} u_b + (1 - \alpha) F_y Z \tag{3-19}$$

where F_y = yield force, D_y = yield displacement, α = ratio of post-elastic to elastic stiffness and Z = variable described by (3-15). This model has been implemented in computer codes 3D-BASIS (Nagarajaiah et al., 1991; Tsopelas et al., 1994a) and the SAP2000 (Computer and Structures, Inc., 1997). The model of (3-19) describes well the behavior of lead-rubber bearings and provides an acceptable representation of the behavior of high damping rubber bearings (see Constantinou and Reinhorn, 1997, for some details). Modifications of this model for the case of very large deformations may be found in Tsopelas et al. (1994b).

The behavior of elastomeric bearings in compression and bending is amenable to rational analysis on the basis of the theory of elasticity and the assumption that rubber exhibits linear-elastic behavior. Kelly (1993) presents an excellent treatment of these problems. Herein we shall present only a sample of this theory.

Consider an elastomeric bearing under compression by a load W and without lateral movement. The bearing will undergo vertical displacement. The vertical stiffness K_v is

$$K_v = \frac{E_c A_r}{T_r} \tag{3-20}$$

where T_r = total rubber thickness, A_r = bonded rubber area and E_c = compression modulus. The compression modulus of the bearing is considerably larger than the elastic modulus of rubber due to the very small thickness of the rubber layers that result in stress conditions of confined compression. It is of interest to review various expressions proposed for the compression modulus.

The 1997 AASHTO draft (American Association of State Highway and Transportation Officials, 1997) uses the empirical expression

$$E_c = \left[\frac{1}{8G\bar{k}S^2} + \frac{1}{K}\right]^{-1} \tag{3-21}$$

where G = shear modulus of rubber, K = bulk modulus of rubber, k = material constant (=*0.75* for rubber of hardness *50*) and S = shape factor (loaded rubber area divided by the area free to bulge in an individual rubber layer). This expression is based on an *ad hoc* modification (term *1/K*) of the expression for the compression modulus assuming incompressible rubber. The correct expression for circular bearings is

$$E_c = \left[\frac{1}{6GS^2 f} + \frac{4}{3K}\right]^{-1} \tag{3-22}$$

in which f = *1* for bearings without a central hole (Kelly, 1993) and f = between *2/3* and *1* for bearings with a central hole (Constantinou et al., 1992). Central holes are typically used in elastomeric bearings for aiding in the curing process and for ease in the positioning of the steel shims (lead-rubber bearings have a central hole filled with lead, so that f = 1). Equation (3-22) produces results in very good agreement with experimental results as it will be shown for the tested prestressed bearing.

Of interest in the analysis of prestressed elastomeric bearings is the change in the height of the bearings on lateral deformation. A number of theoretical solutions have been proposed for the change in height. However, the simplest and one with great practical value is presented by Kelly (1993). Presented herein in a simplified form, the expression for the total reduction in height is

$$v_b^t = \frac{WT_r}{E_c A_r} + \frac{3(GA_r h + WT_r)u_b^2}{\pi^2 E_c I_r} \tag{3-23}$$

where h = height of bearing excluding the end plates (rubber thickness plus thickness of steel shims) and I_r = moment of inertia of the bonded rubber area. In deriving this expression it was assumed that the rotational modulus of the bearings is equal to $E_c/3$ (which is correct for incompressible material) and that the Euler buckling load of the bearing (for the undeformed configuration) is very much larger than load W and quantity GA_r (which is generally true for seismic isolation bearings). The first term in (3-23) represents the reduction of height on initial compression and the second term represents the effect of lateral deformation.

Equation (3-23) may now be used to illustrate the behavior of elastomeric bearings in combined compression and lateral deformation. For this we utilize the properties of the tested elastomeric bearing (it was of low damping rubber): E_c = *187 MPa*, G = *0.4 MPa*, A_r = *24,542 mm*^{2}, I_r = *49x10*^{6} *mm*^{4}, T_r = *47.3 mm* and h = *72 mm* (a more detailed presentation follows in section 3.9). Consider two cases of loading (both are similar to tested conditions): (a) the bearing is under constant load of W = *95 kN* and undergoes lateral movement from zero to u_b = *83 mm*, and (b) the bearing is subjected to load W linearly varying with the lateral displacement from *111 kN* to *22 kN* while the lateral displacement varies from zero to *83 mm*. Figure 3-3 illustrates the load-lateral deformation relation and the calculated total vertical displacement of the bearing. In case 1, we have a continuously increasing downward vertical displacement as we, in general, perceive to be the behavior of the elastomeric bearings. However, in case 2 we observe that the bearing gains

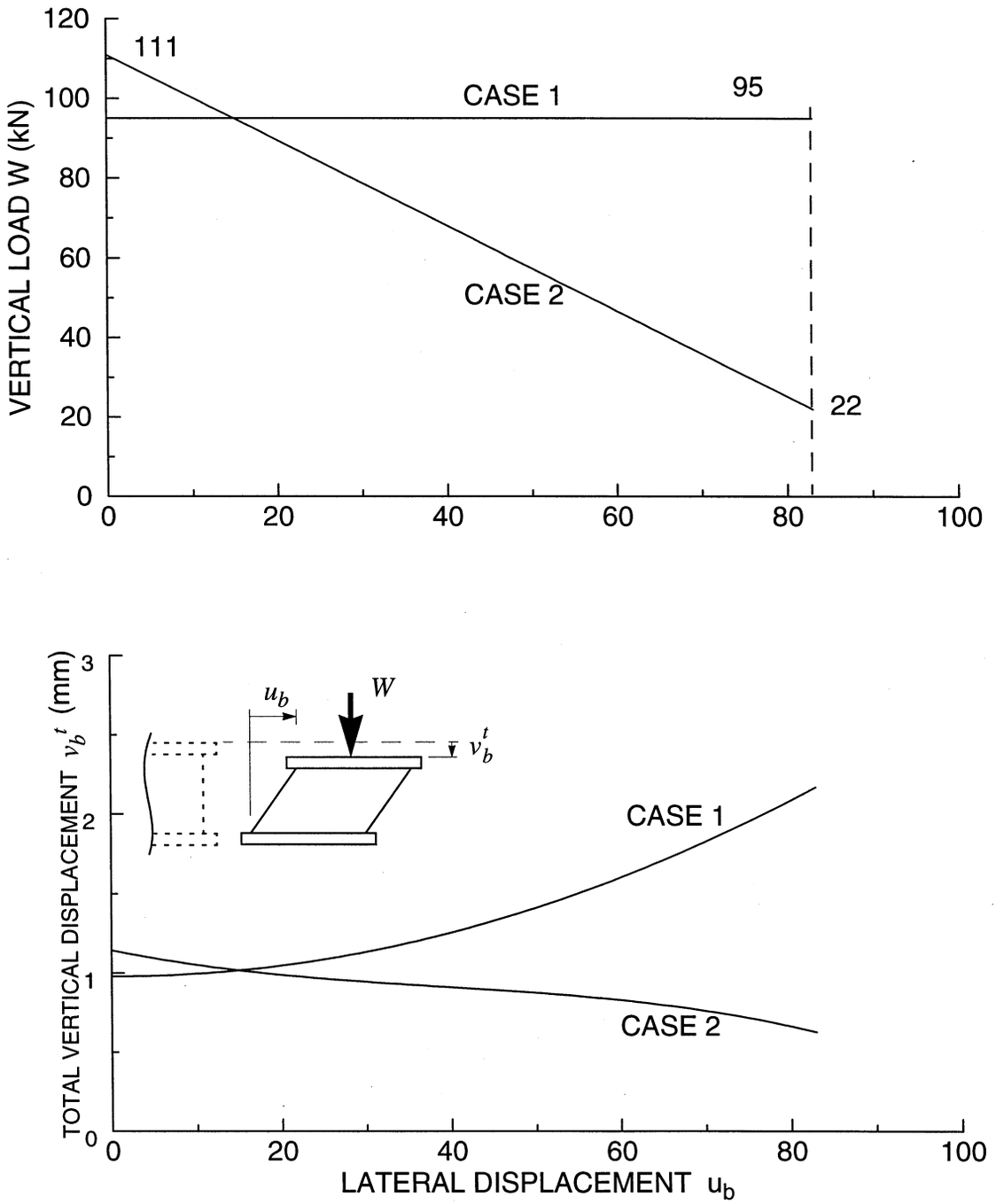

Figure 3-3: Calculated Vertical Displacement of Elastomeric Bearing

height as it is laterally deformed. This is the result of the reduction in axial load as the bearing in laterally deformed. Still, of course, the total vertical bearing displacement is negative, that is, it is in the downward direction.

It is now clear that elastomeric bearings may experience, on lateral deformation, a further reduction in height or an increase in height with respect to their position following application of the gravity load and prior to imposing the lateral movement. That is, the displacement v_b shown in Figure 3-1 for the elastomeric bearing could be in the opposite direction. For the loading shown in Figure 3-3, this additional vertical displacement of the example bearing is about *-1.2 mm* (further height reduction) or *+0.5 mm* (gain in height). These additional displacements are very small and they may appear to have an insignificant impact on the total strain in the tendons of the prestressed bearing. In reality, they do have an important effect. For example, consider the case of initial tendon strain of $\varepsilon_{in} = 7\text{x}10^{-3}$, $l = 1.8$ *m*, $l_t = 1.1$ *m*, $u_b = 83$ *mm* and v_b equal to either *-1 mm* or zero or *+1 mm*. Use of (3-5) results in the following values of the total tendon strain for the three cases of v_b: $7.82\text{x}10^{-3}$, $8.73\text{x}10^{-3}$ and $9.64\text{x}10^{-3}$.

The development of a theory for prestressed elastomeric bearings is complicated by the vertical stiffness of the bearing which exhibits a nonlinear dependence on lateral displacement. It is possible to develop a model in which the bearing has nonlinear vertical force-displacement relation with an instantaneous stiffness equal to dW/dv_b^t (as determined from equation 3-23) and the tendon arrangement has linear-elastic behavior. However, herein we are interested in the development of a simple solution that provides physical insight and which can be carried out easily.

Figure 3-4 illustrates the bearing and tendon arrangement following application of the gravity load W_o and the initial prestress P_{in}. The bearing deforms by an amount v_b^o:

$$v_b^0 = \frac{(W_0 + P_{in})T_r}{E_c A_r} \tag{3-24}$$

At this position, the distance between the pivots A and B is l' and the tendon length is l_t'. Length l_t' is still described by (3-1) with ε_{in} given by (3-7). On lateral deformation u_b, an additional vertical displacement v_b develops, which by virtue of (3-23) is:

$$v_b = v_b^0 - \frac{(W + P_{tV})T_r}{E_c A_r} - \frac{3[GA_r h + (W + P_{tV})T_r]u_b^2}{\pi^2 E_c I_r} \tag{3-25}$$

in which P_{tv} = vertical component of force in the tendon and W = gravity plus additional axial seismic load on the bearing (a known function of displacement u_b with a value W_o when $u_b = 0$). In (3-25), v_b is positive when the bearing gains height and negative otherwise. Moreover, $(W+P_{tV})$ is positive when compressive, and the equation is valid for $(W + P_{tV}) \geq 0$.

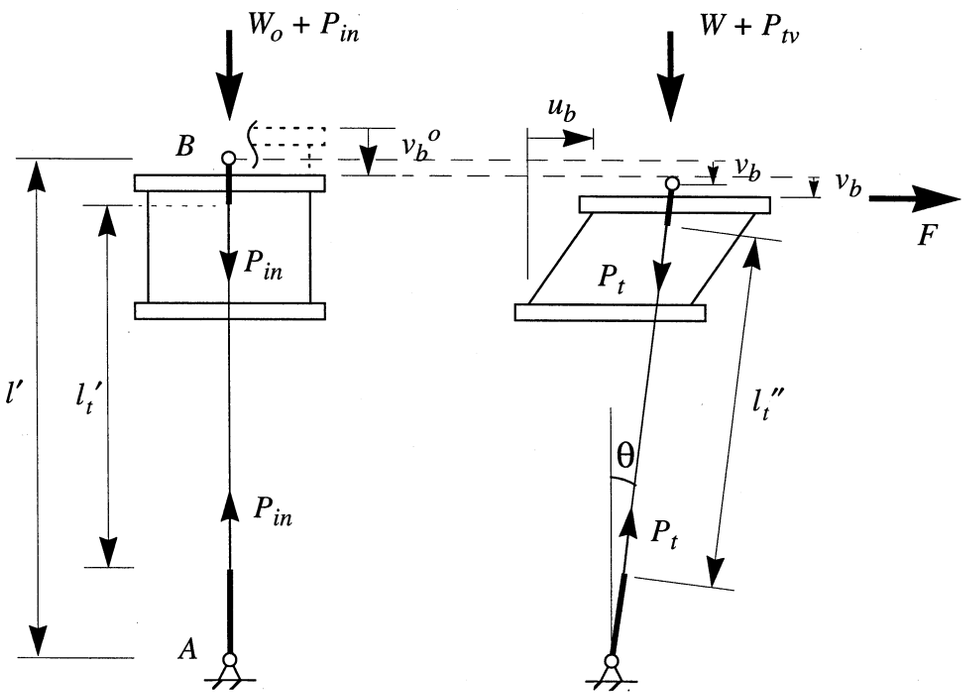

Figure 3-4: Schematic of Prestressed Elastomeric Bearing in Initial and Deformed Configurations

The vertical component of the total tendon force is given by (3-8), (3-10) and (3-11). Moreover, the total tendon strain ε_t is given by (3-5) in which l is given by

$$l = l' - \varepsilon_{in} l_t \tag{3-26}$$

Finally, the lateral force F needed to maintain the motion u_b is described by (see also equation 3-19):

$$F = \alpha \frac{F_y}{D_y} u_b + (1-\alpha) F_y Z + P_{tH} \tag{3-27}$$

where P_{tH} is given by (3-8) and (3-9) with l_t'' given by (3-2). Note that parameters α, F_y and D_y are dependent on the normal bearing load. In general this dependency is not well understood, however, it can be established for a particular bearing on the basis of testing. For low damping elastomeric bearings, as the tested one, these dependencies are minor and can be neglected.

3.6 Procedure for Analysis of Prestressed Isolators

The analysis of prestressed flat sliding and FPS Isolators is straight forward because either $v_b = 0$ or v_b is a known function of the lateral displacement u_b. Figure 3-5 present flow charts for the analysis of these two types of prestressed bearings when the lateral displacement u_b is a known function of time. The numbers in parenthesis in this figure refer to the equations for calculating the relevant quantities. Note that for any arbitrary displacement u_b, the states of strain and stress in

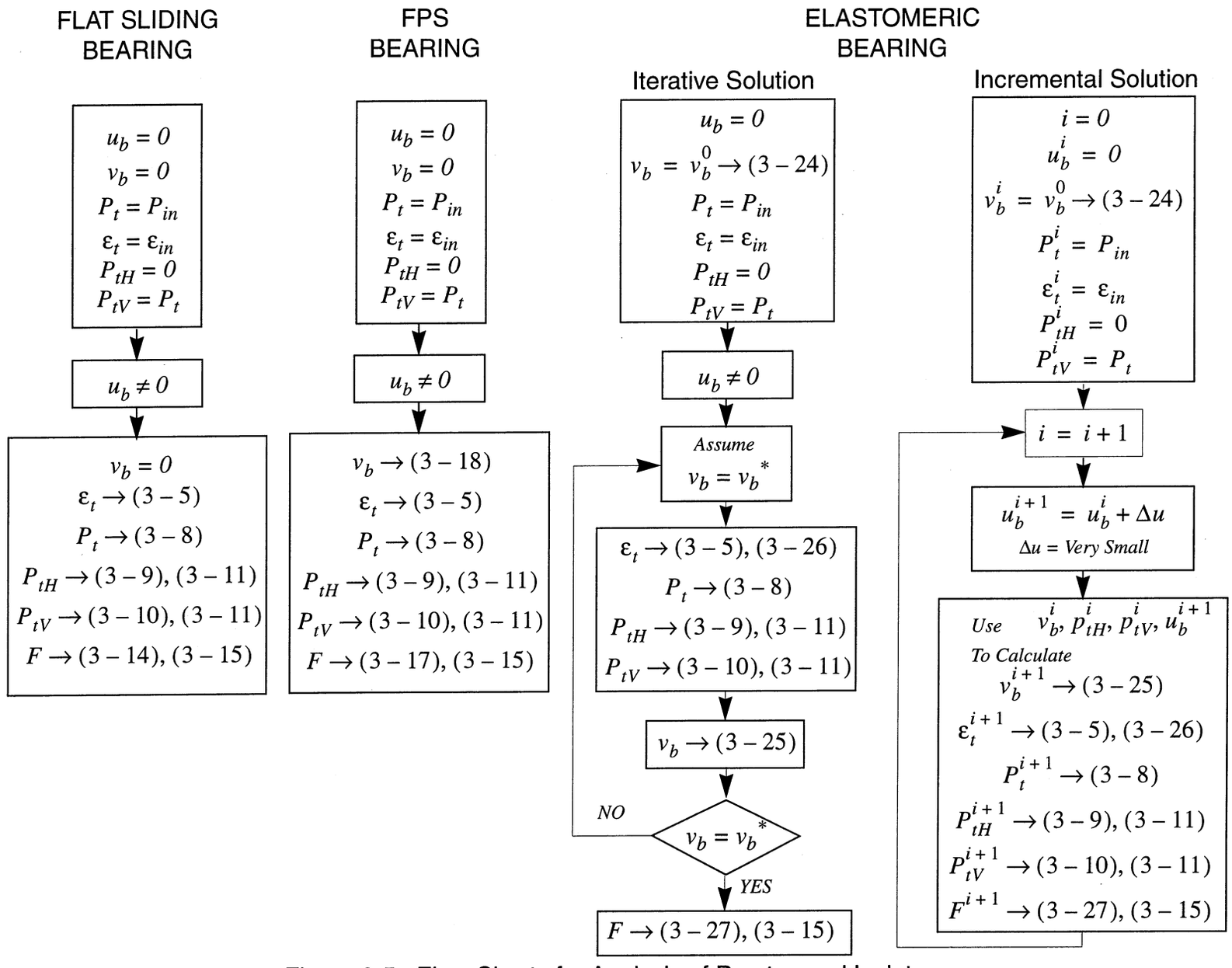

Figure 3-5: Flow Charts for Analysis of Prestressed Isolators

the tendons and the additional forces exerted by the tendons on the bearing can be readily determined. However, to determine the lateral force, F, that is needed to maintain motion of the bearing requires use of either (3-14) or (3-17) together with (3-15). The latter is a differential equation which needs to be integrated by a time-marching technique.

The analysis of prestressed elastomeric bearings is complicated by the dependency of the vertical bearing movement on the axial load. This relation, given by (3-25), is in an implicit form. Two options for analysis in this case are presented in Figure 3-5. One is an iterative solution in which the value of the vertical bearing displacement is assumed and progressively corrected until a required accuracy is achieved. The other is an incremental solution in which during small increments in the lateral displacement (or equivalently small time increments), the vertical bearing displacement and the tendon force are assumed constant. This method of analysis is the most convenient to use when the lateral bearing force needs to be calculated.

3.7 Testing Program

Testing without and with prestress of the following bearings was conducted:

(a) A flat sliding bearing consisting of an unfilled PTFE-stainless steel sliding interface. The PTFE had diameter of *95 mm*, thickness of *3.2 mm* and was recessed *1.6 mm* in a steel plate. The stainless steel was austenitic type 316, polished to mirror finish with a measured surface roughness of *0.04* μ*m* on the arithmetic average scale. The bearing featured a rotational part consisting of a soft adiprene disc. This bearing is described in Tsopelas et al. (1994b, 1996b).

(b) An FPS bearing of radius of curvature R = *558.8 mm* and a contact area of *2027* mm^2 (*50.8 mm* diameter). The sliding interface consisted of polished stainless steel and the PTFE composite No. 1 as described in Constantinou et al. (1993) and Tsopelas et al. (1996a).

(c) An elastomeric bearing consisting of 14 layers of grade 5 (hardness 50 durometer A) low damping natural rubber, each of thickness of *0.125 in* (*3.175 mm*) and 13 steel shims of 14 gage (thickness of *0.0747 in* = *1.9 mm*). The bearing had a central hole of *0.75 in* (*19 mm*) and it featured *0.75 in* (*19 mm*) thick end plates with bolted connections.

Figure 3-6 illustrates the bearing geometry as it was specified to the manufacturer.

Prestress was developed with the tendon arrangement shown in Figure 3-7 (two of these arrangements were utilized for symmetric prestress). The arrangement included a load cell for measuring the initial prestress and the time history of prestress during testing. Spherical bushings were used to prevent the development of bending in the fiberglass tendons.

The tendons were supplied by SUSPA Spannbeton GmbH of Langenfeld, Germany. They were *7.5 mm* in diameter and had a length of *1100 mm*. The exact properties of the tendons were not known. What was known is that the behavior is elastic to strains exceeding 2-percent, the ultimate strain exceeds 2-percent, the modulus of elasticity is *64,000 MPa* (this was confirmed in the testing) and that the total strain should be restricted to less than *0.7*-percent under service conditions and to less than about *1.5*-percent under seismic conditions. Information on its creep behavior was not available other than that it exhibits less creep than steel tendons of comparable strength.

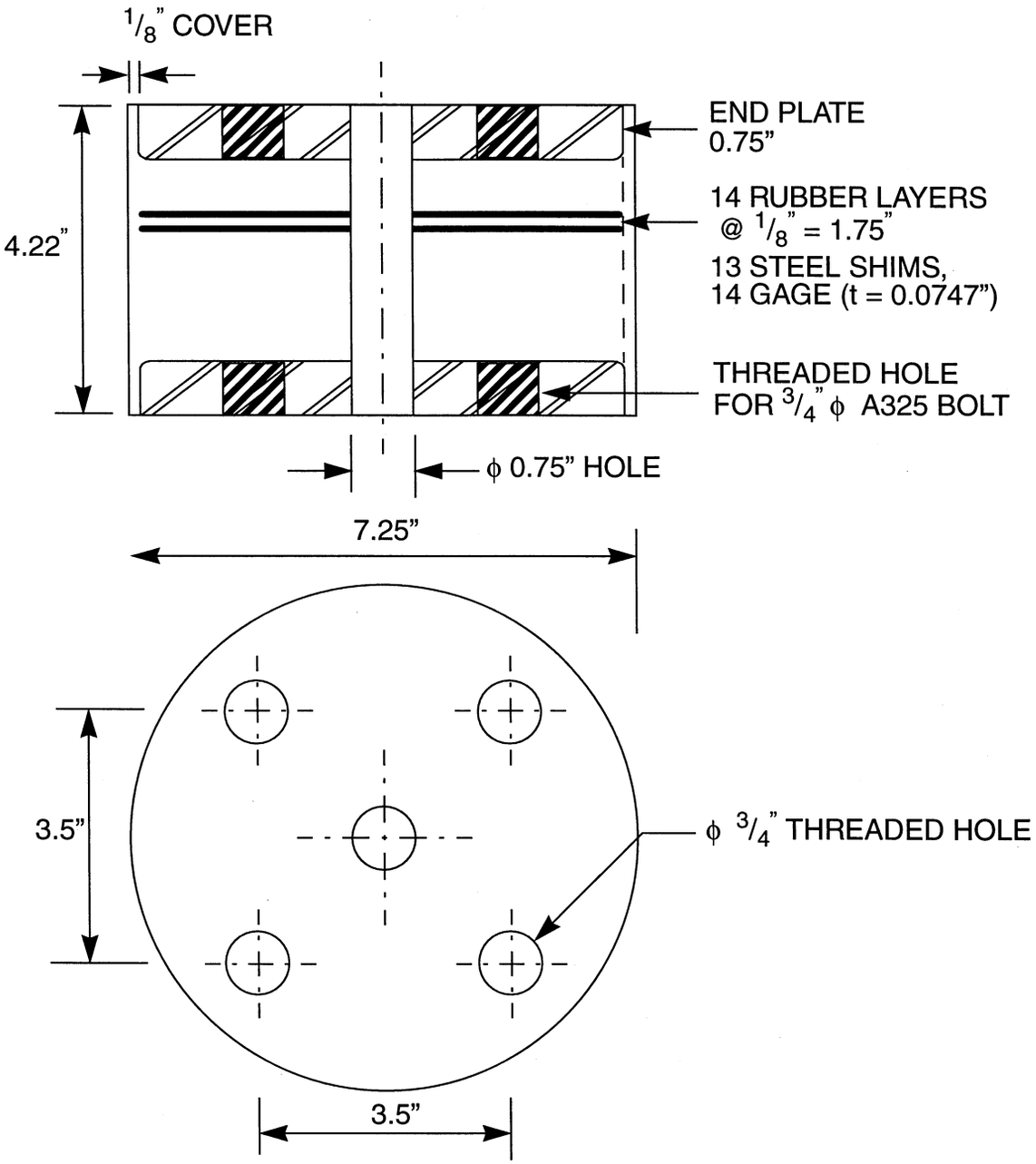

Figure 3-6: Geometry of Tested Elastomeric Bearing (1 in = 25.4 mm)

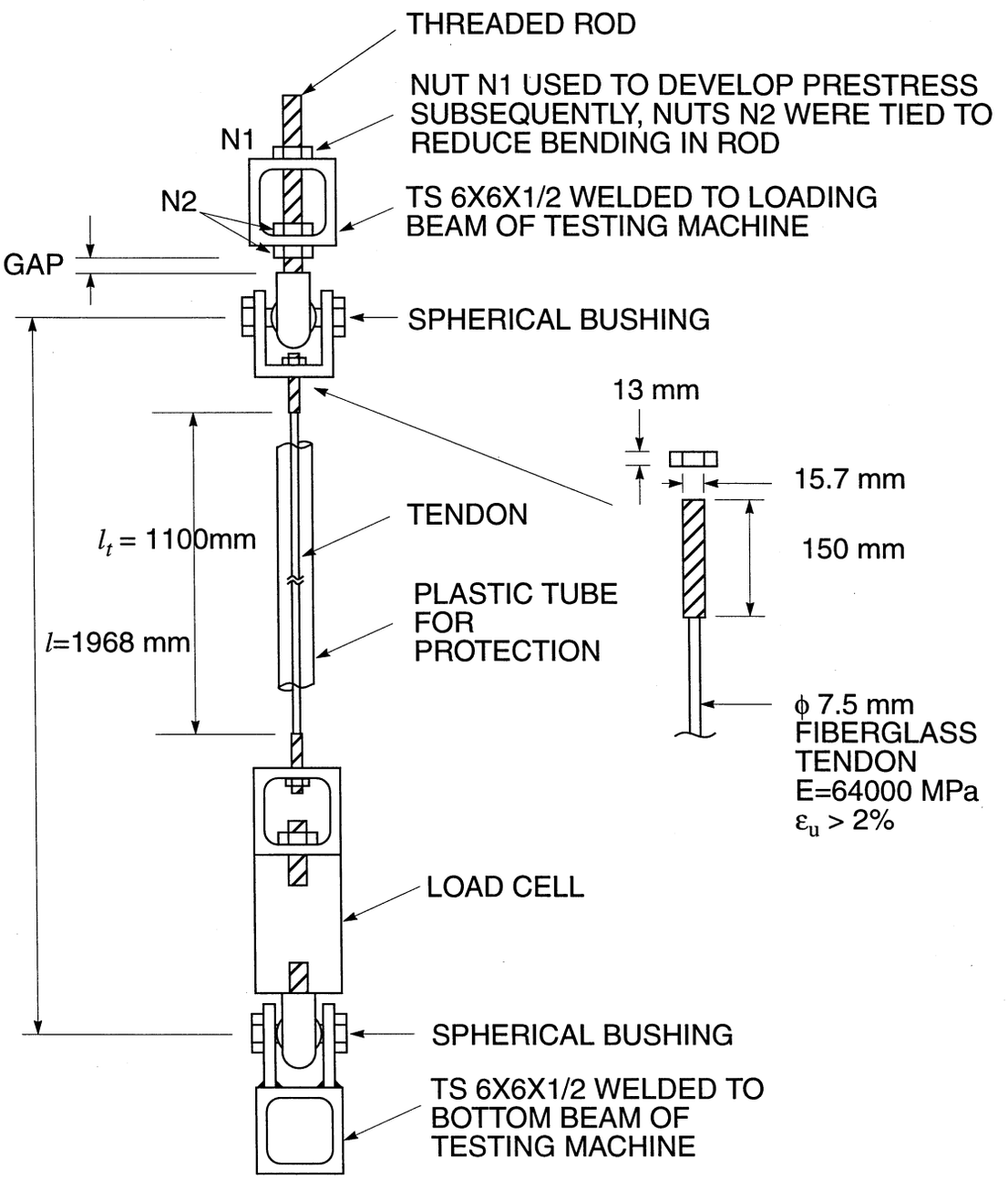

Figure 3-7: Schematic of Prestressing Tendon Arrangement Used in Testing of Prestressed Bearings

The tendons exhibited an exceptional strength (over *1250 MPa*) which was more than sufficient for the requirements of the testing. Nevertheless, the tendon arrangement was enclosed in a plastic tube (see Figures 2-7 and 3-7) for protection against contamination of the laboratory by fine glass fibers (which are highly abrasive) in the case of failure. However, it may be recognized in the Figure 3-7 that the weak link in this arrangement is the connection of the steel threaded end of the tendon to the U-shaped frame above and the square frame below. The used connecting nut of only *13 mm* thickness was insufficient for developing the full strength of the threaded rod end (which was hollow with an inside diameter of *8 mm*) of the tendon. We had failure of the arrangement in two occasions, both occurring at this connection.

The testing program included tests without tendons and with tendons prestressed at three different levels of initial prestress. Moreover, the gravity load included (a) constant load, (b) variable load designated as VL1 and illustrated in Figure 3-8, and (c) variable load designated as VL2 and also illustrated in Figure 3-8.

3.8 Test Results

A representative sample of test results is presented in Appendix A. For a complete list of the test results see Kasalanati (1998). The appendix contains a table describing the conditions of each test and one page of graphs for each of the conducted tests. Herein, we present a sample of results that demonstrate the observed behavior.

Figure 3-9 compares the behavior of the flat sliding bearing without and with the effect of prestress (these are tests FSNT003.001 and FST3003.000 in Appendix A). The bearing was subjected to the shown gravity load (specified constant at *96 kN* but exhibited fluctuations due to the utilized control strategy). In the case of the prestressed bearing the initial total prestress was *40 kN*, which fluctuated due to the lateral movement as shown in the figure. That is, the prestress amounted to *40* to *50*-percent of the gravity load. The recorded lateral force-displacement loops in the two cases are shown in the second row of graphs. First, observe that the loop for the case of no prestress is slightly asymmetric. It is the result of the fluctuations in the gravity load. Second, observe the effect of prestress on the force-displacement loop. It is as predicted by theory, that is, a uniform increase in lateral force due to the initial prestress and a mild displacement-dependent increase in lateral force due to the restoring force provided by the tendons and due to the additional axial force provided by the displaced tendons. Moreover, it is of interest to observe that the loops of normalized lateral bearing force (which is the friction force) versus displacement show typical frictional behavior, with the one of the prestressed bearing exhibiting slightly less friction coefficient as a result of the higher apparent pressure.

Figure 3-10 presents the results in the case of a test with significant fluctuations in the gravity and seismic loads on the flat sliding bearing. The imposed history of vertical load (type VL1 in Figure 3-8) consisted of about *68 kN* of dead load component and a seismic load component (due to overturning moment) that resulted in a total load on the bearing of zero at the extreme negative displacement and about *160 kN* at the extreme positive displacement. It can be a realistic loading condition on a bearing installed under an exterior column of a moment frame. Without prestress the bearing would have experienced uplift. The imposed prestress prevented the occurrence of

uplift and maintained a substantial compressive load on the bearing at all times. This was accomplished at the expense of some *30*-percent increase in the peak gravity (dead load plus seismic load) on the bearing.

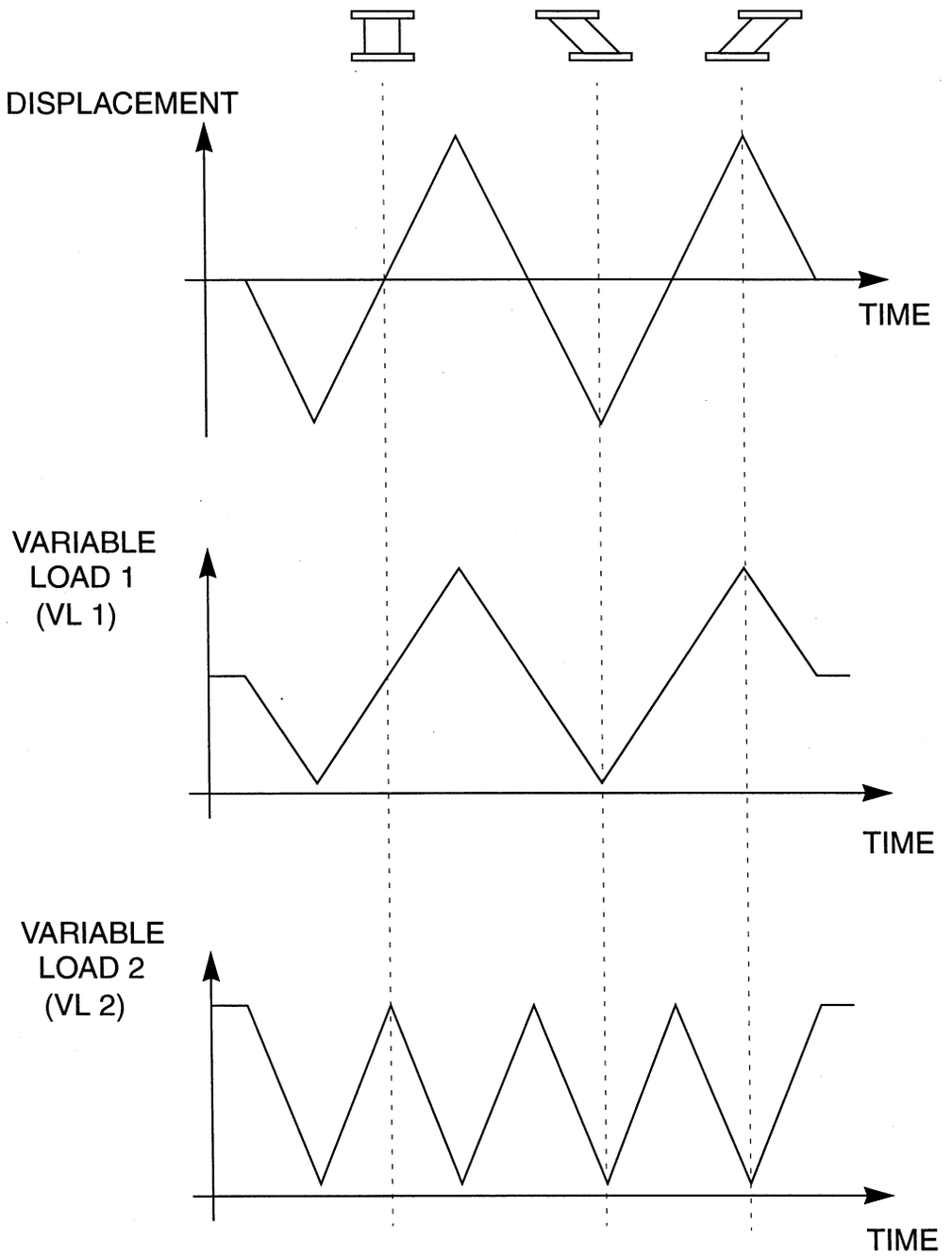

Figure 3-8: Illustration of Variable Gravity Load Types VL1 and VL2

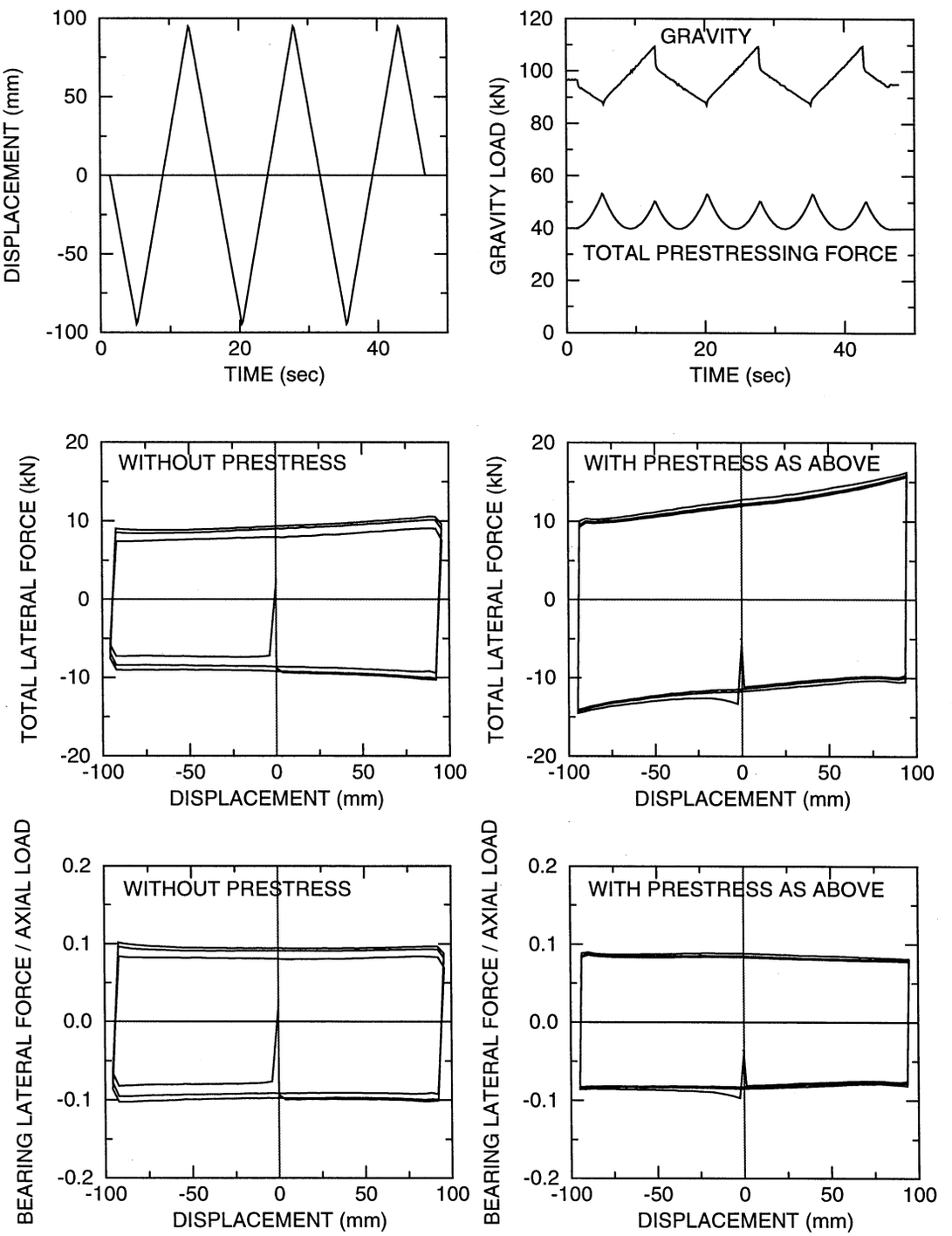

Figure 3-9: Comparison of Behavior of Non-Prestressed and Prestressed Flat Sliding Bearing

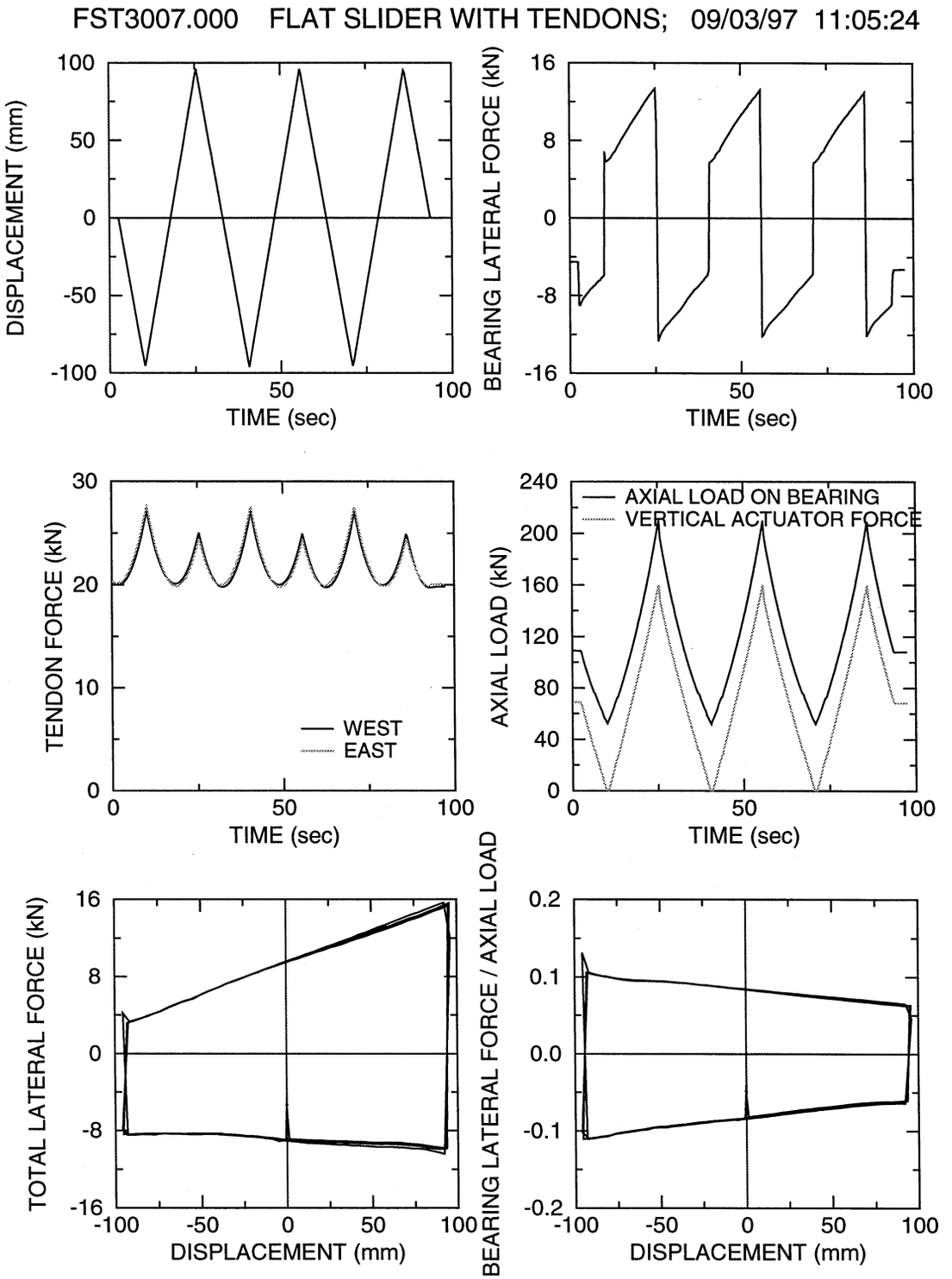

Figure 3-10: Test demonstrating Prevention of Uplift by Prestress in a Flat Sliding Bearing

Figure 3-11 illustrates the behavior of the tested FPS bearing (R = *558.8 mm*) with and without the effect of prestress (these are tests SSNT007.000 and SST1006.000 in Appendix A). The gravity load is of the VL2 type (see Fig. 3-8) in which the load is about *110 kN* when the bearing displacement is zero (say this is the dead load). The gravity load drops to a minimum of about *22 kN* at each extreme bearing displacement, whether positive or negative. When prestressed, the initial prestress is only about *3.4 kN*, that is, the tendons are just taut. However, on lateral movement the prestressing force increases to about *25 kN* at the maximum displacement of *64 mm*.

Without the prestress, the lateral force-displacement loop has the peculiar shape shown in Figure 3-11, in which the force peaks at some displacement less than the amplitude of the motion. This behavior is entirely predictable by (3-16). Within the initial exertion, when displacement u_b varies from zero to *64 mm*, the gravity load may be described by

$$W = W_0 - su_b \tag{3-28}$$

where W_o = *110 kN* and s = *1.375 kN/mm*. Substituting into (3-16) with Z = *1*, it is easily determined that dF/du_b is zero when $u_b = (W_0 - \mu R)/2s$. For μ = *0.045* (this is evident in the normalized loops in Fig. 3-11), the displacement is u_b = *31 mm*. This is the displacement at maximum lateral force. Substituting this value of displacement in (3-28) and using (3-16), the peak lateral force is determine to be *6.7 kN*. Indeed, the calculated values of displacement and peak force are consistent with the experimental results.

The effect of prestress may be seen in the lateral force-displacement loop of Figure 3-11. While the effect is substantial (and this can be seen in all of the test results in Appendix A), the normalized loops (bearing lateral force divided by total normal load vs. displacement) are nearly identical for the two cases. Note that the bearing lateral force is the lateral force excluding the horizontal component of the tendon force. This demonstrates the validity of (3-16) and (3-17).

Figure 3-12 compares the behavior of the tested elastomeric bearing with and without the effect of prestress. In this case, the gravity load was sinusoidal of the VL1 type and there was a small difference between the histories of load as developed in the tests without and with prestress. The initial total prestress was at about *42 kN*.

There are two important observations in the results of Figure 3-12. First, the changes in the prestressing force as a result of lateral bearing movement are minor. Second, the lateral force-displacement relations in the two cases are nearly identical - the difference being a small reduction in the effective stiffness of the prestressed bearing due to the increased axial load.

The observed behavior is typical for low damping elastomeric bearings of which the mechanical properties are marginally affected by the axial load (provided of course, that it is much less than the buckling load). High damping elastomeric bearings exhibit lateral force-displacement characteristics with more dependency on axial load than low damping elastomeric bearings. Nevertheless, this dependency is much less than that in sliding bearings.

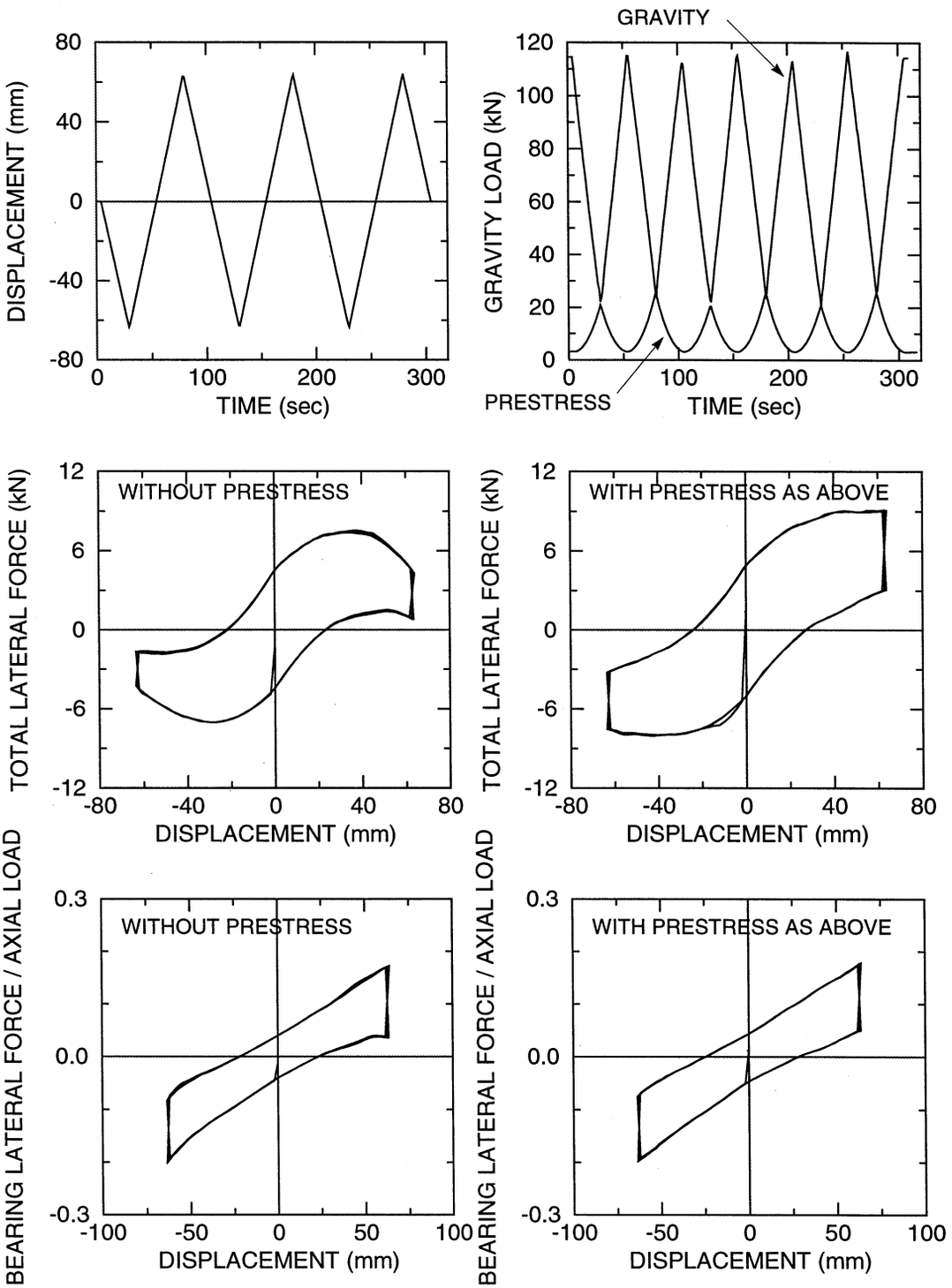

Figure 3-11: Comparison of Behavior of Non-Prestressed and Prestressed FPS Bearing

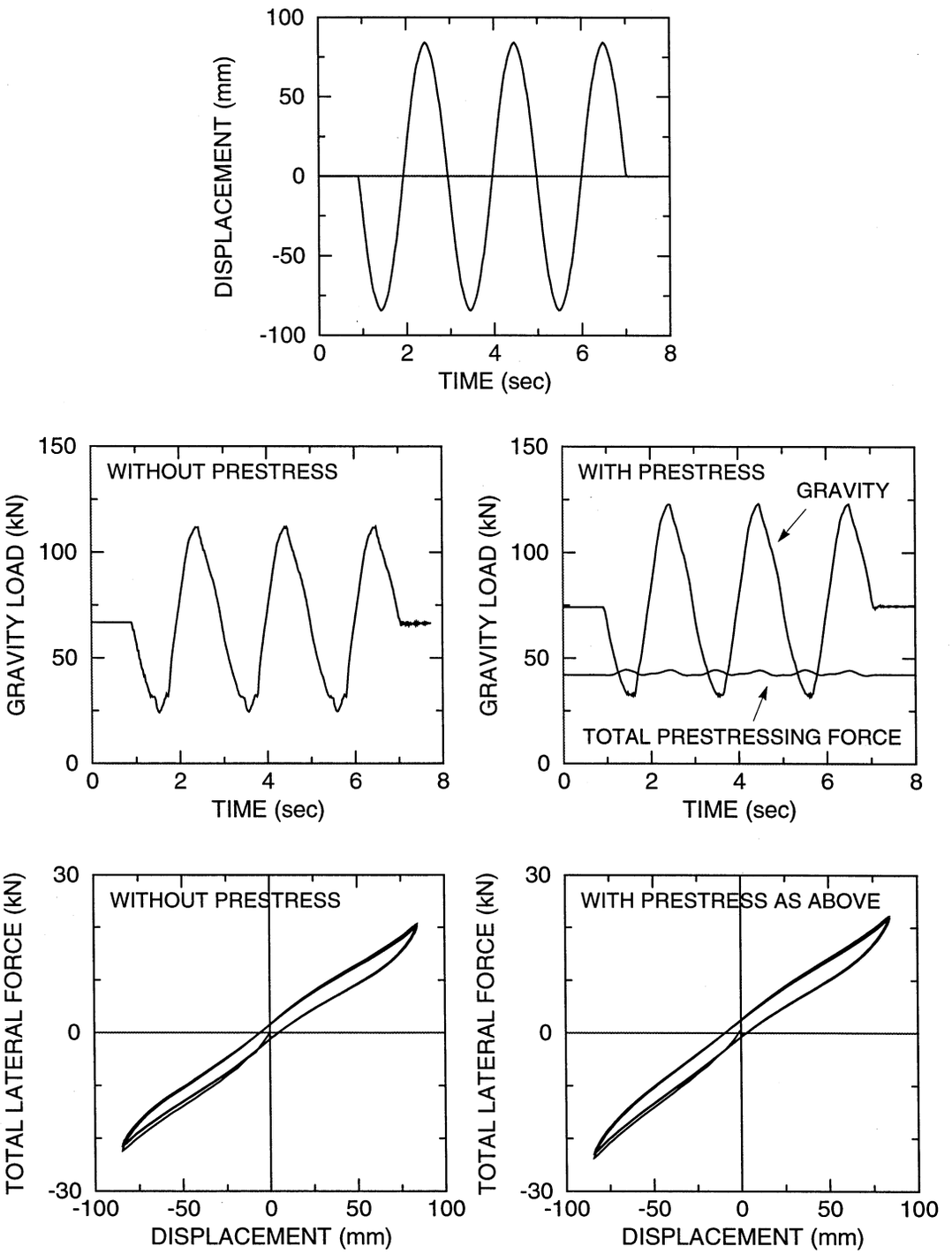

Figure 3-12: Comparison of Behavior of Non-prestressed and Prestressed Elastomeric Bearing

In the results presented in Appendix A as well as in Figures 3-9 to 3-12, the following may be observed:

(a) The force in the two tendons (on west and east sides of the bearing) are not equal but rather they differ by an amount which is more pronounced in the elastomeric bearing. This was caused by the rotation of the bearing about the axis of lateral deformation (longitudinal direction of the loading beam). While small, this rotation causes reduction in the strain of one of the tendons and increase in the strain of the other tendon by an equal amount.

(b) The peak prestressing force (sum of forces in the two tendons) is more when the lateral displacement is positive than when it is negative. For example, in the test of Figure 3-9, the difference between the two peak forces is about *3.4 kN*, whereas in the case of the test of Figure 3-10 is about *5.6 kN*. Although this difference varies from test to test, it is observed in all the tests (see Appendix A). It can be easily explained when considering that the loading beam of the testing machine can not be perfectly levelled, either because of inaccuracies in the initial levelling (the beam could be levelled to with in $\pm$ *0.1* degree - the resolution of the electronic levelling device - but, it could be more due to waviness in the beam), or due to differences in the lengths in the vertical actuator assemblages, or both.

If the angle of inclination is, on the average, ϕ and the amplitude of lateral motion is U, then the difference in the total strain in the tendons when moving with negative displacement than when moving with positive displacement is

$$\Delta\varepsilon_t = \frac{2U\phi}{l_t} \tag{3-29}$$

Therefore, the difference in the total force (two tendons) is

$$\Delta P_t = \frac{4U\phi EA}{l_t} \tag{3-30}$$

where A = area of a single tendon and E = modulus of elasticity of the tendon. For example, in the test of Figure 3-10, $U = 95\ mm$, $A = 44.2\ mm^2$, $l_t = 1100\ mm$, $E = 64{,}000\ MPa$ and say $\phi = 0.3$ degrees. The difference $\Delta P_t = 5.1\ kN$, which is consistent with the experiment.

3.9 Analytical Prediction of Behavior of Tested Prestressed Bearings

A prediction of the behavior of prestressed bearings is presented herein on the basis that the mechanical properties of the bearings are known. For the sliding bearings, this requires knowledge of the coefficient of sliding friction, and particularly its dependencies on velocity of sliding and apparent pressure. For elastomeric bearings, this requires knowledge of the values of the shear and bulk moduli for calculating the vertical deflection, and knowledge of the lateral force-displacement characteristics of the bearing (see eq. 3-19) and their dependencies on axial load (and more generally on frequency of motion and strain in the elastomer).

In our case, a complete knowledge of the mechanical properties of the bearings is not needed. Rather, it is sufficient to know the properties within the narrow range of the parameters varied in the experiments. We choose to simulate the behavior of the flat sliding bearing in test

FST3007.000 (Figure 3-10), of the FPS bearing in test SST1006.000 (Figure 3-11) and of the elastomeric bearing in test E1T3005.000 (Figure 3-12).

The two sliding bearings have been tested under conditions of constant velocity. Therefore, modeling of the dependency of friction on velocity (see Equation 3-13) is not necessary. However, in both tests of the sliding bearings the apparent pressure varied considerably so that the dependency of friction on pressure needs to be considered.

Starting with the flat sliding bearing, we observe (see Figure 3-10) that for test FST3007.000, the axial load varies between about *53 kN* and *200 kN* (the apparent pressure being in the range of *7.4* to *28.2 MPa*). For this range of pressure, the coefficient of friction of unfilled PTFE should have considerable variation (Constantinou et al., 1998). Indeed, this is evident in Figure 3-10. For the sliding velocity in this test (*~12.5 mm/s*) and the aforementioned range of loads, the coefficient of friction may be approximated by

$$\mu = 0.11 - \frac{0.05}{147}(W + P_{tV} - 53) \tag{3-31}$$

where W = gravity load and P_{tV} = vertical component of prestress, both in units of *kN*.

Experiment FST3007.000 has been simulated on the basis of the flow chart of Figure 3-5 and with simultaneous integration of (3-14) and (3-15). The parameters used were: $P_{in} = 40\ kN$, $\varepsilon_{in} = 7.074 \times 10^{-3}$, $l_t = 1100\ mm$, $l = 1968\ mm$, $l_r = 868\ mm$, $D_y = 0.5\ mm$ and $\eta = 3$. Moreover, the time histories of lateral displacement $u_b(t)$ and gravity load $W(t)$ were used as recorded, and with (3-31) substituted in (3-14). Figure 3-13 provides a comparison of experimental and analytical results. The analytical prediction is very good except for a small difference in the tendon force (and accordingly the related effect on the total lateral force). As explained earlier, the tendon force exhibited slightly asymmetric behavior due to an accidental inclination of the loading beam of the testing machine. This accidental inclination was not accounted for in the analytical prediction.

We proceed with the FPS bearing in test SST1006.000 (Figure 3-11). We observe that despite the substantial variation in axial load (*37 to 110 kN*, with apparent pressure in the range of *18.2 to 54.5 MPa*), the coefficient of sliding friction is nearly independent of load with a value $\mu \approx 0.05$. Therefore, we simulate this experiment on the basis of the flow chart of Figure 3-5 and with simultaneous integration of (3-15) and (3-17) with $\mu = 0.057$. The parameters used are: $P_{in} = 3\ kN$, $\varepsilon_{in} = 5.303 \times 10^{-4}$, $R = 558.8\ mm$, $l_t = 1100\ mm$, $l = 1968\ mm$, $l_r = 868\ mm$, $D_y = 0.5\ mm$ and $\eta = 3$. Figure 3-14 compares the experimental and analytical results. Again the analytical prediction is very good except, again, for the tendon force of which the asymmetry in the experiment was caused by an accidental eccentricity of the loading beam of the machine.

The analysis of the prestressed elastomeric bearing requires knowledge of the compression modulus. The bearing was tested to measure its vertical stiffness which is related to the compression modulus (eq. 3-20). It is very interesting to discuss herein the correlation between the experimentally determined and the analytically predicted vertical bearing stiffness. The bearing was subjected to three cycles of axial load in the range of zero to nearly *178 kN* and then

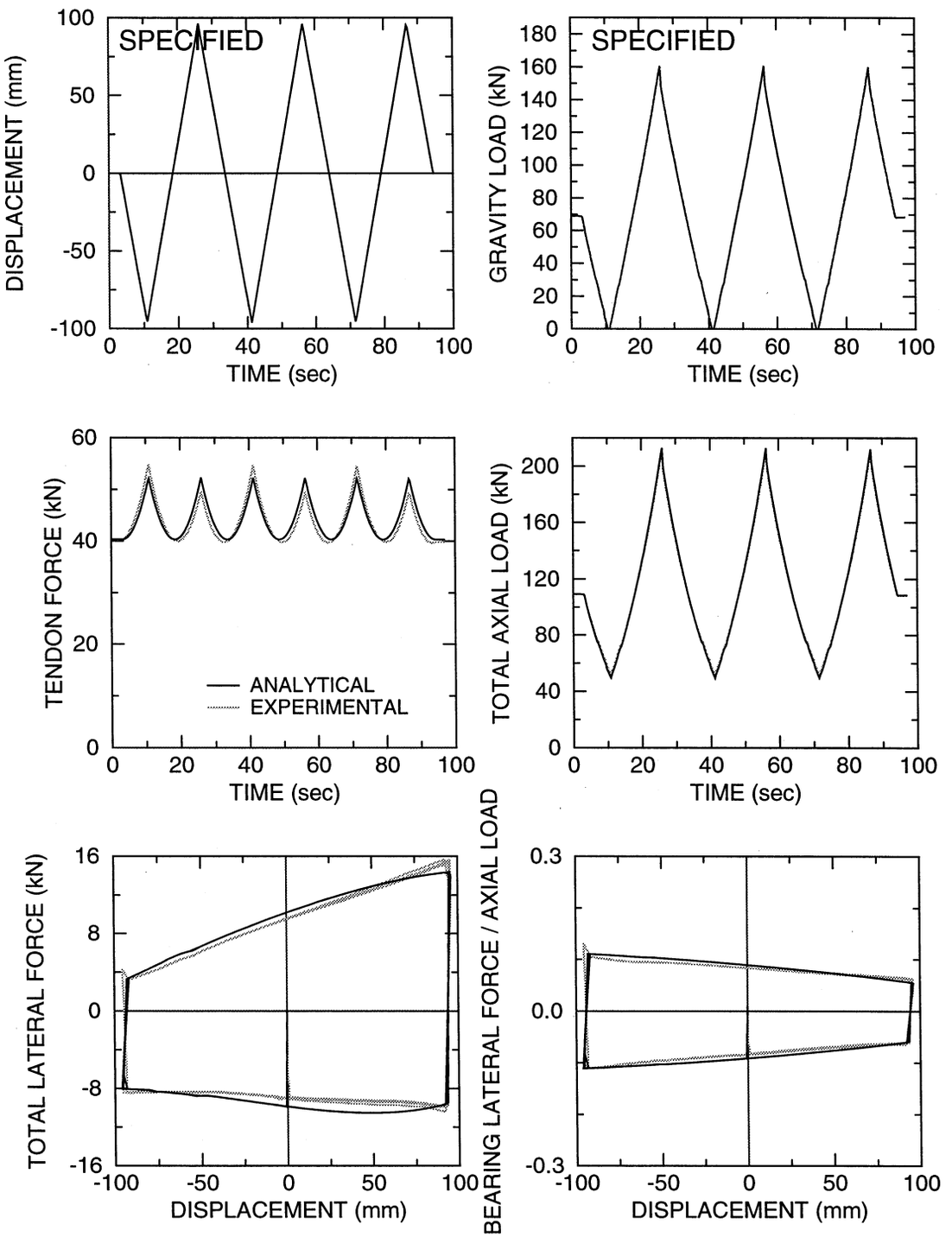

Figure 3-13: Comparison of Analytical and Experimental Behavior of Prestressed Flat Sliding Bearing (Test FST3007.000)

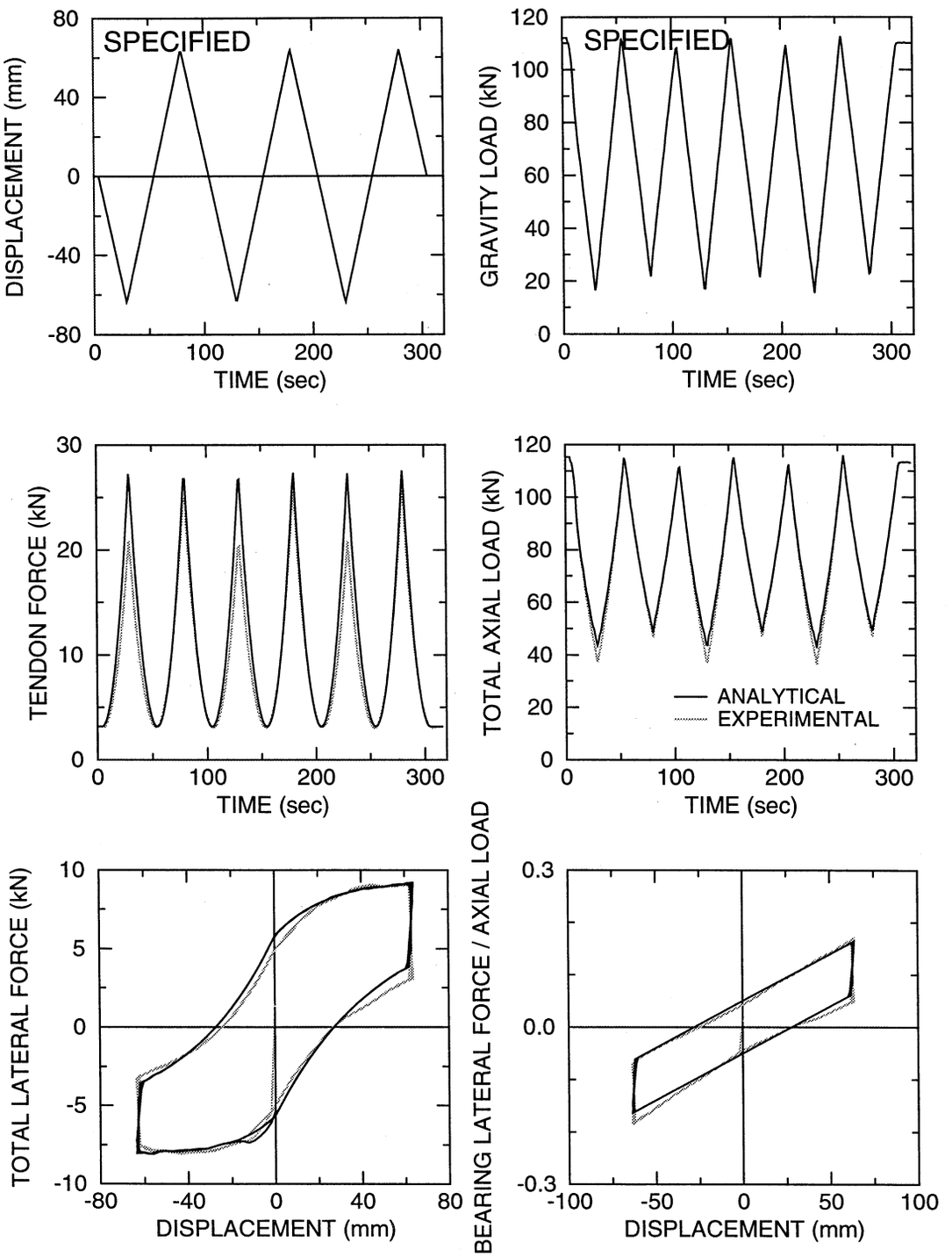

Figure 3-14: Comparison of Analytical and Experimental Behavior of Prestressed FPS Bearing (Test SST1006.000)

back to zero load at constant rates of application ranging from *100 sec* to *3 sec* per cycle. The recorded axial load-vertical deformation curves are presented in Figure 3-15. The reduced values of vertical stiffness are shown directly on this figure. It may be observed that the stiffness is marginally affected by the rate of application of the load. The relevant value of the stiffness is the one at the highest rate of load (*3 sec / cycle*). It is *96.9 kN/mm* (=*553 k/in*).

Predictions of the value of the vertical stiffness were made using (3-20) and (3-21) as per the 1997 AASHTO (American Association of State Highway and Transportation Officials, 1997). For this calculation values of the bulk modulus K, shear modulus G and material constant k were needed. Constant $k = 0.75$ (for rubber of hardness *50*), a value $K = 2070$ *MPa* (*300 ksi*) was assumed and G was measured in a test in which the bearing was loaded to an average pressure of *6.9 MPa* (load *170 kN* divided by the bonded rubber area of $A_r = 24{,}542\ mm^2$) and subjected to sinusoidal lateral motion of *0.5 Hz* frequency and amplitude of *33 mm* (shear strain of *75*-percent). The shear modulus was obtained as the secant modulus (per ASTM Standard D4014) between strains of *25* and *75*-percent. It was determined to be *0.4 MPa* (*58 psi*). The shape factor $S = 12.5$, area $A_r = 24{,}542\ mm^2$ and $T_r = 44.5$ *mm* (see Figure 3-6). The predicted vertical stiffness was *175.4 kN/mm* (*1001 k/in*), that is, nearly twice the actual stiffness.

Subsequently, the theoretically correct equation (3-22) together with (3-20) was utilized for the prediction of vertical stiffness, with factor $f = 0.71$ (see Constantinou et al., 1992). The result is $K_v = 125.4$ *kN/mm* (*716 k/in*), that is, about *30*-percent larger than the experimental value. Our inability to correctly predict the vertical stiffness has been disturbing since it should represent the simplest step in the analysis of the elastomeric bearing. Guessing that the rubber thicknesses may have been different than specified, the bearing was cut at the conclusion of testing and the thickness of the individual rubber layers was measured. Table 3-1 presents the measured thicknesses, and the calculated values of the shape factor and compression modulus of each layer. The latter was determined by use of (3-22). The vertical stiffness was then calculated as

$$K_v = A_r\left[\sum \frac{t_i}{E_{ci}}\right]^{-1} \tag{3-32}$$

where the summation extends over the 14 rubber layers. The result was *552 k/in* (=*96.7 kN/mm*), that is, precisely the measured value. Moreover, the total rubber thickness was found to be slightly more than specified value, that is, $T_r = 47.3$ *mm*.

The prestressed elastomeric bearing has been analyzed for the conditions of test E1T3005.000 (Figure 3-12). The lateral displacement and gravity load histories, $u_b(t)$ and $W(t)$ respectively, were specified (see Figure 3-12). Moreover, $W_o = 115$ *kN*, $P_{in} = 42$ *kN*, $\varepsilon_{in} = 7.427\text{x}10^{-3}$, $l_t = 1100$ *mm*, $l = 1968$ *mm*, $l_r = 868$ *mm*, $T_r = 47.3$ *mm*, $A_r = 24{,}542\ mm^2$, $I_r = 49\text{x}10^6\ mm^4$, $h = 72$ *mm*, $G = 0.4$ *MPa* and $E_c = 187$ *MPa* (this is the effective value calculated by equation 3-20 and using the correct stiffness value of *96.9 kN/mm*). For completeness, the lateral force-displacement characteristics of the bearing are needed. We opt to model the bearing by (3-19) and (3-15) with $D_y = 4$ *mm*, $F_y = 2.5$ *kN* and $\alpha = 0.32$, and assume that these properties are marginally affected by the varying axial load. The determination of these properties has been based on test results under

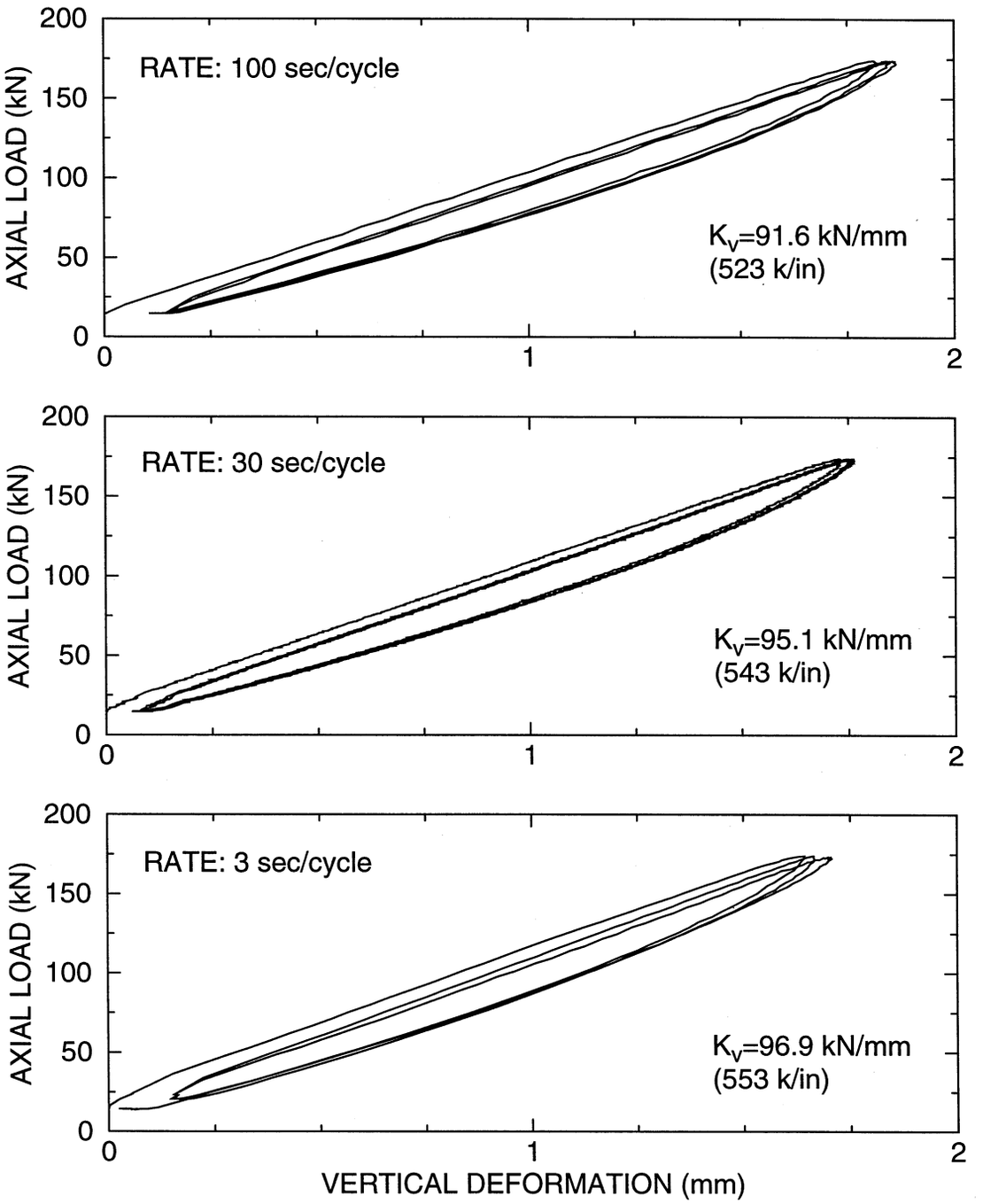

Figure 3-15: Axial Load - Vertical Deformation Curves of Elastomeric Bearing

constant gravity load and the simple theory presented in Constantinou and Reinhorn (1997). The solution was based on the incremental approach of Figure 3-5.

Table 3-1: Measured Thicknesses and Calculated Properties of Individual Layers of Rubber Bearing (1 in = 25.4 mm, 1 ksi = 6.9 MPa)

Layer	Thickness t_i (in)	S_i	E_{ci} (ksi)
1	0.075	20.8	72.5
2	0.093	16.8	53.2
3	0.122	12.8	34.3
4	0.114	13.7	38.4
5	0.172	9.1	18.8
6	0.148	10.6	24.7
7	0.131	11.9	30.3
8	0.147	10.6	24.7
9	0.143	10.9	26.0
10	0.167	9.4	19.9
11	0.139	11.2	27.2
12	0.150	10.4	23.9
13	0.143	10.9	26.0
14	0.120	13.0	35.2

Figure 3-16 compares the experimental and analytical results. It is observed that the analytically predicted tendon force exhibits a behavior that differs from the experimental one. While the differences are relatively small, the analysis predicts:

(a) For the negative lateral displacement, the tendon force has a trend similar to the experimental one but with a higher value. This is due to the prediction of gain in the bearing height (with respect to the position following application of the initial gravity load) as a result of the reduction of the gravity load.

(b) For positive lateral displacement, the tendon force has a trend opposite to the experimental one and with lower value. This is due to the prediction of more reduction in the bearing height (caused by the lateral displacement and increased gravity load) than actually experienced by the tendons.

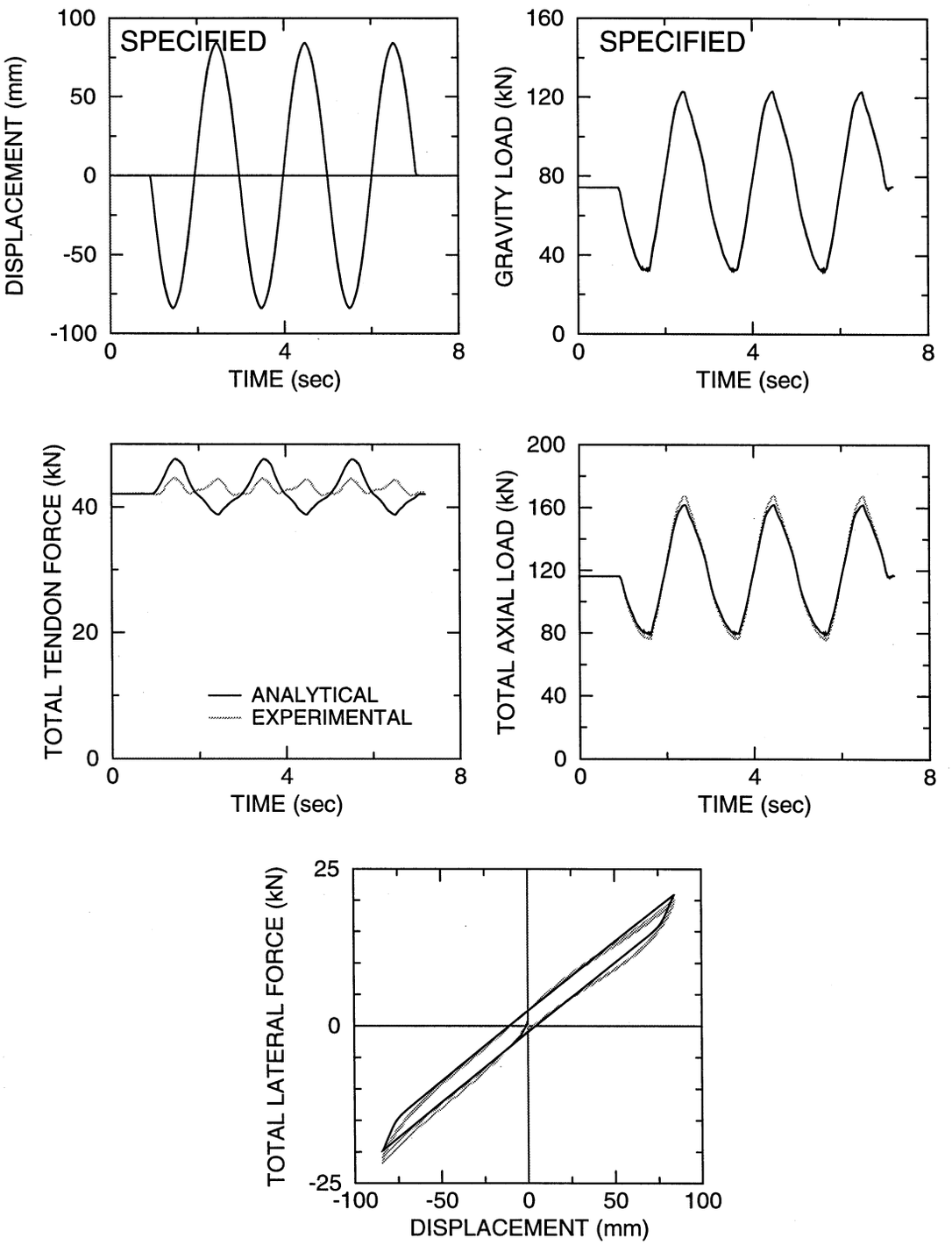

Figure 3-16: Comparison of Analytical and Experimental Behavior of Prestressed Elastomeric Bearing (Test E1T3005.000)

It appears that the utilized theory for predicting the vertical deformation of elastomeric bearings is incorrect. Actually, it is not. The theory predicts the vertical deformation in an average sense, that is, it predicts the vertical deformation if the top steel plate of the bearing remains levelled. In reality, the tested bearing underwent some rotation of its top plate due to (a) imperfect levelling of the loading beam, (b) use of two vertical actuators (three are needed for perfect control of the vertical movement of the loading beam - lateral bracing was used to minimize this problem and stabilize the bearing), and (c) uneven thickness of the rubber layers.

The two prestressing tendons were connected to the west and east sides of the tested bearing. Therefore, they followed the vertical movement of these two sides, which in general are not equal to the average vertical movement. As an example, Figure 3-17 presents time histories of the vertical displacement of the middle points of the four sides of the elastomeric bearing when tested under varying vertical load (this was one of the tests for determining the vertical bearing stiffness). Evidently, the east and west sides of the bearing, to which the tendons were attached, experience significantly different displacements. On the other hand, the north and south sides undergo nearly identical displacements due to the control provided by the two vertical actuators. It should be noted that on lateral bearing deformation the differences in the vertical displacements of the four sides of the bearing should be further magnified.

Based on this explanation it is evident that the analytical prediction of the tendon force is not erroneous. Rather, the experimentally measured force is influenced by effects related to the testing machine. Nevertheless, the prediction of the behavior of the prestressed elastomeric bearing is good.

3.10 Conclusions

The behavior of prestressed isolators has been experimentally studied for the first time. It has been observed that, consistent with the theory, the prestress has significant effects on the behavior of the prestressed bearings. The primary effects of prestress are to increase the axial load on the bearings and to introduce additional lateral stiffness. This lateral stiffness, described by (3-11), may be explored to provide restoring force in isolation systems with insufficient lateral stiffness. Moreover, in sliding bearings with additional axial load increases the frictional resistance and for the spherical FPS bearings it increases the restoring force provided by the bearing itself. While the additional axial load affects also the behavior of elastomeric bearings, the effects were observed to be minor for the tested low damping elastomeric bearings.

In all cases of tested bearings, the experimental response could be predicted with sufficient accuracy by analytical means. Some differences between the experimental and analytical results on the tendon forces could be rationally explained on the basis of rotation of the loading beam of the testing machine.

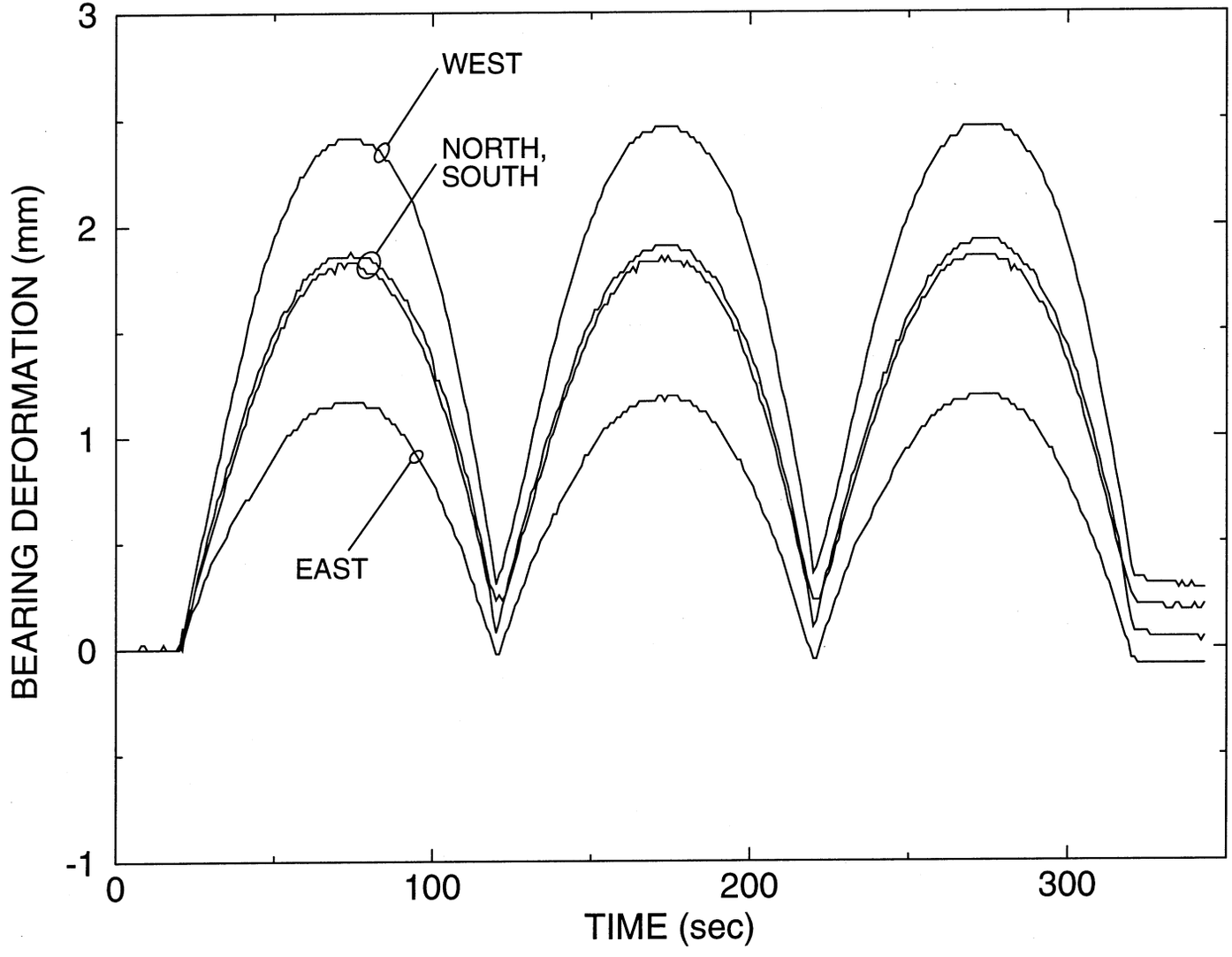

Figure 3-17: Vertical Displacements of Four Sides of Elastomeric Bearing under Varying Axial Load without Lateral Displacement

SECTION 4

BRIDGE MODEL USED IN SHAKE TABLE TESTING

4.1 Introduction

The bridge model used in the shake table testing is identical to the one utilized in previous testing of seismic isolation systems at the University at Buffalo (Constantinou et al., 1993; Tsopelas et al., 1994; Tsopelas and Constantinou, 1994a; Tsopelas and Constantinou, 1994b; Tsopelas et al., 1996a; Tsopelas et al., 1996b; Tsopelas and Constantinou, 1997). This model was configured to represent a two-span bridge with a central flexible pier and stiff abutments.

The model was tested in the following configurations:

(a) Non-isolated with the deck supported at the flexible pier by fixed bearings and at the abutments by elastomeric (expansion) bearings,

(b) Non-isolated as in (a) above and with fluid viscous dampers installed at the abutment locations,

(c) Isolated with the deck supported on low damping elastomeric bearings,

(d) Isolated with the deck supported on high damping elastomeric bearings, and

(e) Isolated with the deck supported on low damping elastomeric bearings and with fluid viscous dampers installed at the abutment locations.

This section presents a description of the bridge model, the utilized seismic isolation and energy dissipation hardware and the conducted testing program.

4.2 Bridge Model

The bridge model is shown in Figure 4-1. At quarter length scale, it had a clear span of 4.8 m, height of 2.53 m and a total weight of 158 kN. The deck consisted of two AISC W14x90 sections 5.2 m long, which were transversely connected by beams of 1.2 m in length. Additional steel and lead weights were added to reach the model deck weight of 140 kN, as determined by similitude requirements. Each pier consisted of two AISC TS 6x6x5/16 columns with the pier top made of a channel detailed to have sufficient torsional rigidity. The tube columns were connected to beams at the bottom, which were bolted to the concrete extension of the shake table. In this configuration, the column loads were transferred at a point located 0.57 m beyond the edge of the shake table. While the overhangs of the concrete shake table could safely carry the column load of over 80 kN, they had some limited vertical flexibility, which resulted in vertical motion of the piers and the supported deck during seismic testing.

The pier on the left side of the model was provided with bracing consisting of two structural tees AISC WT 4x5 in order to simulate stiff abutment behavior. As shown in Figure 4-2, the model represents a two-span bridge in which the braced pier represents the abutment, whereas the flexible pier represents the pier supporting the center point of the deck. The model is appropriate for testing in the longitudinal and vertical directions but not in the transverse direction. It may be recognized in Figure 4-2 that the representation is approximate for the following reasons:

(a) The loads on the pier and abutments are shown in Figure 4-2 with their tributary values

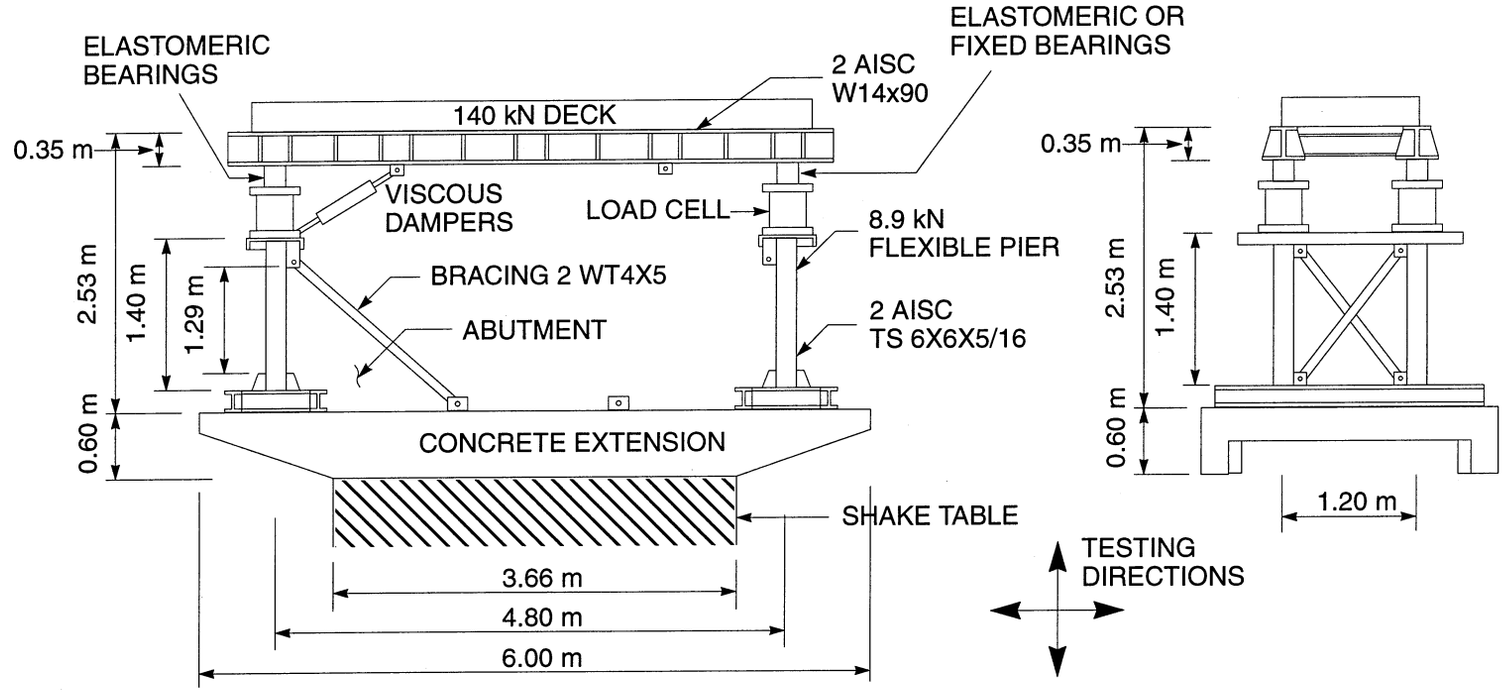

Figure 4-1: Schematic of Quarter Scale Bridge Model

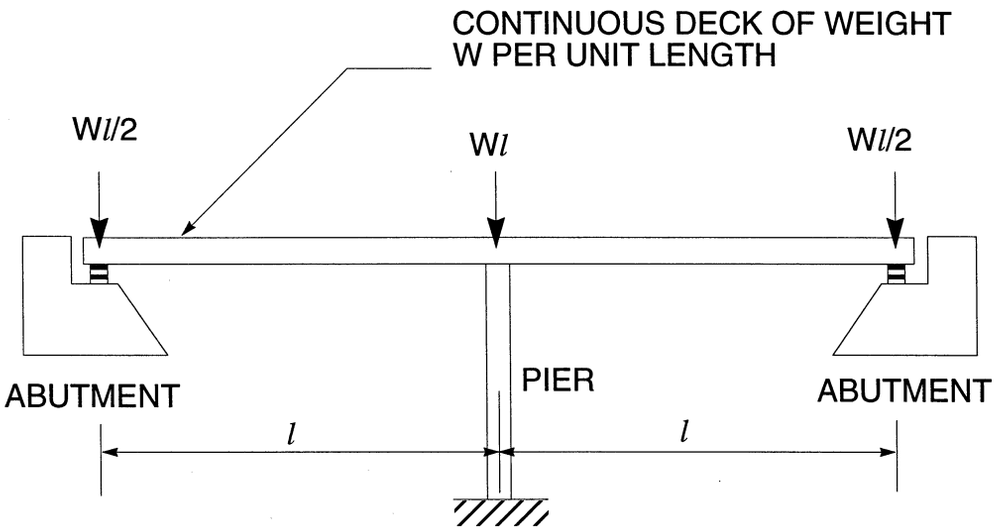

TWO-SPAN, EQUAL LENGTH SPAN BRIDGE

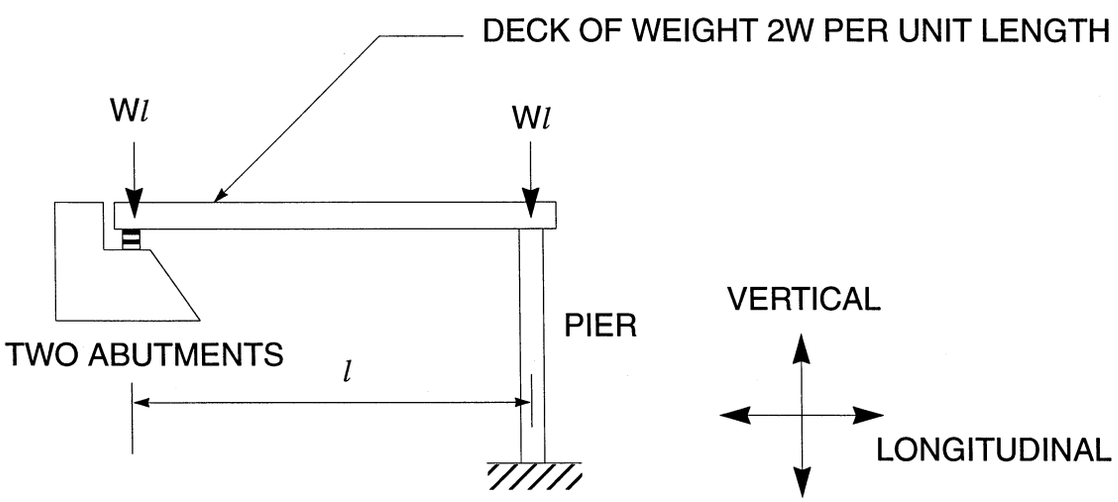

EQUIVALENT ONE SPAN REPRESENTATION

Figure 4-2: Two-span Bridge and Equivalent One-span Representation for Testing in the Longitudinal and Vertical Directions

and not with their exact values. That is, a true one-span representation of a continuous two-span bridge should have more load on the pier than on the two abutments. It should also be recognized that the difference is small and immaterial for the purpose of the testing.

(b) The rotation of the deck at the point above the flexible pier is, in general, different in the two-span bridge and the one-span representation. However, the model featured a vertical stiff deck of which the end rotation was very small and representative of the true condition in the continuous two-span bridge. In turn, the use of a stiff deck in the model prevented the magnification of the vertical acceleration in the deck.

It should be noted that the testing of the this model bridge has been based on the assumption that the abutments (represented by the braced pier) were the strong elements of the bridge substructure, whereas the flexible pier represented the weak element of the substructure. Accordingly, the utilized hardware intended to provide relief to the flexible pier as a result of the reduction of the deck inertia force (use of seismic isolation bearings), through redistribution of the inertia force by transferring it to the strong abutments (use of damping devices), or both.

The flexible pier was designed to have a period of 0.1 s (0.2 s in prototype scale) in its free standing position without the load from the deck. Also, the pier was detailed to yield under the combined effects of gravity load (40 kN on each column) and 50% of the gravity load applied as horizontal load at each bearing location. The stiffness of the pier was verified by pulling the piers against each other on the shake table and results were used to calibrate strain gage load cells of each column.

The design of the model bridge was based on similitude laws for artificial mass simulation (Sabnis 1983). A summary of the scale factors of the model is presented in Table 4-1.

Table 4-1: Scale Factors used in Model Bridge

QUATINTITY	DIMENSION	SCALE FACTOR[1]
Linear Dimension	L	4
Displacement	L	4
Time	T	2
Velocity	LT^{-1}	2
Acceleration	LT^{-2}	1
Frequency	T^{-1}	0.5
Stress / Pressure	$ML^{-1}T^{-2}$	1
Force	MLT^{-2}	16
Strain	-	1

1 - Prototype/Model

4.3 Elastomeric Bearings

Low damping elastomeric bearings were used in the non-isolated bridge configurations without and with fluid dampers and in the isolated bridge configuration without and with fluid dampers. Moreover, high damping elastomeric bearings were used in the isolated bridge configuration.

The mechanical characteristics of these bearings were obtained through the testing of individual bearings with the bearing testing machine described in Section 2.

4.3.1 Low Damping Elastomeric Bearings

The elastomeric bearings were designed to provide a period to the isolated bridge model of about 1.0 sec in the scale of the experiment (that is, 2.0 sec in prototype scale). While it was desirable to achieve a longer period, this was not possible due to stability problems with the resulting slender bearings. Accordingly, the bearings were specified to be of a standard natural rubber grade and hardness: grade 3 per ASTM D4014 and hardness 50, durometer A. Figure 4-3 shows the geometry of these bearings. They consisted of 12 rubber layers of *6.35 mm* (*0.25 in.*) thickness each, 11 shim plates of 11 gage and with bonded rubber diameter of *140 mm* (*5.5 in.*). The end plates were *19 mm* (*0.75 in.*) thick and featured threaded holes to which masonry plates were bolted. In turn, these masonry plates were bolted on the bridge deck and piers below. That is, the bearing connections were of the bolted type.

Calculations were based on the assumption of a rubber shear modulus $G = 0.69\ MPa$ (*100 psi*), which for bonded rubber area $A_r = 15{,}394\ mm^2$ and total rubber thickness $T_r = 76.2\ mm$ (*3 in.*) give a lateral stiffness of *0.14 kN/mm* per bearing. Accordingly, the period for weight of *140 kN* on four bearings is *1.0 sec*.

It may be recognized in Figure 4-3 that the bearing had a low shape factor $S = 5.5$, which is uncharacteristic of isolation bearings but common in bridge expansion bearings. The safety of the bearings was assessed on the basis of the 1997 AASHTO (American Association of State Highway and Transportation Officials, 1997) for a bearing displacement $d = 75\ mm$ and axial load $P = 45\ kN$. The resulting total shear strain in the rubber was 3.20 or higher when considering the effect of rotation of the bearings on top of the flexible pier. Regardless, the total strain is well within the allowable limit of 5.50 for the seismic loading combination.

However, the concern with this bearing has been its stability. The buckling load in the undeformed configuration P_{cr} was estimated by (Kelly, 1993):

$$P_{cr} = \frac{\pi^2 G D^4}{32\sqrt{2} t_i T_r} \tag{4-1}$$

where D = bonded rubber diameter and t_i = thickness of individual rubber layers. It was $P_{cr} = 119.5\ kN$. To estimate the buckling load in the deformed configuration P_{cr}', use was made of the approximate relation

$$P_{cr}' = P_{cr}\frac{A_{re}}{A_r} \tag{4-2}$$

where A_{re} = reduced bonded rubber area (overlap area between the top bonded and bottom bonded rubber areas of the displaced bearing). For $d = 75\ mm$, the ratio $A_{re}/A_r = 0.352$. Therefore, $P_{cr}' = 42\ kN$. This provides a safety factor of 1.17 if the axial load is $35\ kN$ (just the gravity load). Considering additional axial load due to the vertical acceleration, it is evident that the bearing would operate at its theoretical buckling load.

One should note that the difficulties encountered with the elastomeric bearings are the result of the reduced scale of the experiments, in which we could not maintain the typical low aspect ratio (height to diameter) of full size elastomeric bearings. These problems are not typically encountered with full size elastomeric bearings, except maybe in applications of low structural weight and large bearing displacements.

Five identical bearings were manufactured in a single batch. All five bearings were tested in the bearing testing machine. The bearings were subjected to lateral sinusoidal movement of frequency in the range of *0.01* to *1.0 Hz* and amplitude corresponding to rubber shear strain of *35*, *69* and *103*-percent. Figure 4-4 presents the recorded lateral force-lateral displacement loops for bearing No. 3 (which was not used in the shake table testing), whereas Table 4-2 presents the mechanical properties extracted from these loops. These include the effective stiffness K_{eff} and damping ratio β as defined in the 1997 AASHTO (American Association of State Highway and Transportation Officials, 1997) for each of the three cycles of movement and the average values over the three cycles. Moreover, the effective shear modulus, G_{eff}, was determined from

$$K_{eff} = \frac{G_{eff}A_r}{T_r} \tag{4-3}$$

The bearing exhibited an apparently stable behavior during testing. The loops of Figure 4-4 also show no evidence of incipient buckling. Moreover, the five bearings did not exhibit identical behavior. For example, Table 4-3 presents the mechanical properties for bearing No. 4. At the relevant frequency of *1.0 Hz* and strains of *70*-percent or higher, the effective shear modulus is about *0.80 MPa*. That is, it is about *15*-percent more than assumed in the design. Accordingly, the period of the bridge model on four of these bearings should be about *0.93 sec* rather than the target value of *1.0 sec*. Moreover, the damping ratio is about *6*-percent.

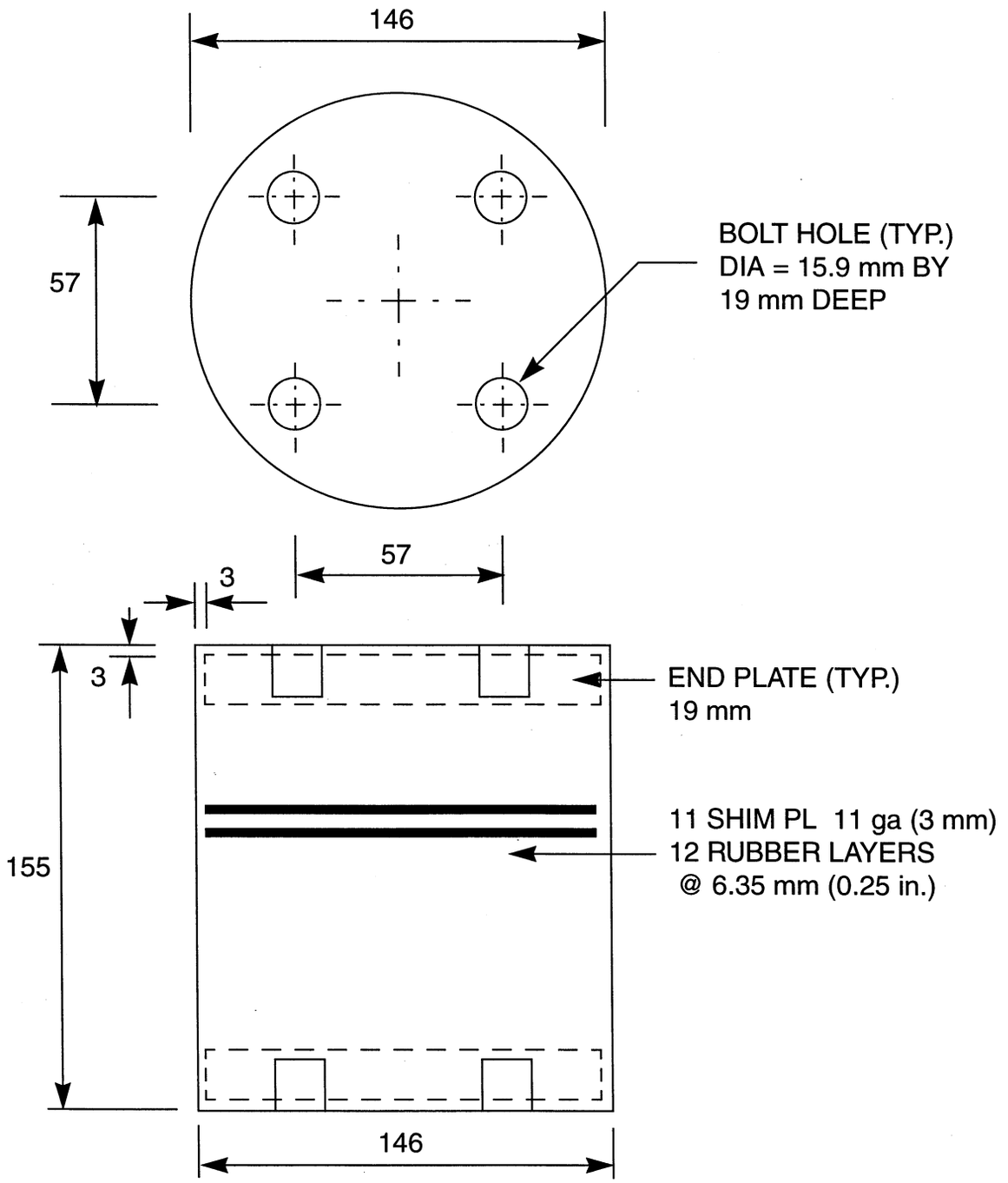

Figure 4-3: Schematic of Elastomeric Bearing

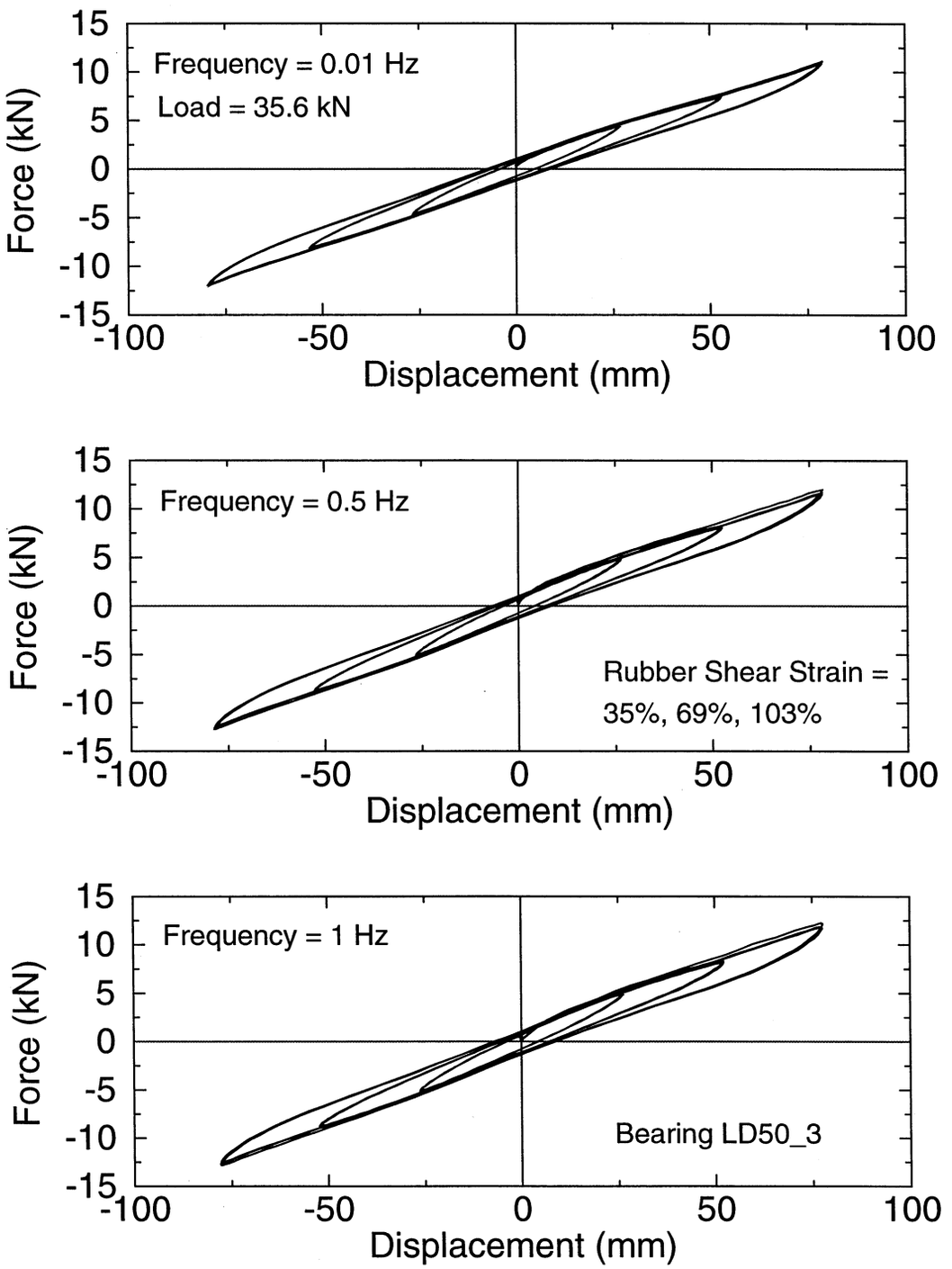

Figure 4-4: Lateral Force - Lateral Displacement Loops of Low Damping Elastomeric Bearing No. 3

Table 4-2: Mechanical Properties of Low Damping Elastomeric Bearing No. 3

Frequency (Hz)	Strain	K_{eff} 1 (kN/mm)	K_{eff} 2 (kN/mm)	K_{eff} 3 (kN/mm)	K_{eff} Avg (kN/mm)	G_{eff} (MPa)	β 1	β 2	β 3	β Avg
0.01	1.04	0.146	0.144	0.144	0.145	0.72	0.051	0.052	0.052	0.052
0.50	1.03	0.157	0.154	0.154	0.155	0.77	0.058	0.055	0.054	0.056
1.00	1.02	0.161	0.157	0.157	0.158	0.78	0.060	0.058	0.057	0.058
0.01	0.69	0.146	0.146	0.145	0.146	0.72	0.062	0.064	0.064	0.063
0.50	0.69	0.161	0.160	0.159	0.160	0.79	0.067	0.063	0.062	0.064
1.00	0.69	0.165	0.163	0.162	0.163	0.81	0.067	0.065	0.064	0.065
0.01	0.35	0.169	0.169	0.169	0.169	0.84	0.076	0.078	0.078	0.077
0.50	0.35	0.189	0.187	0.186	0.187	0.93	0.076	0.074	0.072	0.074
1.00	0.34	0.194	0.191	0.191	0.192	0.95	0.075	0.074	0.073	0.074

1: first cycle, 2: second cycle, 3: third cycle, Avg: average of three cycles

Table 4-3: Mechanical Properties of Low Damping Elastomeric Bearing No. 4

Frequency (Hz)	Strain	K_{eff} 1 (kN/mm)	K_{eff} 2 (kN/mm)	K_{eff} 3 (kN/mm)	K_{eff} Avg (kN/mm)	G_{eff} (MPa)	β 1	β 2	β 3	β Avg
0.01	1.04	0.168	0.158	0.155	0.160	0.79	0.073	0.062	0.061	0.066
0.50	1.03	0.169	0.165	0.164	0.166	0.82	0.063	0.060	0.059	0.061
1.00	1.02	0.171	0.167	0.166	0.168	0.83	0.064	0.062	0.061	0.062
0.01	0.69	0.152	0.152	0.152	0.152	0.75	0.072	0.074	0.074	0.073
0.50	0.69	0.169	0.166	0.165	0.167	0.83	0.073	0.068	0.067	0.069
1.00	0.68	0.172	0.170	0.169	0.170	0.84	0.072	0.069	0.069	0.070
0.01	0.35	0.173	0.174	0.173	0.173	0.86	0.091	0.094	0.094	0.093
0.50	0.35	0.197	0.195	0.194	0.196	0.97	0.084	0.078	0.078	0.080
1.00	0.34	0.204	0.200	0.200	0.201	1.00	0.082	0.079	0.078	0.080

1: first cycle, 2: second cycle, 3: third cycle, Avg: average of three cycles

4.3.2 High Damping Elastomeric Bearings

The high damping rubber bearings were of the same geometry as the low damping rubber bearings (Figure 4-3) and of hardness 55, durometer A. Four bearings were produced in a single batch (referred to as bearings 1,2,3 and 4 of batch No. 1) with the intention of testing all four bearings prior to their use in the shake table testing. However, during compression testing of the first bearing, it was observed that bulging was uneven and the assumption was made that it delaminated. It was cut for inspection to find that one of the steel shims was misaligned, which resulted in the uneven bulging. Subsequently, bearing No. 2 was tested and two more bearings were ordered (to be referred to as bearings 5, 6 of batch No. 2).

Table 4-4 presents the mechanical properties of the tested bearing. Note that the tests were conducted in the sequence presented in the table and under constant axial load of *35.6 kN*. Two important observations can be made on the results of Table 4-4:

(a) The damping is exceptionally high with a value exceeding *0.2* for the conditions of interest (frequency of *1.0 Hz*, large strain), and

(b) The bearing exhibits a progressive reduction of its effective stiffness. For example, observe in Table 4-4 the average value of G_{eff} in the three cycles of test. In the first test it is *0.62 MPa*, in the second it is *0.53 MPa*, in the fifth test it is *0.45 MPa* and in the last test (test No. 26) it is *0.46 MPa* (all identical tests at frequency of *1.0 Hz* and shear strain of about *125*-percent). The recorded force-displacement loops in these four identical tests are shown in Figure 4-5.

It is clear that the bearing exhibits differences between its unscragged (virgin) properties and its scragged properties. Figure 4-6 illustrates the reduction of effective stiffness with increasing number of cycles. Evidently, the unscragged (initial) stiffness is about *50*-percent higher than the scragged (stable) stiffness. This is also evident in the loops of Figure 4-5.

Based on the currently accepted notion (however, supported by some experimental evidence - see Cho and Retamal, 1993) that the scragged properties are not stable but rather the rubber exhibits recovery to its unscragged properties, it was decided not to test the remaining four bearings. Rather, the bearings were directly installed in the isolated bridge model for shake table testing in order to observe their behavior during repeated strong excitation (selected to be the El Centro earthquake scaled up by a factor of two).

Of interest is to discuss the exceptionally high damping of the tested bearing. One possibility is that the high damping is not truly a mechanical property of the rubber but rather the result of the near-instability conditions of testing. Use of (4-1) and (4-2) predicts a theoretical buckling load less than the carried load (*35 kN*) at the displacement corresponding to a shear strain of *125*-percent. On the other hand, the loops of Figure 4-5 demonstrate positive incremental force-carrying capability, that is, the bearing is stable.

Table 4-4: Mechanical Properties of High Damping Elastomeric Bearing No. 2

Frequency (Hz)	Strain	K_{eff} 1 (kN/mm)	K_{eff} 2 (kN/mm)	K_{eff} 3 (kN/mm)	K_{eff} Avg (kN/mm)	G_{eff} (MPa)	β 1	β 2	β 3	β Avg
1.00	1.27	0.147	0.117	0.109	0.124	0.62	0.217	0.217	0.222	0.219
1.00	1.26	0.117	0.104	0.100	0.107	0.53	0.215	0.228	0.206	0.217
0.50	1.29	0.095	0.085	-	0.090	0.45	0.240	0.260	-	0.250
0.01	1.30	0.058	0.055	0.052	0.055	0.27	0.258	0.283	0.291	0.277
1.00	1.26	0.099	0.088	0.085	0.091	0.45	0.246	0.261	0.265	0.257
1.00	1.02	0.093	0.083	0.081	0.085	0.42	0.275	0.294	0.298	0.288
0.50	1.03	0.081	0.073	0.070	0.075	0.37	0.288	0.310	0.312	0.303
0.01	1.03	0.046	0.044	0.044	0.045	0.22	0.334	0.350	0.350	0.344
2.00	0.65	0.136	0.125	0.123	0.128	0.63	0.219	0.227	0.227	0.224
1.50	0.67	0.124	0.113	0.110	0.116	0.57	0.230	0.246	0.250	0.242
1.00	0.68	0.114	0.103	0.100	0.106	0.52	0.243	0.261	0.263	0.255
0.50	0.69	0.101	0.092	0.089	0.094	0.46	0.255	0.273	0.273	0.267
0.01	0.69	0.056	0.052	0.051	0.053	0.26	0.307	0.331	0.333	0.323
2.00	0.33	0.210	0.197	0.192	0.200	0.99	0.179	0.184	0.182	0.182
1.50	0.34	0.195	0.186	0.182	0.187	0.93	0.179	0.188	0.187	0.184
1.00	0.34	0.182	0.172	0.169	0.174	0.86	0.181	0.193	0.192	0.189
0.50	0.34	0.163	0.155	0.152	0.157	0.77	0.189	0.199	0.197	0.195
0.01	0.34	0.093	0.090	0.089	0.091	0.45	0.218	0.233	0.234	0.228

Table 4-4: Continued

Frequency (Hz)	Strain	K_{eff} 1 (kN/mm)	K_{eff} 2 (kN/mm)	K_{eff} 3 (kN/mm)	K_{eff} Avg (kN/mm)	G_{eff} (MPa)	β 1	β 2	β 3	β Avg
2.00	0.10	0.286	0.276	0.275	0.279	1.38	0.168	0.176	0.173	0.173
1.50	0.10	0.279	0.268	0.266	0.271	1.34	0.163	0.176	0.174	0.171
1.00	0.10	0.262	0.258	0.256	0.259	1.28	0.167	0.174	0.172	0.171
0.50	0.10	0.238	0.232	0.231	0.234	1.16	0.168	0.180	0.179	0.176
0.01	0.10	0.141	0.143	0.144	0.143	0.71	0.194	0.200	0.197	0.197
0.01	1.30	0.074	0.065	0.062	0.067	0.33	0.206	0.216	0.222	0.214
1.00	0.74	0.123	0.112	0.106	0.114	0.56	0.314	0.271	0.305	0.297
1.00	1.21	0.100	0.091	0.087	0.093	0.46	0.217	0.224	0.228	0.224

1: first cycle, 2: second cycle, 3: third cycle, Avg: average of three cycles

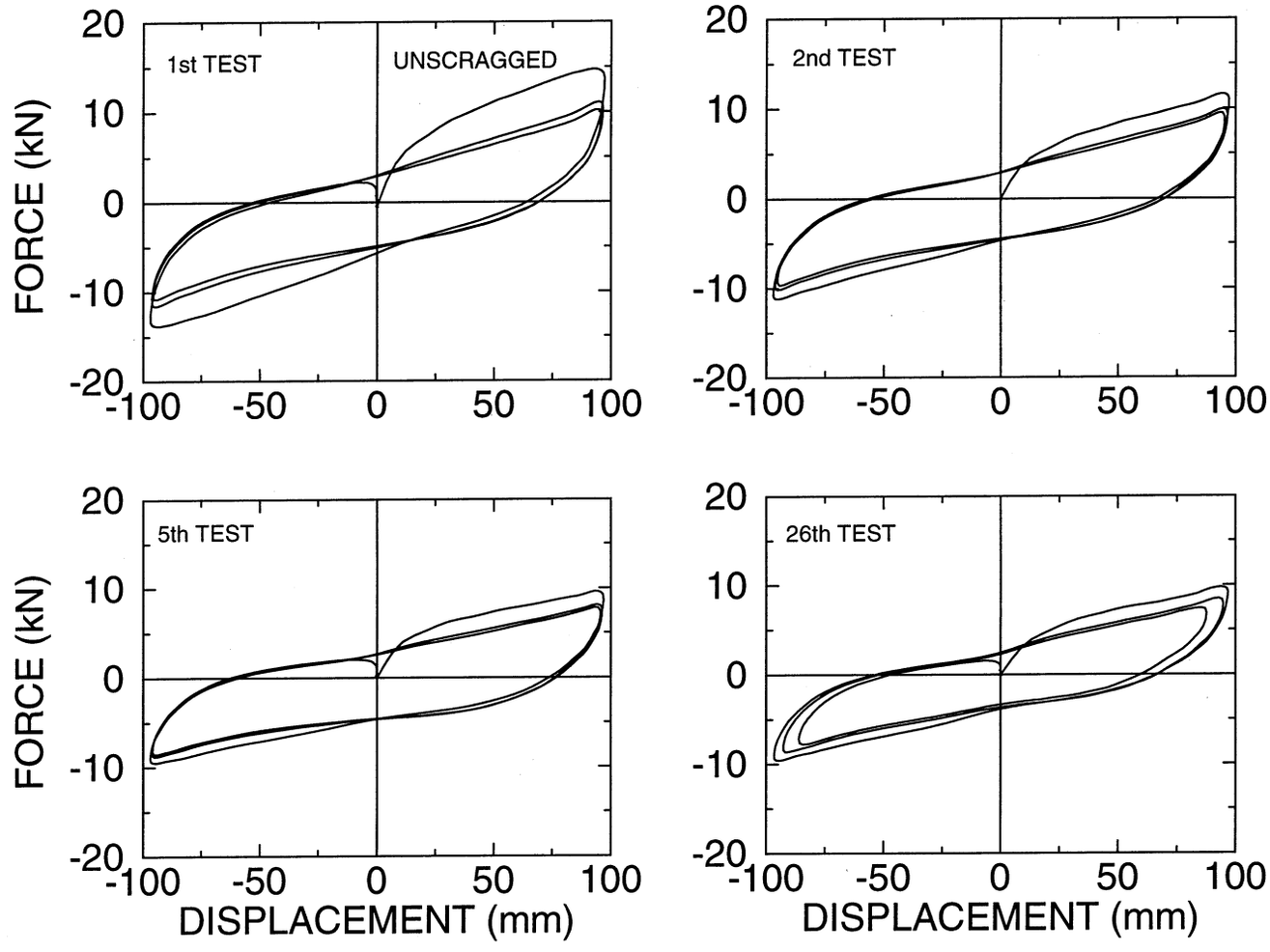

Figure 4-5: Lateral Force-Lateral Displacement Loops of High Damping Elastomeric Bearing No. 2

(all tests are at frequency 1.0 Hz)

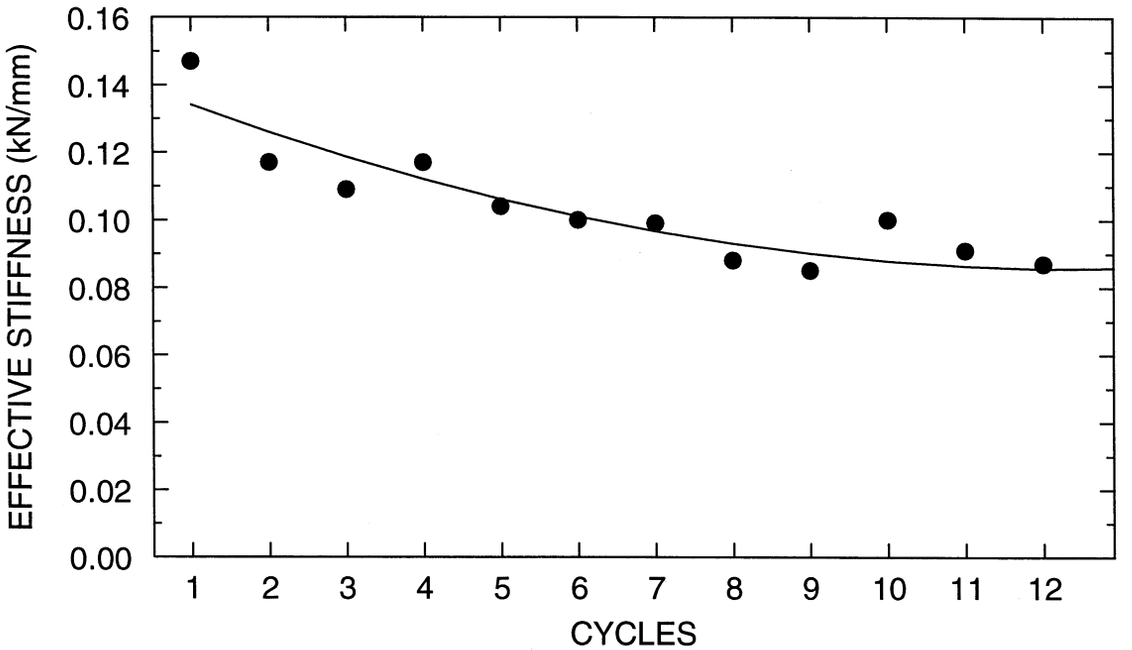

Figure 4-6: Effective Stiffness of High Damping Elastomeric Bearing No. 2 as Function of Number of Cycles (all tests at frequency of 1.0 Hz and strain of 125-percent)

Of interest is to discuss the exceptionally high damping of the tested bearing. One possibility is that the high damping is not truly a mechanical property of the rubber but rather the result of the near-instability conditions of testing. Use of (4-1) and (4-2) predicts a theoretical buckling load less than the carried load (*35 kN*) at the displacement corresponding to a shear strain of *125*-percent. On the other hand, the loops of Figure 4-5 demonstrate positive incremental force-carrying capability, that is, the bearing is stable.

Another possibility is that the rubber was insufficiently cured, a condition known to produce high damping but also unstable properties and creep, and, likely, significant aging effects. Indeed, the tested bearing No. 2 and bearings No. 3 and 4 (which were used in the shake table testing) exhibited significant creep. For example, bearing No. 2 was kept in the testing machine under the weight of the loading beam (14.7 kN) and observed over a period of several days. It showed clear evidence of creep which was manifested as a small lateral displacement of the middle part of the bearing. A similar condition was observed in bearings No. 3 and 4 on the shake table (note that bearings No. 2, 3 and 4 were from batch No. 1). However, no such behavior was observed for the other two bearings, No. 5 and 6 from batch No. 2, which were used on the shake table.

Additional information on the mechanical properties of the high damping elastomeric bearings was obtained during the shake table testing of the isolated bridge model. The model was subjected to a series of identical tests (with El Centro earthquake, component S00E, scaled up by a factor of 2.0). Figure 4-7 presents the force-displacement loops recorded in three of these tests. The loops on the left are those of a bearing from batch No. 1, which was installed on the abutment side. The loops on the right are those of a bearing from batch No. 2, which was installed on the flexible pier side. Moreover, the tests were conducted in the sequence shown, with test No. 1 conducted first

(unscragged conditions), test No. 3 third and so on (other tests were conducted in-between these tests).

The loops shown in Figure 4-7 were used to obtain estimates of the effective stiffness and damping of each bearing. For this, the loop corresponding to the maximum exertion was utilized. Lines corresponding to a linear-elastic representation of the behavior were drawn (see Figure 4-7), from which the effective stiffness was determined. For the calculation of the damping, the semi-loop corresponding to the maximum displacement was used to obtain the half area enclosed by the loop. The damping was then obtained as

$$\beta = \frac{2(\text{Half Area of Loop})}{2\pi K_{eff} d_{max}^2} \tag{4-4}$$

where d_{max} = maximum bearing displacement. The calculated values of effective stiffness, damping and maximum strain ($\gamma_{max} = d_{max}/T_r$) are shown directly on the graphs of Figure 4-7. Comparing now to the results of Table 4-4 at strain of about *68*-percent and frequency of *1.0 Hz* (the values in the table correspond to scragged conditions), we observe consistency between the results obtained in the testing with sinusoidal motion (Figure 4-4) and the results obtained in seismic testing (Figure 4-7). However, the latter have lower damping values which may be the effect of the testing method and of the approximate way of estimating damping (Eq. 4-4).
Nevertheless, it is evident in Figure 4-7 that the bearings produced in two different batches exhibit nearly the same mechanical properties. Based on these properties, the period of the isolated bridge model is estimated to be in the range of *0.9* to *1.1 sec* with damping of the order of *20*-percent. That is, despite the uncertainty on the origin of the high damping (likely it was the incomplete curing of the rubber), the isolated bridge with high damping elastomeric bearings exhibited properties beyond expectation. Accordingly, the test results obtained in the shake table testing provided a good set of data to compare against those obtained with the combined low damping elastomeric bearing - viscous damping device isolation system.

4.4 Viscous Damping Devices

Linear and nonlinear viscous damping devices were utilized in the testing of the isolated bridge model with low damping elastomeric bearings. The linear dampers were designed on the basis of providing a damping ratio of *30*-percent of critical to the isolated bridge model. Calculations were based on the assumption of an effective period of $T = 0.85$ *sec*, bridge deck weight of $W = 140$ *kN* and damper installation at an angle of $\theta = 45$ degrees (the dampers were finally installed symmetrically inclined in space at an angle of *45* degrees with respect to the longitudinal bridge axis - they could provide damping force in both the longitudinal and the transverse directions). The provided viscous damping ratio β_v is

$$\beta_v = \frac{CgT}{4\pi W} \tag{4-5}$$

where C = effective damping coefficient of the two devices in the longitudinal direction. Each linear damper has output force F_D related to the velocity of the piston of the damper V_D

$$F_D = C_0 V_D \tag{4-6}$$

so that $C = 2\ C_o\ cos^2\theta$. Accordingly, for $\beta_v = 0.3$ the damping coefficient C_o should have a value of *0.063 kN-s/mm.*

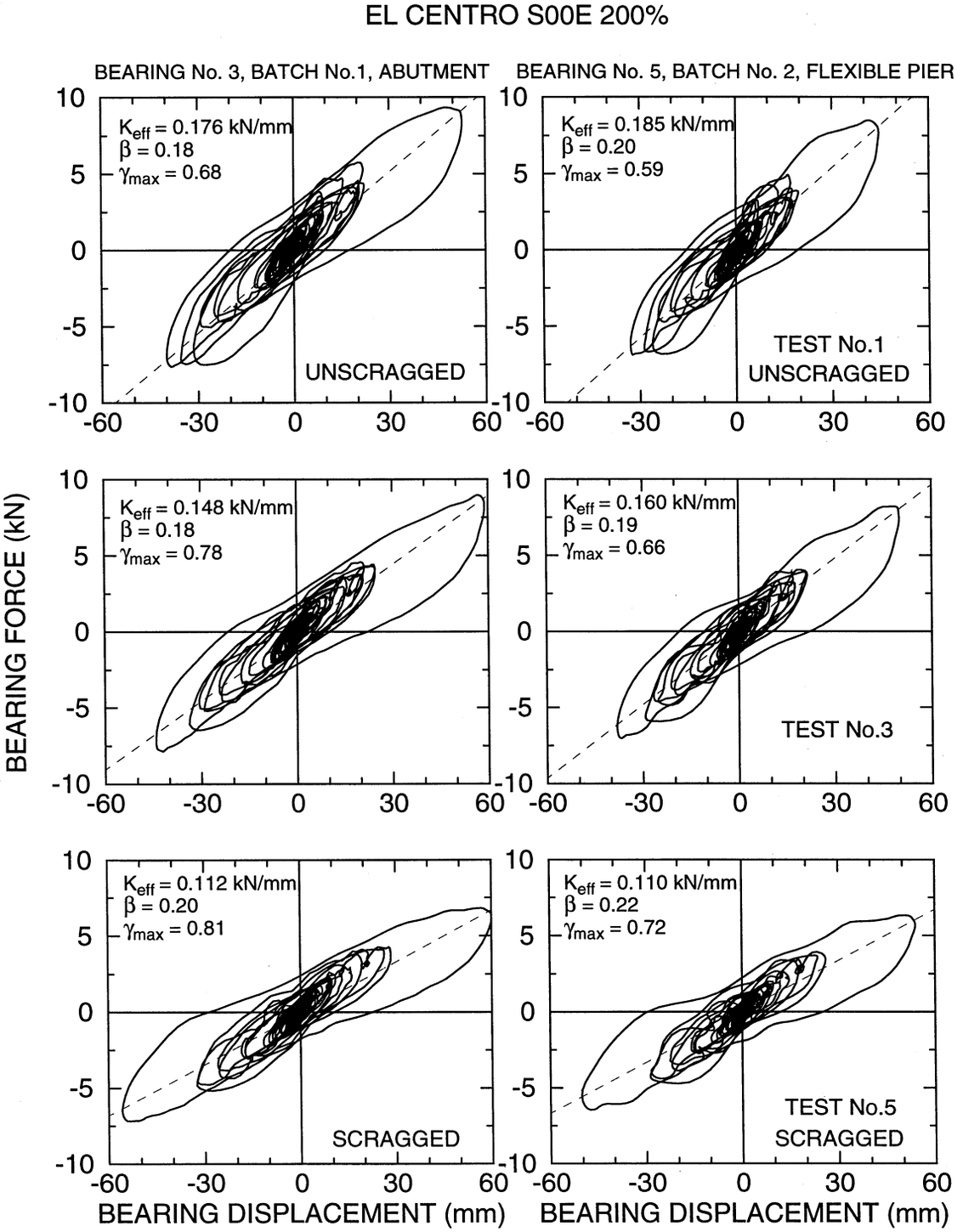

Figure 4-7: Force-Displacement Loops of Individual High Damping Elastomeric Bearings Recorded in Sequence of Identical Shake Table Tests

Two linear dampers of the run-through rod construction (without accumulator), damping coefficient C_o = *0.063 kN-s/mm*, displacement capacity of $\pm$*51 mm* and rated force of *30 kN* were specified to the manufacturer.

The nonlinear dampers were specified to have the same displacement capacity and a damping force-velocity relation described by

$$F_D = C_N|V_D|^{\delta}\text{sign}(V_D) \tag{4-7}$$

where C_N = *2.12 kN(s/mm)*$^{0.4}$ and δ = *0.4*. That is, the nonlinear dampers were specified to produce the same output force as the linear dampers at a velocity of *350 mm/s*.

Figure 4-8 illustrates the geometry of the viscous dampers. The dampers were supplied with spherical bushings capable of 17 degrees of rotation (the demand was less than 5 degrees). For the installation in the bridge model, the dampers were furnished with load cells which were installed as shown in Figure 4-8.

The dampers were tested by imposing sinusoidal motion of specified amplitude and frequency to their piston rod and then measuring the needed force to maintain this motion (with the load cell shown in Figure 4-8). Figures 4-9 and 4-10 present force-displacement loops obtained in the testing of one linear and one nonlinear damper. The other two dampers exhibited nearly identical behavior.

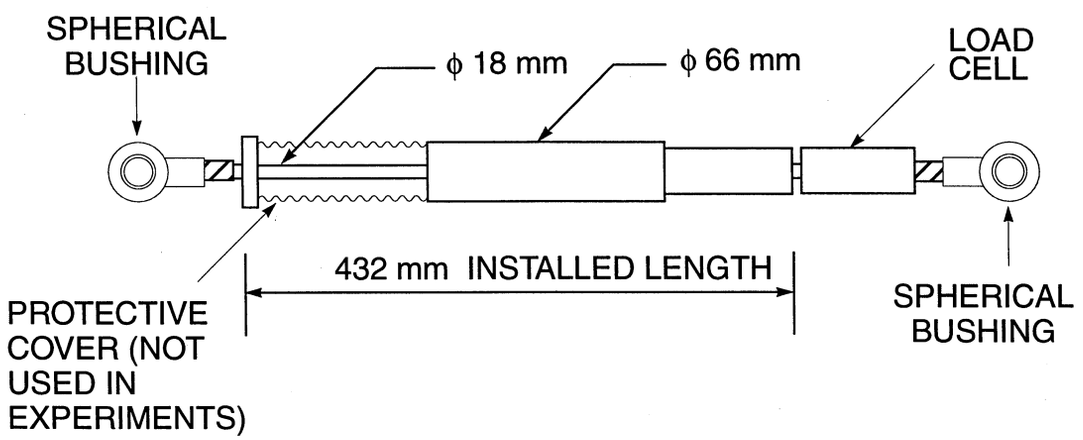

Figure 4-8: Schematic of Viscous Damper

Tests were conducted for frequencies up to *10 Hz* without observing any evidence of restoring force developed by the dampers. Accordingly, the dampers exhibited pure viscous behavior, which could be identified in graphs of the peak damping force (at zero displacement) versus the peak velocity (amplitude times circular frequency) as discussed in Seleemah and Constantinou (1997). Figure 4-11 presents such graphs for the two dampers. The linear damper exhibits a behavior which can be approximated by (4-6) with C_o = *0.0664 kN-s/mm*. Also, the nonlinear damper behavior could be approximated by (4-7) with C_N = *2.226 kN (s/mm)*$^{0.397}$. That is, both dampers exhibited the specified behavior with very good accuracy.

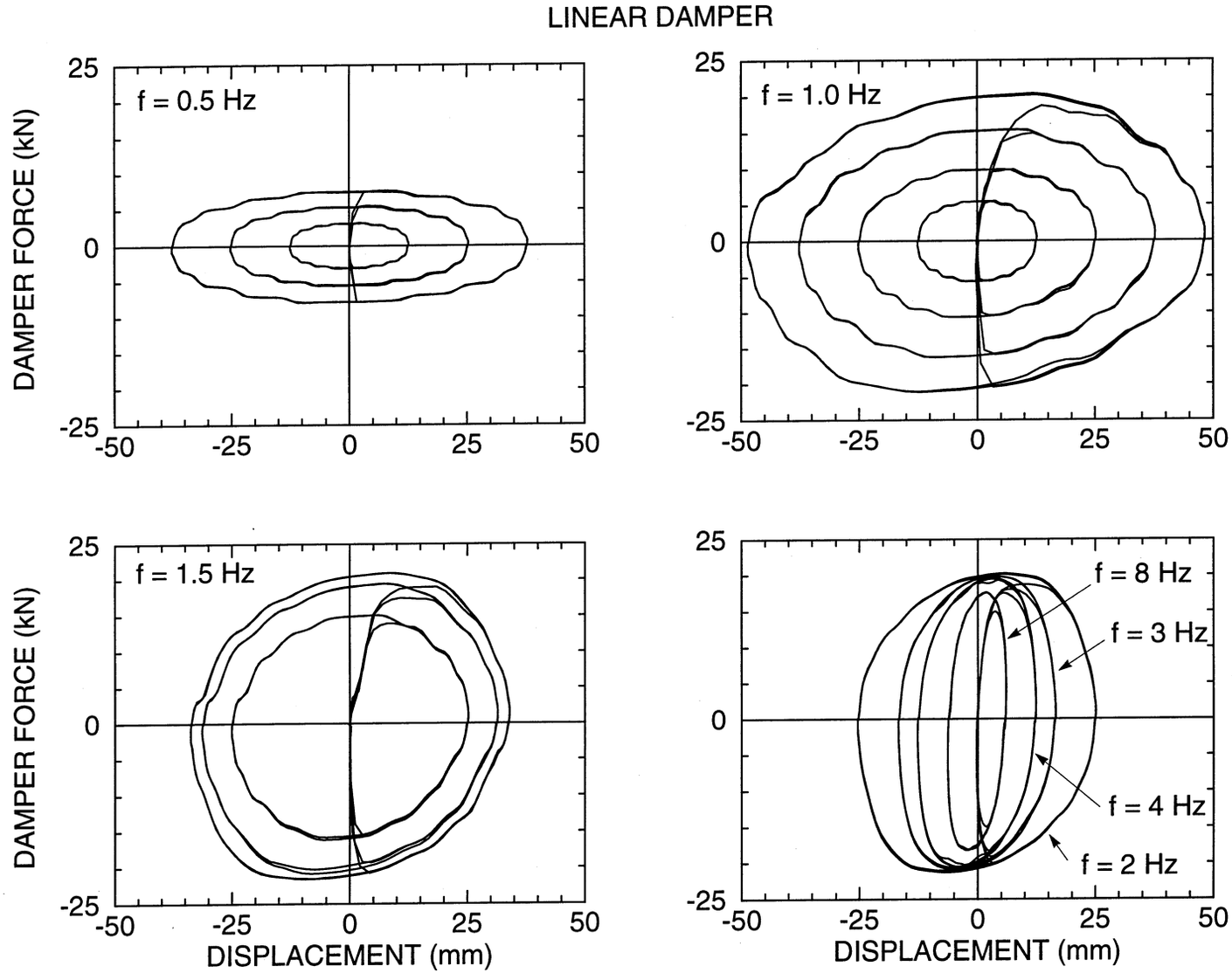

Figure 4-9: Recorded Force-Displacement Loops of Linear Fluid Viscous Damper in Tests with Sinusoidal Motion

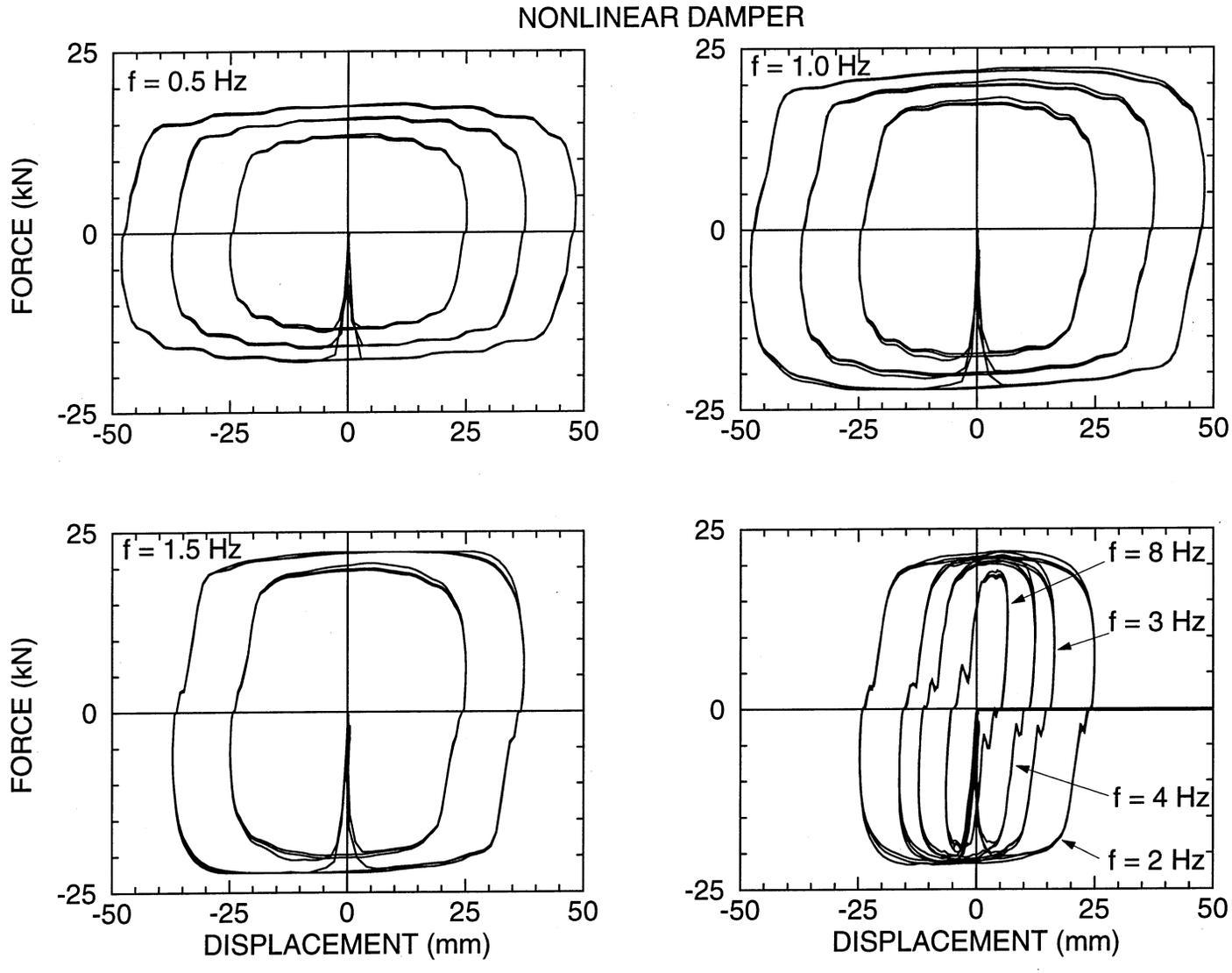

Figure 4-10: Recorded Force-Displacement Loops of Nonlinear Fluid Viscous Damper in Tests with Sinusoidal Motion

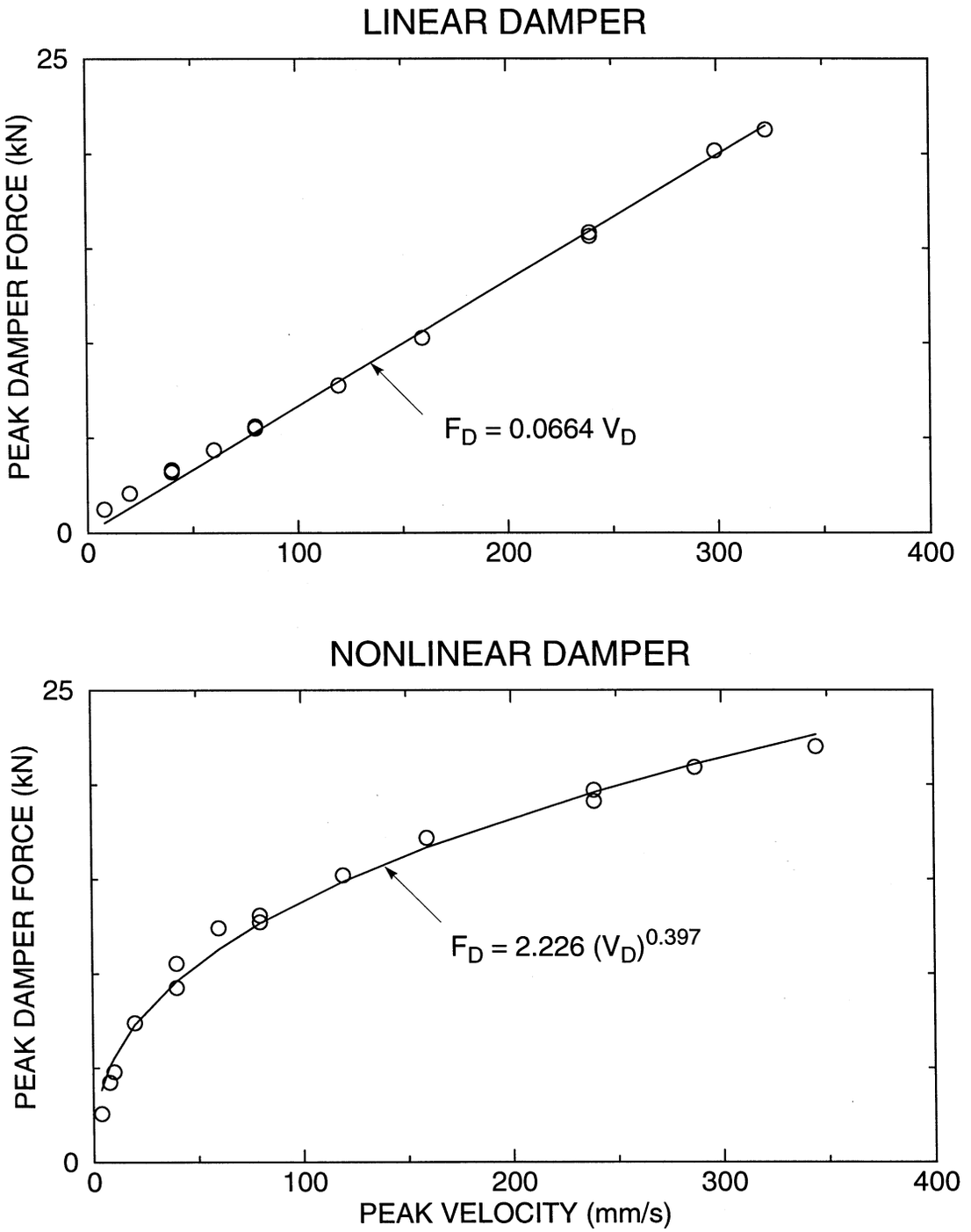

Figure 4-11: Relation of Peak Damping Force and Peak Velocity of Tested Fluid Viscous Dampers

4.5 Tested Bridge Configurations

A total of seven configurations of the bridge model were tested. Figure 4-12 presents a schematic description of these configurations. These configurations are:

1. Non-isolated bridge (N0FS Test Series): Two low damping elastomeric bearings on the abutment served the purpose of expansion bearings. Two identical bearings were installed on the flexible pier and locked with side plates to represent fixed bearings (allowing limited rotation but no relative displacement).

2. Non-isolated bridge with linear dampers (NLFS Test Series): Two linear dampers were installed at the abutment side of the non-isolated bridge in (1) above. The dampers were connected at the center of the abutment and were inclined towards the two girders of the deck, to which they were connected. Figure 4-13 presents a side view and a front view of the abutment with details of the damper installation. Moreover, Figure 4-14 presents a schematic of the geometry of installation of the dampers. They were installed between points A and B (located just above the top of the abutment at its center) and points C and D (located just below the bottom flange of the two girders of the bridge deck). Points A and C, and B and D represented the centers of the spherical bushings of the two dampers, respectively. The angle between the damper axis and the longitudinal bridge direction was 45 degrees.

   It should be noted that on movement of the deck, the angle between the damper axis and the longitudinal bridge direction changes. The minimum value of the angle is obtained at the maximum possible deck movement, which is about *70 mm* (calculated on the basis of the damper displacement capacity - *50 mm*). It is *42.3* degrees (evaluated from the geometry of Figure 4-14 with a distance AC' equal to *776 mm* rather than *706 mm*). Accordingly, the angle varied during testing between the values of 42.3 and 47.7 degrees.

3. Non-isolated bridge with nonlinear dampers (NNFS Test Series): Two nonlinear dampers were installed at the abutment of the non-isolated bridge in place of the linear dampers. The configuration was otherwise identical to the one described in (2) above.

4. Bridge isolated with low damping elastomeric bearings (L0FS Test Series): The bridge deck was isolated with four low damping elastomeric bearings, with two mounted on the abutment and the other two on the flexible pier.

5. Bridge isolated with low damping elastomeric bearings and linear dampers (LLFS test series): Two linear dampers were added at the abutment of the isolated structure described in (4) above. The dampers were installed in the same way as in the non-isolated bridge (described in (2) above). Figure 4-15 presents a view of the model on the shake table.

6. Bridge isolated with low damping elastomeric bearings and nonlinear dampers (LNFS test series): Two nonlinear dampers were installed at the abutment of the isolated structure in place of the linear dampers. The configuration was otherwise identical to the one described in (5) above.

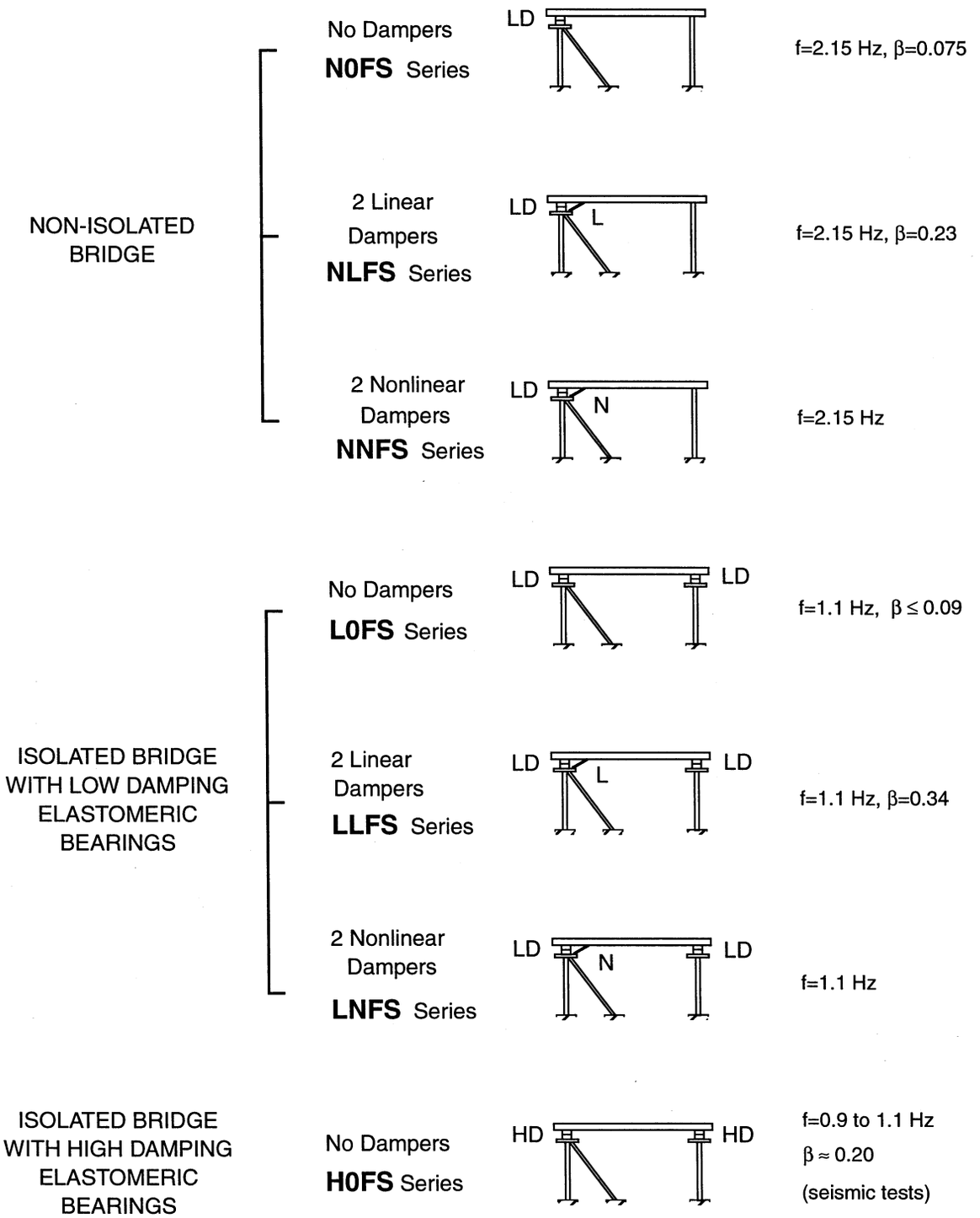

(LD: Low Damping Elastomeric Bearing, HD: High Damping Elastomeric Bearing
L: Linear Viscous Dampers, N: Nonlinear Viscous Dampers)

Figure 4-12: Illustration of Tested Bridge Configurations

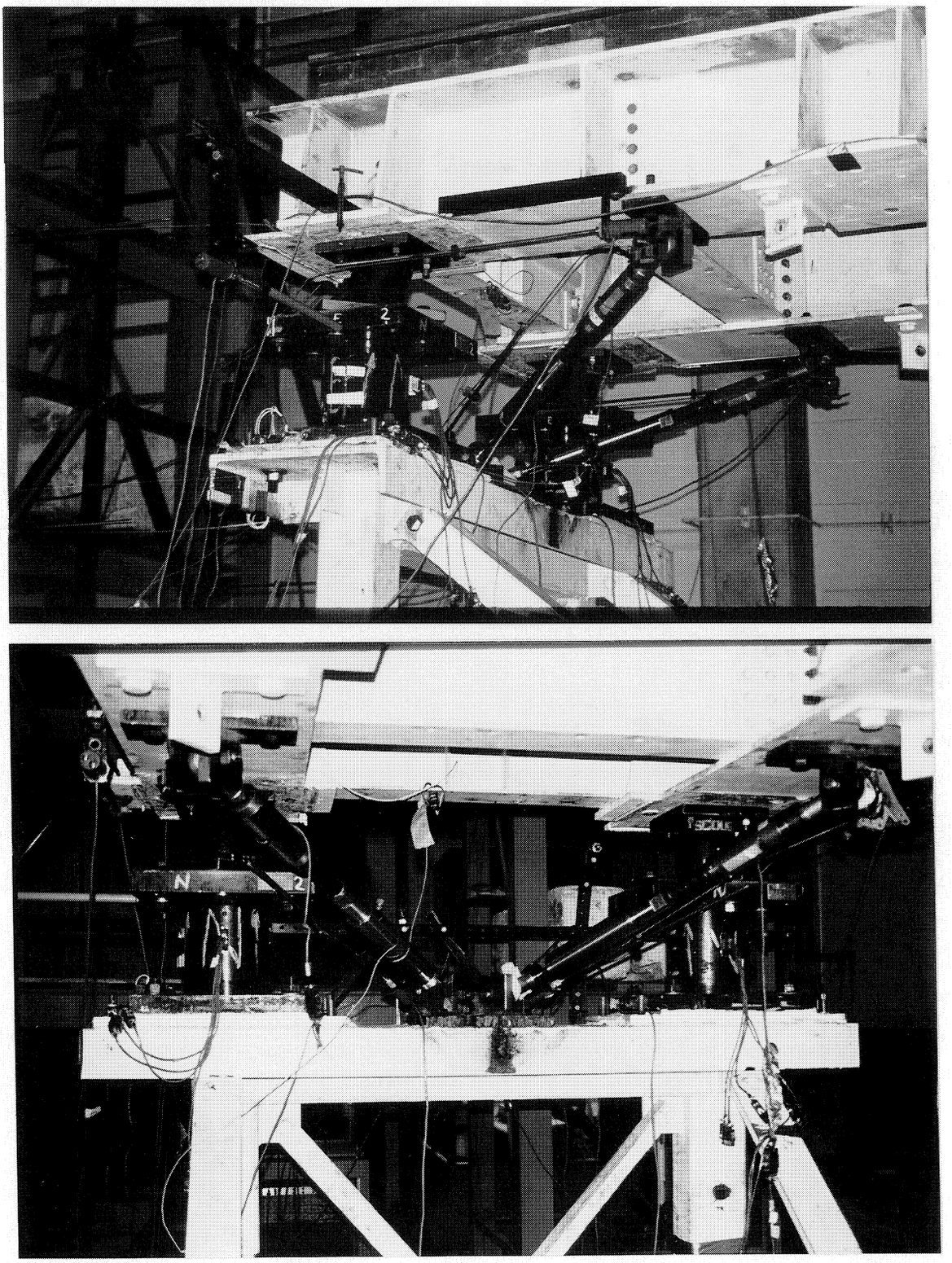

Figure 4-13: Detail of Installation of Fluid Dampers at the Abutment Location (top is side view and bottom is front view)

7. Bridge isolated with high damping elastomeric bearings (H0FS Test Series): In this configuration the bridge was isolated with four high damping elastomeric bearings in a configuration that was otherwise identical to the one described in (4) above.

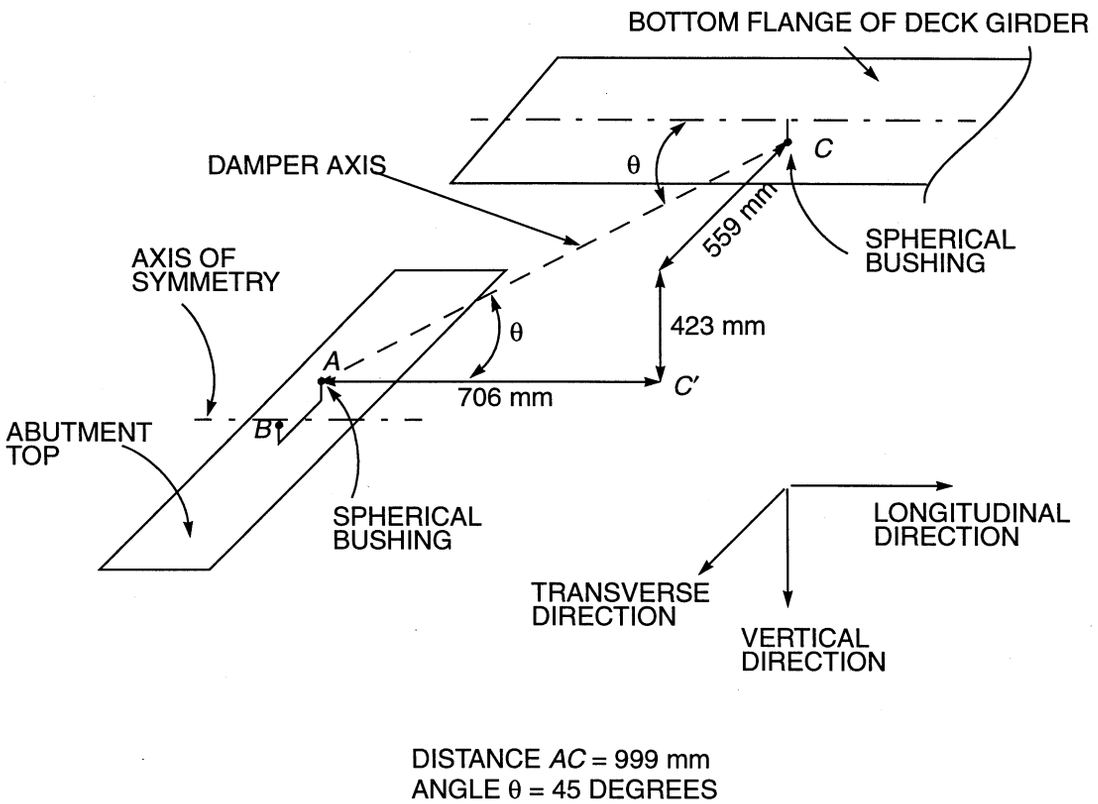

Figure 4-14: Geometry of Installation of Fluid Dampers

4.6 Identification of Basic Properties of Tested Bridge Configurations

The isolated bridge model without and with linear viscous dampers and the non-isolated bridge model without and with linear viscous dampers were tested under banded (*0 to 25 Hz*) white noise excitation at the shake table for identifying the basic properties of the bridge.

During testing, transfer functions were obtained as the ratio of the Fourier transform of the deck horizontal acceleration (measured directly above the bearings) to the Fourier transform of the horizontal table acceleration. Figure 4-16 presents the amplitude of these transfer functions for the four tested configurations. These functions demonstrate a response that is essentially one of a single-degree-of-freedom system. Actually, the transfer functions exhibited a minor secondary peak (with a value of about 0.125) at the frequency of *12 Hz*. This secondary peak is associated with the second mode of vibration which is dominated by the response of the flexible pier (which had a frequency of about 10 Hz in its free standing position without the deck on top of it).

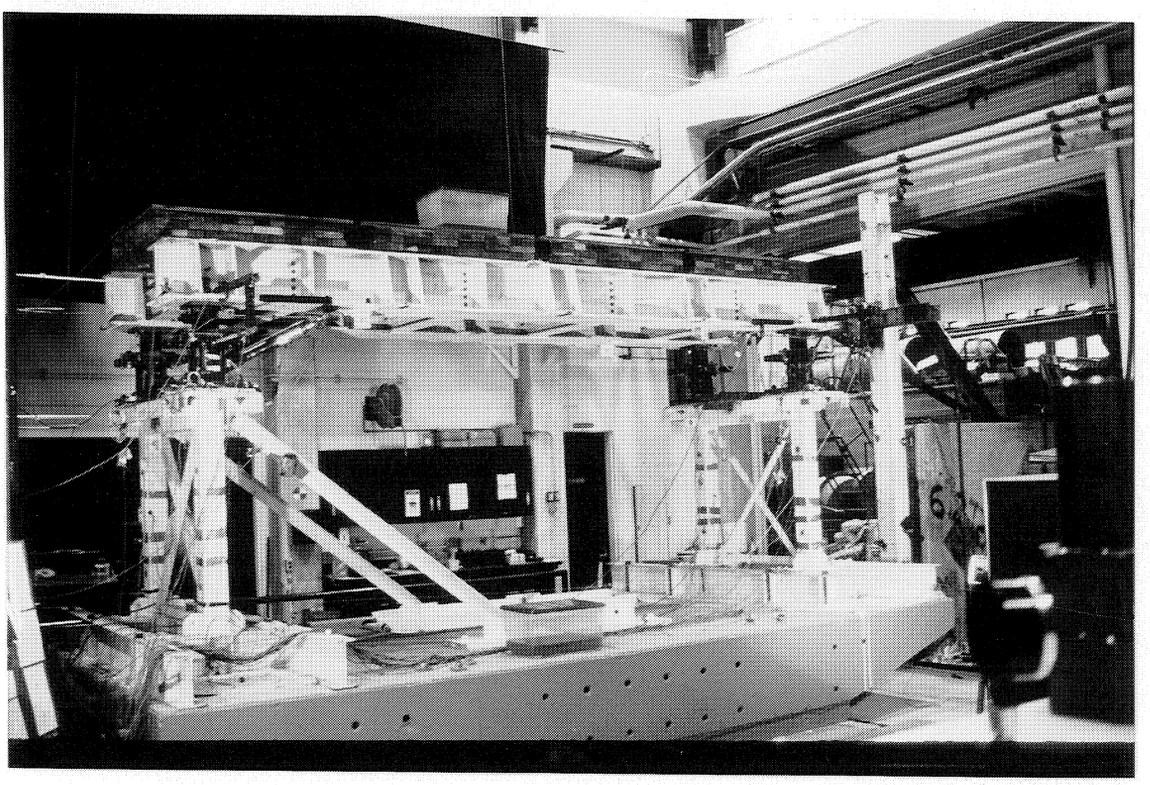

Figure 4-15: View of Isolated Bridge with Low Damping Elastomeric Bearings and Viscous Dampers on the Shake Table

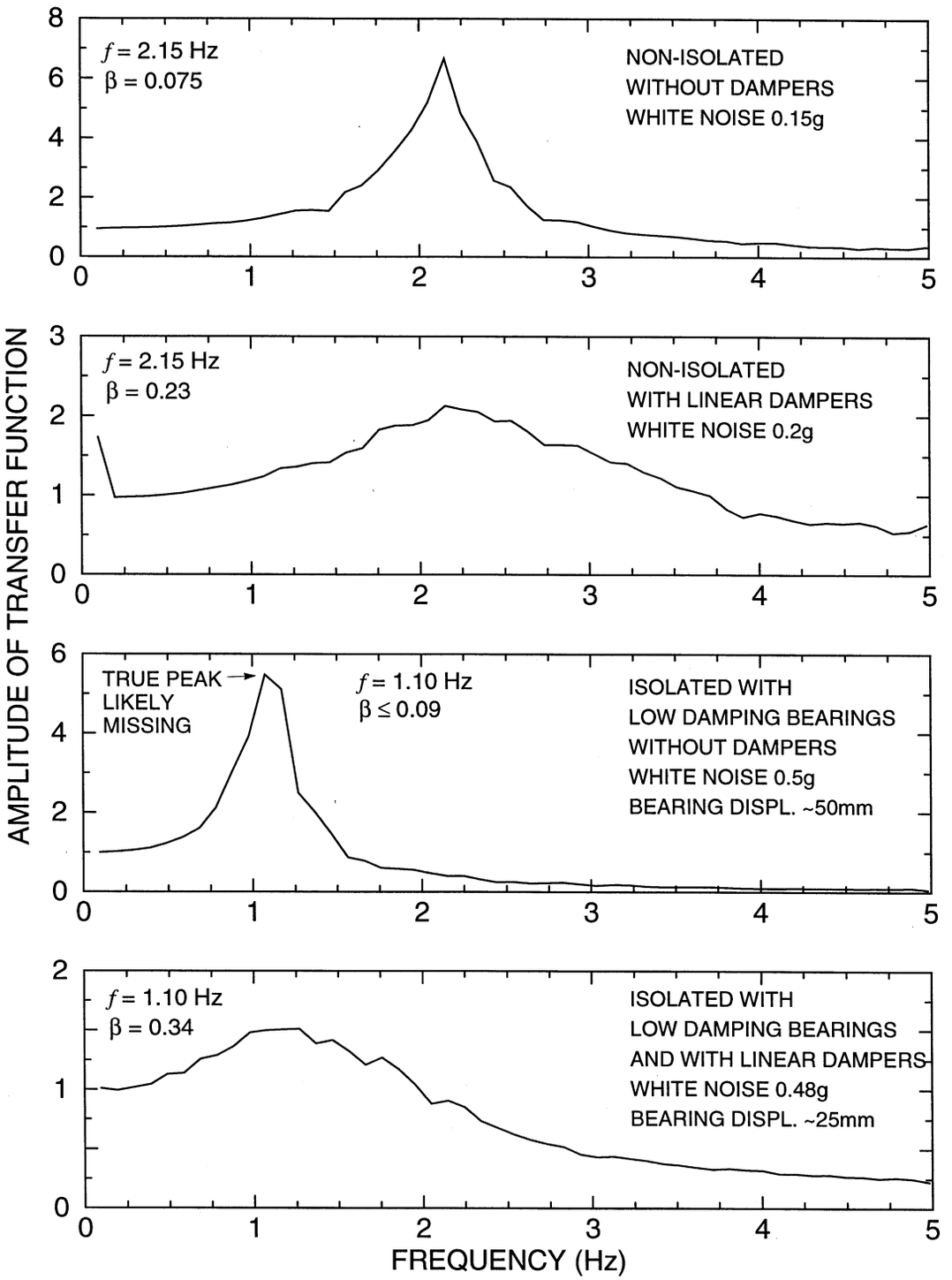

Figure 4-16: Amplitude of Transfer Functions Obtained in White Noise Excitation of Various Bridge Configurations

The identified properties of fundamental frequency, f, and damping ratio, β, are presented directly on Figure 4-16. The following observations may be made:

(a) The addition of linear viscous dampers does not change the fundamental frequency of the system. This was expected since the dampers were truly viscous.

(b) The damping ratio obtained in the case of the non-isolated bridge without dampers is larger than expected. Given that the system responds in the elastic range without any inelastic action in the columns, energy dissipation results from the deformation of the two bearings on top of the abutment. These two bearings were subjected to motion of frequency of about *2.0 Hz* and small shear strain. The damping ratio should have been of the order of *0.04* (see Table 4-2; damping should be about *0.08* if the entire deck weight was supported by the bearings). The additional energy dissipation originated primarily in the overhangs of the concrete extension of the shake table which underwent vertical motion during testing and developed cracks (see also Constantinou et al., 1993; Tsopelas et al., 1994b who observed the same phenomenon).

(c) The damping ratio provided by the linear viscous dampers can be obtained from (4-5), which for the tested systems can be written as

$$\beta_v = \frac{C_0 cos^2\theta g}{2\pi f W} \tag{4-8}$$

where C_o = *0.0664 kN-s/mm*, θ = *45* degrees, W = *140 kN* and f = fundamental frequency. For the tested non-isolated configuration, (4-8) predicts β_v = *0.17* whereas the identified value is *0.23*. The difference is damping provided by the concrete extension of the shake table but it can also by in-part error in the measurement due to insufficient speed of data acquisition.

Use of (4-8) for the case of the isolated bridge with dampers gives β_v = *0.34*, whereas the identified value is *0.34*. The identified value should have been higher if we consider that the low damping elastomeric bearings have a contribution of about *0.06* (see Table 4-2) to the total damping. In the case of white noise testing the identified damping ratio is less than expected due to heating of the viscous dampers in this strong and long excitation (typically, the excitation lasted about 60 seconds).

(d) The identified damping ratio for the case of isolated bridge without dampers (β = *0.09*) may have been overestimated due to insufficient speed of data acquisition that resulted in a lower peak value of the amplitude of the transfer function.

The identified basic properties are shown directly on the graphs of Figure 4-12 for direct comparison. We have included in this figure values of these properties obtained in the seismic testing of the isolated bridge with high damping elastomeric bearings. Moreover, we did not include any values of the damping ratio for the case of the bridge with nonlinear viscous dampers. In this case, the damping ratio is dependent on the level of movement of the deck with respect to the table. It is, in general, larger than the damping ratio for the corresponding case with linear dampers.

4.7 Instrumentation

The instrumentation of the model bridge consisted of load cells, accelerometers and displacement transducers. Sufficient care was taken to measure each important quantity by one direct measurement and one or more indirect measurements. For example, all bearing displacements

were measured directly by the displacement transducers mounted at the bearing level. These values were checked with the values obtained from calculating the difference between the deck and pier displacements. This redundancy was required for checking the validity of important measurements and also for safeguarding against instrument malfunctions.

Figure 4-17 shows the overall instrumentation diagram of the tested structure. The total number of monitored channels varied from 49 to 55 based on the configuration (e.g., the addition of dampers increased the number of channels by four). A list of all monitored channels is given in Table 4-5 for the case of the isolated bridge with fluid viscous dampers.

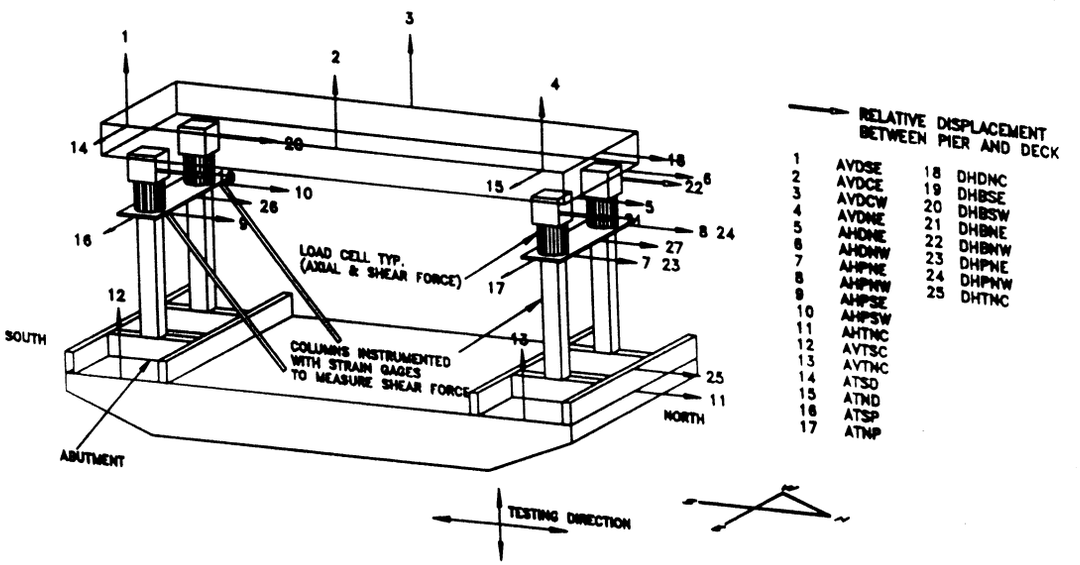

Figure 4-17: Overall Instrumentation Diagram

4.8 Testing Program

The bridge model was tested with 18 different earthquake motions. The motions consisted of historic earthquake records and artificial motions compatible with Japanese bridge design spectra. A number of earthquake motions were recorded in the 1994 Northridge earthquake and the 1995 Japanese Kobe earthquake. All had near fault characteristics with a significant peak ground velocity. Table 4-6 presents a list of the 18 horizontal components utilized in the testing and their peak ground motion characteristics in prototype scale.

Each of these earthquake records was scaled either down or up in acceleration, velocity and displacement so that a wide range of seismic intensities was created. Moreover, testing was conducted with only one horizontal component and, in selected cases, with combined horizontal and vertical components. This resulted in a total of 183 earthquake simulation tests. Table 4-7

provides a list of tests that were conducted on the bridge model. Note that the testing of the isolated bridge model with high damping elastomeric bearings was concluded early due to failure of one of the bearings.

Table 4-5: List of Data Acquisition Channels in the Case of the Isolated Bridge with Fluid Dampers

Channel Number	Notation	Instrument[1]	Unit	Response Measured
1	Time	CLOCK	sec	Time
2	N1	LOAD CELL	kips	Bearing Axial Force - South West
3	SX1	LOAD CELL	kips	Bearing Shear Force - Longitudinal - South West
4	SY1	LOAD CELL	kips	Bearing Shear Force - Transverse - South West
5	N2	LOAD CELL	kips	Bearing Axial Force - South East
6	SX2	LOAD CELL	kips	Bearing Shear Force - Longitudinal - South East
7	SY2	LOAD CELL	kips	Bearing Shear Force - Transverse - South East
8	N3	LOAD CELL	kips	Bearing Axial Force - North West
9	SX3	LOAD CELL	kips	Bearing Shear Force - Longitudinal - North West
10	SY3	LOAD CELL	kips	Bearing Shear Force - Transverse - North West
11	N4	LOAD CELL	kips	Bearing Axial Force - North East
12	SX4	LOAD CELL	kips	Bearing Shear Force - Longitudinal - North East
13	SY4	LOAD CELL	kips	Bearing Shear Force - Transverse - North East
14	NTOT	-	kips	Combined Bearing Axial Load (N1+N2+N3+N4)
15	SUMSX_34	-	kips	Combined Bearing Shear Force (SX3+SX4)
16	AHTNC	ACCL	g	Table Horizontal Accl. - North Side at Center
17	AHPNE	ACCL	g	Pier Horizontal Accl. - North East
18	AHPNW	ACCL	g	Pier Horizontal Accl. - North West
19	AHPSE	ACCL	g	Pier Horizontal Accl. - South East
20	AHPSW	ACCL	g	Pier Horizontal Accl. - South West
21	AHDNE	ACCL	g	Deck Horizontal Accl. - North East Corner
22	AHDNW	ACCL	g	Deck Horizontal Accl. - North West Corner
23	AVDSE	ACCL	g	Deck Vertical Accl. - South East Corner
24	AVDCE	ACCL	g	Deck Vertical Accl. - East Side at Center

Table 4-5: Continued

Channel Number	Notation	Instrument[1]	Unit	Response Measured
25	AVDCW	ACCL	g	Deck Vertical Accl. - West Side at Center
26	AVDNW	ACCL	g	Deck Vertical Accl. - North West Corner
27	AVTSC	ACCL	g	Table Vertical Accl. - South Side at Center
28	AVTNC	ACCL	g	Table Vertical Accl. - North Side at Center
29	ATSD	ACCL	g	Deck Transverse Accl. - South Side
30	ATND	ACCL	g	Deck Transverse Accl. - North Side
31	ATSP	ACCL	g	Pier Transverse Accl. - South
32	ATNP	ACCL	g	Pier Transverse Accl. - North
33	DHTSE	DT	inch	Table Horizontal Displ. - South East Corner
34	DHTSW	DT	inch	Table Horizontal Displ. - South West Corner
35	DHPSE	DT	inch	Pier Total Horizontal Displ. - South East
36	DHPSW	DT	inch	Pier Total Horizontal Displ. - South West
37	DHDSE	DT	inch	Deck Total Horizontal Displ. - South East
38	DHDSW	DT	inch	Deck Total Horizontal Displ. - South West
39	DHBSE	DT	inch	Bearing Horizontal Displ. - South East
40	DHBSW	DT	inch	Bearing Horizontal Displ. - South West
41	DHBNE	DT	inch	Bearing Horizontal Displ. - North East
42	DHBNW	DT	inch	Bearing Horizontal Displ. - North West
43	DHTNC	DT	inch	Table Horizontal Displ. - North Side at Center
44	DHPNC	DT	inch	Pier Total Horizontal Displ. - North Side at Center
45	DRIFT_NP	-	inch	Pier Drift (DHPNC - DHTNC)
46	DDE	DT	inch	Displacement of East Side Damper at Abutment
47	DDW	DT	inch	Displacement of West Side Damper at Abutment
48	LCDW	LOAD CELL	kips	Force of West Side Damper at Abutment
49	LCDE	LOAD CELL	kips	Force of East Side Damper at Abutment
50	CLSE	LOAD CELL	Volt	Column Shear Force - South East
51	CLSW	LOAD CELL	Volt	Column Shear Force - South West
52	CLNE	LOAD CELL	Volt	Column Shear Force - North East
53	CLNW	LOAD CELL	Volt	Column Shear Force - North West

1 - ACCL = Accelerometer; DT = Displacement Transducer

Table 4-6: List of Earthquake Motions and Characteristics in Prototype Scale

NOTATION	EXCITATION (all are horizontal Components)	PEAK GROUND MOTION		
		DISPL (mm)	VELOC (mm/sec)	ACCL (g)
EL CENTRO S00E	Imperial Valley, May 18 1940, Component S00E	108.7	334.5	0.34
TAFT N21E	Kern County, July 21, 1952, Component N21E	67.1	157.2	0.16
HACHINOHE N-S	Tokachi, Japan, May 16, 1968 Hachinohe, Component N-S	118.9	357.1	0.23
AKITA N-S	Nihonkai Chuubu, Japan, May 23, 1983, Component N-S	146.0	292.0	0.19
MIYAGIKEN OKI	Miyaki, Japan, June 12, 1978 Ofunato-Bochi, Component E-W	50.8	141.0	0.16
PACOIMA S74W	San Fernando, February 9, 1971, Pacoima Dam, Component S74W	108.2	568.2	1.08
PACOIMA S16E	San Fernando, February 9, 1971, Pacoima Dam, Component S16E	365.3	1132.3	1.17
JP LEVEL 2 G.C. 1	Artificial Compatible with Japanese Level 1, Ground Condition 1	90.0	215.0	0.10
JP LEVEL 2 G.C. 2	Artificial Compatible with Japanese Level 1, Ground Condition 2	69.0	251.0	0.12
JP LEVEL 2 G.C. 3	Artificial Compatible with Japanese Level 1, Ground Condition 2	132.0	274.0	0.14
JP LEVEL 1 G.C. 1	Artificial Compatible with Japanese Level 2, Ground Condition 1	526.0	864.0	0.37
JP LEVEL 1 G.C. 2	Artificial Compatible with Japanese Level 2, Ground Condition 2	527.0	998.0	0.43
JP LEVEL 1 G.C. 3	Artificial Compatible with Japanese Level 2, Ground Condition 3	700.0	1121.0	0.45
NR SYLMAR 90°	Northridge-Sylmar, Parking lot, January 17, 1994, Component 90°	152.2	769.3	0.60
NR NEWHALL 90°	Northridge-Newhall, LA County Fire Station, January 17, 1994, Component 90°	176.0	748.4	0.58
NR NEWHALL 360°	Northridge-Newhall, LA County Fire Station, January 17, 1994, Component 360°	304.7	947.2	0.589
KOBE N-S	Kobe Station, Japan, January 17, 1995, Component N-S	207.4	914.3	0.83
MEXICO N90W	Mexico City, September 19, 1985 SCT building, Component N90W	212.0	605.0	0.17

Table 4-7: List of Earthquake Simulation Tests Conducted on Bridge Model

EARTHQUAKE RECORD	INTENSITY	NON-ISOLATED			LOW DAMPING BEARINGS			High Damping Bearings
		N0FS	NLFS	NNFS	L0FS	LLFS	LNFS	H0FS
EL CENTRO S00E	50%	✓	-	-	-	-	-	-
	100%	-	✓	✓	✓	✓	✓	✓
	200%	-	-	-	✓	✓	✓	✓
	100% H+V	-	✓	✓	✓	✓	✓	✓
	200% H+V	-	-	-	✓	✓	✓	✓
TAFT N21E	50%	✓	-	-	-	-	-	-
	100%	✓	✓	✓	✓	✓	✓	✓
	200%	-	✓	✓	✓	✓	✓	✓
	300%	-	-	-	-	✓	✓	-
	400%	-	-	-	-	✓	✓	✓
	100% H+V	✓	-	✓	-	-	-	✓
	200% H+V	-	✓	✓	✓	✓	✓	-
	400% H+V	-	-	-	-	✓	✓	✓
HACHINOHE N-S	25%	✓	-	-	-	-	-	-
	50%	✓	-	-	-	-	-	-
	100%	-	✓	✓	✓	✓	✓	-
	200%	-	-	-	✓	✓	✓	✓
	300%	-	-	-	-	✓	✓	✓
AKITA N-S	50%	-	-	✓	-	-	-	-
	100%	-	✓	✓	✓	✓	✓	✓
	200%	-	-	-	-	✓	✓	✓
MIYAGIKEN OKI	100%	✓	✓	✓	✓	✓	✓	✓
	200%	-	✓	✓	✓	✓	✓	✓
	300%	-	✓	✓	✓	✓	✓	✓
	500%	-	-	-	-	✓	✓	✓
PACOIMA S74W	25%	-	✓	✓	-	-	-	-
	50%	-	-	✓	-	✓	-	-
	75%	-	-	-	-	-	-	-
	100%	-	-	-	✓	✓	✓	✓
PACOIMA S16E	25%	-	✓	✓	-	-	-	-
	50%	-	-	✓	-	-	-	-
	75%	-	-	-	✓	✓	-	-
	100%	-	-	-	-	✓	✓	✓
	100% H+V	-	-	-	-	✓	✓	-
JP LEVEL 1 G.C. 1	100%	✓	✓	✓	✓	✓	✓	✓
JP LEVEL 1 G.C. 2	100%	✓	✓	✓	✓	✓	✓	✓
JP LEVEL 1 G.C. 3	100%	✓	✓	✓	✓	✓	✓	✓
JP LEVEL 2 G.C. 1	75%	-	-	-	✓	✓	✓	-
	100%	-	-	-	-	✓	✓	✓
JP LEVEL 2 G.C. 2	50%	-	-	-	-	-	✓	-
	100%	-	-	-	-	-	✓	✓
JP LEVEL 2 G.C. 3	75%	-	-	-	-	-	✓	-
	100%	-	-	-	-	-	✓	✓
NORTHRIDGE SYL-MAR 90°	50%	-	-	-	-	✓	-	-
	75%	-	-	-	-	✓	-	-
	100%	-	-	-	✓	✓	✓	-
	150%	-	-	-	-	-	✓	-
	100% H+V	-	-	-	✓	✓	✓	-
	150% H+V	-	-	-	-	-	✓	-
NORTHRIDGE NEWHALL 90°	100%	-	-	-	-	✓	-	-
	100% H+V	-	-	-	✓	✓	-	-
NORTHRIDGE NEWHALL 360°	50%	-	-	-	-	✓	-	-
	75%	-	-	-	✓	✓	-	-
	100%	-	-	-	-	✓	✓	-
	100% H+V	-	-	-	-	✓	✓	-
KOBE - KOBE STATION N-S	50%	-	-	-	-	✓	-	-
	100%	-	-	-	✓	✓	✓	-
	100% H+V	-	-	-	-	✓	✓	-
MEXICO CITY N90W	50%	-	✓	✓	-	✓	-	-
	60%	-	-	-		✓	-	-
	80%	-	-	-	-	✓	-	-
	100%	-	✓	✓	-	✓	✓	-
TOTAL NUMBER OF EXPERIMENTS		10	17	21	24	46	40	25

Each record was compressed in time by a factor of two to conform to the similitude requirements. Figures 4-18 to 4-35 present the recorded time histories of the table motion in the tests with the input being the earthquake signals of Table 4-6. The acceleration and displacement records were directly measured, where as the velocity record was obtained from numerical differentiation of the displacement record. The figures show also the 5-percent damped response spectra of the table motion, which are compared to the spectra of the target records. It is evident that the shake table-produced motions are in acceptable agreement with the target motions.

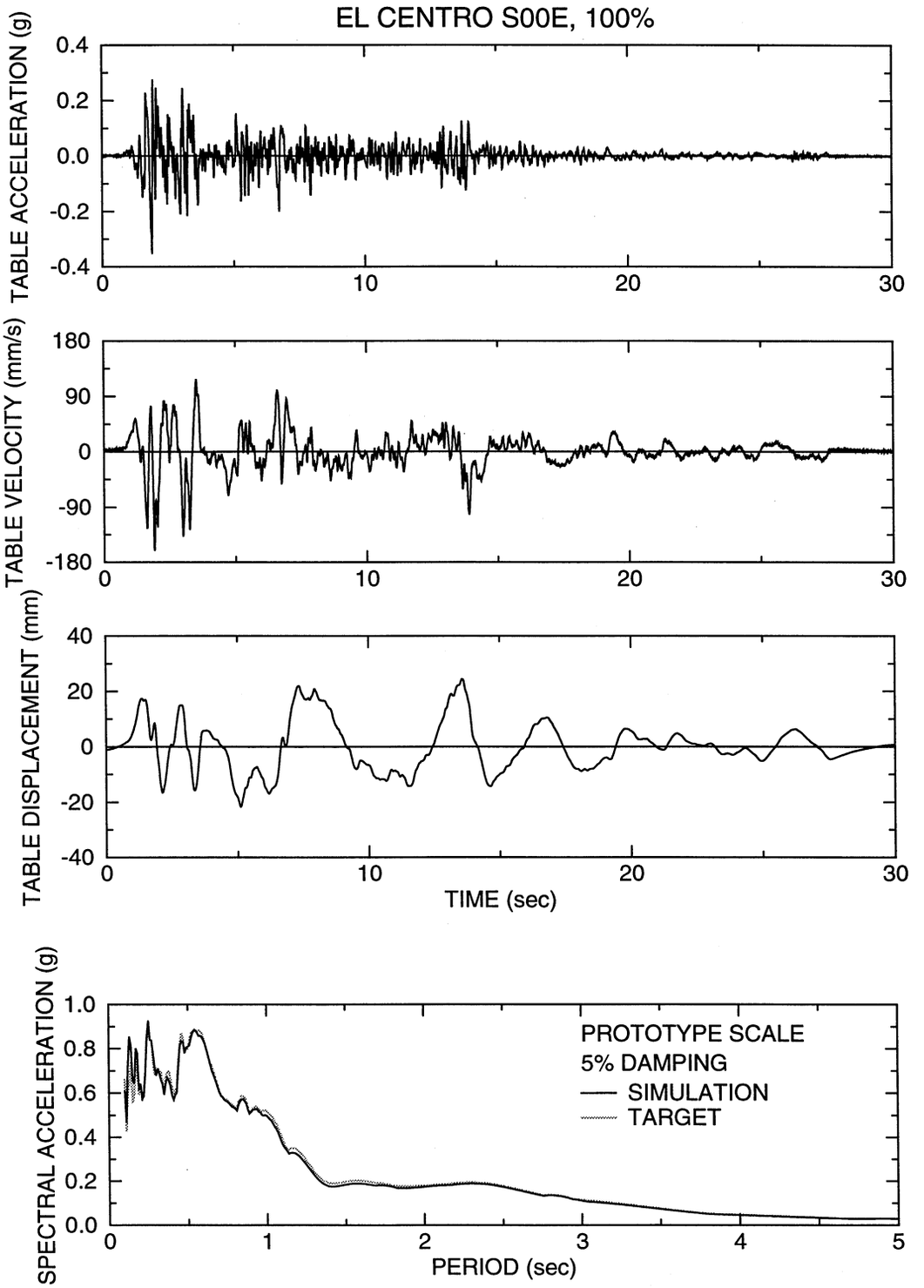

Figure 4-18: Time Histories of Displacement, Velocity and Acceleration and Acceleration Response Spectrum of Shake Table Motion for the El Centro S00E 100% Excitation

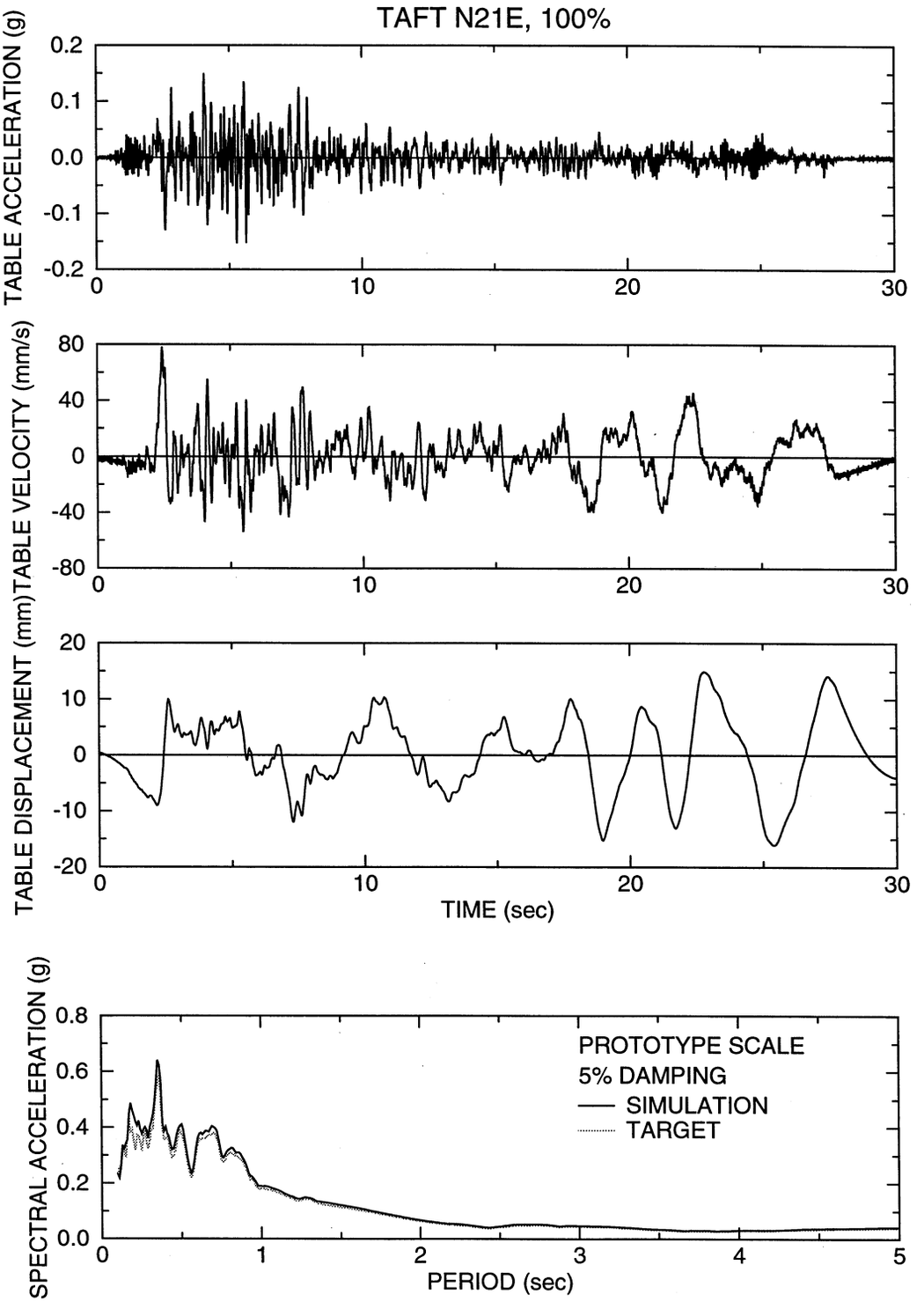

Figure 4-19: Time Histories of Displacement, Velocity and Acceleration and Acceleration Response Spectrum of Shake Table Motion for the Taft N21E 100% Excitation

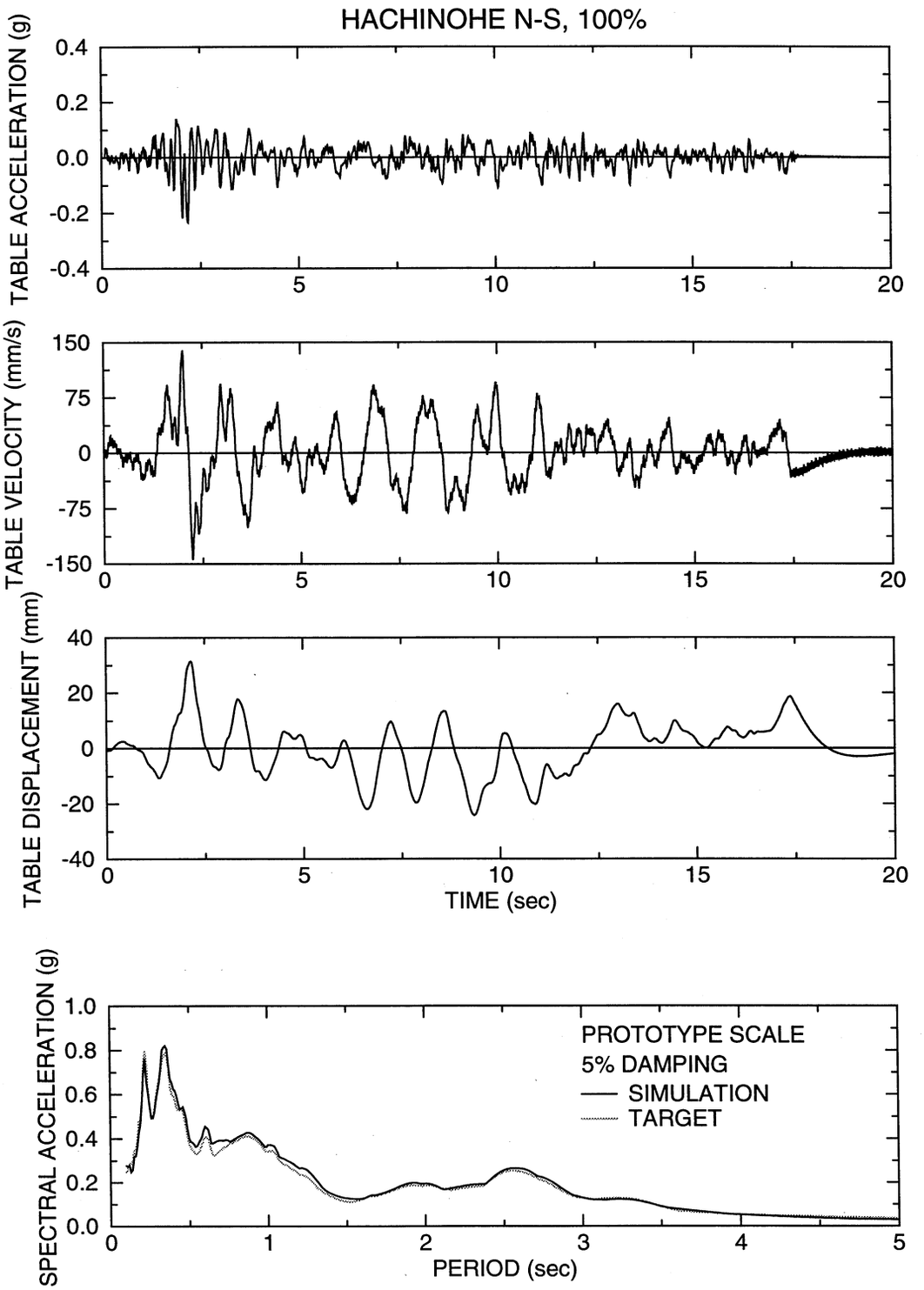

Figure 4-20: Time Histories of Displacement, Velocity and Acceleration and Acceleration Response Spectrum of Shake Table Motion for the Hachinohe N-S 100% Excitation

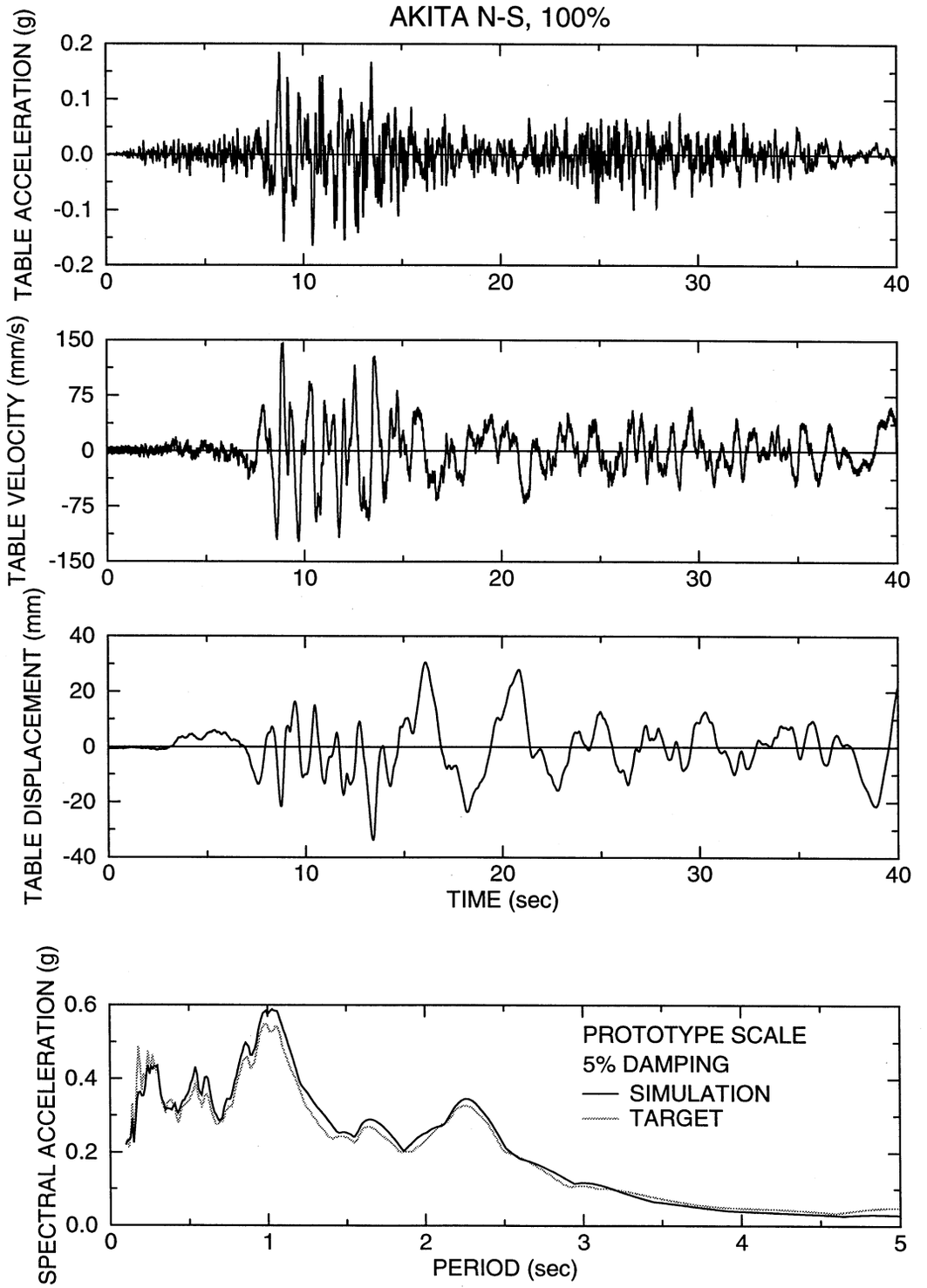

Figure 4-21: Time Histories of Displacement, Velocity and Acceleration and Acceleration Response Spectrum of Shake Table Motion for the Akita N-S 100% Excitation

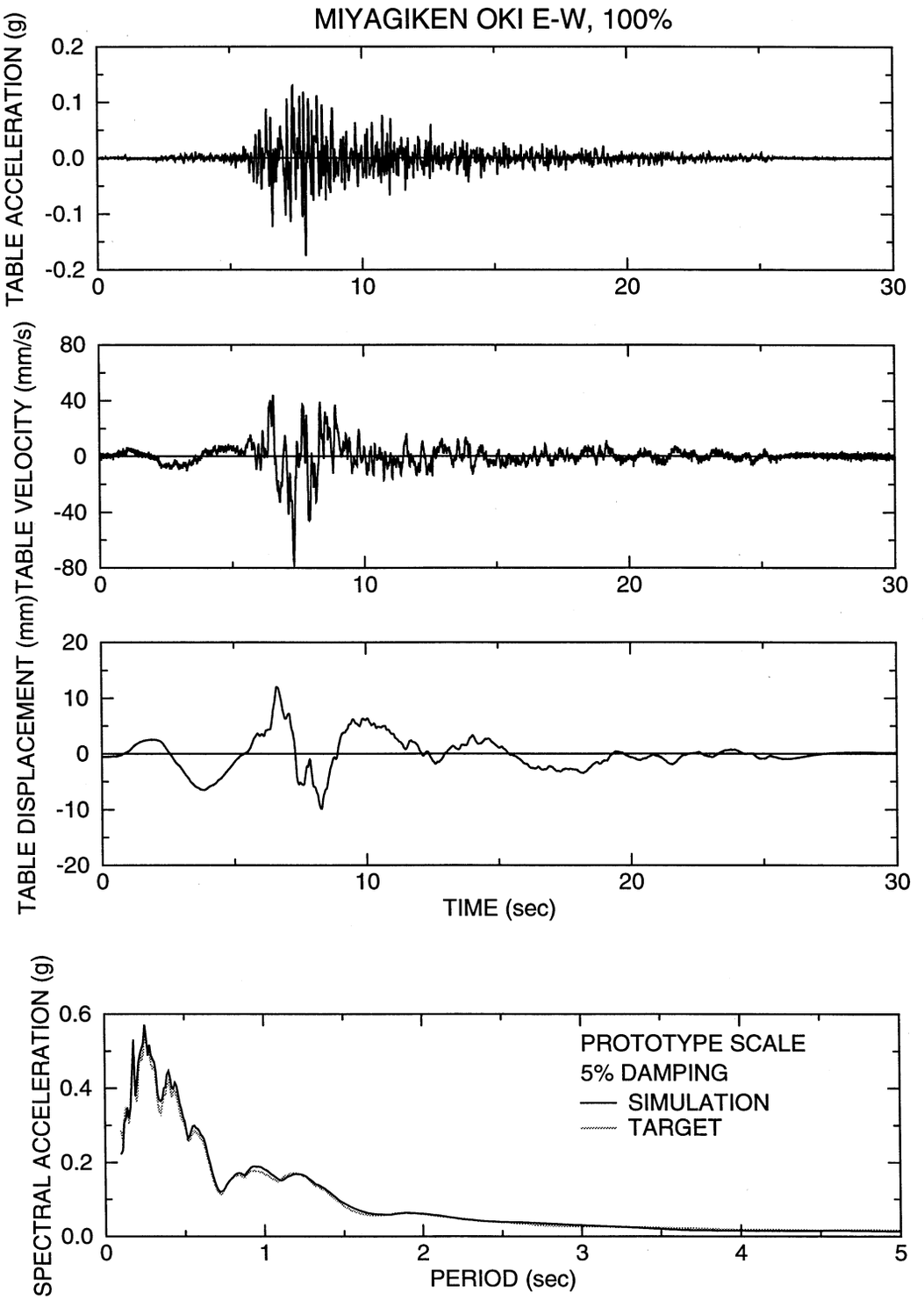

Figure 4-22: Time Histories of Displacement, Velocity and Acceleration and Acceleration Response Spectrum of Shake Table Motion for the Miyagiken Oki 100% Excitation

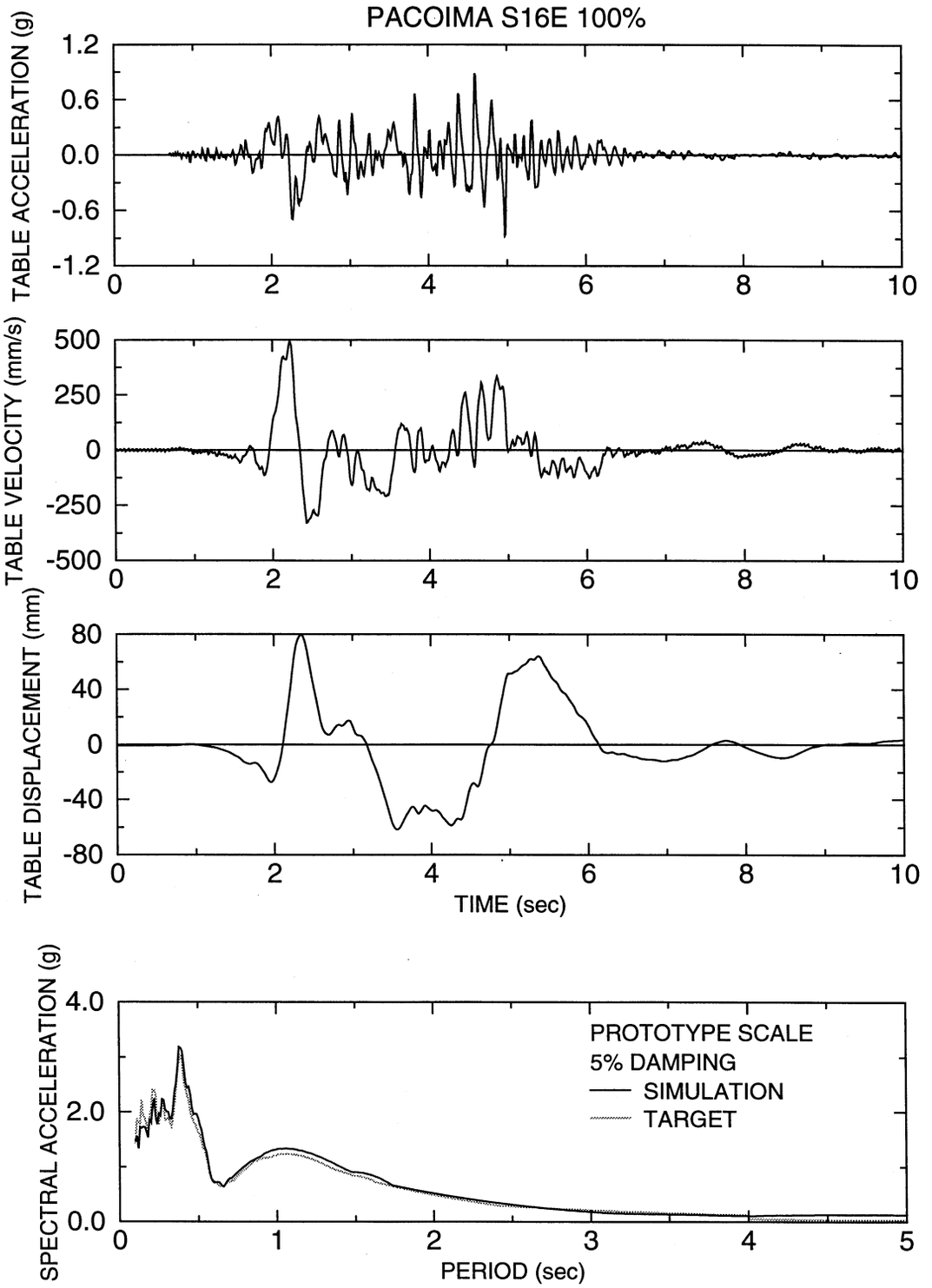

Figure 4-23: Time Histories of Displacement, Velocity and Acceleration and Acceleration Response Spectrum of Shake Table Motion for the Pacoima S16E 100% Excitation

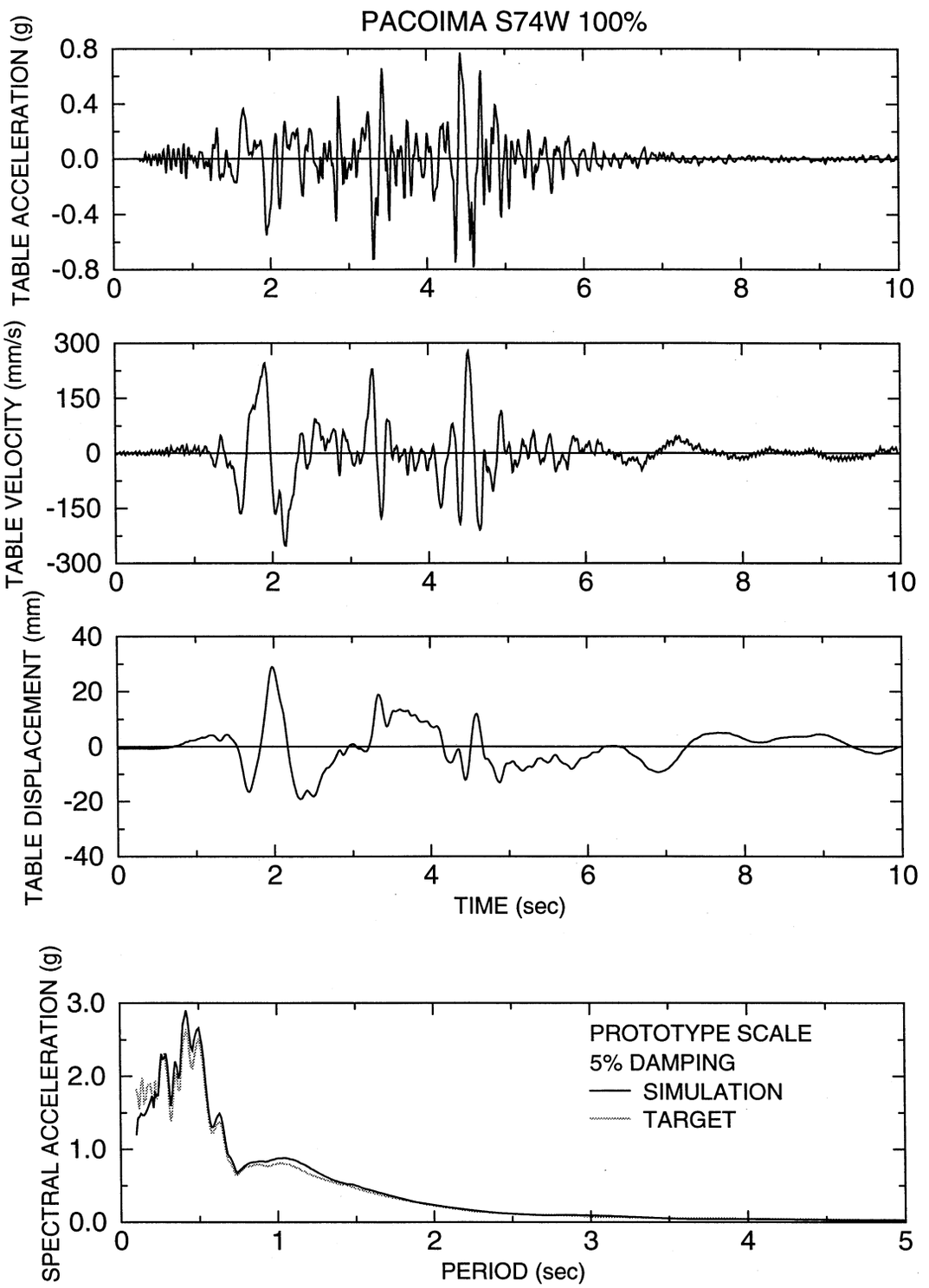

Figure 4-24: Time Histories of Displacement, Velocity and Acceleration and Acceleration Response Spectrum of Shake Table Motion for the Pacoima S74W 100% Excitation

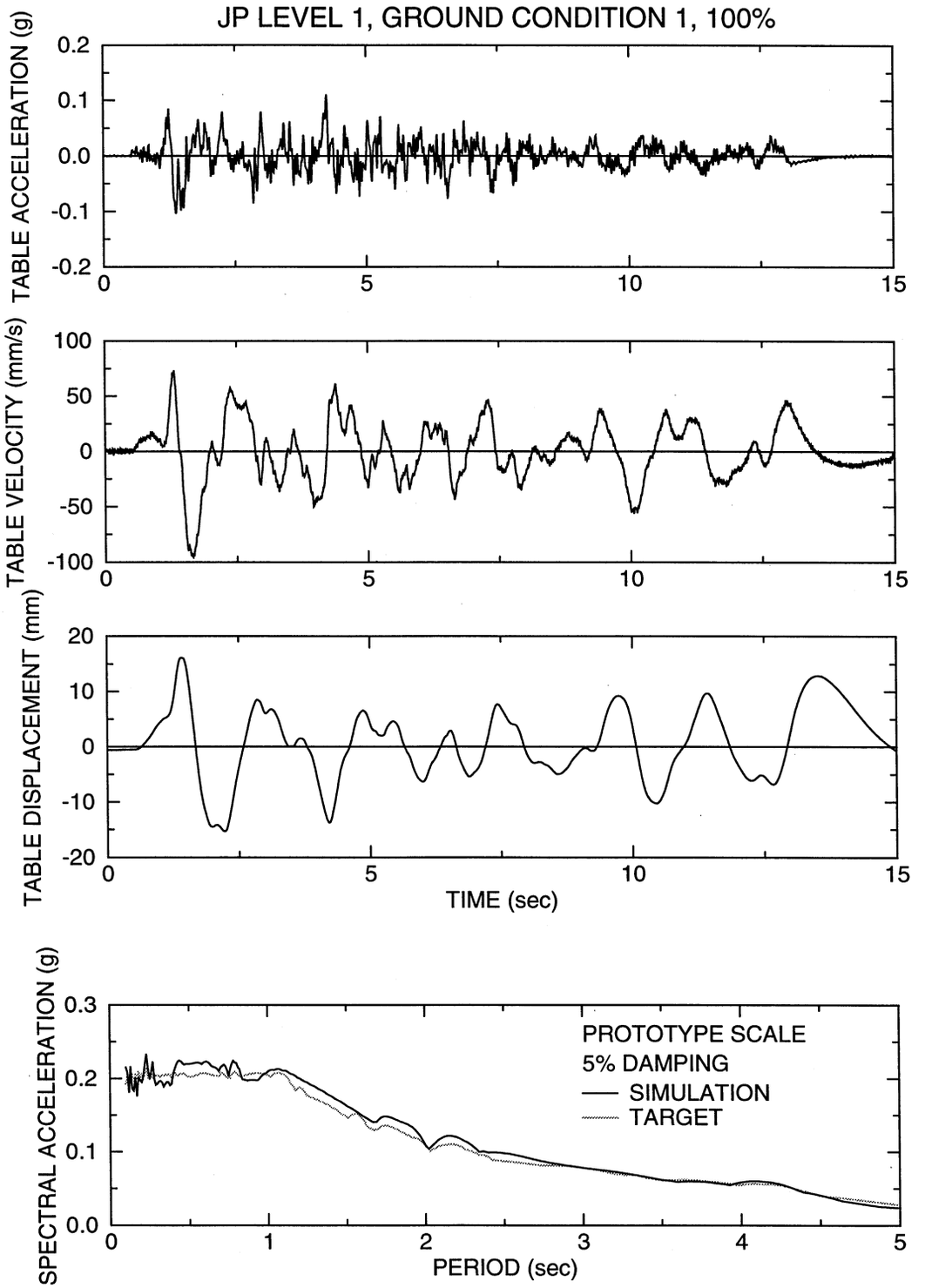

Figure 4-25: Time Histories of Displacement, Velocity and Acceleration and Acceleration Response Spectrum of Shake Table Motion for the JP Level1, Ground Condition 1 100% Excitation

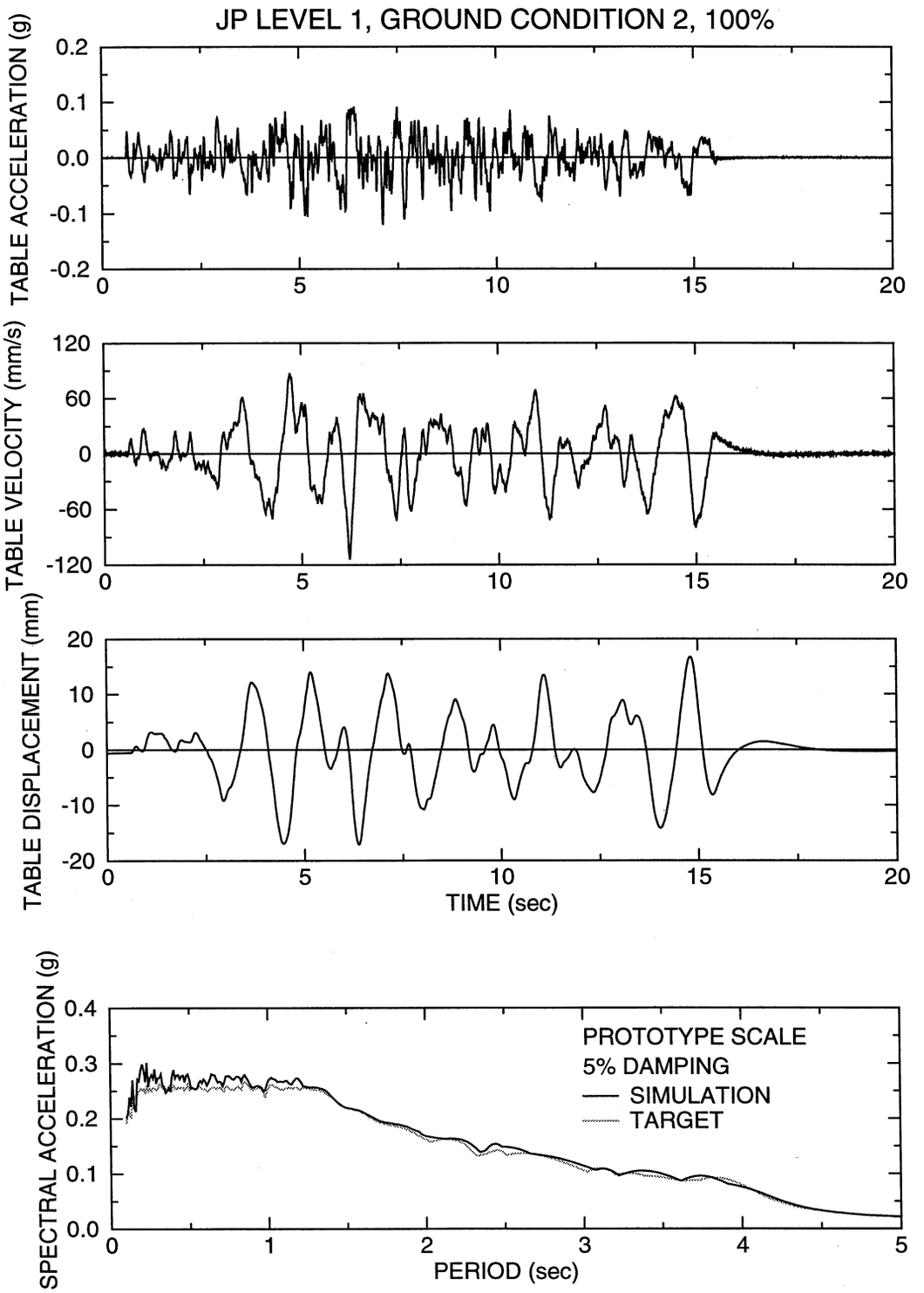

Figure 4-26: Time Histories of Displacement, Velocity and Acceleration and Acceleration Response Spectrum of Shake Table Motion for the JP Level1, Ground Condition 2 100% Excitation

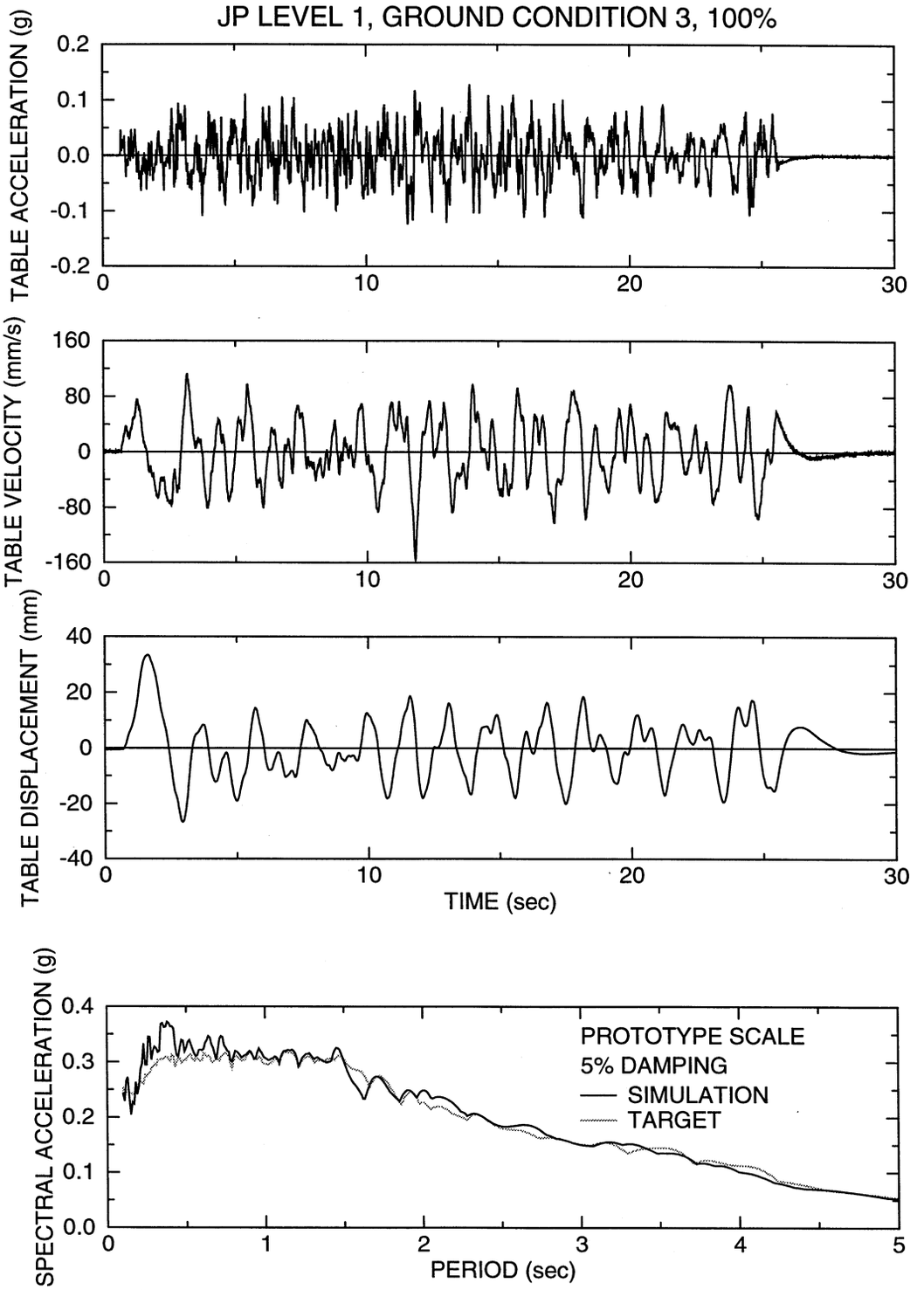

Figure 4-27: Time Histories of Displacement, Velocity and Acceleration and Acceleration Response Spectrum of Shake Table Motion for the JP Level1, Ground Condition 3 100% Excitation

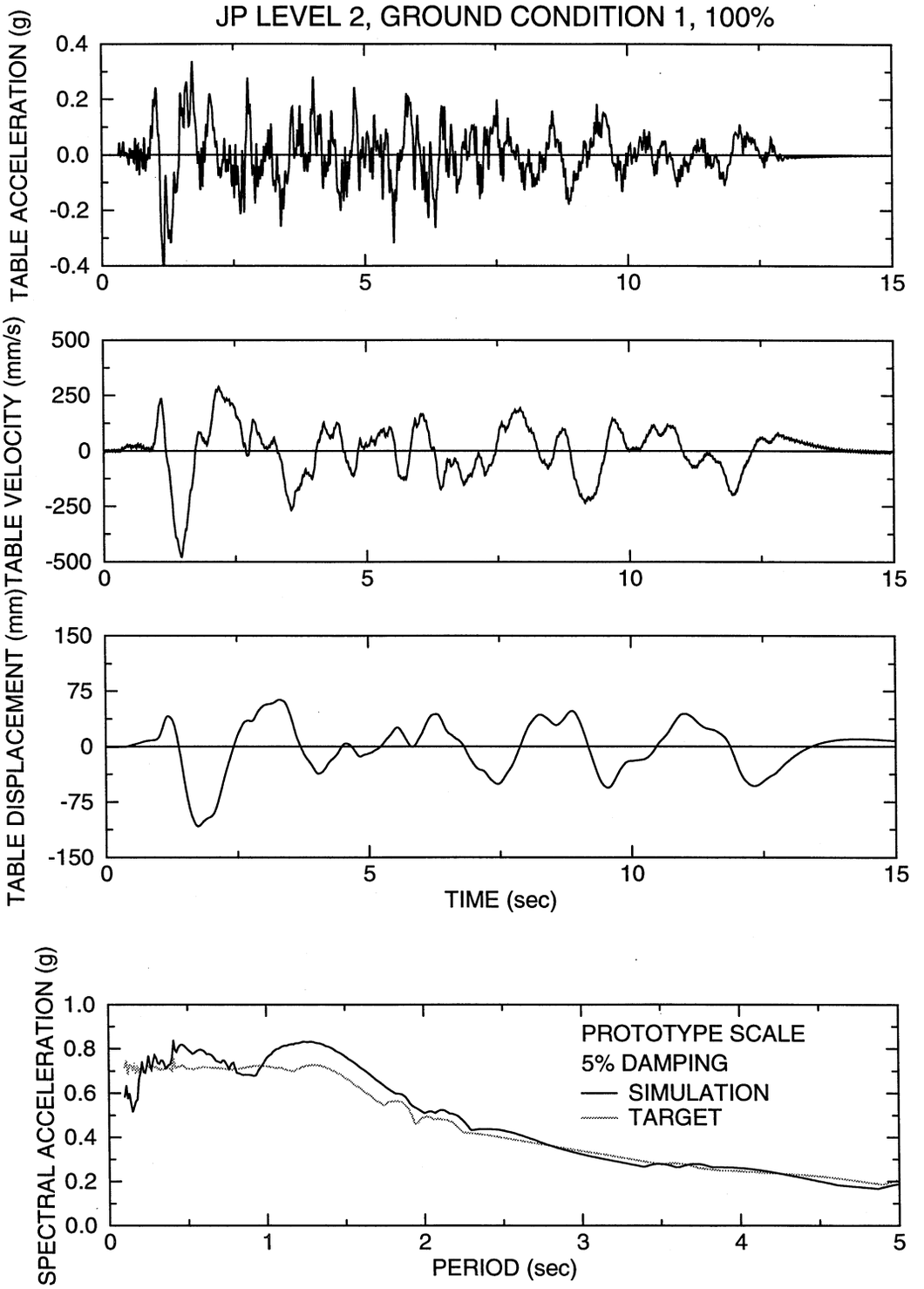

Figure 4-28: Time Histories of Displacement, Velocity and Acceleration and Acceleration Response Spectrum of Shake Table Motion for the JP Level2, Ground Condition 1 100% Excitation

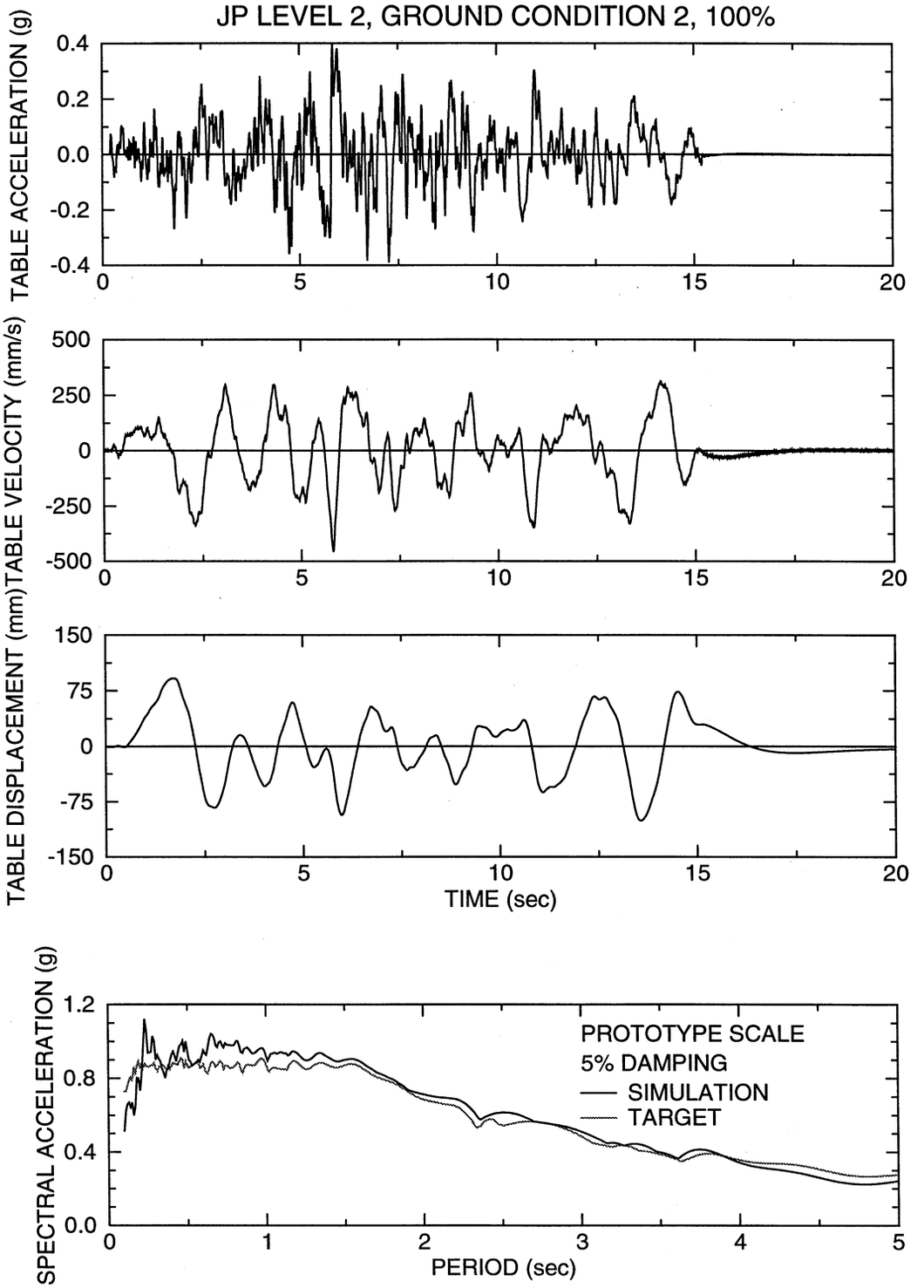

Figure 4-29: Time Histories of Displacement, Velocity and Acceleration and Acceleration Response Spectrum of Shake Table Motion for the JP Level2, Ground Condition 2 100% Excitation

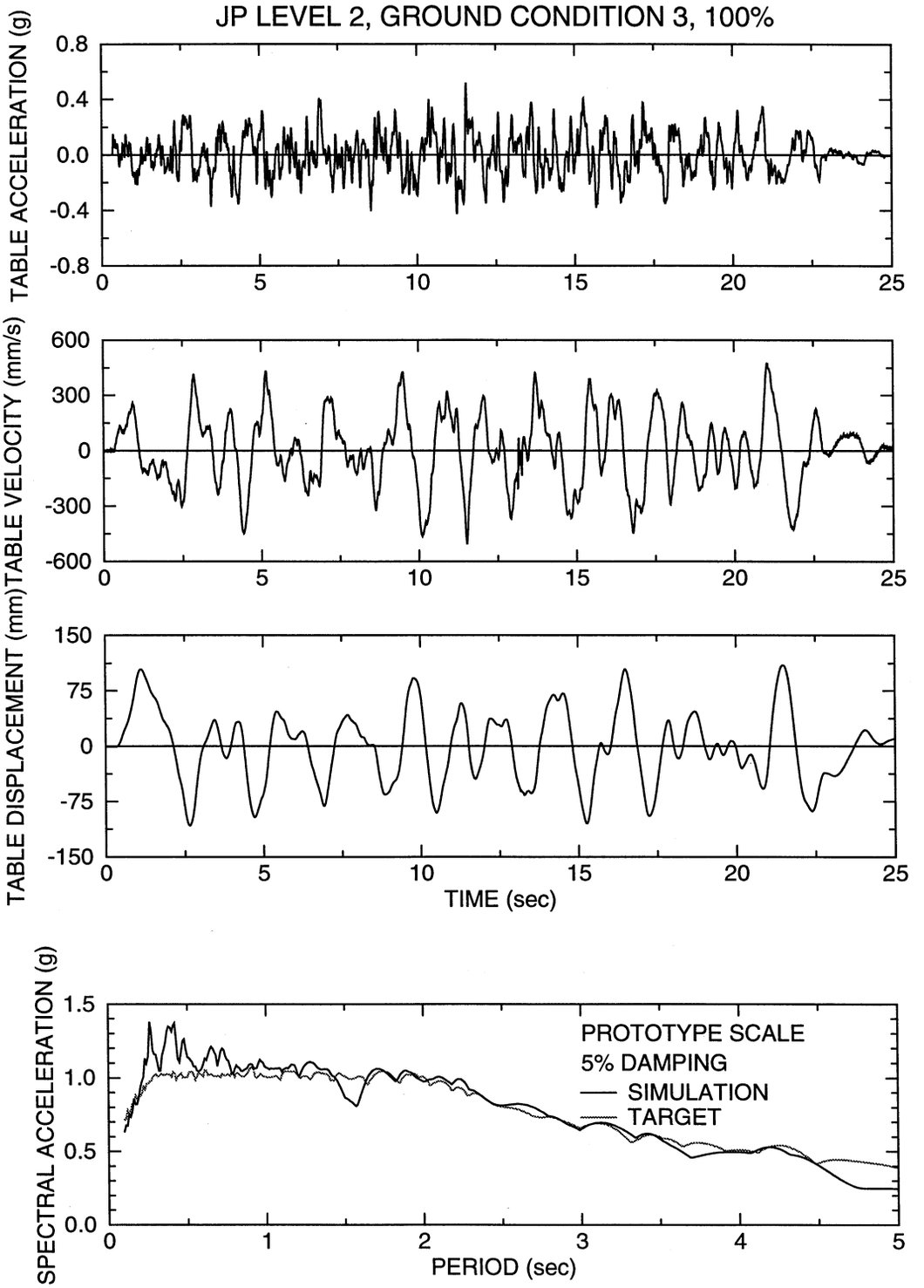

Figure 4-30: Time Histories of Displacement, Velocity and Acceleration and Acceleration Response Spectrum of Shake Table Motion for the JP Level2, Ground Condition 3 100% Excitation

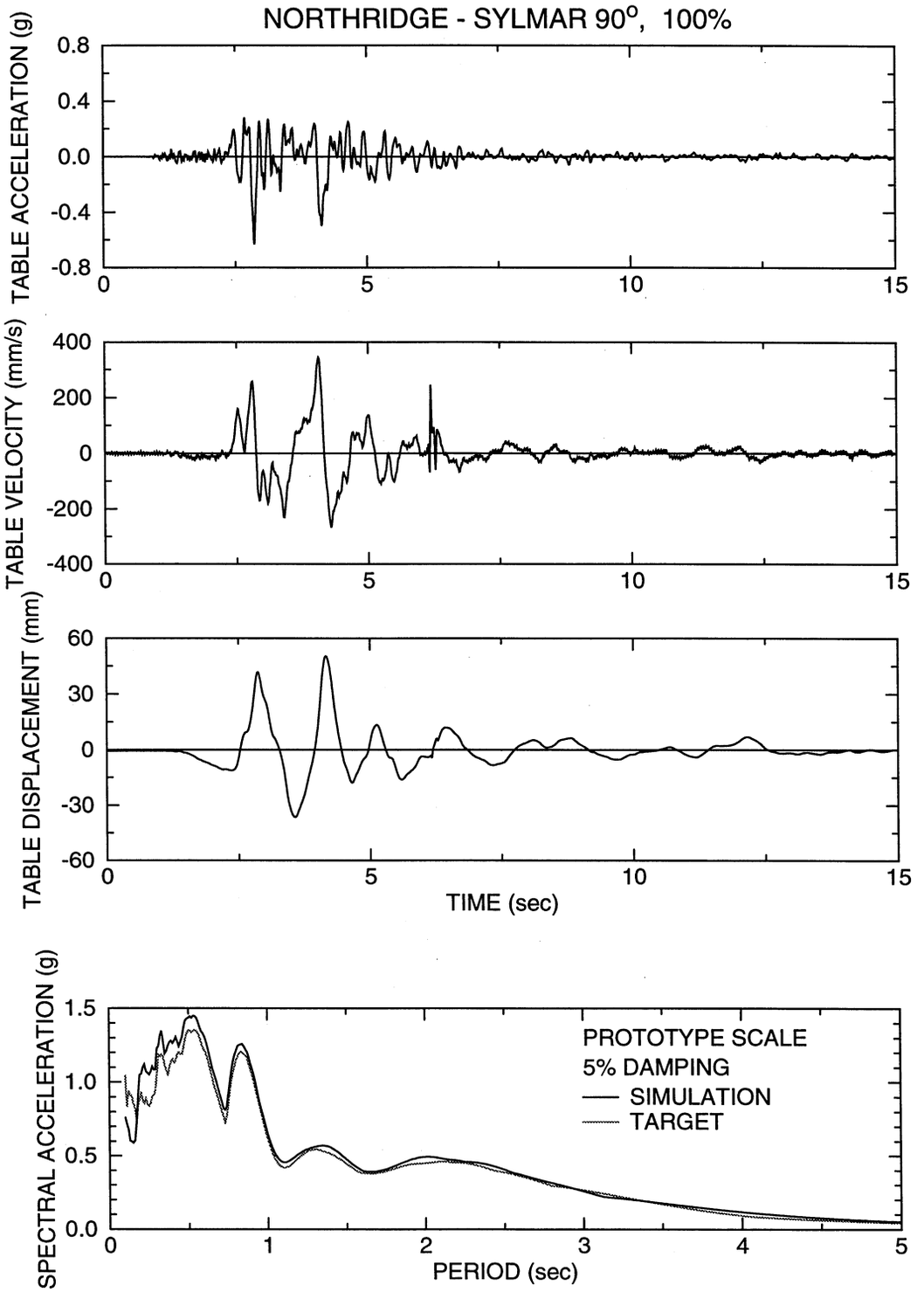

Figure 4-31: Time Histories of Displacement, Velocity and Acceleration and Acceleration Response Spectrum of Shake Table Motion for the Northridge, Sylmar 90° 100% Excitation

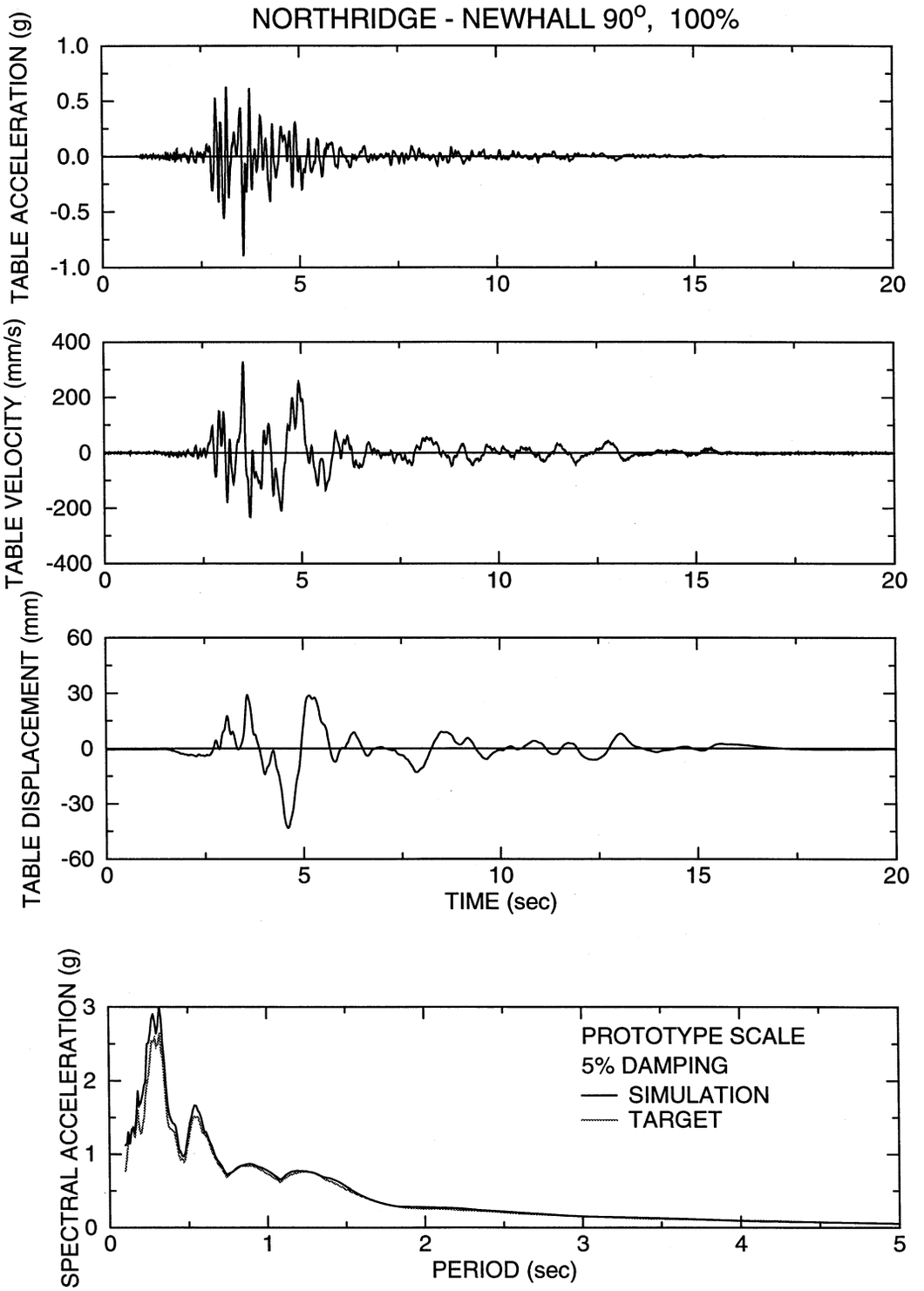

Figure 4-32: Time Histories of Displacement, Velocity and Acceleration and Acceleration Response Spectrum of Shake Table Motion for the Northridge, Newhall 90° 100% Excitation

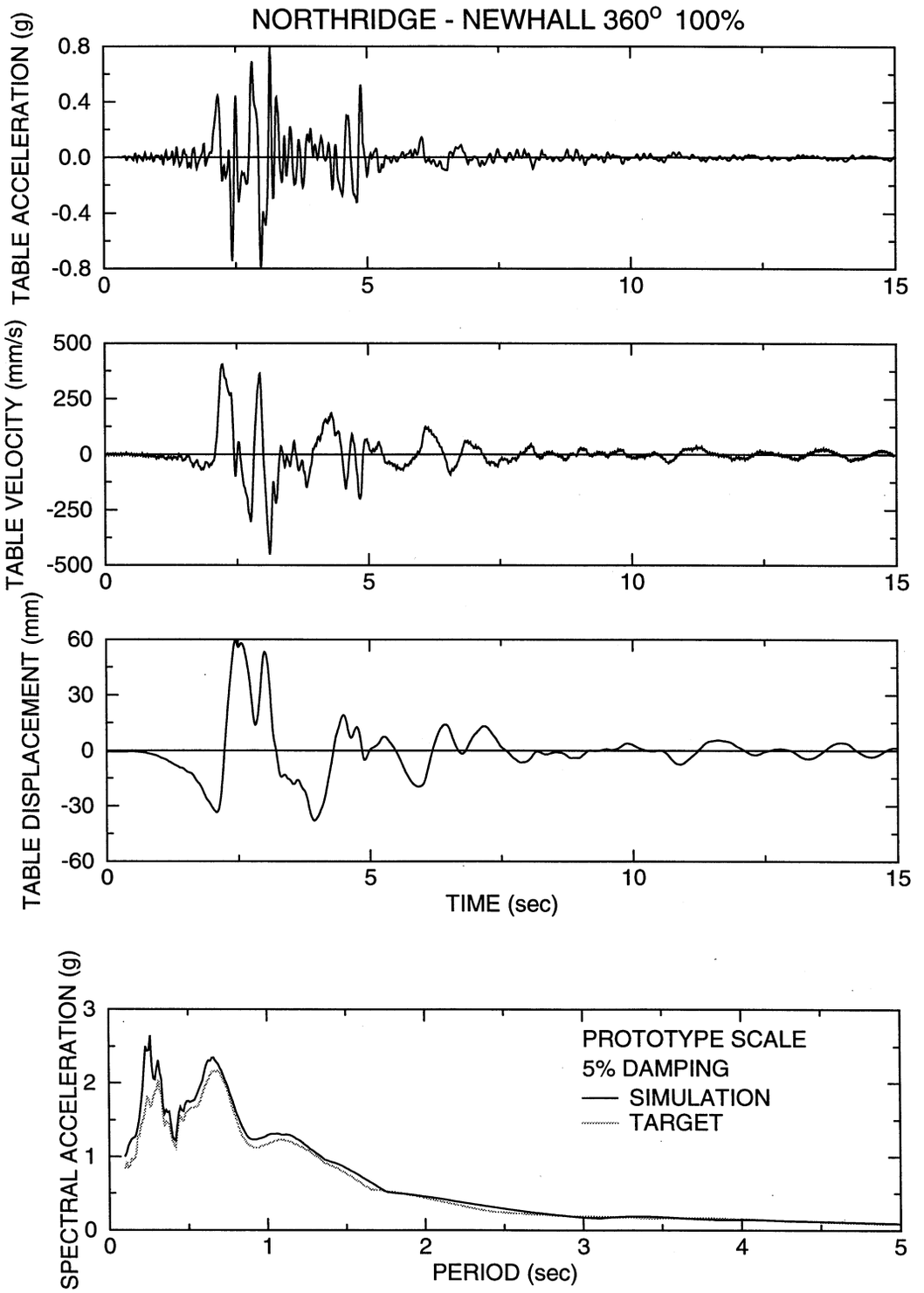

Figure 4-33: Time Histories of Displacement, Velocity and Acceleration and Acceleration Response Spectrum of Shake Table Motion for the Northridge, Newhall 360° 100% Excitation

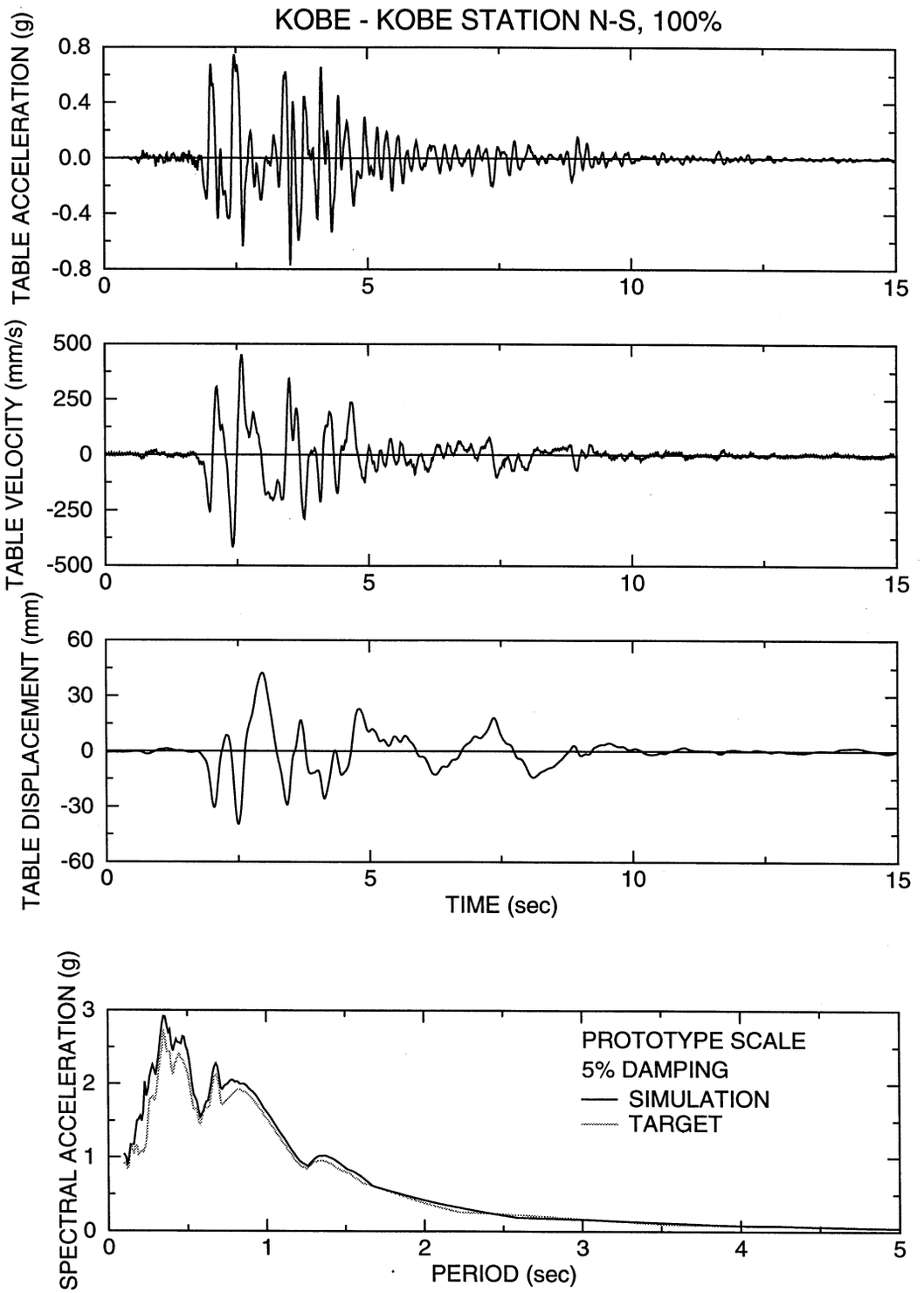

Figure 4-34: Time Histories of Displacement, Velocity and Acceleration and Acceleration Response Spectrum of Shake Table Motion for the Kobe Station N-S 100% Excitation

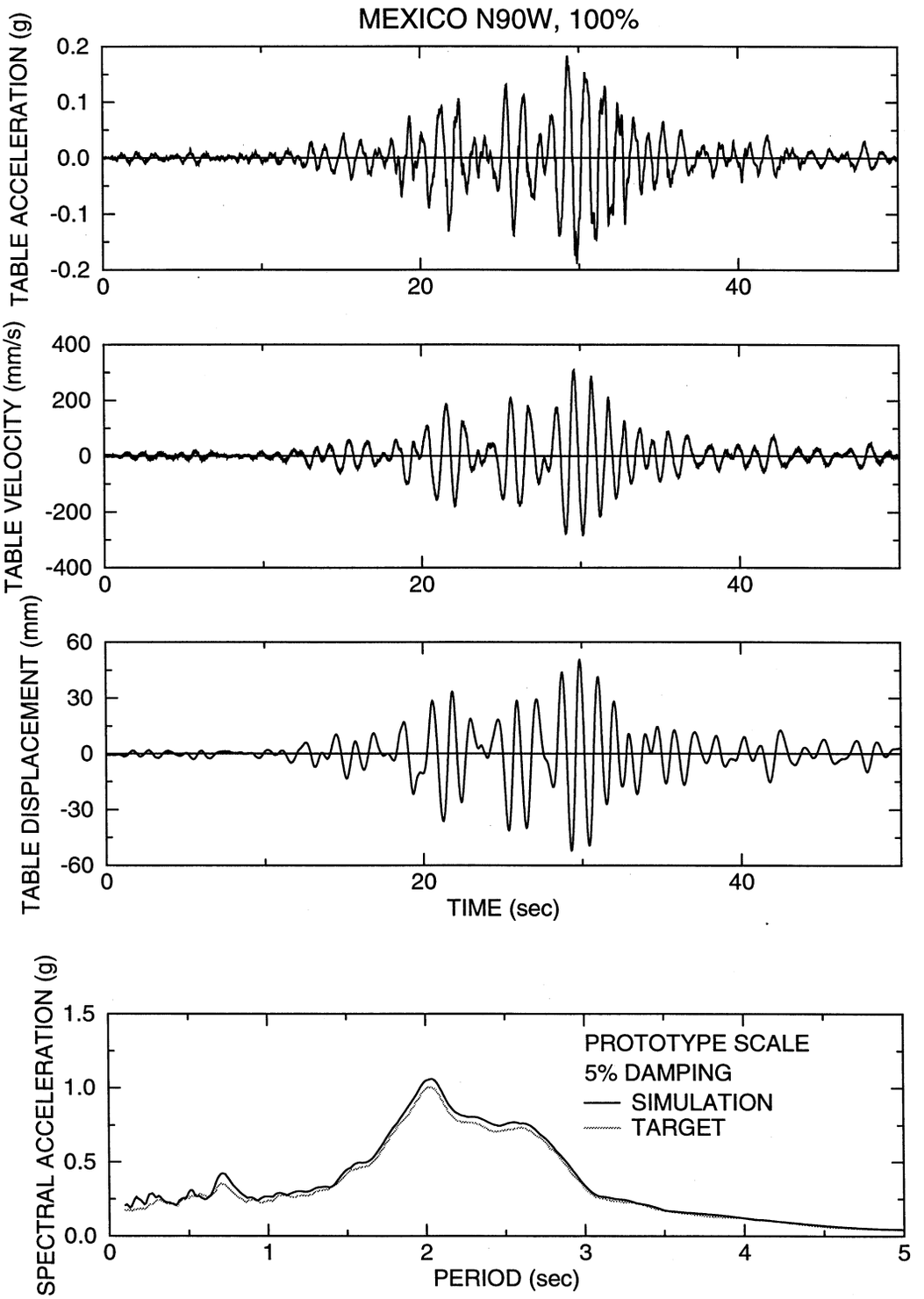

Figure 4-35: Time Histories of Displacement, Velocity and Acceleration and Acceleration Response Spectrum of Shake Table Motion for the Mexico City N90W 100% Excitation

SECTION 5

RESULTS OF EARTHQUAKE SIMULATOR TESTING OF NON-ISOLATED BRIDGE CONFIGURATIONS

5.1 Introduction

The range of tests performed on the model bridge form a good basis for comparison of different configurations. The non-isolated bridge configurations were tested at low seismic intensity levels to protect the pier from undergoing inelastic deformations. However, the low seismic intensity tests were performed on all seven configurations for a uniform comparison. These tests included the following motions: JP Level 1, Ground Motions 1, 2 and 3 at 100%, Miyagiken Oki at 100% and Taft N21E at 100%. In this section, the performance of the non-isolated configurations is presented in detail.

5.2 Test Results

A total of 48 tests were performed on the three non-isolated bridge configurations. The experimental results are presented in Table 5-1. The table lists the following parameters for each test:

1. Peak Values of Table Motion: the displacement and acceleration of the table were directly measured, whereas the table velocity was determined by numerical differentiation of displacement record.
2. Peak Values of Abutment Response. The following are reported:
   (a) Bearing Displacement: the peak value of the south-east bearing displacement. This value was checked by comparing it to the value obtained from the difference between the deck and abutment displacements.
   (b) Bearing Shear Force: peak value of bearing shear force measured by the load cells placed under the abutment bearings. This value was normalized by the total deck weight (140kN). Note that this force represents the force in two abutments in the two-span configuration.
   (c) Damper Force: the peak value of the sum of forces measured in the two dampers was multiplied by the cosine of the angle of inclination (45 degrees) and normalized by the total deck weight of 140 kN. That is, this force is the longitudinal component of the damper forces at the two abutments.
   (d) Total Shear Force: the peak value of the sum of bearing shear force and damper longitudinal forces normalized by the total deck weight. Note that this value is not equal to the sum of the peak bearing shear force and the peak damper longitudinal forces because the peak values occur at different times.
   (e) Abutment Drift: the peak value of displacement of the top of the abutment with respect to the base of the abutment.
   (f) Abutment Acceleration: the peak value of the acceleration of the abutment top as measured at the base of the load cells on top of the abutment. The value closely matches the peak table acceleration value.
3. Peak Values of Flexible Pier Response. The following are reported:

(a) Pier Shear Force: the peak value of pier shear force as measured at the column mid-height by the strain gage load cells and normalized by the total deck weight. This value was favorably compared with the calculated value from the bearing load cells and the pier top acceleration records.
(b) Pier Drift: the peak value of the pier drift as calculated from records of the pier top displacement and the table displacement measurements with respect to a fixed frame.
(c) Pier Acceleration: the peak value of acceleration measured at the top of the pier near the base of the bearing load cells.

4. Total Shear Force: this value is the sum of the abutment total shear force (bearing plus damper longitudinal forces) and the flexible pier shear force, normalized by the total deck weight. The peak value is reported in Table 5-1.
5. Deck Acceleration: the peak value of the horizontal acceleration of deck. This value is in acceptable good correlation with the normalized total shear force described in 4. above.

Table 5-1 presents the experimental results in groups that correspond to the same input motion, however at varying scales. The tests were not conducted in the presented sequence. Actually, the sequence of testing did not have any effect on the results because the properties of the bridge model, of the elastomeric bearings and of the dampers remained virtually unchanged during testing. For this, care has been taken to prevent inelastic action in the flexible pier. Moreover, sufficient idle time between experiments was allowed in order to avoid unrealistic increases of the temperature in the dampers.

It may be noted in Table 5-1 that the recorded table peak motion is not the same for earthquakes specified to be identical. The reason for this imperfect control of the shake table is the significant effect of table-structure interaction, which was affected by the intensity of the excitation and the characteristics of the tested system. Moreover, two tests (No. NLFS012.1 and NLFS013.1) were mistakenly conducted at time scale of 1.0 (that is, without compression of the time by factor of 2.0).

Appendix B contains experimental results in graphical form for a number of the conducted tests. For a complete graphical presentation of the results see Kasalanati (1998).

During the testing of the model bridge (in all configurations) it was observed that the overhangs of the shake table extension, which supported the abutment and pier (Fig. 4-1), underwent vertical motion even when only horizontal table motion was imposed. The two overhangs did not move in unison. Rather, the motion of the two overhangs was anti-symmetric with the two sides moving with different amplitudes and content in frequency. It was concluded that this vertical motion of the overhangs was the combined result of table-structure interaction, vertical flexibility of the overhangs and difference in the vertical stiffness of the overhangs. As identified earlier by Constantinou et al. (1993) and Tsopelas et al. (1994b), the concrete extension had cracking due to the applied eccentric load and misplacement of its reinforcement. This phenomenon resulted in increased severity of tests. The abutment and flexible pier experienced out of phase vertical input at their base in all tests.

Table 5-1: Results of Testing of Non-Isolated Bridge Configurations

TEST	EXCITATION	PEAK TABLE MOTION			ABUTMENT						PIER			Total Shear /Wt	DECK ACCL. (g)
		DISPL (mm)	VEL (mm/s)	ACCL. (g)	Bearing Displ. (mm)	Bearing Shear /Wt	Damper Force /Wt	Total Shear /Wt	Abut. Drift (mm)	Abut. Accl. (g)	Pier Shear /Wt	Pier Drift (mm)	Pier Accl. (g)		
N0FS002.1	EL CENTRO S00E 50%	12.2	76.	0.18	13.4	0.047	-	0.047	0.7	0.17	0.189	8.5	0.17	0.227	0.24
NLFS002.1	EL CENTRO S00E 100%	24.6	152.	0.34	10.9	0.040	0.113	0.131	1.3	0.35	0.165	7.0	0.19	0.230	0.24
NNFS002.1	EL CENTRO S00E 100%	25.9	165.	0.32	8.9	0.036	0.186	0.212	1.2	0.48	0.140	6.7	0.27	0.307	0.33
NLFS003.1	EL CENTRO S00E H+V 100%	23.5	160.	0.31	12.3	0.043	0.117	0.140	1.2	0.33	0.185	7.9	0.22	0.257	0.28
NNFS003.1	EL CENTRO S00E H+V 100%	28.5	157.	0.33	9.1	0.037	0.186	0.212	1.4	0.52	0.142	6.8	0.27	0.313	0.33
N0FS003.1	TAFT N21E 50%	8.0	42.	0.07	4.9	0.021	-	0.021	0.4	0.08	0.070	3.0	0.06	0.090	0.10
N0FS004.1	TAFT N21E 100%	16.1	78.	0.15	9.8	0.035	-	0.035	0.6	0.15	0.136	6.1	0.13	0.168	0.18
NLFS004.1	TAFT N21E 100%	16.3	80.	0.15	5.4	0.023	0.052	0.062	0.8	0.15	0.077	3.8	0.10	0.124	0.13
NLFS005.1	TAFT N21E 200%	32.3	155.	0.33	11.5	0.041	0.093	0.117	1.0	0.29	0.167	7.4	0.18	0.245	0.25
NNFS004.1	TAFT N21E 100%	13.9	70.	0.15	2.7	0.018	0.106	0.119	0.6	0.18	0.047	2.4	0.14	0.153	0.16
NNFS005.1	TAFT N21E 200%	28.1	132.	0.31	5.8	0.028	0.155	0.172	0.9	0.33	0.091	4.9	0.20	0.233	0.25
N0FS005.1	TAFT N21E H+V 100%	13.9	63.	0.16	9.8	0.035	-	0.035	0.6	0.20	0.133	5.8	0.11	0.163	0.19
NLFS006.1	TAFT N21E H+V 200%	23.7	99.	0.31	9.9	0.031	0.078	0.100	0.9	0.38	0.132	6.4	0.18	0.201	0.22
NNFS006.1	TAFT N21E H+V 100%	14.0	68.	0.16	2.7	0.018	0.110	0.123	0.7	0.24	0.048	2.4	0.16	0.155	0.17
NNFS007.1	TAFT N21E H+V 200%	28.2	139.	0.30	5.7	0.028	0.157	0.173	1.2	0.42	0.090	5.3	0.22	0.231	0.26

Wt = Weight of the Deck = 140 kN

All Configurations are for **F**lexible North Pier and **S**tiff South Abutment

The Reported Forces at the Abutment Represent the Forces on Two Abutments

Bearing Displacement and Pier Drift are Average Values from Two Measurements

N0FS - Without Dampers

NLFS - With Linear Viscous Dampers at Abutment

NNFS - With Nonlinear Viscous Dampers at Abutment

Table 5-1: Continued

TEST	EXCITATION	PEAK TABLE MOTION			ABUTMENT						PIER			Total Shear /Wt	DECK ACCL. (g)
		DISPL (mm)	VEL (mm/s)	ACCL. (g)	Bearing Displ. (mm)	Bearing Shear /Wt	Damper Force /Wt	Total Shear /Wt	Abut. Drift (mm)	Abut. Accl. (g)	Pier Shear /Wt	Pier Drift (mm)	Pier Accl. (g)		
N0FS006.1	HACHINOHE NS 25%	7.7	33.	0.07	4.4	0.022	-	0.022	0.4	0.07	0.063	2.9	0.06	0.082	0.09
N0FS007.1	HACHINOHE NS 50%	15.6	66.	0.12	9.7	0.038	-	0.038	0.5	0.12	0.131	6.2	0.11	0.163	0.17
NLFS007.1	HACHINOHE N-S 100%	31.6	131.	0.23	12.0	0.045	0.075	0.100	1.0	0.23	0.170	7.7	0.20	0.243	0.25
NNFS008.1	HACHINOHE NS 100%	31.6	143.	0.23	6.2	0.030	0.138	0.145	0.9	0.27	0.093	5.6	0.21	0.199	0.21
N0FS008.1	MIYAGIKEN OKI 100%	12.0	78.	0.16	10.3	0.038	-	0.038	0.4	0.16	0.145	6.5	0.14	0.178	0.19
NLFS008.1	MIYAGIKEN OKI 100%	12.1	77.	0.16	3.1	0.018	0.035	0.046	0.4	0.15	0.056	2.1	0.08	0.096	0.10
NLFS009.1	MIYAGIKEN OKI 200%	24.2	154.	0.31	8.0	0.032	0.065	0.089	0.6	0.31	0.120	5.0	0.16	0.187	0.19
NLFS010.1	MIYAGIKEN OKI 300%	36.4	237.	0.45	13.4	0.047	0.103	0.134	1.0	0.47	0.206	8.6	0.24	0.298	0.30
NNFS009.1	MIYAGIKEN OKI 100%	12.1	73.	0.15	2.3	0.012	0.098	0.108	0.6	0.16	0.039	2.0	0.13	0.135	0.14
NNFS010.1	MIYAGIKEN OKI 200%	24.3	152.	0.31	5.3	0.022	0.141	0.158	1.0	0.28	0.080	4.4	0.20	0.217	0.23
NNFS011.1	MIYAGIKEN OKI 300%	36.6	228.	0.46	9.0	0.035	0.171	0.197	1.3	0.40	0.132	6.4	0.26	0.294	0.32
N0FS009.1	JP LEVEL 1 GC 1 100%	16.2	100.	0.11	10.8	0.041	-	0.041	0.6	0.11	0.155	6.9	0.15	0.189	0.19
NLFS016.1	JP LEVEL 1 G.C. 1 100%	16.2	99.	0.11	6.2	0.028	0.043	0.054	0.5	0.14	0.085	4.1	0.12	0.123	0.13
NNFS017.1	JP LEVEL 1 GC 1 100%	16.5	102.	0.11	2.5	0.016	0.100	0.113	0.6	0.15	0.044	2.4	0.13	0.144	0.15
N0FS010.1	JP LEVEL 1 GC 2 100%	17.4	112.	0.12	15.3	0.052	-	0.052	0.7	0.14	0.225	9.7	0.21	0.268	0.27
NLFS017.1	JP LEVEL 1 G.C. 2 100%	17.4	116.	0.12	7.7	0.032	0.049	0.063	0.5	0.13	0.107	5.0	0.13	0.148	0.16
NNFS018.1	JP LEVEL 1 GC 2 100%	17.6	114.	0.11	3.0	0.016	0.100	0.113	0.7	0.13	0.047	2.5	0.13	0.144	0.15

Wt = Weight of the Deck = 140 kN

All Configurations are for **F**lexible North Pier and **S**tiff South Abutment

The Reported Forces at the Abutment Represent the Forces on Two Abutments

Bearing Displacement and Pier Drift are Average Values from Two Measurements

N0FS - Without Dampers

NLFS - With Linear Viscous Dampers at Abutment

NNFS - With Nonlinear Viscous Dampers at Abutment

Table 5-1: Continued

TEST	EXCITATION	PEAK TABLE MOTION			ABUTMENT						PIER			Total Shear /Wt	DECK ACCL. (g)	
		DISPL (mm)	VEL (mm/s)	ACCL. (g)	Bearing Displ. (mm)	Bearing Shear /Wt	Damper Force /Wt	Total Shear /Wt	Abut. Drift (mm)	Abut. Accl. (g)	Pier Shear /Wt	Pier Drift (mm)	Pier Accl. (g)			
N0FS011.1	JP LEVEL 1 GC 3 100%	33.5	157.	0.13	18.0	0.058	-	0.058	1.1	0.13	0.252	11.5	0.23	0.298	0.31	
NLFS018.1	JP LEVEL 1 G.C. 3 100%	33.3	158.	0.13	7.4	0.031	0.052	0.067	0.5	0.14	0.106	4.7	0.13	0.146	0.16	
NNFS019.1	JP LEVEL 1 GC 3 100%	33.3	164.	0.14	3.1	0.019	0.104	0.113	0.7	0.18	0.053	3.1	0.15	0.150	0.16	
NLFS011.1	AKITA N-S 100%	42.7	183.	0.24	14.3	0.051	0.106	0.121	1.0	0.23	0.212	9.4	0.24	0.287	0.29	
NNFS012.1	AKITA NS 50%	16.9	75.	0.10	1.8	0.013	0.073	0.082	0.4	0.10	0.032	1.7	0.10	0.103	0.11	
NNFS020.1	AKITA NS 100%	33.8	148.	0.18	5.1	0.025	0.124	0.135	0.7	0.21	0.076	4.2	0.17	0.170	0.18	
NLFS012.1	PACOIMA S74W 25%	25.6	137.	0.23	15.7	0.053	0.105	0.121	1.1	0.23	0.230	10.3	0.25	0.313	0.32	*
NNFS013.1	PACOIMA S74W 25%	6.8	68.	0.23	3.5	0.019	0.135	0.143	0.8	0.33	0.057	3.2	0.16	0.179	0.19	
NNFS021.1	PACOIMA S74W 50%	14.3	139.	0.44	7.0	0.030	0.176	0.186	1.1	0.64	0.107	6.0	0.26	0.262	0.29	
NLFS013.1	PACOIMA S16E 25%	63.4	207.	0.28	10.2	0.038	0.092	0.105	0.9	0.32	0.143	6.7	0.18	0.203	0.21	*
NNFS014.2	PACOIMA S16E 25%	17.8	115.	0.21	3.4	0.020	0.105	0.114	0.7	0.23	0.055	3.2	0.15	0.141	0.15	
NNFS022.1	PACOIMA S16E 50%	36.1	222.	0.42	9.9	0.041	0.149	0.168	1.3	0.45	0.151	8.2	0.28	0.286	0.31	
NLFS014.1	MEXICO CITY N90W 50%	26.0	152.	0.10	5.5	0.026	0.031	0.045	0.4	0.09	0.078	3.7	0.11	0.110	0.11	
NLFS015.1	MEXICO CITY N90W 100%	52.2	302.	0.18	12.8	0.047	0.054	0.082	1.2	0.18	0.182	8.6	0.22	0.232	0.24	
NNFS015.1	MEXICO CITY 50%	26.1	156.	0.10	2.5	0.016	0.070	0.075	0.6	0.09	0.040	2.4	0.10	0.095	0.10	
NNFS016.1	MEXICO CITY 100%	52.3	307.	0.19	7.5	0.036	0.120	0.136	1.2	0.19	0.111	6.8	0.21	0.205	0.22	

Wt = Weight of the Deck = 140 kN

All Configurations are for **F**lexible North Pier and **S**tiff South Abutment

The Reported Forces at the Abutment Represent the Forces on Two Abutments

Bearing Displacement and Pier Drift are Average Values from Two Measurements

* Tests mistakenly conducted with time scale of 1.0

N0FS - Without Dampers

NLFS - With Linear Viscous Dampers at Abutment

NNFS - With Nonlinear Viscous Dampers at Abutment

5.3 Interpretation of Results

A simple way of interpreting the experimental results is to present peak values of key response quantities versus a parameter which characterizes the intensity of the input motion. For such a parameter, we use the peak table velocity because the tested system has a fundamental period which is within the long-period range of typical response spectra (0.47 sec in the scale of the experiment or 0.93 sec in prototype scale).

Figure 5-1 presents the peak values of various response quantities of the non-isolated bridge versus the peak table velocity. The important observation in this figure is that the addition of viscous dampers causes a substantial reduction in the bearing displacement (which is the same as the flexible pier displacement) and a substantial reduction in the pier shear force. Of importance is that these reductions are achieved with a simultaneous reduction in the total shear force (that is, inertia force) that is transmitted to the substructure. Moreover, the reduction of pier shear force is achieved at the expense of increased force transmitted to the abutments (where the dampers are located). That is, the addition of dampers resulted in a reduction of the inertia force and in an effective re-distribution of the inertia force to the desired elements of the substructure.

Re-distribution of the inertia force may be achieved in a variety of ways, of which one is by utilizing bearings of higher stiffness. However, such an approach will not result in a simultaneous reduction of the inertia force. Rather, it may cause the opposite effect. Effective means of re-distribution of the inertia force in non-isolated configurations, which can also reduce the inertia force, require the use of energy dissipation mechanisms. Examples are viscous damping devices and lead-rubber bearings.

It may be observed in Table 5-1 that in all tests the use of nonlinear dampers resulted in more damper force and more shear force at the abutment location than when linear dampers were used. This result may be explained by recalling that the two types of dampers were designed to deliver the same force at a velocity (along the axis of the damper) equal to 350 mm/s. Had this velocity been exceeded, then the nonlinear dampers would have transferred lesser force than the linear dampers to the abutment. Noting that the bridge model had a fundamental frequency of 2.15 Hz, the bearing displacements were less than 10 mm and the dampers were placed at an angle of 45 degrees, the peak velocity along the damper axis did not exceed 100 mm/s (calculated as pseudo velocity = $2\pi \times 2.15 \times 10 \times \cos 45$). Accordingly, the nonlinear dampers delivered substantially higher damping force than the linear dampers.

Another useful effect obtained with the use of damping devices is illustrated in Figure 5-2. The recorded shear force - drift loops of the flexible pier are shown for the three cases of non-isolated bridge configurations when excited by motions of significantly different content in frequency. These motions are the Japanese, level 1 and ground conditions 1 (rock), 2 (medium soil) and 3 (deep, soft soil). The conventional, non-isolated bridge (without dampers) responds with a noted sensitivity to the ground conditions (see also Appendix B for records of the displacement histories). However, the bridge with damping devices responds with a marked insensitivity to the details of the input.

Finally, it is worthy of noting in the results of Table 5-1 and of Appendix B that the effect of the vertical acceleration on the response of the bridge, whether with or without dampers, is minor.

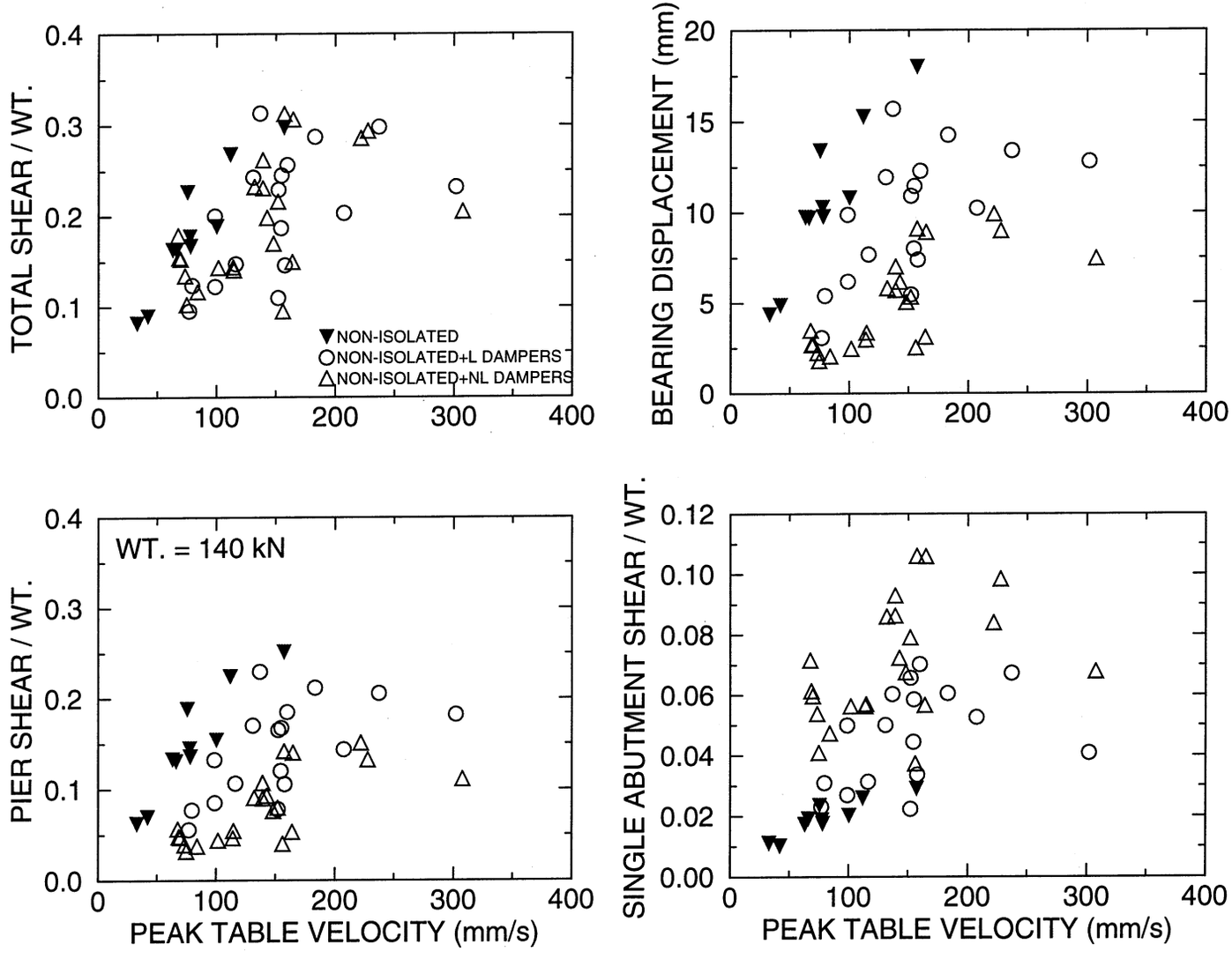

Figure 5-1: Comparison of Peak Response Values of Various Non-isolated Bridge Configurations

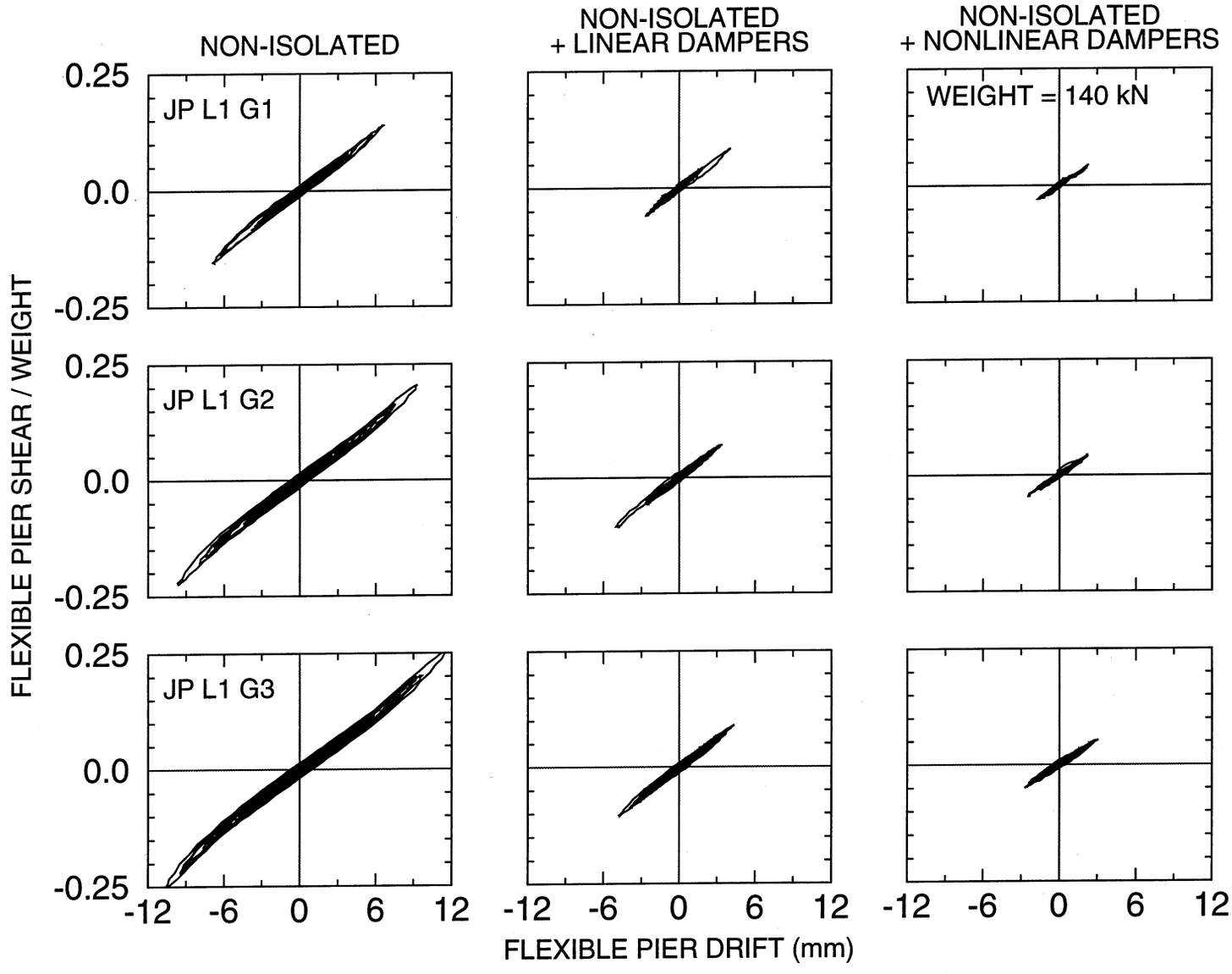

Figure 5-2: Comparison of Performance of Non-isolated Bridge Configurations in Earthquakes of Significantly Different Contents in Frequency (JP Level 1 Motions)

5.4 Conclusions

A useful first set of experimental data on the behavior of non-isolated bridges enhanced with energy dissipation devices has been generated. While the test data are limited to the case of elastic substructure behavior, they provide strong evidence on the significance of added damping in substantially reducing the displacement response with a simultaneous reduction in the total shear force transmitted to the bridge substructure. Moreover, the use of damping devices allows for effective re-distribution of the reduced inertia forces to the desired locations, that is, the strong elements of the substructure.

It is important to emphasize that the simultaneous reduction of displacements and inertia forces was accomplished by the introduction of damping, whereas other feasible methods of reducing the displacement response, such as the enhancement of stiffness at the abutment locations, results in increases of the inertia forces.

Moreover, the introduction of damping to the bridge system resulted in a marked insensitivity of the response to the frequency characteristics of the seismic input, whereas the opposite was observed in the case of the bridge system without added damping.

SECTION 6

RESULTS OF EARTHQUAKE SIMULATOR TESTING OF ISOLATED BRIDGE CONFIGURATIONS

6.1 Introduction

The isolated bridge configurations included low and high damping elastomeric isolation systems, and the low damping elastomeric systems with added linear and nonlinear viscous dampers. Each of these configurations could withstand much stronger seismic excitations than the non-isolated configurations. However, a set of low intensity tests was conducted to form a basis for comparison with the non-isolated configurations and also to test the effectiveness of these systems under low intensity excitation. The results of these tests are presented in this section, followed by an interpretation which focuses on the effects of scragging, the benefits of seismic isolation, the significance of damping, the importance of added damping in near-source seismic excitation, and on the benefits and drawbacks of using nonlinear viscous damping.

6.2 Test Results

A total of 135 tests were performed on the four isolated bridge configurations. Table 6-1 presents peak values of response quantities obtained in the testing. Moreover, Appendices C to F present the results in graphical form for a number of the conducted tests. For a complete graphical presentation of the results see Kasalanati (1998). The response quantities presented in Table 6-1 are:

(a) The peak values of displacement, velocity and acceleration of the shake table. Of these, the displacement and acceleration were directly measured, whereas the velocity was obtained by numerical differentiation of the displacement record.

(b) The bearing displacement, bearing shear force, longitudinal component of damping force, and total shear force at the abutment location. These forces represent the peak values of forces on two abutments.

(c) Abutment drift measured as the displacement of the abutment top (at the connection to the load cell above) with respect to the shake table.

(d) Abutment acceleration measured at the abutment top.

(e) The bearing displacement at the flexible pier location.

(f) The pier shear force as measured by the strain gage load cells in the columns of the flexible pier.

(g) Pier drift and pier acceleration.

(h) Total shear at the isolation system level. This is the combined force in the abutment and the flexible pier bearings and the longitudinal component of the damping forces.

(i) Deck acceleration as the average of measurements by instruments AHDNE and AHDNW (instruments 5 and 6 in Figure 4-17).

The results in Table 6-1 are presented in groups corresponding to the same earthquake excitation but of varying intensity. That is, the results of tests are not presented in the sequence in which the tests were conducted. For the high damping elastomeric isolation system the sequence of testing was important since the bearings were installed without any prior testing (unscragged conditions). Special note will be made on the behavior of the system in repetitive testing when the results are interpreted.

Table 6-1: Results of Testing of Isolated Bridge Configurations

TEST	EXCITATION	PEAK TABLE MOTION			ABUTMENT						PIER				Isolation System Total Shear /Wt	DECK ACCL. (g)
		DISPL (mm)	VEL (mm/s)	ACCL. (g)	Bearing Displ. (mm)	Bearing Shear /Wt	Damper Force /Wt	Total Shear /Wt	Abut. Drift (mm)	Abut. Accl. (g)	Bearing Displ. (mm)	Pier Shear /Wt	Pier Drift (mm)	Pier Accl. (g)		
L0FS002.1	EL CENTRO S00E 100%	24.4	161.	0.35	26.1	0.072	-	0.072	0.7	0.35	21.8	0.070	3.6	0.49	0.136	0.15
L0FS003.1	EL CENTRO S00E 200%	48.7	325.	0.64	60.8	0.136	-	0.136	1.6	0.63	51.9	0.135	7.5	0.96	0.263	0.29
LLFS001.1	EL CENTRO S00E 100%	24.3	159.	0.34	11.9	0.040	0.090	0.097	0.7	0.37	10.2	0.039	2.3	0.43	0.122	0.13
LLFS002.1	EL CENTRO S00E200% - 1	48.7	313.	0.61	28.8	0.077	0.157	0.175	1.3	0.63	25.2	0.073	4.4	0.78	0.214	0.23
LLFS002.2	EL CENTRO S00E 200% - 2	53.1	349.	0.68	32.1	0.084	0.169	0.187	1.5	0.70	28.2	0.077	4.8	0.90	0.232	0.25
LNFS002.1	EL CENTRO S00E 100%	28.1	163.	0.32	8.1	0.034	0.176	0.189	2.2	0.46	6.8	0.034	2.2	0.47	0.207	0.23
LNFS003.1	EL CENTRO S00E 200%	55.9	329.	0.62	19.7	0.066	0.218	0.250	3.1	0.95	17.1	0.066	4.2	1.07	0.296	0.32
H0FS001.1	EL CENTRO S00E 200% - 1	55.7	325.	0.58	51.4	0.168	-	0.168	1.3	0.66	44.8	0.134	7.8	1.05	0.284	0.30
H0FS001.2	EL CENTRO S00E 200% - 2	55.8	328.	0.57	56.6	0.153	-	0.153	1.2	0.68	49.3	0.132	8.0	1.08	0.270	0.30
H0FS001.3	EL CENTRO S00E 200% - 3	55.6	332.	0.58	57.5	0.151	-	0.151	1.2	0.70	50.4	0.128	8.5	1.12	0.264	0.29
H0FS001.4	EL CENTRO S00E 200% - 4	55.7	333.	0.58	58.6	0.125	-	0.125	1.0	0.72	52.4	0.109	6.6	1.13	0.220	0.24
H0FS001.5	EL CENTRO S00E 200% - 5	56.0	327.	0.57	59.3	0.122	-	0.122	0.9	0.72	54.2	0.108	6.5	1.12	0.212	0.23
H0FS012.1	EL CENTRO S00E 100%	27.9	170.	0.29	25.8	0.073	-	0.073	0.5	0.35	22.8	0.065	3.7	0.51	0.131	0.14
L0FS004.1	EL CENTRO S00E H+V 100%	23.6	156.	0.30	32.4	0.084	-	0.084	0.9	0.38	27.3	0.085	4.4	0.51	0.159	0.18
L0FS005.1	EL CENTRO S00E H+V 200%	47.4	315.	0.66	71.6	0.160	-	0.160	1.7	0.78	61.2	0.159	8.7	1.20	0.306	0.34
LLFS003.1	EL CENTRO S00E H+V 100%	35.2	173.	0.35	17.0	0.053	0.094	0.102	1.3	0.42	14.9	0.051	2.8	0.51	0.144	0.16
LLFS004.1	EL CENTRO S00E H+V 200%	70.0	367.	0.70	39.8	0.102	0.170	0.194	2.5	0.70	34.8	0.093	5.5	1.21	0.274	0.31
LLFS004.2	EL CENTRO S00E H+V 200%	53.1	348.	0.68	31.8	0.085	0.172	0.192	2.9	0.69	28.3	0.078	4.9	0.91	0.229	0.26
LNFS004.1	EL CENTRO S00E H+V 100%	28.1	172.	0.33	8.2	0.033	0.177	0.189	2.2	0.47	6.9	0.034	2.1	0.46	0.208	0.23

Wt = Weight of the Deck = 140 kN
All Configurations are for **F**lexible North Pier and **S**tiff South Abutment
The Reported Forces at the Abutment Represent the Forces on Two Abutments
Bearing Displacements and Pier Drifts are Average Values from Two Measurements

L0FS - Low Damping Elastomeric Bearings (No Dampers)
LLFS - Low Damping Elastomeric Bearings and Linear Viscous Dampers
LNFS - Low Damping Elastomeric Bearings and Nonlinear Viscous Dampers
H0FS - High Damping Elastomeric Bearings (N0 Dampers)

Table 6-1: Continued

TEST	EXCITATION	PEAK TABLE MOTION			ABUTMENT						PIER				Isolation System Total Shear /Wt	DECK ACCL. (g)
		DISPL (mm)	VEL (mm/s)	ACCL. (g)	Bearing Displ. (mm)	Bearing Shear /Wt	Damper Force /Wt	Total Shear /Wt	Abut. Drift (mm)	Abut. Accl. (g)	Bearing Displ. (mm)	Pier Shear /Wt	Pier Drift (mm)	Pier Accl. (g)		
LNFS005.1	EL CENTRO S00E H+V 200%	55.9	335.	0.65	19.5	0.067	0.218	0.252	3.3	0.91	16.9	0.068	4.3	1.18	0.298	0.32
H0FS002.1	EL CENTRO S00E H+V 200%	55.4	330.	0.59	59.1	0.146	-	0.146	1.3	0.74	52.2	0.128	7.9	1.17	0.259	0.29
H0FS013.1	EL CENTRO S00E H+V 100%	28.0	171.	0.30	25.9	0.074	-	0.074	0.5	0.37	23.1	0.066	3.9	0.50	0.133	0.15
L0FS006.1	TAFT N21E 100%	16.1	78.	0.15	15.3	0.049	-	0.049	0.5	0.17	12.6	0.045	2.4	0.25	0.092	0.10
L0FS007.1	TAFT N21E 200%	32.3	158.	0.32	33.2	0.086	-	0.086	0.8	0.31	27.7	0.083	4.5	0.52	0.163	0.18
LLFS023.1	TAFT N21E 100%	16.1	77.	0.15	7.4	0.029	0.044	0.060	0.5	0.15	5.9	0.025	1.4	0.21	0.079	0.08
LLFS005.1	TAFT N21E 200%	32.4	158.	0.33	15.6	0.053	0.084	0.110	0.9	0.30	12.7	0.048	2.6	0.41	0.146	0.15
LLFS006.1	TAFT N21E 300%	48.7	237.	0.49	24.8	0.074	0.122	0.156	1.3	0.46	20.8	0.068	3.6	0.63	0.208	0.22
LLFS007.1	TAFT N21E 400%	64.9	316.	0.67	33.5	0.092	0.170	0.205	1.7	0.63	28.7	0.086	4.6	0.84	0.266	0.27
LNFS006.1	TAFT N21E 200%	28.1	130.	0.31	6.6	0.030	0.152	0.175	2.0	0.32	5.7	0.034	2.1	0.38	0.197	0.21
LNFS007.1	TAFT N21E 100%	13.8	69.	0.15	2.6	0.016	0.106	0.116	1.2	0.16	2.4	0.018	1.1	0.18	0.128	0.13
LNFS008.1	TAFT N21E 300%	42.4	198.	0.47	12.9	0.047	0.195	0.228	2.6	0.53	11.1	0.048	3.4	0.56	0.261	0.27
LNFS009.1	TAFT N21E 400%	56.4	269.	0.62	20.9	0.065	0.225	0.264	3.3	0.81	18.3	0.064	4.5	0.79	0.306	0.32
H0FS003.1	TAFT N21E 200%	27.9	129.	0.31	27.2	0.088	-	0.088	0.7	0.33	23.4	0.071	4.2	0.44	0.154	0.17
H0FS004.1	TAFT N21E 400%	56.0	254.	0.65	59.8	0.153	-	0.153	1.1	0.70	53.0	0.129	7.6	0.92	0.271	0.29
H0FS014.1	TAFT N21E 100%	13.9	66.	0.15	12.2	0.047	-	0.047	0.4	0.16	10.8	0.037	2.3	0.20	0.082	0.09
L0FS008.1	TAFT N21E H+V 200%	28.0	130.	0.31	30.2	0.080	-	0.080	1.2	0.40	25.4	0.076	4.3	0.61	0.153	0.17
LLFS008.1	TAFT N21E H+V 200% - 1	23.8	105.	0.33	8.5	0.029	0.074	0.088	0.8	0.37	7.0	0.026	2.2	0.41	0.102	0.14
LLFS008.2	TAFT N21E H+V 200% - 2	28.1	133.	0.33	15.9	0.054	0.085	0.109	1.1	0.37	13.2	0.047	3.0	0.49	0.148	0.16

Wt = Weight of the Deck = 140 kN
All Configurations are for **F**lexible North Pier and **S**tiff South Abutment
The Reported Forces at the Abutment Represent the Forces on Two Abutments
Bearing Displacements and Pier Drifts are Average Values from Two Measurements

L0FS - Low Damping Elastomeric Bearings (No Dampers)
LLFS - Low Damping Elastomeric Bearings and Linear Viscous Dampers
LNFS - Low Damping Elastomeric Bearings and Nonlinear Viscous Dampers
H0FS - High Damping Elastomeric Bearings (N0 Dampers)

Table 6-1: Continued

TEST	EXCITATION	PEAK TABLE MOTION			ABUTMENT						PIER				Isolation System Total Shear /Wt	DECK ACCL. (g)
		DISPL (mm)	VEL (mm/s)	ACCL. (g)	Bearing Displ. (mm)	Bearing Shear /Wt	Damper Force /Wt	Total Shear /Wt	Abut. Drift (mm)	Abut. Accl. (g)	Bearing Displ. (mm)	Pier Shear /Wt	Pier Drift (mm)	Pier Accl. (g)		
LLFS009.1	TAFT N21E H+V 400%	56.4	261.	0.69	36.0	0.096	0.161	0.208	3.0	0.82	30.4	0.090	6.5	1.13	0.278	0.30
LNFS010.1	TAFT N21E H+V 200%	28.1	134.	0.32	7.4	0.030	0.155	0.175	2.3	0.43	6.8	0.036	2.5	0.66	0.195	0.21
LNFS011.1	TAFT N21E H+V 400%	56.6	274.	0.66	21.5	0.067	0.221	0.248	5.4	0.97	19.0	0.073	5.7	1.16	0.288	0.36
H0FS005.1	TAFT N21E H+V 400%	56.2	263.	0.69	61.0	0.152	-	0.152	1.5	1.	54.2	0.127	8.1	1.36	0.270	0.30
H0FS015.1	TAFT N21E H+V 100%	13.9	68.	0.16	12.4	0.048	-	0.048	0.4	0.20	10.9	0.038	2.7	0.32	0.084	0.10
L0FS009.1	HACHINOHE NS 100%	31.4	134.	0.23	18.3	0.055	-	0.055	0.6	0.23	15.1	0.054	2.8	0.29	0.103	0.12
L0FS010.1	HACHINOHE NS 200%	63.1	269.	0.49	59.4	0.134	-	0.134	1.6	0.50	50.5	0.132	7.3	0.72	0.257	0.28
LLFS010.1	HACHINOHE N-S 100%	31.6	134.	0.23	13.5	0.046	0.071	0.104	0.9	0.23	11.2	0.040	2.1	0.27	0.138	0.14
LLFS011.1	HACHINOHE N-S 200%	63.2	269.	0.49	27.9	0.077	0.134	0.193	1.7	0.47	24.0	0.069	3.7	0.65	0.252	0.26
LLFS012.1	HACHINOHE N-S 300%	94.5	412.	0.78	42.9	0.105	0.205	0.291	2.8	0.74	38.1	0.095	5.5	0.94	0.378	0.38
LNFS012.1	HACHINOHE N-S 100%	31.5	144.	0.23	7.8	0.032	0.133	0.143	1.9	0.26	6.8	0.035	2.3	0.27	0.171	0.19
LNFS013.1	HACHINOHE N-S 200%	63.1	276.	0.46	21.8	0.064	0.182	0.234	3.7	0.50	19.6	0.064	4.8	0.56	0.288	0.33
LNFS014.2	HACHINOHE N-S 300%	94.4	425.	0.75	38.8	0.097	0.221	0.302	5.4	0.70	35.5	0.098	7.2	0.76	0.387	0.44
H0FS006.1	HACHINOHE NS 200%	62.8	266.	0.48	42.9	0.106	-	0.106	0.9	0.54	37.8	0.089	6.6	0.68	0.188	0.20
H0FS007.1	HACHINOHE NS 300% - 1	94.0	407.	0.75	74.8	0.170	-	0.170	1.6	0.84	66.9	0.142	8.9	1.12	0.300	0.32
H0FS007.2	HACHINOHE NS 300% - 2	94.5	412.	0.76	82.6	0.176	-	0.176	1.5	0.82	75.1	0.140	9.4	1.13	0.295	0.33
L0FS011.1	AKITA NS 100%	42.5	177.	0.24	49.6	0.115	-	0.115	1.1	0.23	42.8	0.113	6.0	0.37	0.218	0.25
LLFS013.1	AKITA N-S 100%	44.5	185.	0.25	24.3	0.070	0.101	0.142	1.3	0.24	20.6	0.062	3.5	0.28	0.192	0.21
LLFS014.1	AKITA N-S 200%	89.2	387.	0.49	51.2	0.125	0.203	0.292	2.7	0.46	44.7	0.113	6.3	0.64	0.383	0.42

Wt = Weight of the Deck = 140 kN
All Configurations are for **F**lexible North Pier and **S**tiff South Abutment
The Reported Forces at the Abutment Represent the Forces on Two Abutments
Bearing Displacements and Pier Drifts are Average Values from Two Measurements

L0FS - Low Damping Elastomeric Bearings (No Dampers)
LLFS - Low Damping Elastomeric Bearings and Linear Viscous Dampers
LNFS - Low Damping Elastomeric Bearings and Nonlinear Viscous Dampers
H0FS - High Damping Elastomeric Bearings (N0 Dampers)

Table 6-1: Continued

TEST	EXCITATION	PEAK TABLE MOTION			ABUTMENT						PIER				Isolation System Total Shear /Wt	DECK ACCL. (g)
		DISPL (mm)	VEL (mm/s)	ACCL. (g)	Bearing Displ. (mm)	Bearing Shear /Wt	Damper Force /Wt	Total Shear /Wt	Abut. Drift (mm)	Abut. Accl. (g)	Bearing Displ. (mm)	Pier Shear /Wt	Pier Drift (mm)	Pier Accl. (g)		
LNFS015.1	AKITA N-S 100%	33.7	145.	0.18	7.4	0.031	0.123	0.137	1.5	0.22	5.7	0.030	2.1	0.22	0.161	0.17
LNFS016.1	AKITA N-S 200%	67.6	291.	0.35	23.0	0.075	0.184	0.248	3.0	0.54	19.3	0.068	4.5	0.50	0.304	0.31
H0FS008.1	AKITA NS 100%	33.7	144.	0.18	29.1	0.084	-	0.084	0.5	0.18	25.9	0.070	4.4	0.25	0.148	0.16
H0FS009.1	AKITA NS 200%	67.4	282.	0.35	71.9	0.163	-	0.163	1.2	0.36	65.3	0.132	8.5	0.59	0.279	0.32
L0FS012.1	MIYAGIKEN OKI 100%	12.0	79.	0.17	11.0	0.036	-	0.036	0.4	0.20	9.1	0.036	1.8	0.25	0.069	0.08
L0FS013.1	MIYAGIKEN OKI 200%	24.2	160.	0.36	19.1	0.056	-	0.056	0.5	0.38	16.2	0.066	3.1	0.49	0.105	0.12
L0FS014.1	MIYAGIKEN OKI 300%	36.3	236.	0.53	27.9	0.077	-	0.077	0.8	0.58	24.6	0.094	4.5	0.78	0.144	0.17
LLFS045.1	MIYAGIKEN OKI 100%	12.0	77.	0.17	4.3	0.021	0.040	0.051	0.4	0.17	3.3	0.020	1.0	0.19	0.065	0.07
LLFS046.1	MIYAGIKEN OKI 200%	24.2	157.	0.34	10.0	0.037	0.071	0.093	0.6	0.35	8.3	0.036	1.8	0.42	0.117	0.13
LLFS015.1	MIYAGIKEN OKI 300%	36.3	239.	0.51	15.0	0.046	0.104	0.127	0.9	0.53	13.2	0.043	2.4	0.66	0.153	0.17
LLFS016.1	MIYAGIKEN OKI 500%	60.6	402.	0.98	24.2	0.070	0.185	0.216	1.6	0.94	21.4	0.064	3.8	1.06	0.250	0.27
LNFS017.1	MIYAGIKEN OKI 100%	12.1	76.	0.17	2.4	0.014	0.098	0.106	1.1	0.16	2.0	0.016	1.0	0.23	0.115	0.12
LNFS018.1	MIYAGIKEN OKI 200%	24.3	148.	0.32	4.9	0.023	0.146	0.159	1.7	0.33	4.3	0.027	1.7	0.37	0.174	0.18
LNFS019.1	MIYAGIKEN OKI 300%	36.5	230.	0.49	8.7	0.034	0.180	0.197	2.3	0.46	7.7	0.041	2.1	0.54	0.220	0.23
LNFS020.1	MIYAGIKEN OKI 500%	60.9	398.	0.90	18.3	0.061	0.226	0.242	3.0	0.87	16.7	0.068	4.2	1.11	0.279	0.32
H0FS016.1	MIYAGIKEN OKI 100%	12.0	76.	0.18	7.9	0.037	-	0.037	0.3	0.21	7.2	0.029	1.7	0.22	0.064	0.08
H0FS017.1	MIYAGIKEN OKI 200%	24.3	155.	0.35	16.4	0.066	-	0.066	0.4	0.42	14.1	0.052	2.8	0.43	0.111	0.12
H0FS018.1	MIYAGIKEN OKI 300%	36.5	234.	0.54	23.4	0.079	-	0.079	0.6	0.64	21.0	0.073	4.2	0.66	0.136	0.15
H0FS019.1	MIYAGIKEN OKI 500%	60.7	394.	0.87	43.8	0.108	-	0.108	1.2	1.07	38.5	0.116	6.3	1.23	0.187	0.22

Wt = Weight of the Deck = 140 kN
All Configurations are for **F**lexible North Pier and **S**tiff South Abutment
The Reported Forces at the Abutment Represent the Forces on Two Abutments
Bearing Displacements and Pier Drifts are Average Values from Two Measurements

L0FS - Low Damping Elastomeric Bearings (No Dampers)
LLFS - Low Damping Elastomeric Bearings and Linear Viscous Dampers
LNFS - Low Damping Elastomeric Bearings and Nonlinear Viscous Dampers
H0FS - High Damping Elastomeric Bearings (N0 Dampers)

Table 6-1: Continued

TEST	EXCITATION	PEAK TABLE MOTION			ABUTMENT						PIER				Isolation System Total Shear /Wt	DECK ACCL. (g)
		DISPL (mm)	VEL (mm/s)	ACCL. (g)	Bearing Displ. (mm)	Bearing Shear /Wt	Damper Force /Wt	Total Shear /Wt	Abut. Drift (mm)	Abut. Accl. (g)	Bearing Displ. (mm)	Pier Shear /Wt	Pier Drift (mm)	Pier Accl. (g)		
L0FS015.1	PACOIMA S74W 100%	26.2	237.	0.83	50.1	0.116	-	0.116	1.3	0.91	42.8	0.119	6.2	1.22	0.221	0.26
LLFS024.1	PACOIMA S74W 50%	17.8	160.	0.55	16.7	0.053	0.093	0.113	0.8	0.51	14.0	0.046	2.7	0.70	0.155	0.16
LLFS017.1	PACOIMA S74W 100%	35.6	319.	0.97	32.4	0.087	0.177	0.208	1.7	0.95	27.7	0.080	4.8	1.41	0.276	0.29
LNFS021.1	PACOIMA S74W 100%	28.9	277.	0.79	22.1	0.069	0.211	0.236	3.2	1.05	19.9	0.087	4.8	1.11	0.274	0.31
H0FS010.1	PACOIMA S74W 100%	28.5	278.	0.86	52.0	0.110	-	0.110	0.9	1.02	47.5	0.108	5.7	1.30	0.202	0.24
L0FS016.1	PACOIMA S16E 75%	81.2	512.	0.93	97.2	0.227	-	0.227	2.8	1.11	82.6	0.226	12.0	1.64	0.433	0.48
LLFS018.1	PACOIMA S16E 75%	84.4	530.	0.92	44.6	0.110	0.263	0.284	2.3	0.96	39.0	0.105	6.5	1.06	0.340	0.35
LLFS019.1	PACOIMA S16E 100%	108.9	679.	1.16	57.7	0.138	0.356	0.351	3.5	1.15	50.8	0.128	9.1	1.66	0.431	0.43
LLFS020.1	PACOIMA S16E H+V 100%	79.0	491.	0.84	49.9	0.121	0.237	0.283	NA	0.88	46.5	0.123	NA	1.27	0.387	0.41
LNFS022.1	PACOIMA S16E 100%	79.7	492.	0.88	56.6	0.139	0.245	0.346	5.7	1.06	49.0	0.140	8.3	1.53	0.458	0.51
LNFS023.1	PACOIMA S16E H+V 100%	79.4	507.	0.91	50.8	0.122	0.256	0.339	NA	1.19	48.4	0.193	NA	1.80	0.455	0.50
H0FS011.1	PACOIMA S16E 100%	78.9	493.	0.94	106.0	0.234	-	0.234	2.2	1.23	95.5	0.204	11.8	1.40	0.414	0.46
L0FS017.1	JP LEVEL 2 GC 1 75%	80.2	344.	0.29	86.0	0.204	-	0.204	1.8	0.30	74.6	0.188	9.9	0.35	0.379	0.42
LLFS021.1	JP LEVEL 2 G.C. 1 75%	80.9	350.	0.29	32.4	0.087	0.130	0.176	1.3	0.36	27.8	0.081	4.6	0.35	0.234	0.25
LLFS022.1	JP LEVEL 2 G.C. 1 100%	107.5	469.	0.39	45.3	0.112	0.181	0.237	1.9	0.43	38.9	0.104	6.1	0.45	0.304	0.33
LNFS024.1	JP LEVEL 2 G.C. 1 75%	81.1	358.	0.32	17.8	0.059	0.165	0.181	2.5	0.43	15.3	0.063	4.0	0.42	0.224	0.26
LNFS025.1	JP LEVEL 2 G.C. 1 100%	108.2	478.	0.41	29.5	0.085	0.200	0.253	3.3	0.66	25.2	0.090	5.9	0.56	0.307	0.34
H0FS023.1	JP LEVEL 2 GC 1 100%	107.9	469.	0.41	84.8	0.216	-	0.216	1.4	0.44	78.6	0.160	10.0	0.54	0.353	0.39
LNFS026.1	JP LEVEL 2 G.C. 2 50%	50.4	224.	0.19	11.1	0.041	0.144	0.171	1.9	0.28	9.0	0.042	3.1	0.27	0.200	0.21

Wt = Weight of the Deck = 140 kN
All Configurations are for **F**lexible North Pier and **S**tiff South Abutment
The Reported Forces at the Abutment Represent the Forces on Two Abutments
Bearing Displacements and Pier Drifts are Average Values from Two Measurements

L0FS - Low Damping Elastomeric Bearings (No Dampers)
LLFS - Low Damping Elastomeric Bearings and Linear Viscous Dampers
LNFS - Low Damping Elastomeric Bearings and Nonlinear Viscous Dampers
H0FS - High Damping Elastomeric Bearings (N0 Dampers)

Table 6-1: Continued

TEST	EXCITATION	PEAK TABLE MOTION			ABUTMENT						PIER				Isolation System Total Shear /Wt	DECK ACCL. (g)	
		DISPL (mm)	VEL (mm/s)	ACCL. (g)	Bearing Displ. (mm)	Bearing Shear /Wt	Damper Force /Wt	Total Shear /Wt	Abut. Drift (mm)	Abut. Accl. (g)	Bearing Displ. (mm)	Pier Shear /Wt	Pier Drift (mm)	Pier Accl. (g)			
LNFS027.1	JP LEVEL 2 G.C. 2 100%	100.9	457.	0.40	37.5	0.109	0.226	0.312	3.9	0.53	32.7	0.106	7.4	0.47	0.395	0.41	
H0FS024.1	JP LEVEL 2 GC 2 100%	100.9	455.	0.42	82.5	0.148	-	0.148	1.4	0.46	75.5	0.123	8.2	0.62	0.253	0.29	
LNFS028.1	JP LEVEL 2 G.C. 3 75%	82.7	372.	0.32	19.4	0.061	0.194	0.212	3.4	0.48	16.7	0.065	4.6	0.46	0.261	0.27	
LNFS029.1	JP LEVEL 2 G.C. 3 100%	109.9	507.	0.52	32.9	0.090	0.225	0.280	11.5	0.65	28.5	0.092	6.5	0.60	0.353	0.37	
H0FS025.1	JP LEVEL 2 GC 3 100%	109.6	509.	0.55	131.7	0.301	-	0.301	2.3	0.57	123.4	0.211	12.4	0.75	0.484	0.54	*
L0FS018.1	JP LEVEL 1 GC 1 100%	16.1	95.	0.11	22.7	0.063	-	0.063	0.6	0.11	19.0	0.058	3.0	0.14	0.120	0.13	
LLFS025.1	JP LEVEL 1 G.C. 1 100%	16.3	97.	0.11	9.0	0.036	0.042	0.068	0.5	0.13	7.3	0.031	1.8	0.13	0.095	0.10	
LNFS030.1	JP LEVEL 1 G.C. 1 100%	16.4	109.	0.11	3.4	0.019	0.100	0.108	1.1	0.16	2.8	0.020	1.1	0.13	0.118	0.12	
H0FS020.1	JP LEVEL 1 GC 1 100%	16.2	100.	0.11	17.5	0.064	-	0.064	0.5	0.11	15.1	0.051	3.0	0.16	0.109	0.12	
L0FS021.1	JP LEVEL 1 GC 2 100%	17.1	114.	0.12	30.4	0.079	-	0.079	0.7	0.13	25.8	0.077	4.0	0.17	0.150	0.17	
LLFS026.1	JP LEVEL 1 G.C. 2 100%	17.3	114.	0.12	11.6	0.039	0.054	0.079	0.6	0.13	9.4	0.034	1.9	0.15	0.108	0.12	
LNFS031.1	JP LEVEL 1 G.C. 2 100%	17.6	117.	0.12	4.2	0.019	0.099	0.109	1.2	0.15	3.1	0.022	1.4	0.16	0.118	0.13	
H0FS021.1	JP LEVEL 1 GC 2 100%	17.5	119.	0.12	24.4	0.077	-	0.077	0.5	0.13	21.3	0.065	3.9	0.15	0.134	0.15	
L0FS019.1	JP LEVEL 1 GC 3 100%	33.4	156.	0.13	40.5	0.097	-	0.097	0.9	0.13	34.2	0.096	5.2	0.16	0.186	0.20	
LLFS027.1	JP LEVEL 1 G.C. 3 100%	33.5	158.	0.13	11.8	0.039	0.055	0.077	0.6	0.13	9.7	0.035	1.9	0.16	0.108	0.12	
LNFS032.1	JP LEVEL 1 G.C. 3 100%	33.3	294.	0.14	4.5	0.022	0.111	0.111	NA	0.17	3.8	0.023	NA	0.24	0.119	0.13	
H0FS022.1	JP LEVEL 1 GC 3 100%	33.4	159.	0.13	23.7	0.074	-	0.074	0.5	0.13	20.6	0.062	3.7	0.15	0.130	0.14	
L0FS020.1	NORTHRIDGE SYL. 90° 100%	49.8	339.	0.58	83.6	0.179	-	0.179	2.1	0.57	71.7	0.179	9.9	0.57	0.348	0.38	
LLFS028.1	NORTHRIDGE SYLMAR 90° 50%	24.9	167.	0.30	18.4	0.059	0.081	0.120	1.0	0.34	15.4	0.052	2.9	0.25	0.168	0.17	

Wt = Weight of the Deck = 140 kN
All Configurations are for **F**lexible North Pier and **S**tiff South Abutment
The Reported Forces at the Abutment Represent the Forces on Two Abutments
Bearing Displacements and Pier Drifts are Average Values from Two Measurements

L0FS - Low Damping Elastomeric Bearings (No Dampers)
LLFS - Low Damping Elastomeric Bearings and Linear Viscous Dampers
LNFS - Low Damping Elastomeric Bearings and Nonlinear Viscous Dampers
H0FS - High Damping Elastomeric Bearings (N0 Dampers)

* Failure of SW Elastomeric Bearing

Table 6-1: Continued

TEST	EXCITATION	PEAK TABLE MOTION			ABUTMENT						PIER				Isolation System Total Shear /Wt	DECK ACCL. (g)
		DISPL (mm)	VEL (mm/s)	ACCL. (g)	Bearing Displ. (mm)	Bearing Shear /Wt	Damper Force /Wt	Total Shear /Wt	Abut. Drift (mm)	Abut. Accl. (g)	Bearing Displ. (mm)	Pier Shear /Wt	Pier Drift (mm)	Pier Accl. (g)		
LLFS029.1	NORTHRIDGE SYLMAR 90° 75%	37.4	251.	0.44	29.1	0.081	0.117	0.170	1.5	0.47	24.6	0.073	4.1	0.37	0.237	0.24
LLFS030.1	NORTHRIDGE SYL. 90° 100%	49.8	340.	0.60	39.4	0.101	0.158	0.222	2.1	0.62	33.7	0.093	5.2	0.51	0.301	0.31
LNFS033.1	NORTHRIDGE SYL. 90° 100%	50.4	344.	0.63	34.7	0.093	0.202	0.265	NA	0.84	30.5	0.098	6.5	0.58	0.348	0.38
LNFS034.1	NORTHRIDGE SYL. 90° 150%	75.5	517.	0.99	62.7	0.150	0.236	0.361	5.9	1.28	54.8	0.143	9.8	0.87	0.490	0.54
L0FS022.1	NORTHRIDGE Syl. 90° H+V 100%	49.8	341.	0.59	86.6	0.187	-	0.187	2.6	0.68	74.2	0.187	11.0	0.86	0.362	0.40
LLFS031.1	NORTHRIDGE Syl. 90° H+V 100%	49.7	344.	0.62	40.1	0.104	0.155	0.216	1.9	0.66	33.9	0.097	6.4	0.83	0.300	0.31
LNFS035.1	NORTHRIDGE Syl. 90° H+V 100%	50.5	356.	0.64	34.9	0.091	0.203	0.264	4.3	0.78	31.5	0.110	7.4	1.11	0.350	0.38
LNFS036.1	NORTHRIDGE Syl. 90° H+V 150%	75.4	534.	1.	62.8	0.149	0.236	0.360	6.7	1.48	55.6	0.172	12.2	1.43	0.491	0.53
LLFS032.1	NORTHRIDGE Newhall 90° 100%	43.6	311.	0.99	24.6	0.067	0.145	0.183	1.6	0.94	21.4	0.060	3.7	1.22	0.232	0.24
L0FS023.1	NORTHRIDGE NH 90° H+V 100%	43.2	329.	0.90	57.8	0.133	-	0.133	1.9	1.01	50.8	0.157	8.4	1.63	0.262	0.30
LLFS033.1	NORTHRIDGE NH 90° H+V 100%	43.5	323.	0.96	24.3	0.066	0.168	0.189	2.6	1.02	21.4	0.059	5.1	1.34	0.219	0.29
L0FS025.1	NORTHRIDGE Newhall 360° 75%	43.5	322.	0.61	68.6	0.147	-	0.147	1.6	0.65	58.7	0.153	8.1	0.79	0.285	0.31
LLFS034.1	NORTHRIDGE Newhall360° 50%	29.4	208.	0.37	20.3	0.056	0.127	0.161	1.3	0.36	18.0	0.051	2.8	0.43	0.205	0.22
LLFS035.1	NORTHRIDGE Newhall 360° 75%	44.1	322.	0.60	28.9	0.076	0.200	0.246	2.1	0.58	26.2	0.068	4.1	0.72	0.300	0.32
LLFS036.1	NORTHRIDGE Newhall 360° 100%	58.9	438.	0.85	38.2	0.098	0.279	0.332	2.8	0.81	32.8	0.090	5.5	1.06	0.393	0.42
LNFS037.1	NORTHRIDGE Newhall 360° 100%	59.4	451.	0.81	38.3	0.094	0.241	0.324	4.0	0.94	35.7	0.111	5.8	1.20	0.409	0.43
LLFS037.1	NORTHRIDGE NH 360°H+V100%	58.8	454.	0.86	40.8	0.108	0.284	0.334	3.5	1.	37.2	0.107	8.7	1.50	0.384	0.39

Wt = Weight of the Deck = 140 kN
All Configurations are for **F**lexible North Pier and **S**tiff South Abutment
The Reported Forces at the Abutment Represent the Forces on Two Abutments
Bearing Displacements and Pier Drifts are Average Values from Two Measurements

L0FS - Low Damping Elastomeric Bearings (No Dampers)
LLFS - Low Damping Elastomeric Bearings and Linear Viscous Dampers
LNFS - Low Damping Elastomeric Bearings and Nonlinear Viscous Dampers
H0FS - High Damping Elastomeric Bearings (N0 Dampers)

Table 6-1: Continued

TEST	EXCITATION	PEAK TABLE MOTION			ABUTMENT						PIER				Isolation System Total Shear /Wt	DECK ACCL. (g)
		DISPL (mm)	VEL (mm/s)	ACCL. (g)	Bearing Displ. (mm)	Bearing Shear /Wt	Damper Force /Wt	Total Shear /Wt	Abut. Drift (mm)	Abut. Accl. (g)	Bearing Displ. (mm)	Pier Shear /Wt	Pier Drift (mm)	Pier Accl. (g)		
LNFS038.1	NORTHRIDGE NH 360°H+V100%	59.6	426.	0.78	38.9	0.096	0.248	0.318	5.3	1.11	34.4	0.120	8.0	1.64	0.396	0.44
L0FS024.1	KOBE - KOBE STATION NS 100%	41.7	445.	0.81	93.5	0.224	-	0.224	2.8	0.80	80.8	0.238	11.6	1.28	0.411	0.47
LLFS038.1	KOBE - KOBE STATION N-S 50%	21.1	210.	0.38	18.1	0.054	0.148	0.162	1.3	0.36	15.7	0.048	2.5	0.40	0.181	0.20
LLFS039.1	KOBE - KOBE STATION NS 100%	42.4	450.	0.86	35.7	0.085	0.311	0.344	2.8	0.80	33.3	0.081	5.9	1.21	0.377	0.41
LNFS039.1	KOBE - KOBE STATION NS 100%	42.4	448.	0.77	37.6	0.094	0.256	0.322	4.1	1.14	34.4	0.094	5.8	0.97	0.394	0.44
LLFS040.1	KOBE - KOBE ST. N-S H+V 100%	43.1	443.	0.93	37.3	0.095	0.310	0.342	4.1	0.91	33.7	0.089	8.1	1.45	0.391	0.38
LNFS040.1	KOBE - KOBE ST. N-S H+V 100%	42.3	455.	0.83	36.2	0.082	0.258	0.324	5.0	1.18	33.9	0.102	6.0	1.58	0.392	0.41
LLFS041.1	MEXICO CITY N90W 50%	25.0	145.	0.09	15.7	0.050	0.051	0.081	0.7	0.10	12.8	0.044	2.6	0.11	0.120	0.13
LLFS042.1	MEXICO CITY N90W 60%	30.0	175.	0.12	20.2	0.061	0.063	0.099	0.9	0.12	16.6	0.054	3.1	0.15	0.145	0.15
LLFS043.1	MEXICO CITY N90W 80%	40.0	234.	0.15	30.0	0.082	0.086	0.134	1.3	0.15	25.1	0.074	4.4	0.16	0.195	0.21
LLFS044.1	MEXICO CITY N90W 100%	52.2	305.	0.18	42.3	0.106	0.121	0.175	1.8	0.18	35.7	0.097	5.8	0.25	0.254	0.27
LNFS041.1	MEXICO CITY N90W 100%	52.1	309.	0.19	14.2	0.050	0.131	0.159	2.7	0.20	11.9	0.049	3.9	0.22	0.193	0.21

Wt = Weight of the Deck = 140 kN
All Configurations are for **F**lexible North Pier and **S**tiff South Abutment
The Reported Forces at the Abutment Represent the Forces on Two Abutments
Bearing Displacements and Pier Drifts are Average Values from Two Measurements

L0FS - Low Damping Elastomeric Bearings (No Dampers)
LLFS - Low Damping Elastomeric Bearings and Linear Viscous Dampers
LNFS - Low Damping Elastomeric Bearings and Nonlinear Viscous Dampers
H0FS - High Damping Elastomeric Bearings (N0 Dampers)

Testing of the isolated bridge was conducted with a number of records from the 1994 Northridge and 1995 Japanese Kobe earthquakes. These records together with some from the 1971 San Fernando earthquake were characterized by near-fault conditions with high ground velocity. Unfortunately, testing of the high damping elastomeric isolation system was not conducted with the Northridge and Kobe motions due to failure of the bearings.

It is important to note in Table 6-1 that the peak table motion is not the same for motions that were specified to be identical. The reasons for this phenomenon were the table-structure interaction and the occasionally insufficient hydraulic power in the stronger inputs (which was affected by the demand for power from the other experiments conducted in the laboratory at the same time). Due to the long-period characteristics of the tested isolated bridge, the relevant parameter for assessing the intensity of the seismic input is the peak table velocity.

6.3 Interpretation of Results

6.3.1 Behavior of High Damping Elastomeric System under Unscragged and Scragged Conditions

The high damping elastomeric bearings were installed in the bridge model without prior testing. Accordingly, they exhibited unscragged properties. As evaluated in Section 4 from the testing of another bearing, the unscragged conditions were characterized by a stiffness approximately 50-percent higher than the scragged one. It has been assumed that the scragged properties are not stable and that recovery to the unscragged properties occurs after some time. Accordingly, repetitive testing with the same strong excitation was conducted. The interest was to observe the bearing displacement response and the force transferred to the substructure under scragged conditions and under conditions following recovery (presumed to be the same as the unscragged conditions).

Testing with the El Centro S00E (horizontal component only) motion scaled up by factor 2.0 (denoted in Table 6-1 as El Centro S00E 200%) was conducted first. The same test was repeated two more times, it was followed by four other tests, and then again repeated twice. Figure 6-1 presents the force-displacement loops of the southwest abutment and the northwest flexible pier bearings recorded in the first (unscragged), third and fifth tests in this sequence. These graphs, together with the results in Table 6-1, demonstrate that during the scragging process there is a substantial drop in the effective stiffness of the isolation system from about 0.83 kN/mm in the first test to about 0.54 kN/mm in the fifth test (indeed as determined in the testing of the first bearing, the unscragged stiffness is about 50-percent larger than the scragged stiffness). Moreover, there is a reduction in the characteristic strength of the system, from about 10.5 kN in the first test to about 8.9 kN in the fifth test.

In terms of the displacement response, we observe a minor difference between the unscragged and scragged conditions. As seen in Table 6-1, under unscragged bearing conditions (test H0FS001.1) the bearing displacements are about 15-percent less than the displacements under scragged bearing conditions. However, there is a marked difference in the force transmitted to the

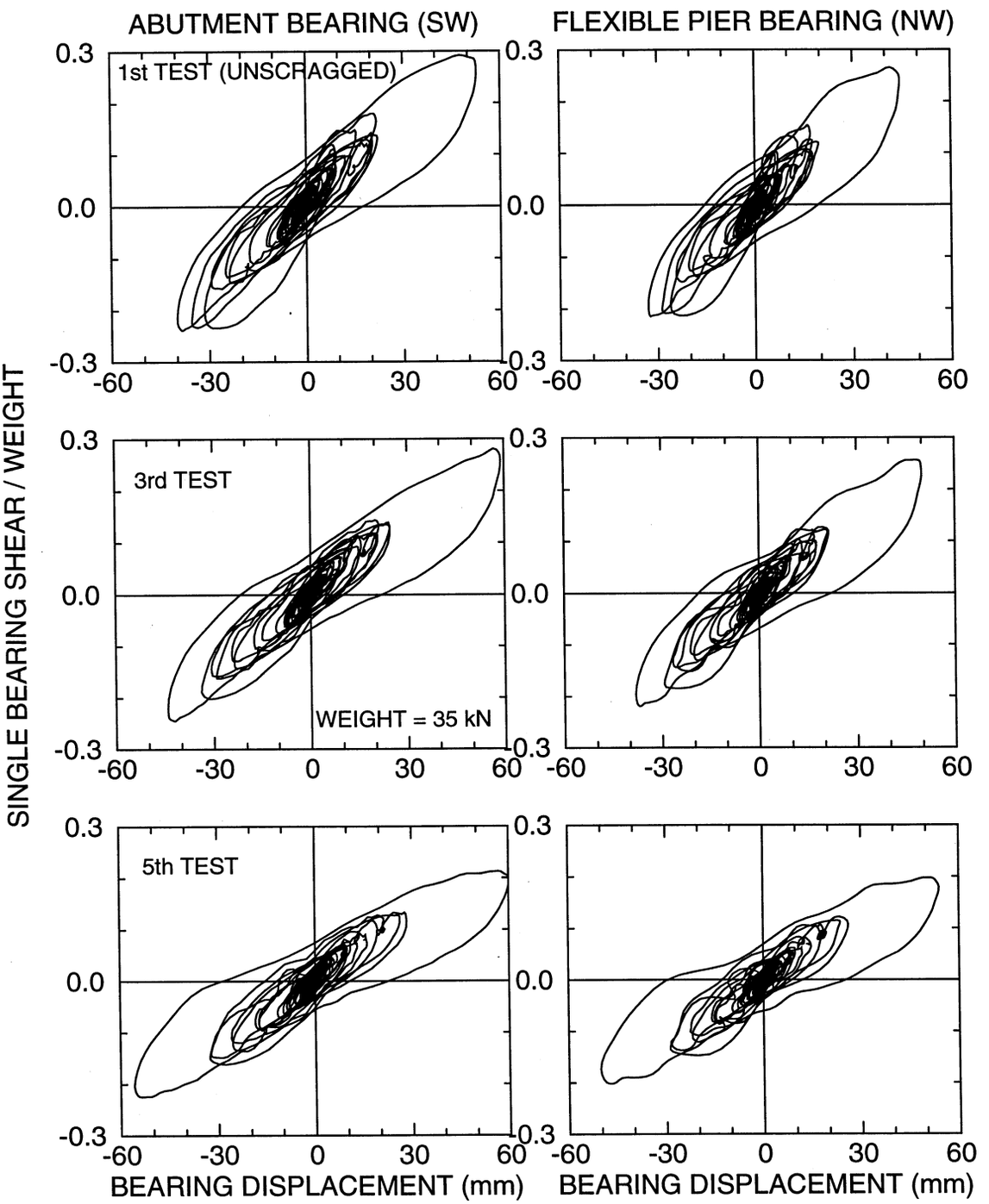

Figure 6-1: Comparison of Force-Displacement Loops of High Damping Elastomeric Bearings in Repetitive Testing with El Centro S00E 200% Input

substructure. As seen in Table 6-1, the peak total shear force in the isolation system changes from 0.284 to 0.212 times the deck weight. That is, the force transmitted to the substructure under unscragged conditions is about 30-percent higher than the force transmitted under scragged conditions.

Of interest is to note that the observed differences are entirely predictable on the basis of the simple equations in the 1997 AASHTO (American Association of State Highway and Transportation Officials, 1997). Specifically, the isolation system displacement, d, and the isolation system force, F are related to the effective period, T_{eff}, and damping coefficient, B (which is related to the effective damping) by:

$$d \sim \frac{T_{eff}}{B} \tag{6-1}$$

$$F \sim \frac{1}{BT_{eff}} \tag{6-2}$$

where the symbol ~ denotes proportionality. For the tested system the following parameters were determined from the experimental data. For unscragged conditions (first test): $T_{eff} = 0.83$ *sec*, $\beta = 0.16$, $B = 1.38$. For scragged conditions (fifth test): $T_{eff} = 1.02$ *sec*, $\beta = 0.18$, $B = 1.44$.

Assigning subscripts s for the scragged conditions and u for the unscragged conditions, we have on the basis of (6-1) and (6-2):

$$\frac{d_s - d_u}{d_s} = 1 - \frac{T_{effu} \cdot B_s}{T_{effs} \cdot B_u} \tag{6-3}$$

$$\frac{F_u - F_s}{F_s} = \frac{B_s \cdot T_{effs}}{B_u \cdot T_{effu}} - 1 \tag{6-4}$$

For the tested system, (6-3) gives 0.15 and (6-4) gives 0.28, that is, in good agreement with the experiments.

We conclude that analysis of isolated structures on the basis of the scragged properties of high damping bearings may underestimate the isolation system forces by a significant amount when comparing to the conditions of the bearings after some time in service (herein we presume that the bearings recover their unscragged properties).

6.3.2 Comparison of Behavior of Non-isolated and Isolated Bridge Configurations without Dampers

Figure 6-2 presents a comparison of key response quantities of the non-isolated and the isolated bridge configurations without dampers. These response quantities are presented as functions of the peak table velocity, which is an appropriate measure of intensity of the seismic input for the

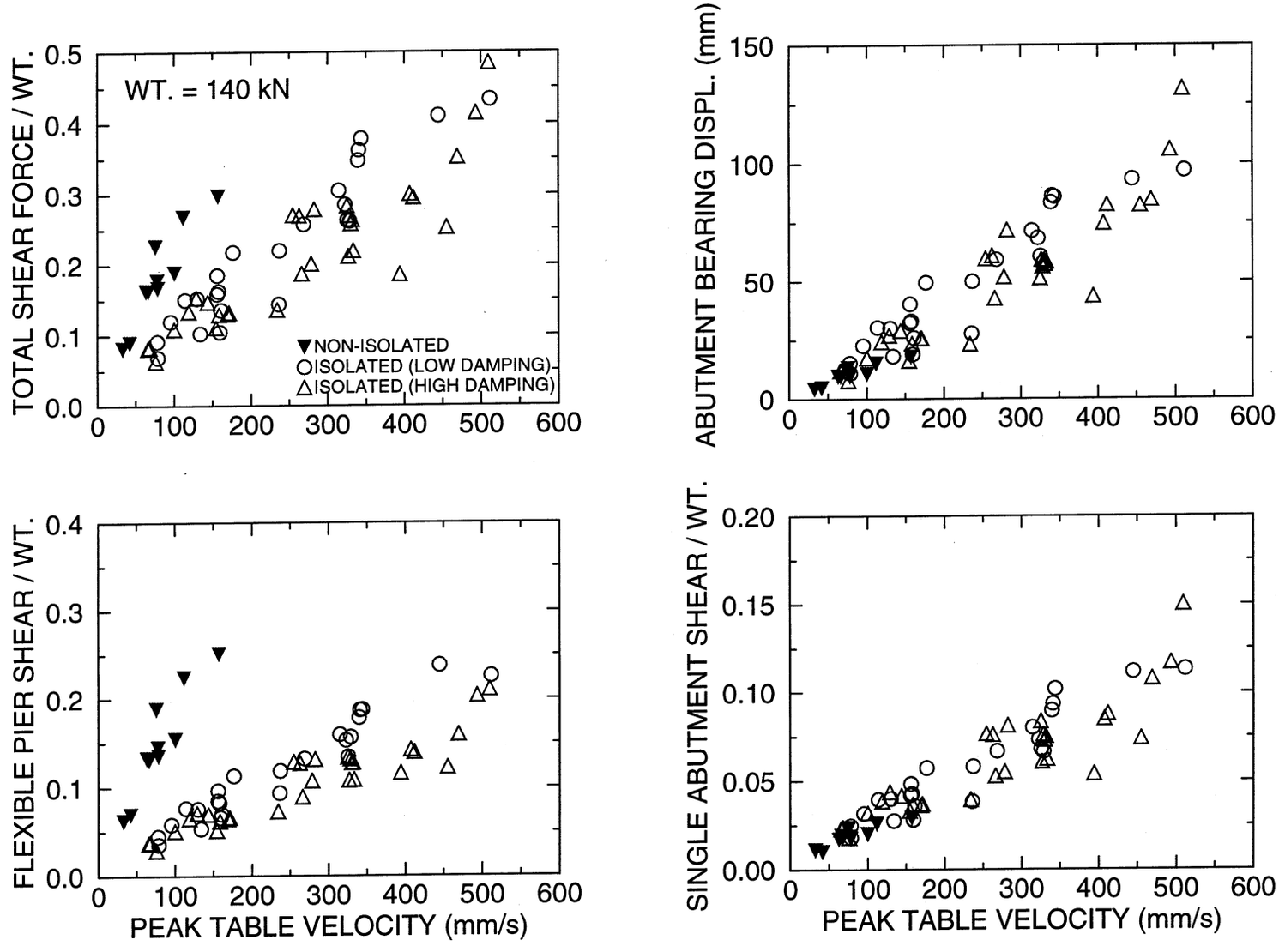

Figure 6-2: Comparison of Peak Response of Non-isolated and Isolated Bridge Configurations without Dampers

tested flexible systems. This figure clearly demonstrates the effects of isolation: reduction of the shear force transmitted to the vulnerable pier at the expense of larger bearing displacements and accordingly larger force transmitted to the abutments.

However, the interesting result in this figure is that the response of the isolated bridge with low damping elastomeric bearings is, in many tests, not very different from the response of the high damping elastomeric system. One would expect an overall superior performance from the high damping elastomeric system given that the two systems had essentially the same effective period but substantially different effective damping (less than 0.09 in the low damping system versus about 0.15 to 0.20 for the high damping system).

Accordingly, we proceed with a direct comparison of response of the low and high damping elastomeric systems under the same seismic excitation. Figures 6-3 to 6-6 present comparisons of time histories of the abutment bearing displacements, isolation system shear force versus bearing displacement loops and the flexible pier shear force versus pier drift loops in the tests with the Hachinohe NS 200%, El Centro S00E 200%, Japanese Level 1 and Ground Condition 3 (soft soil) 100%, and Pacoima Dam S74W 100% horizontal seismic input.

Starting with Figure 6-3 we observe the benefits offered by the high damping elastomeric system. There is a reduction in bearing displacement which is consistent with equation (6-1). That is, when considering an effective damping of about 7 to 8-percent for the low damping system (so that $B \approx 1.10$) and effective damping of about 15 to 20-percent for the high damping system (so that $B \approx 1.45$), we expect a ratio of peak displacement in the two systems of about $1.10/1.45 \approx 0.75$ provided that the effective period is the same.

In the case of the El Centro input (Figure 6-4) there is very little difference in the displacement response of the two systems due to the larger effective period of the high damping elastomeric system. However, the benefit of reduction of the force transmitted to the substructure is evident.

The great benefit of increased damping is seen in the case of the Japanese Level 1, ground condition 3 input (Figure 6-5). Due to the existence of strong, long period components in this input the two systems are essentially driven to resonance. Accordingly, the high damping system shows a clearly superior performance which can not be predicted on the basis of equation (6-1). For such a case, the ratio of peak displacements may be approximately calculated by

$$\frac{d_h}{d_l} \approx \frac{\beta_l}{\beta_h} \tag{6-5}$$

where the subscripts h and l denote high damping and low damping systems, respectively, and β is the effective damping. Equation (6-5) is based on the known displacement magnification relation at resonance of harmonically excited systems (Chopra, 1995). Approximately for the two systems in Figure 6-5, β_l = 0.08 and β_h = 0.15. Accordingly, (6-5) results in $d_h/d_l \approx 0.53$, which is consistent with the experimental results.

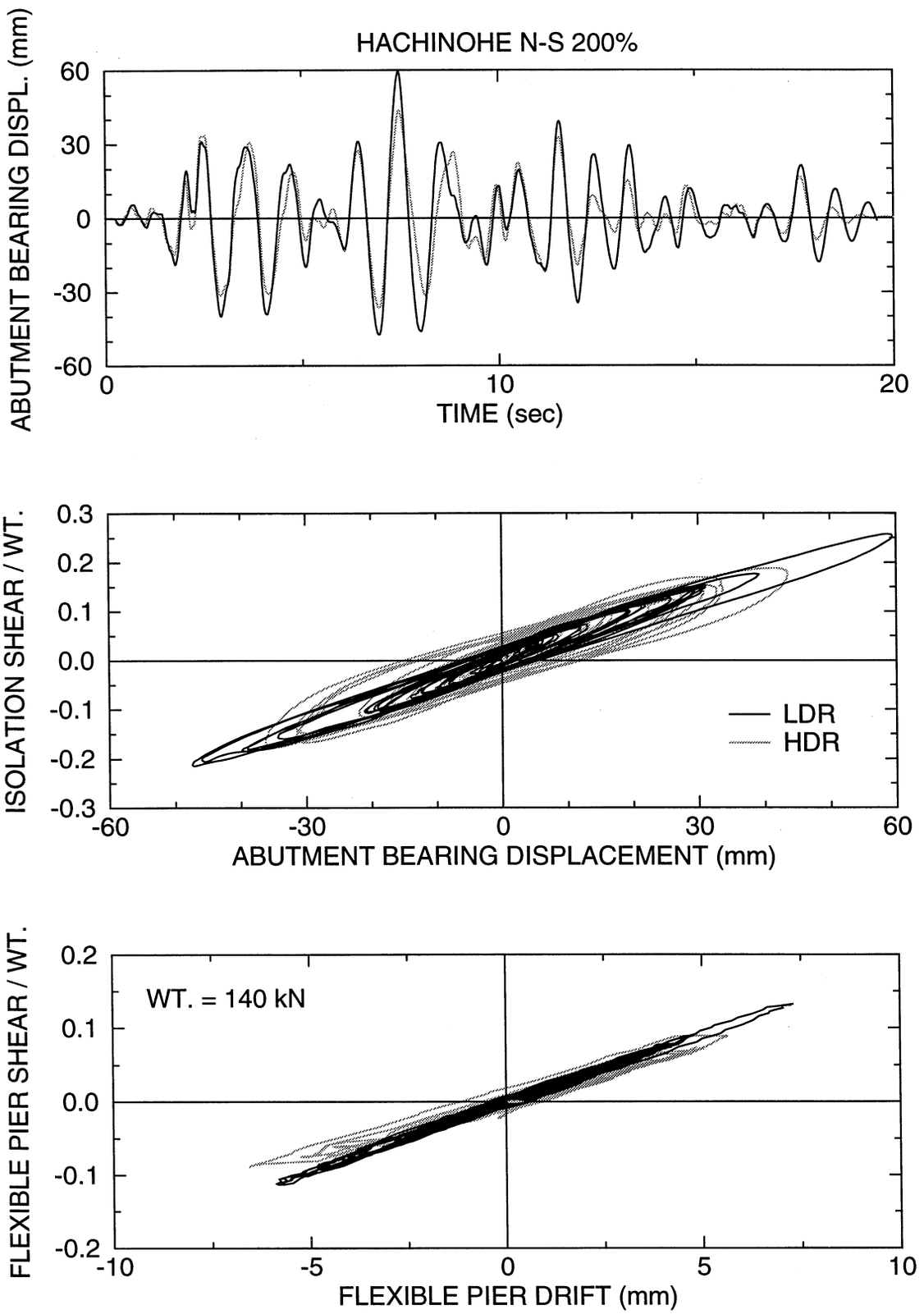

Figure 6-3: Comparison of Response of Isolated Bridge with Elastomeric Systems for Hachinohe N-S 200% Input

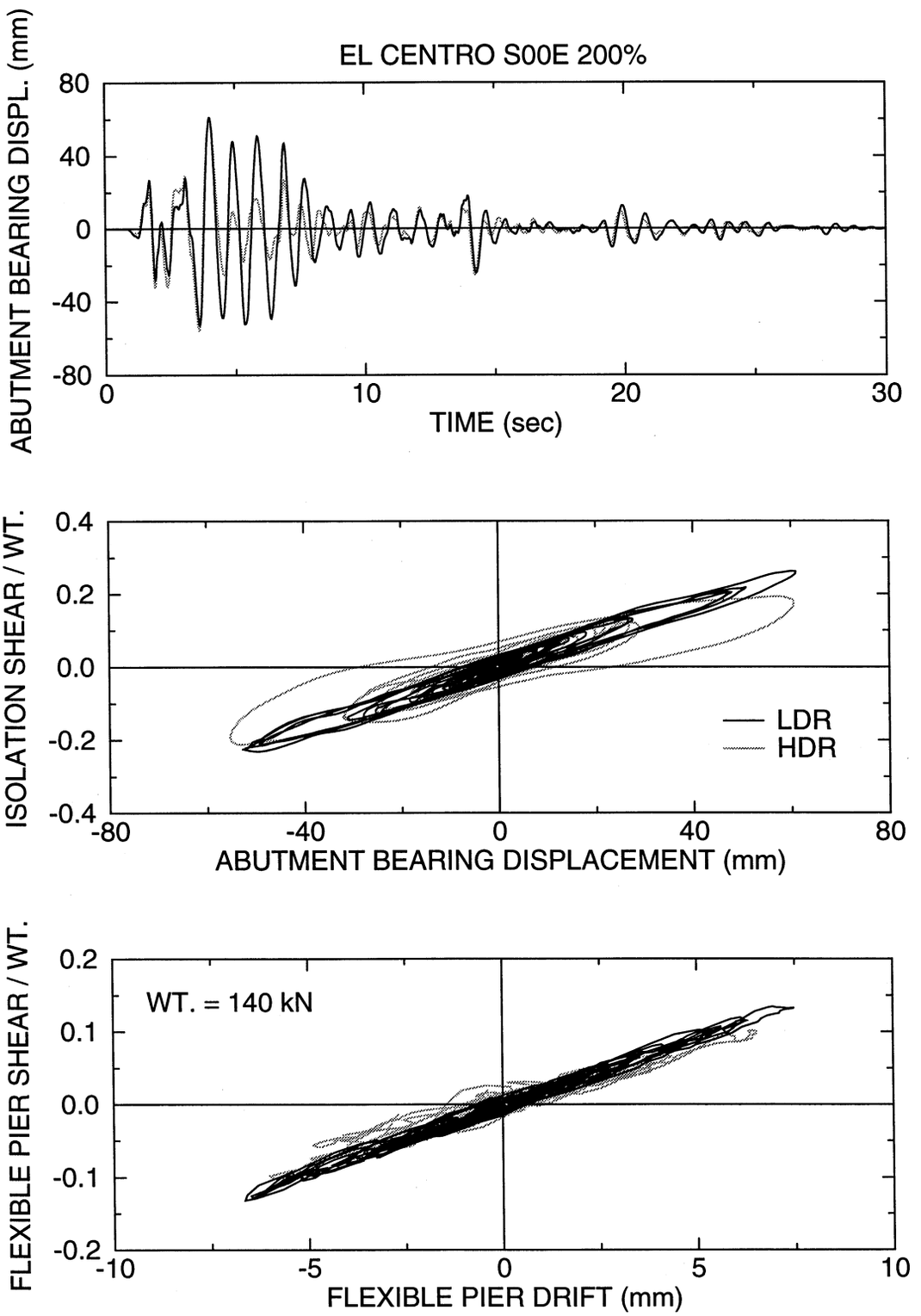

Figure 6-4: Comparison of Response of Isolated Bridge with Elastomeric Systems for El Centro S00E 200% Input

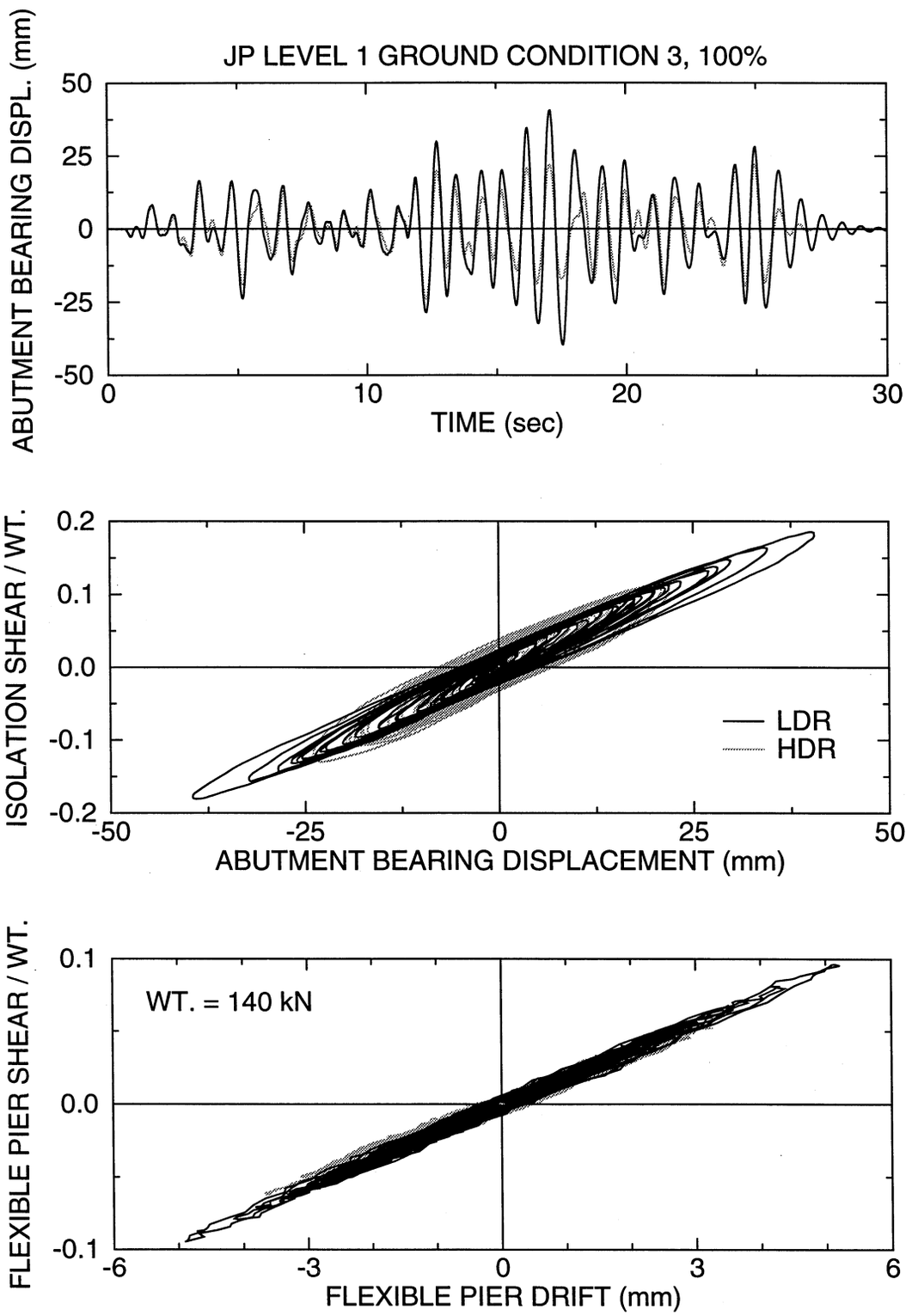

Figure 6-5: Comparison of Response of Isolated Bridge with Elastomeric Systems for Japanese Level 1, Ground Condition 3, 100% Input

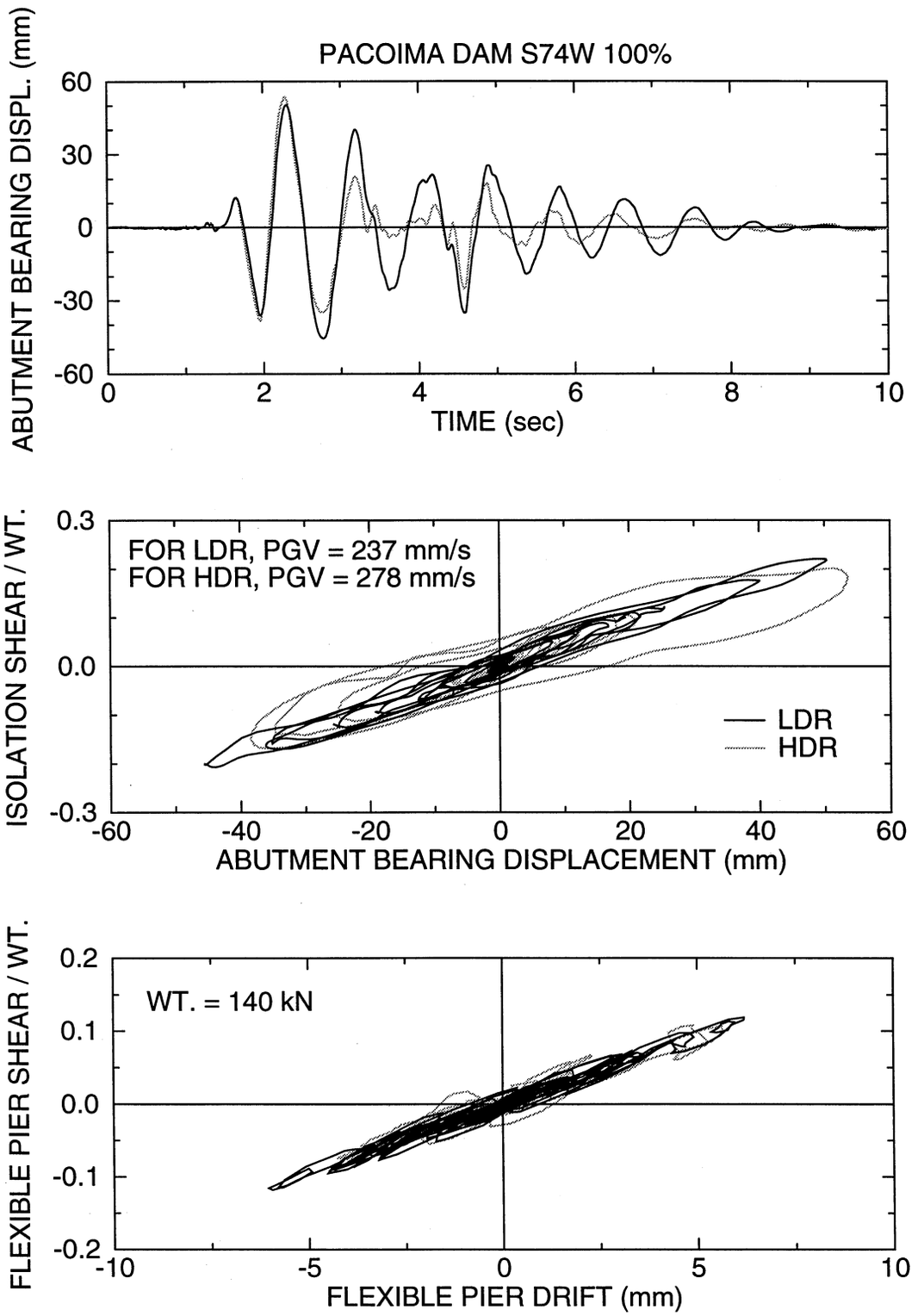

Figure 6-6: Comparison of Response of Isolated Bridge with Elastomeric Systems for Pacoima Dam S74W 100% Input

Finally, we discuss the case of the Pacoima Dam S74W input (Figure 6-6). To start, we note that the inputs in the two tests differed in terms of the peak table velocity (278 mm/s in the high damping system and 237 mm/s in the low damping system). If we approximately adjust the displacement of the low damping system to correspond to the input of 278 mm/s peak table velocity, we obtain an abutment bearing displacement of nearly 59 mm versus the 52 mm measured displacement of the high damping system. There is, therefore, some benefit offered by the high damping system in reducing the displacements. However, the benefit is not as large as in other types of input. We recognize the near-fault characteristics of this input (however, not as prevalent as in other inputs), which will be further discussed later in this report.

Unfortunately, testing of the high damping elastomeric system was not conducted with other motions having prevalent near-fault characteristics due to failure of one of high damping elastomeric bearings. However, we could obtain a very good set of results when we tested the two systems with the Pacoima Dam record, component S16E. This motion contained a clear high velocity shock. The two systems were tested for different specified intensities of this input (see Table 6-1) but for some unknown reason the motion of the table was nearly identical. Figure 6-7 presents a comparison of the recorded response in the two tests (tests L0FS016.1 and H0FS011.1). The inputs are nearly the same with the low damping system excited by slightly higher peak velocity. It may be observed that the two systems experienced nearly the same peak bearing displacements and peak force in the isolation system. The higher damping did not have any effect during the cycle of movement caused by the input velocity shock. However, it had a substantial effect during the subsequent cycles (which were essentially cycles of free vibration response).

Concluding, we note that the high damping elastomeric bearings were effective in the reduction of displacement and accordingly force in the structure in motions lacking high velocity shocks which are characteristics of near-fault motions. This issue will be further discussed when the results of testing of the system with added viscous dampers are presented.

6.3.3 Failure of Elastomeric Bearings

During the testing of the high damping elastomeric system with the Japanese level 2 and ground condition 3 (soft soil) input (test No. H0FS025.1), the southwest abutment bearing failed. Figure 6-8 presents plots of the force displacement loops of the four bearings during this test.

The displacements of the bearings reached rubber shear strains of about 175-percent for which the bearings were theoretically unstable. However, the bearings appeared stable and exhibited some stiffening at large strains (beyond approximately 120-percent) which was characteristic of the utilized rubber compound. The bearing at the southwest side on top of the abutment failed in a combined de-bonding of rubber from the top end plate and fracture of rubber in the top layer. It was bearing No. 3 from batch No. 1 which was likely improperly cured and exhibited significant creep. The fact that the failure initiated as de-bonding of the rubber from the steel plate further reinforces the notion of improper curing.

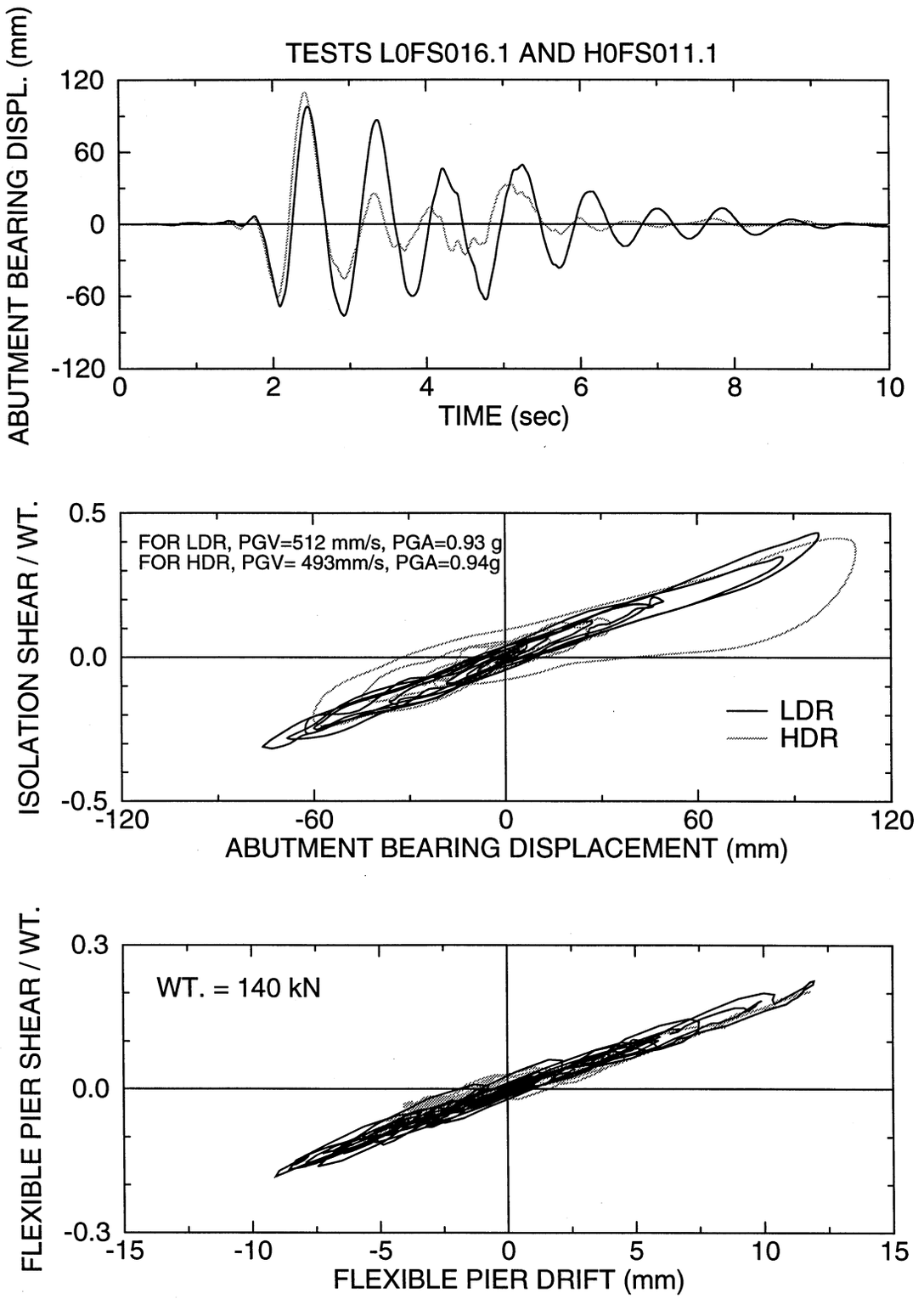

Figure 6-7: Comparison of Response of Isolated Bridge with Elastomeric Systems for Pacoima Dam S16E Input

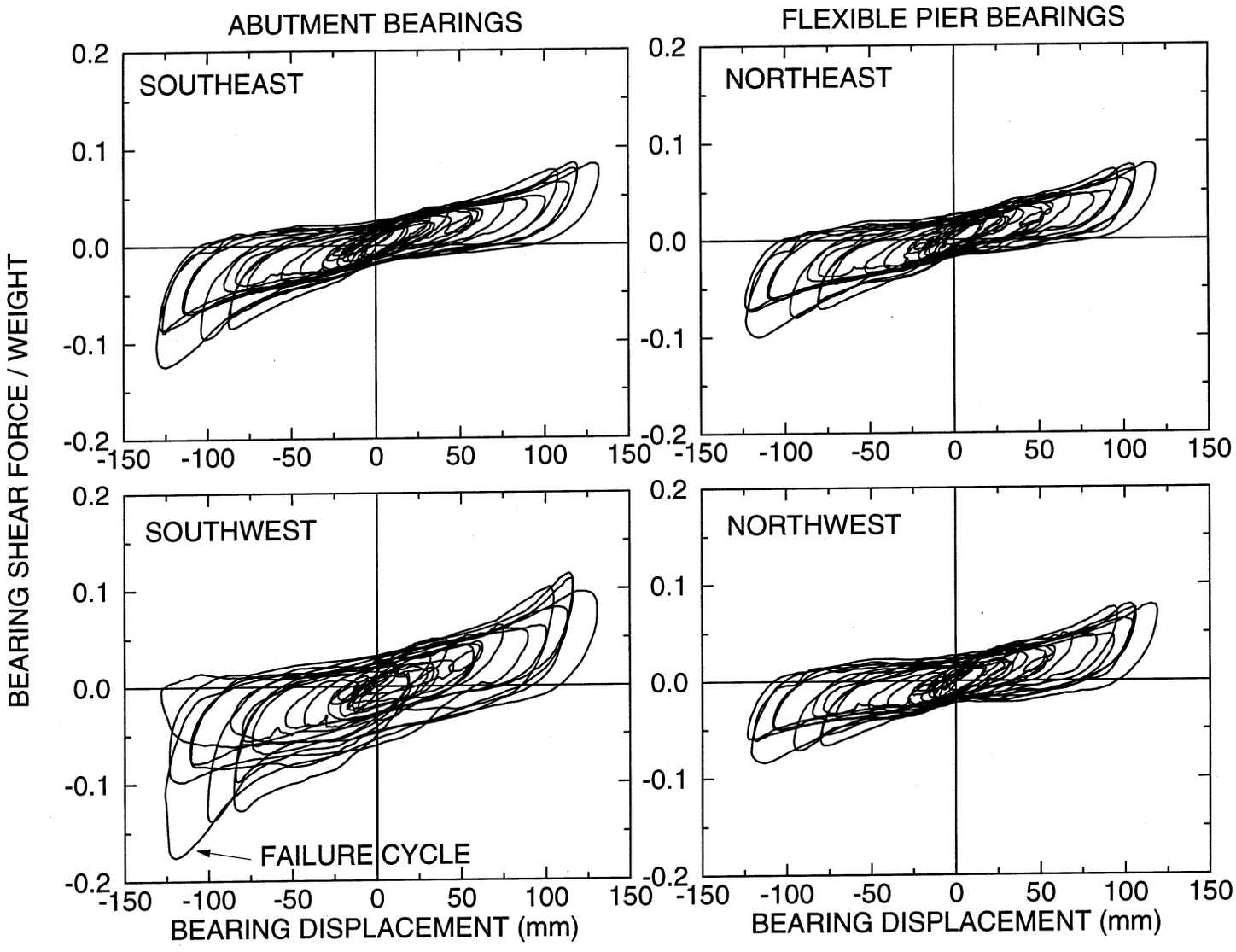

Figure 6-8: Shear Force-Displacement Loops of High Damping Elastomeric Bearings in Failure Test (Japanese Level 2, Ground Condition 3, Test No. H0FS025.001)

Figure 6-9 shows a view of the failed bearing in which the failure region is visible. Note that the bearing still carries the weight of the deck but it has some distortion as well as visible bulging of individual layers. The bulging was the result of excessive creep and it was present before the failure test (actually, both bearings from batch No. 1 had similar bulging). The failure of the bearing was not apparent during testing. Rather it was detected afterwards due to the permanent distortion of the bearing. It should be recognized that this failure was dependent on the condition of the bearings (improperly cured) and the nearly unstable condition of their operation. It is impossible to extrapolate the failure results to the scale of prototype bearings. Nevertheless, it is encouraging to observe that the failure was not catastrophic.

6.3.4 Comparison of High Damping Elastomeric System and Linear Viscous Damper System

Comparison of the two systems is interesting because they primarily differed in their damping characteristics with the system with linear dampers having approximately twice the effective damping of the high damping elastomeric system. However, the comparison is limited by the fact of not having tested the high damping elastomeric system with the records from the 1994 Northridge and 1995 Kobe earthquakes.

Nevertheless, a good picture of the behavior of the two systems is provided in Figure 6-10 where the peak response of the two systems is presented as a function of the peak table velocity. It is evident that the system with linear viscous dampers has substantially less bearing displacement and flexible pier shear force response than the high damping elastomeric system. Moreover, the two systems have about the same total shear force at the isolation level. However, due to the redistribution of this force provided by the viscous dampers, more force is transmitted to the strong abutment by the system with dampers.

Interesting observations can be made when the response of the two systems is directly compared for the same or nearly the same seismic input. For this comparison we choose the El Centro S00E and the Pacoima Dam S16E inputs. Figures 6-11 and 6-12 present comparisons of the recorded time histories of abutment bearing displacement, loops of isolation system force versus abutment bearing displacement and loops of flexible pier shear force versus pier drift of the two systems.

For the case of El Centro S00E 200% (Figure 6-11), the input in the two tests was essentially the same. The benefits offered by the viscous damper system are apparent and significant: reduction of bearing displacement to about half without any increase in the isolation system total shear force.

For the case of Pacoima Dam S16E (Figure 6-12), the input in the two tests is not the same. The input in the case of the system with dampers is stronger with the peak table velocity being nearly 40-percent larger than that of the input in the case of the high damping elastomeric system. Despite the difference in the intensity of the input, the system with viscous dampers undergoes substantially lesser displacement response (approximately half) while the peak isolation system force is nearly the same in the two systems.

Figure 6-9: View of Failed Bearing (note that it still carries the weight of the deck)

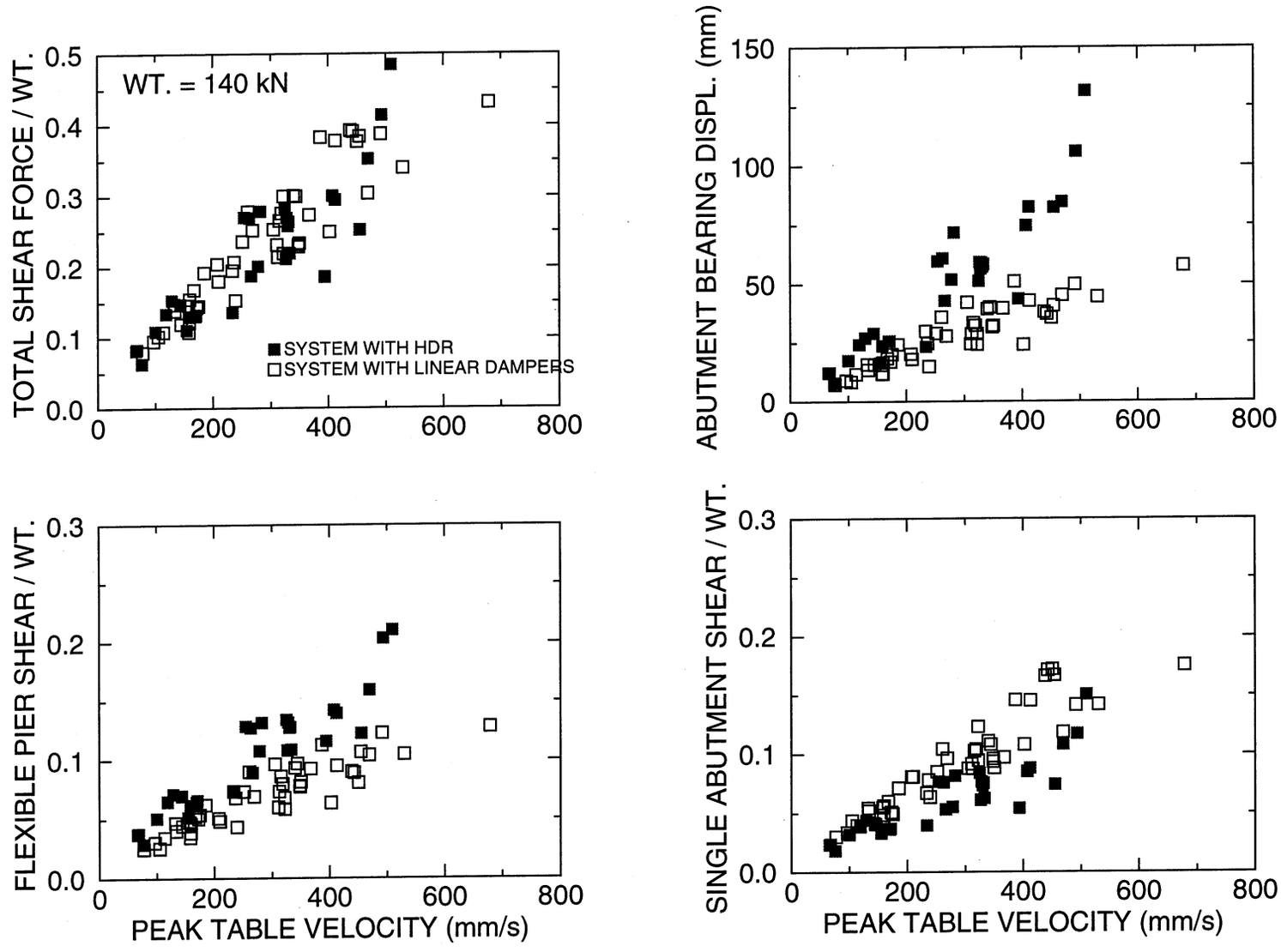

Figure 6-10: Comparison of Peak Response of Isolated Bridge with High Damping Elastomeric System and with Linear Viscous Damper System

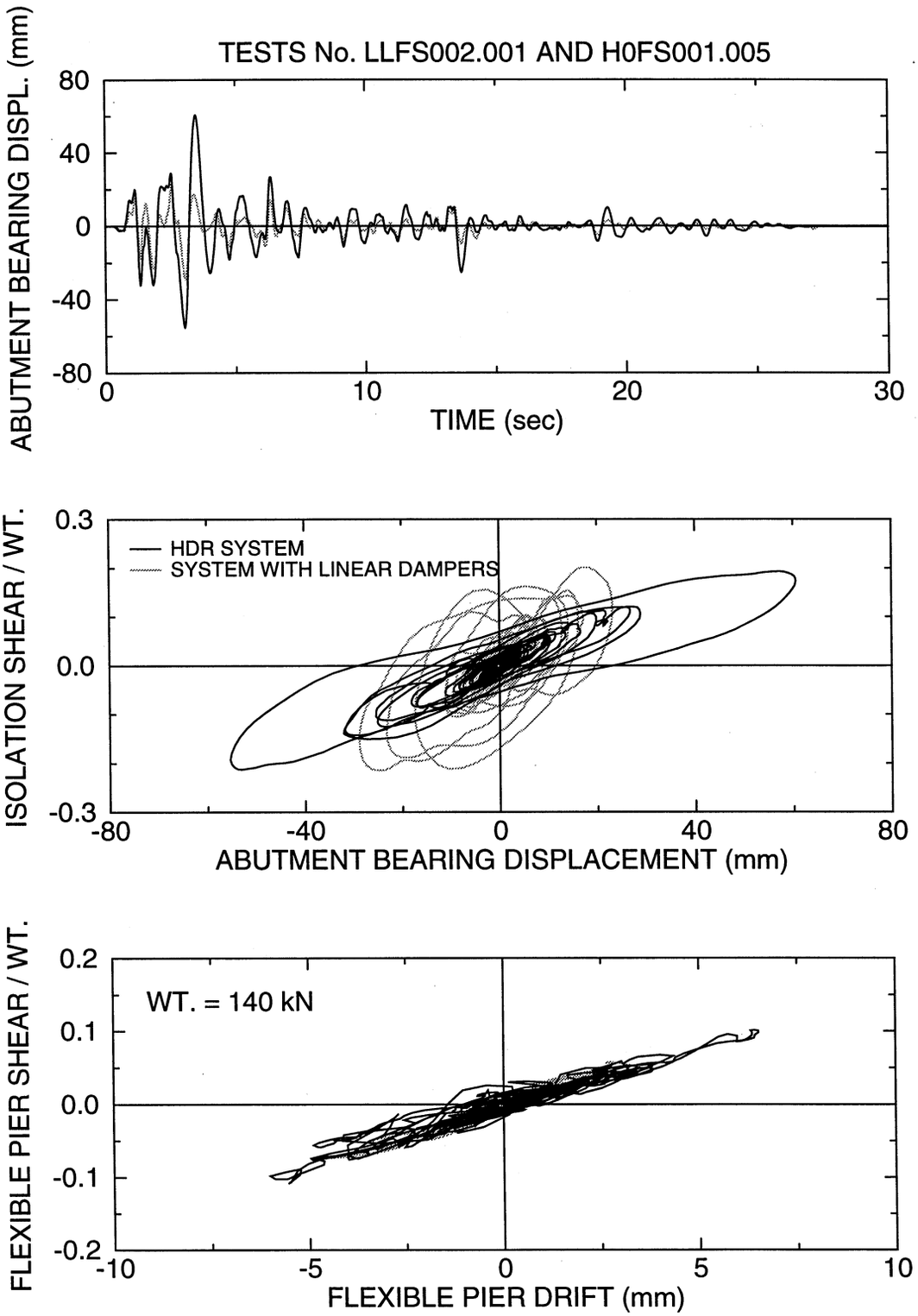

Figure 6-11: Comparison of Response of Isolated Bridge with High Damping Elastomeric System and with Linear Viscous Damper System for the El Centro S00E 200% Input

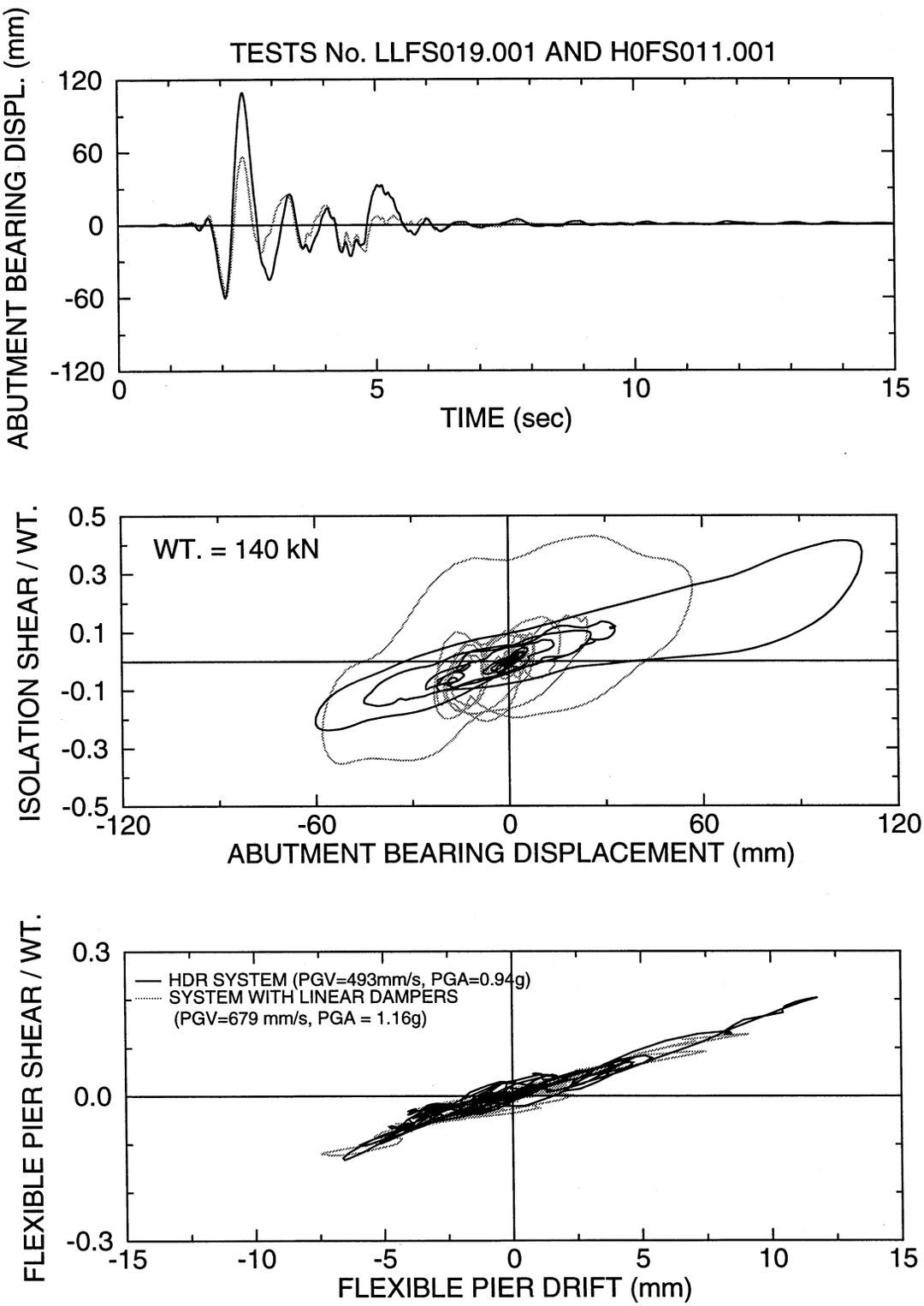

Figure 6-12: Comparison of Response of Isolated Bridge with High Damping Elastomeric System and with Linear Viscous Damper System for the Pacoima Dam S16E Input

Concluding, we note that the use of viscous damping in the isolation systems is particularly beneficial in reducing the displacement response. However, it should also be noted that for the tested systems, the resulting substructure forces for strong seismic excitation were large and of about the same magnitude whether the dampers were utilized or not. Reduction of these forces may be accomplished by the use of more flexible elastomeric bearings together with viscous dampers.

6.3.5 Comparison of Isolated Systems with Linear and Nonlinear Viscous Dampers

The nonlinear viscous dampers were designed to deliver the same force as the linear dampers at the velocity of 350 mm/s along the axis of the damper. For the angle of 45 degrees of placement of the dampers, this limit on velocity corresponds to approximately 495 mm/s relative velocity at the isolation system level in the longitudinal bridge direction. Such high relative velocities were not reached in the majority of tests of the isolated bridge with dampers. Accordingly, in most tests the nonlinear viscous dampers mobilized a substantially larger damping force than the linear dampers. The result was a further reduction in the bearing displacement at the expense of increased total shear force at the isolation system. Figure 6-13 presents a comparison of recorded isolation system loops of the two systems in identical or nearly so seismic excitations. These tests were selected to demonstrate the substantial effect of the nonlinear dampers to further reduce displacement and without or with minor increase in the peak isolation system force.

A different picture emerges in the comparison of loops obtained in motions characterized by near-fault conditions, which are presented in Figure 6-14. It is observed that in all three cases of input the bearing displacements are nearly the same for the systems with linear and with nonlinear dampers. We investigate this further by differentiating the records of damper displacements to obtain the peak damper velocities. They are presented in Table 6-2 together with measured values of the peak damper forces. Clearly, the achieved velocities exceed the limit of 350 mm/s for which the two dampers were designed to deliver the same damping force. The effect is that the nonlinear dampers mobilized lesser peak damping force than the linear ones as it is also evident in the loops of Figure 6-14. This provides an explanation for the observed behavior.

Table 6-2: Peak Damper Velocities and Forces in Tests with Motions Having Near-Fault Characteristics

INPUT MOTION	LINEAR DAMPERS				NONLINEAR DAMPERS			
	TEST No.	PEAK TABLE VEL (mm/s)	PEAK DAMPER VEL[1] (mm/s)	PEAK DAMPER FORCE[1] (kN)	TEST No.	PEAK TABLE VEL (mm/s)	PEAK DAMPER VEL[1] (mm/s)	PEAK DAMPER FORCE[1] (kN)
NORTHRIDGE NEWHALL360°	LLFS036.1	438	359	28.1	LNFS037.1	451	419	25.0
KOBE NS	LLFS039.1	450	386	31.3	LNFS039.1	448	461	25.8
PACOIMA DAM S16E	LLFS019.1	679	443	35.8	LNFS022.1	492	477	26.2

1: Each Damper (values in two dampers were slightly different; reported value is average)

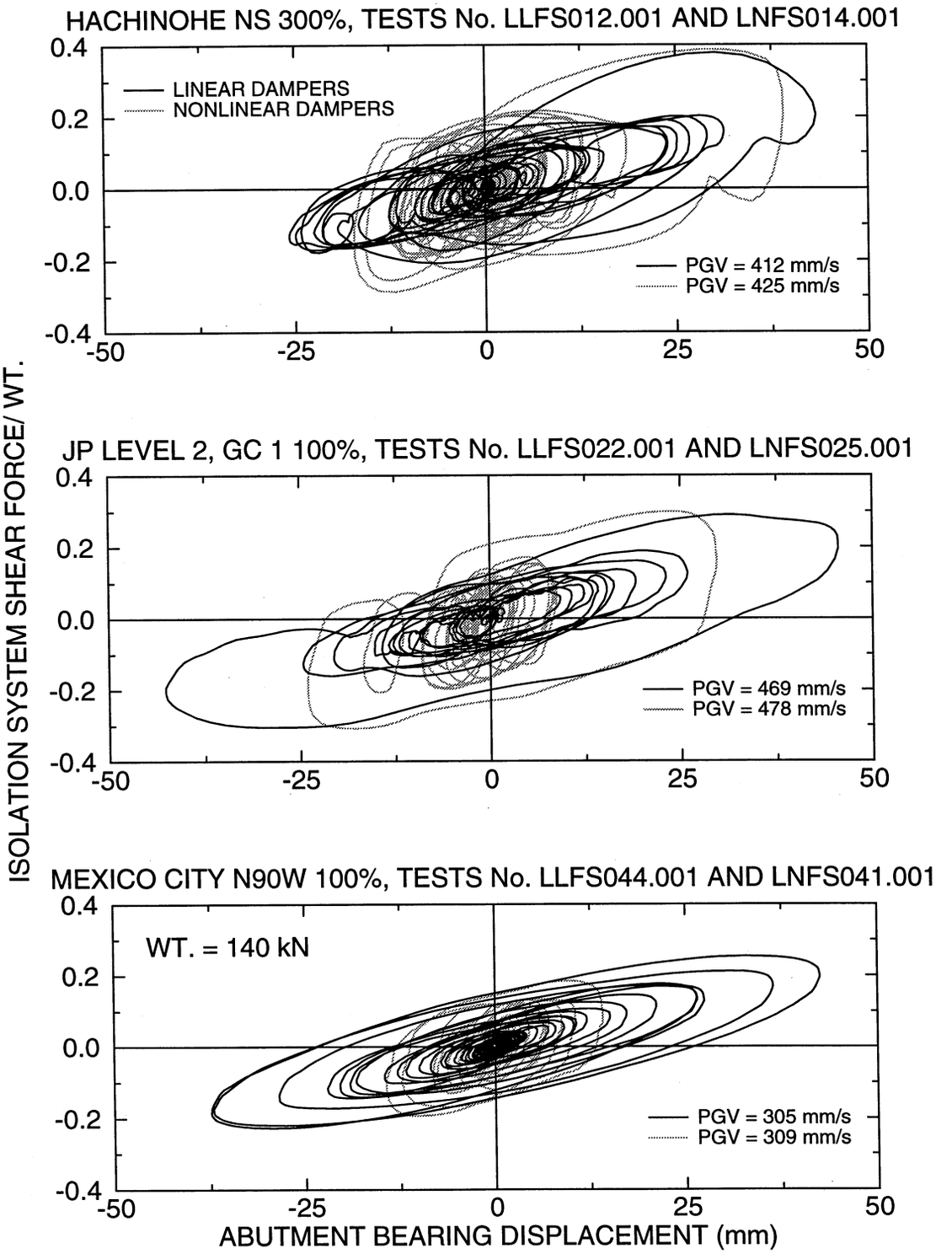

Figure 6-13: Comparison of Isolation System Force-Displacement Loops of Systems with Viscous Dampers in Selected Motions

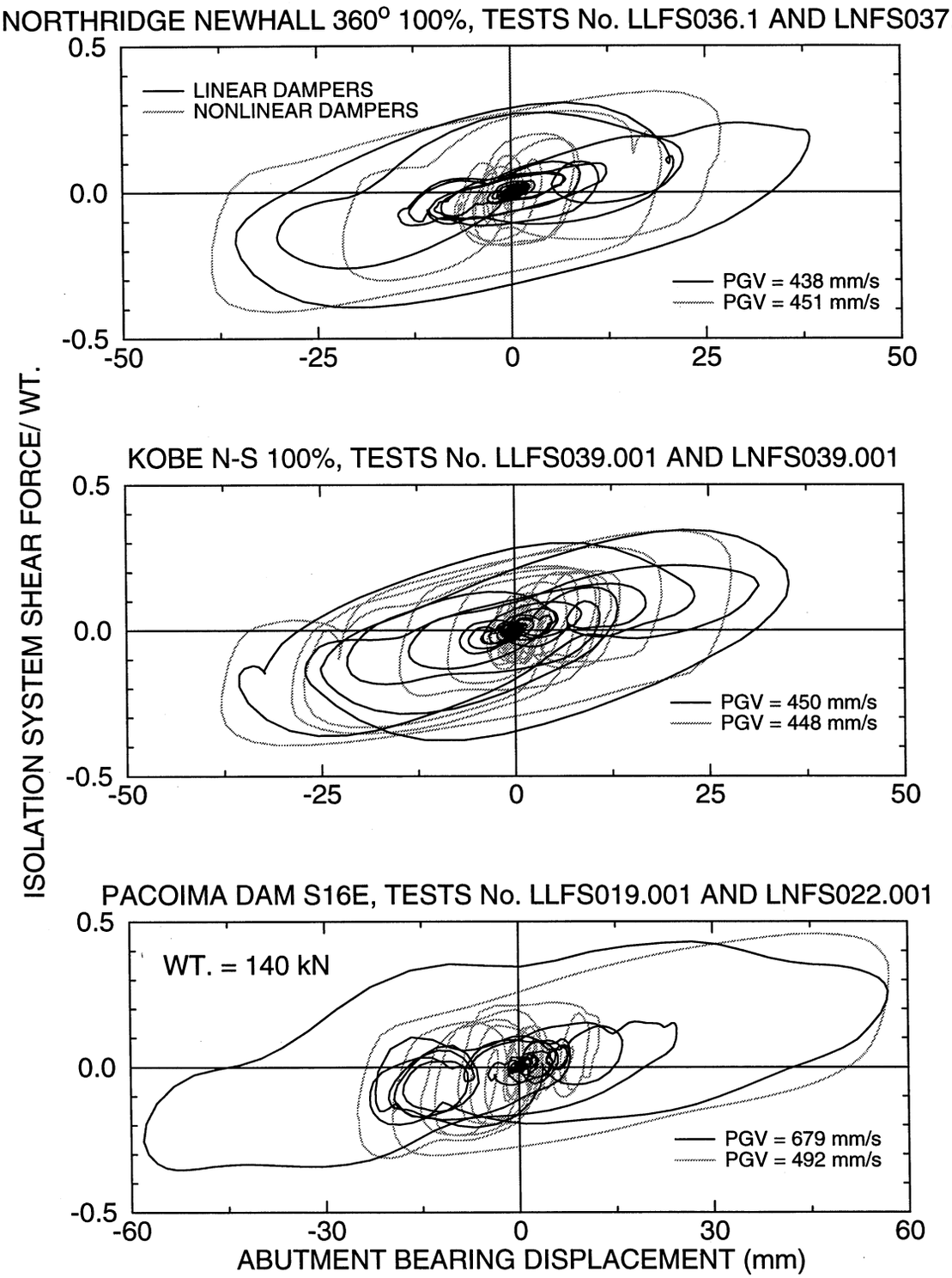

Figure 6-14: Comparison of Isolation System Force-Displacement Loops of Systems with Viscous Dampers in Selected Motions with Near-Fault Characteristics

An interesting observation may be made in the results of Figure 6-14. The system with the nonlinear dampers has a slightly larger peak isolation system force than the one with linear dampers, whereas both undergo about the same peak displacement. One may question the benefit offered by the nonlinear dampers. To discuss this we start with an explanation for this behavior. Simply, the nonlinear dampers mobilize a larger damping force at low velocities, that is, at displacements near their peak value. The result is obvious when considering that the isolation system force is the superposition of the damping and the restoring (from the bearings) forces.

The benefit, then, offered by the nonlinear dampers is to achieve a behavior comparable to that of the linear dampers with a lesser peak damping force (provided that velocities are large enough). The result is lower cost for the damper and connections, and lesser uncertainty in the value of peak damper force. It becomes now obvious that an optimal design of the nonlinear dampers is to have linear behavior for a range of low velocities (which, however, depends on the characteristics of the input motion) and nonlinear behavior for large velocities.

It is interesting to study the time histories of the bearing displacements for the two systems in the motions with near-fault characteristics, as shown in Figure 6-15. The following are observed:

(a) The peak response occurs as the result of some strong velocity shock in the input, which is preceded by input of lesser intensity.

(b) During excitation by the preceding input, the system with nonlinear dampers undergoes lesser displacement than the system with linear dampers due to the substantially larger damping force that the nonlinear dampers deliver.

(c) At the instant of application of the strong velocity shock, the two systems are at different stages of motion in terms of both displacement and velocity with respect to the table. That is, while the two systems are subjected to same, more or less, velocity shock, they undergo motion thereafter that depends on their characteristics (in this case they differ by the damping force they deliver) and their initial conditions (which are different due to the effects of the preceding seismic input). It just happens that they end up with the same peak displacement.

(d) In the motion that follows the peak response (primarily free vibration response), the system with nonlinear dampers undergoes progressively lesser displacement response due to its higher damping.

It should be clear now that the conditions of movement (the initial conditions) at the instant of application of the strong velocity shock have a significant impact on the peak response of the system. To elucidate this we present analysis results of a simple system subjected to ground shock. We consider a rigid mass supported by an isolation system which has linear elastic and viscous characteristics with period equal to 1.0 sec and damping equal to 0.30 (that is, very similar to the tested system with linear viscous dampers). It is subjected at the ground with half cycle of sinusoidal acceleration history of peak velocity equal to 0.5 m/s and duration equal to 0.2 sec. The relative displacement is numerically calculated on the assumption of zero initial conditions and then again with nonzero initial velocity conditions. The time histories of displacement are presented in Figure 6-16. The results clearly demonstrate the importance of initial conditions. It may be recognized that for this case of a linear-viscous system the total response is simply the superposition of the response due to the input for zero initial conditions and the free vibration response due to the initial conditions.

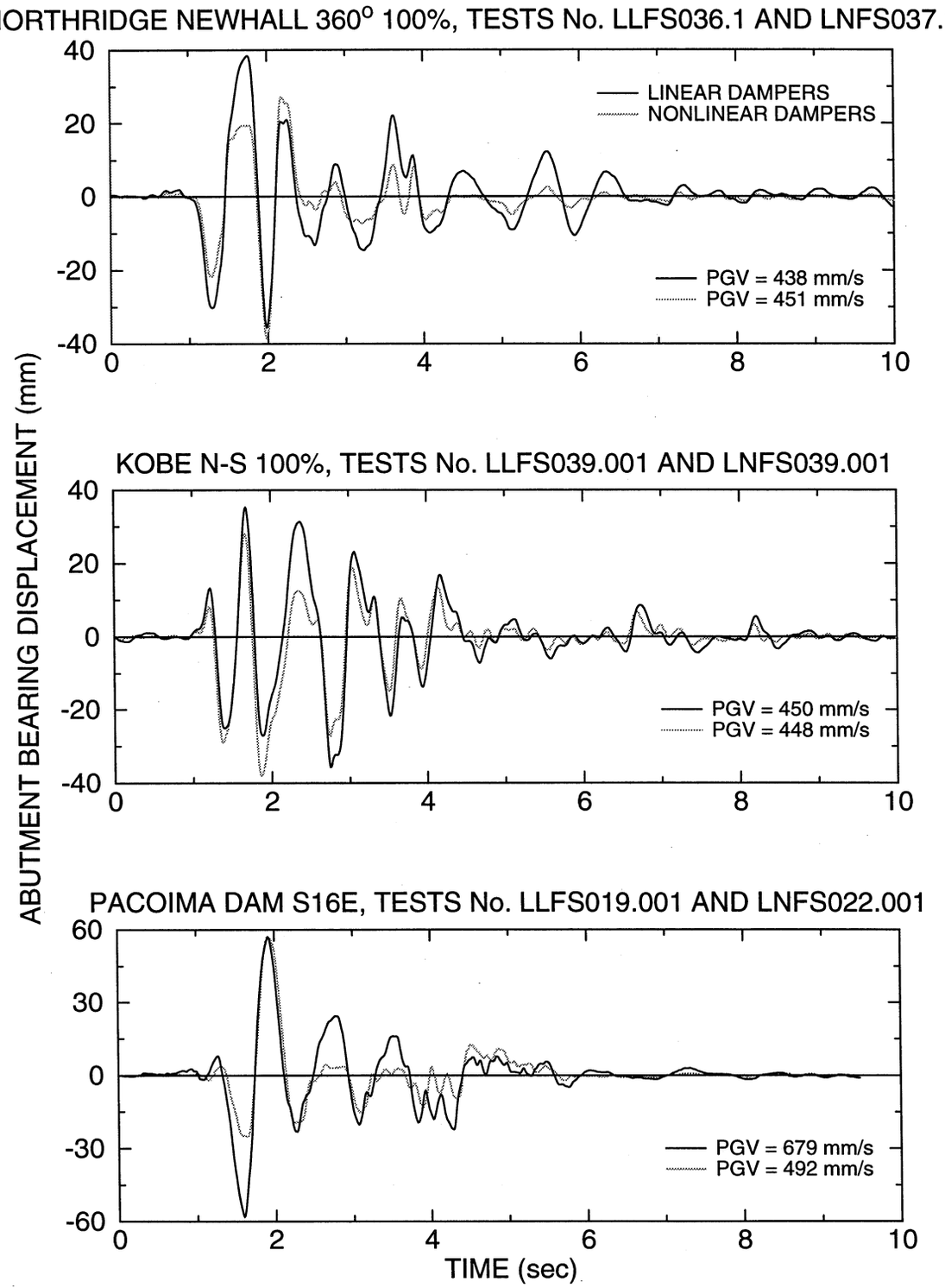

Figure 6-15: Comparison of Time Histories of Abutment Bearing Displacement of Systems with Viscous Dampers in Selected Motions with Near-Fault Characteristics

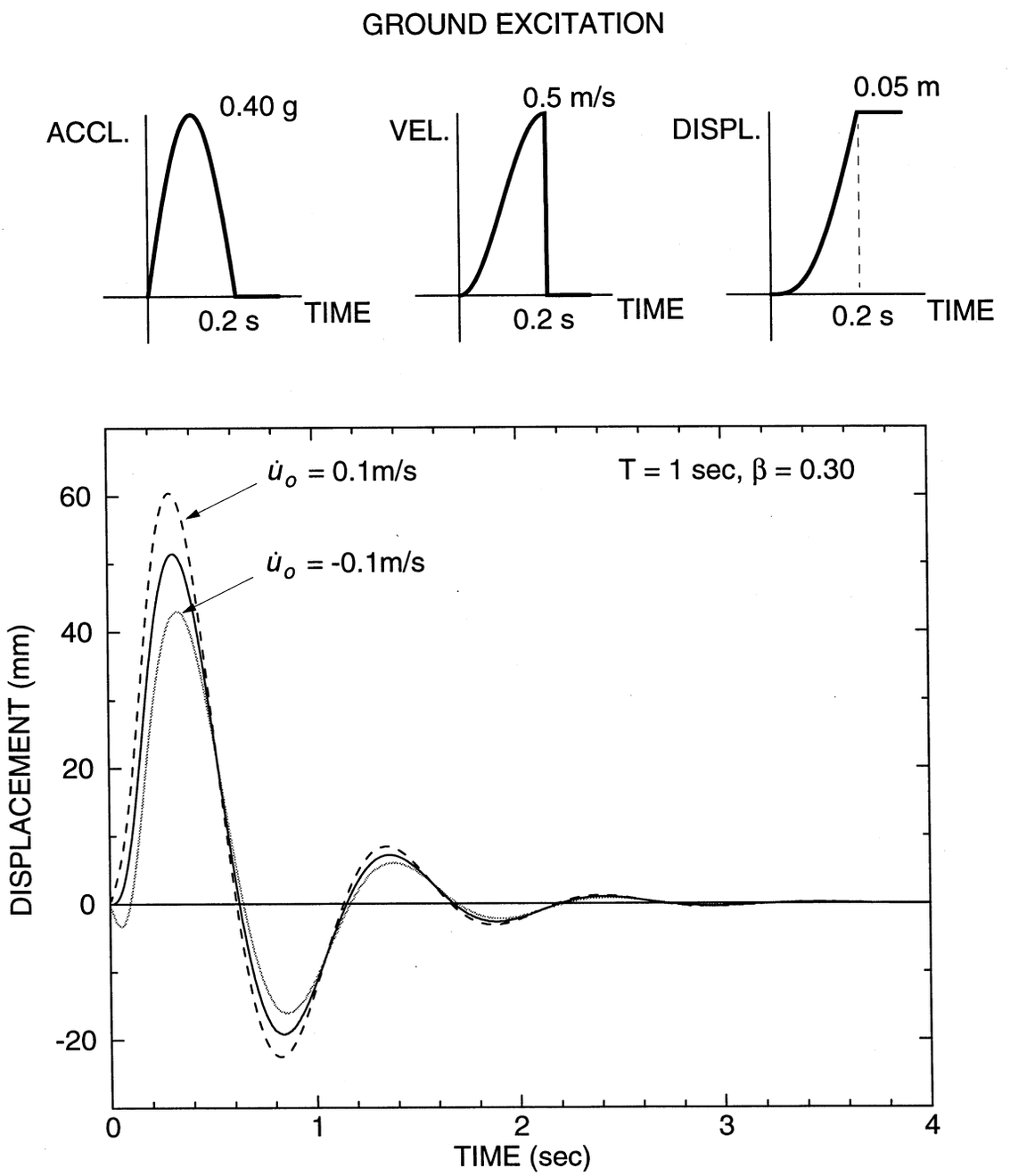

Figure 6-16: Calculated Displacement Histories of Linear-Elastic, Viscous Oscillator Subjected to 0.5 m/s Velocity Shock and Having Zero and Non-zero Initial Conditions of Velocity

6.3.6 Effect of Vertical Ground Acceleration

A number of tests were conducted with horizontal only excitation and then again with combined horizontal and vertical excitation. The results in Table 6-1 demonstrate minor effect on the isolation system force and displacement but some effect on the flexible pier shear force and drift. The effects seen on the drifts of the pier and abutment may be entirely the result of vertical vibration in the instruments used to measure displacement. The same phenomenon occurs in the instruments used to measure the bearing displacements but the effect is insignificant due to the much larger displacements of the bearings by comparison to the pier and abutment drifts. Moreover, the recordings of pier shear forces may have been also affected by the vertical excitation. Note that the strain gauge shear load cells in the columns of the flexible pier were calibrated in the absence of vertical load. Accordingly, the measurement may be affected by the vertical load, particularly when is variable.

Figures 6-17 and 6-18 present comparisons of the recorded response of two of the tested isolation systems in tests without and with the vertical ground component. The effects of vertical ground acceleration are clearly insignificant.

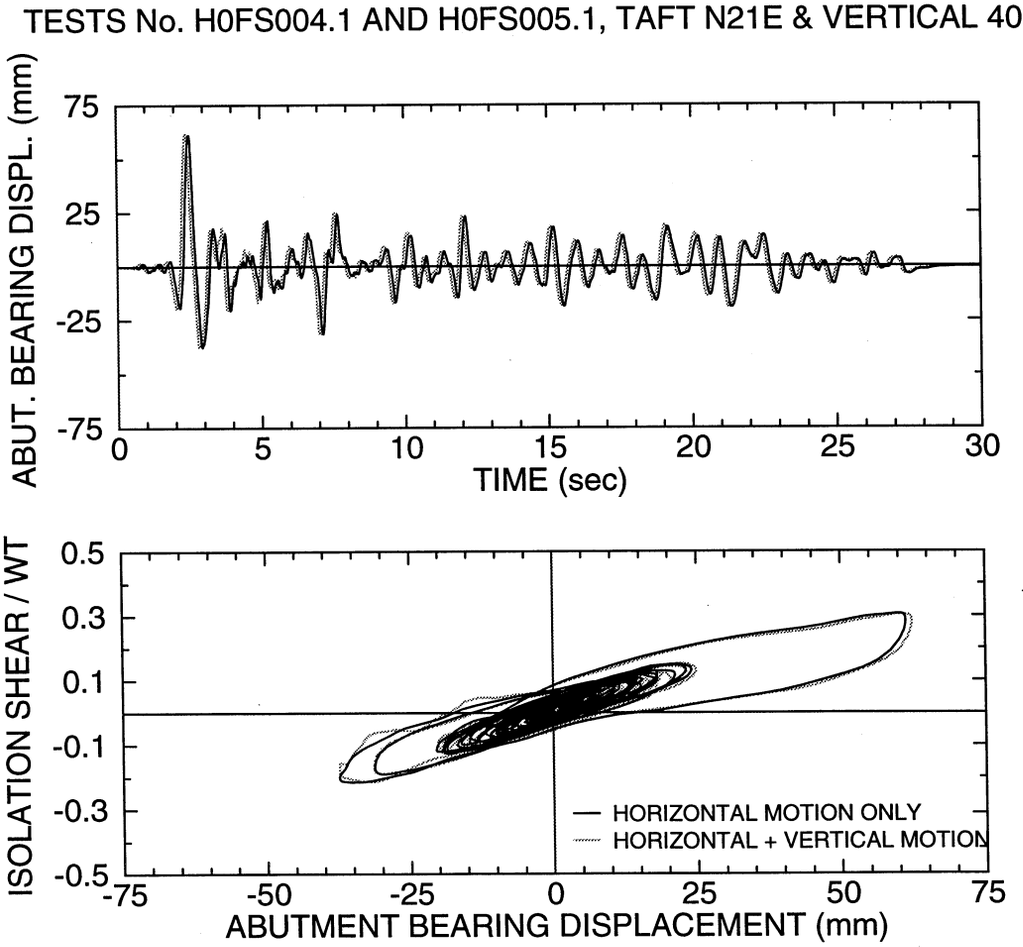

Figure 6-17: Effects of Vertical Acceleration on the Response of High Damping Elastomeric Isolation System

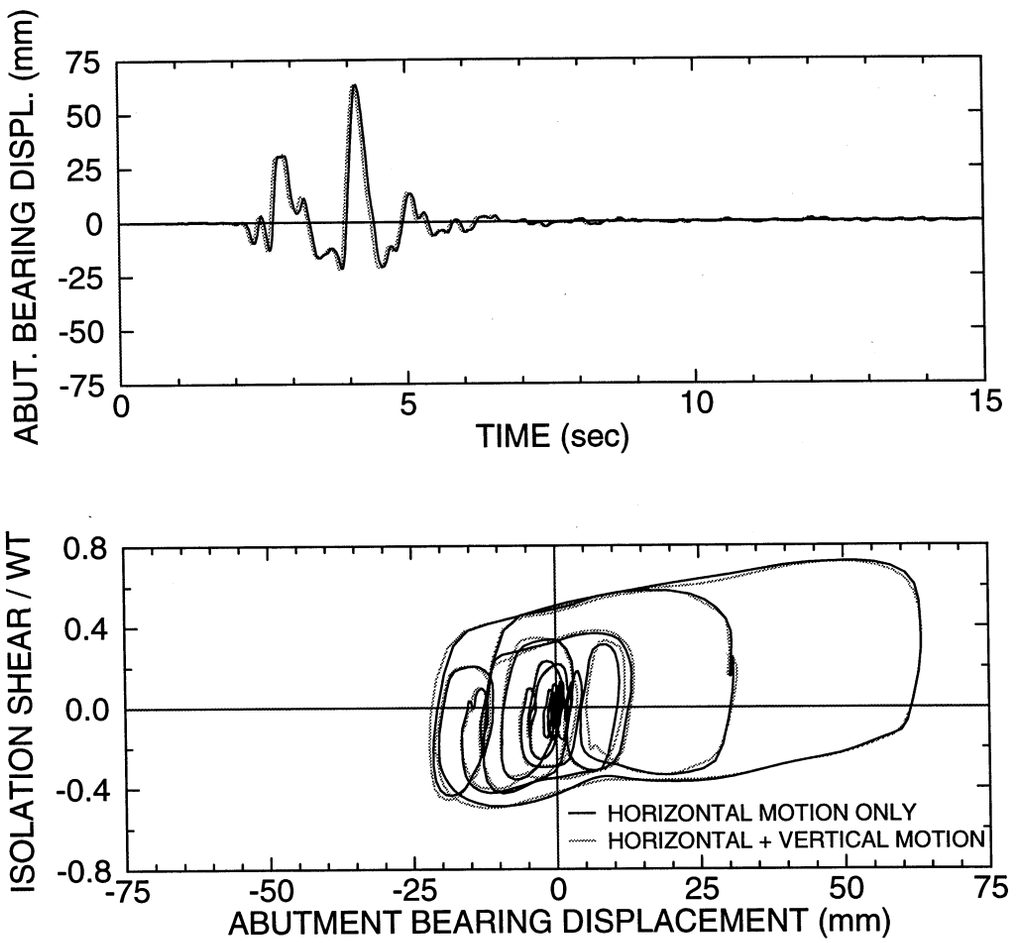

Figure 6-18: Effect of Vertical Acceleration on the Response of Elastomeric Isolation System with Nonlinear Dampers

It is of interest to note that significant vertical accelerations were recorded in the vertical direction at the bases of the abutment and flexible pier during these tests. For example, in the testing of the high damping elastomeric system with the Taft N21E and Vertical at 400% (test No. H0FS005.1) the vertical accelerations reached 0.69g. Figure 6-19 shows the recorded axial load on the abutment southeast bearing as function of the bearing horizontal displacement in this test and in the test without the vertical component of excitation (test No. H0FS004.1). The figures show the records for a time window corresponding to the maximum bearing exertion. It may be observed that there is a significant variation in the axial load which is consistent with the recorded peak vertical acceleration. The axial load varies between about 8 and 60 kN, whereas the gravity load for this bearing was 36.3 kN. Despite this significant variation we observe an insignificant effect on the response of the isolated bridge, which is primarily manifested as waviness in the loops as seen in Figure 6-17. It is also interesting to observe that the peak axial load on the bearing occurs at a substantial lateral displacement, which in this case is about 2/3 of the peak displacement.

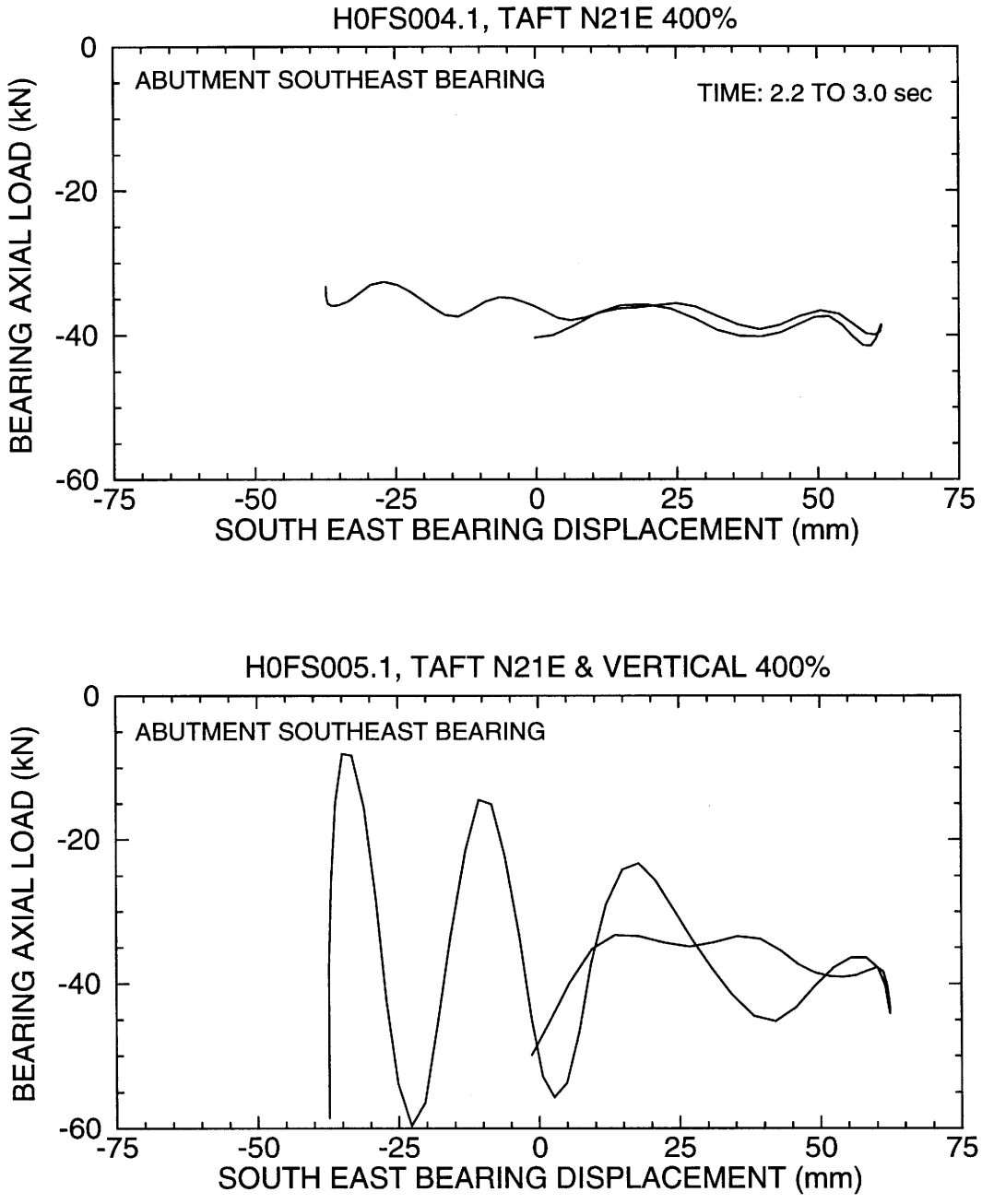

Figure 6-19: Recorded Axial Load on Bearing as Function of Lateral Displacement in Testing of the High Damping Elastomeric Isolation System

6.4 Conclusions

The testing of the elastomeric isolation systems allowed for a number of interesting observations. One is on the effect of the scragging phenomenon in the case of the high damping elastomeric systems. Consideration of only the scragged properties of the bearings and neglect of the likelihood of full recovery to the unscragged conditions could result in substantial underestimation of the inertia forces. In the conducted tests this underestimation was of the order of 30-percent. This results provides justification for the requirement in the 1997 AASHTO (American Association of State Highway and Transportation Officials, 1997) to consider the scragging and recovery phenomenon in the analysis of isolated bridges.

Damping in high damping elastomeric bearings is, as expected beneficial in the reduction of displacement and accordingly of inertia forces. This has been observed throughout the testing except for motions with strong near-source characteristics. In this case, the amount of damping provided by the high damping elastomeric bearings did not offer any advantage over the low damping elastomeric bearings in reducing either the displacement or the force response of the tested bridge. This phenomenon has been explained on the basis of different initial conditions in the motion of the two systems at the instant of application of the velocity shock in the near-fault seismic input. Stated differently, the additional damping provided by the high damping elastomeric system was insufficient to affect the response of the system in the seismic motions with strong near-source characteristics.

However, the addition of viscous damping, whether of linear or nonlinear nature, provided for a marked reduction in the displacement response without an increase in the isolation system force. It appears that significant added damping is needed in isolated structures at locations susceptible to seismic motions with strong near-source characteristics. The experiments provided data that in motions with strong near-source characteristics, such as the Pacoima Dam S16E input, added linear viscous damping of the order of 30-percent of critical are needed to reduce displacement to low levels. While the recorded displacements were exceptionally low, they were achieved at the expense of damper forces with horizontal components of the order of 25-percent of the deck weight.

The use of properly designed nonlinear dampers produces results comparable to those of the linear dampers in motions with strong near-source characteristics, however with lower peak damper forces. As seen fro example in Table 6-2, the nonlinear dampers operated at peak forces of about 10 to 20-percent lower than the peak forces in the linear dampers while the isolated bridge response in terms of the peak displacement and peak isolation system shear force were about the same. This represents the main advantage offered by the nonlinear dampers.

Another interesting observation made in the testing of the elastomeric isolation systems is the minor effect of the vertical ground acceleration on the response of these systems. While significant fluctuations in the axial load on the bearings were recorded, they had a negligible effect on the behavior of the system.

SECTION 7

ANALYTICAL PREDICTION OF RESPONSE OF TESTED BRIDGE

7.1 Introduction

The analytical prediction of the response of the tested bridge is presented for the case of the isolated configurations. This prediction was based on standard models which are commonly used to describe the behavior of the isolation system components. Specifically:

(a) The viscous damping devices were modeled by (4-6) and (4-7) as calibrated on the basis of component tests of the devices (see Figure 4-11).

(b) The elastomeric bearings were modeled as bilinear hysteretic elements based on test data at the relevant frequency, axial load and design displacement.

These simple analytical models resulted in responses which were in good agreement with the experimental response. Some difficulties were encountered in the prediction of the response of the high damping elastomeric isolation system. However, these difficulties were the result of the changing properties of the bearings during the scragging process and other unknown effects which, likely, are not typical of high damping elastomeric bearings. Nevertheless, the prediction of the response was, in general, with in the acceptable limits of $\pm$15-percent of the exact response.

7.2 Analytical Model of the Bridge

The analytical model of the bridge with an abutment and a flexible pier is shown in Figure 7-1. It is based on the model presented by Constantinou et al. (1993) and Tsopelas et al. (1994) for the same bridge but tested with different isolation systems. In this configuration the model has three degrees of freedom: (a) displacement of the deck with respect to the table (U_d), (b) displacement of the flexible pier top with respect to the table (U_p), and (c) the rotation of the flexible pier at its top (ϕ_p). The displacement and rotation at the top of the abutment are negligible and were ignored in the analysis.

In this model the deck and the pier top (consisting of the channel and the load cells) were assumed to be rigid blocks. The pier was modeled as a beam element of length L_p, moment of inertia I_p, and modulus of elasticity E_p. This beam element is fixed to the table and connected at the top to a rigid block of height h_{pc}, mass m_{pc}, and mass moment of inertia I_{pc}. Isolation elements connect the pier top and the deck. Moreover, isolation element connect the deck and the top of the rigid abutment.

Free body diagrams of the deck and the flexible pier are shown in Figure 7-2. The following equations of motion were derived by consideration of dynamic equilibrium of the deck and pier in the horizontal direction and the pier top in the rotational direction.

$$m_d(\ddot{U}_d + \ddot{U}_g) + F_{iso1} + F_{iso2} = 0 \tag{7-1}$$

$$m_{pc}(\ddot{U}_p + \ddot{U}_g - h_{cm}\ddot{\phi}_{pc}) + F_p - F_{iso1} = 0 \tag{7-2}$$

$$I_{pc}\ddot{\phi}_{pc} + M_p + F_p h_{cm} + F_{iso}(h_{pc} - h_{cm}) = 0 \tag{7-3}$$

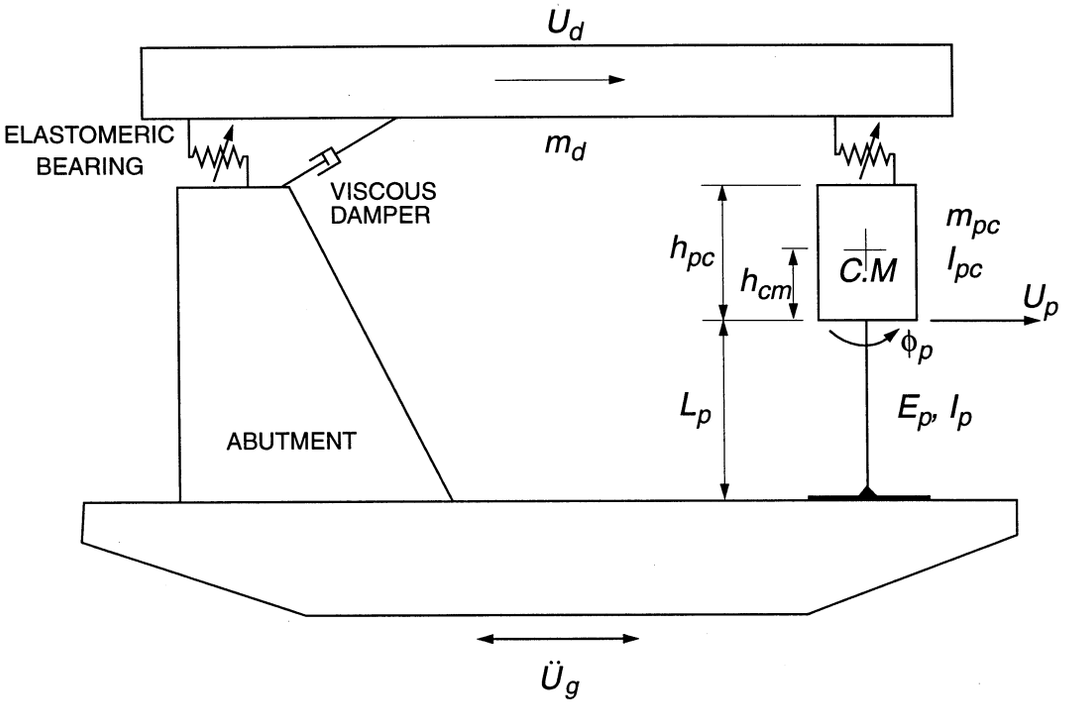

Figure 7-1: Model of the Isolated Bridge in the Longitudinal Direction

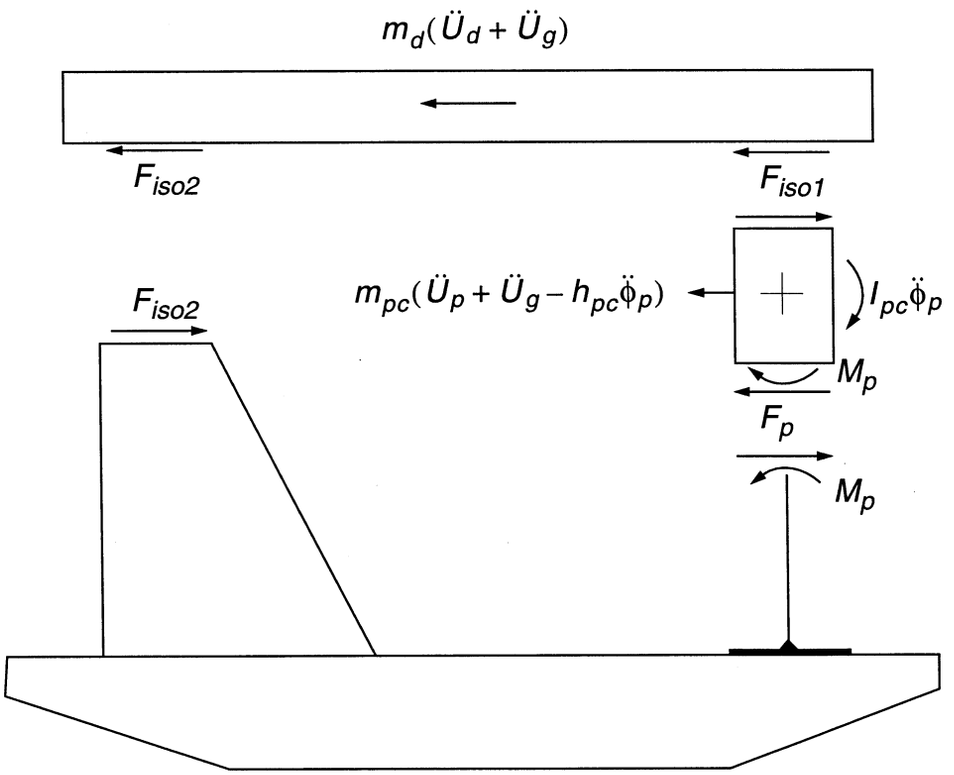

Figure 7-2: Free Body Diagram of Bridge Model

where F_{iso1} and F_{iso2} are isolation system forces (combined bearing forces and damper forces), and F_p and M_p are, respectively, the shear force and bending moment at the pier top. These forces are related to the displacement and rotation of the pier as follows:

$$\begin{Bmatrix} F_p \\ M_p \end{Bmatrix} = E_p I_p \begin{bmatrix} \frac{12}{L_p^3} & \frac{6}{L_p^2} \\ \frac{6}{L_p^2} & \frac{4}{L_p} \end{bmatrix} \begin{Bmatrix} U_p \\ \phi_p \end{Bmatrix} + \begin{bmatrix} C_p^1 & 0 \\ 0 & C_p^2 \end{bmatrix} \begin{Bmatrix} \dot{U}_p \\ \dot{\phi}_p \end{Bmatrix} \tag{7-4}$$

The first part of the (7-4) describes the elastic forces while the second part accounts for linear viscous energy dissipation in the piers.

7.3 Analytical Modeling of Isolation Components

7.3.1 Low Damping Elastomeric Bearings

The properties of the low damping elastomeric bearings are dependent on various testing conditions such as the shear strain (γ) and the frequency of testing (f). Component tests provide these properties for particular values of shear strain and frequency. In the current study, the isolated bridge had a natural frequency of 1.1 Hz. Thus, component tests performed at 1 Hz frequency form a suitable basis for developing the analytical model for the elastomeric bearings.

The elastomeric bearing is modeled by a bi-linear hysteretic model as illustrated in Figure 7-3. A suitable model for this behavior has been described in Section 3 (see equation 3-19) but is repeated herein for completeness. The lateral force F is given by:

$$F = \alpha \frac{F_y}{D_y} U + (1 - \alpha) F_y Z \tag{7-5}$$

or

$$F = K_d U + QZ \tag{7-6}$$

where F_y = the yield strength, D_y = the yield displacement, α = the ratio of post-elastic to elastic stiffness, K_d = post-elastic stiffness, Q = characteristic strength and U is the lateral displacement. Moreover, Z is a variable described by (3-15).

The values of K_d and Q can be computed from the values of effective stiffness K_{eff} and equivalent viscous damping β, which are obtained from the component testing. As described by AASHTO (American Association of State Highway and Transportation Officials, 1997), K_{eff} and β are calculated from the experimental data using:

$$K_{eff} = \frac{F_p - F_n}{\Delta_p - \Delta_n} \tag{7-7}$$

and

$$\beta = \frac{1}{2\pi} \times \frac{\text{EDC Area}}{K_{eff} D^2} \tag{7-8}$$

where Δ_p and Δ_n are the maximum positive and negative test displacements, respectively, and F_p and F_n are the maximum positive and maximum negative forces at the instance of displacements Δ_p and Δ_n, respectively. EDC is the minimum area of three hysteresis loops at the design displacement D. Values of K_{eff} and β for the tested low damping elastomeric bearing have been presented in Table 4-2.

.

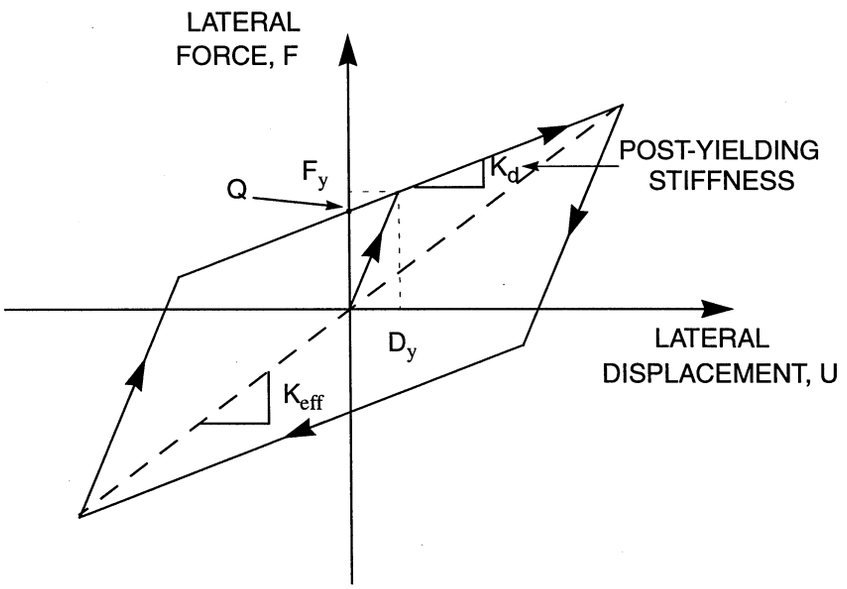

Figure 7-3: Bi-linear Hysteretic Model for Elastomeric Bearing

The post-elastic stiffness and characteristic strength of the bearing may be related to K_{eff} and β by (Constantinou and Reinhorn, 1997):

$$K_d = K_{eff}\left[1 - \frac{\pi\beta D}{2(D - D_y)}\right] \tag{7-9}$$

$$Q = \frac{\pi\beta K_{eff} D}{2(D - D_y)} \tag{7-10}$$

where D is the displacement of the bearing during testing.

Figure 7-4 presents experimental loops obtained in the testing of a low damping elastomeric bearing at three different displacement amplitudes corresponding to rubber shear strains of 33, 67 and 100-percent and at the relevant frequency of 1 Hz. Next to each loop, the values of effective stiffness, K_{eff}, and damping β are given (see Table 4-2). Equations 7-9 and 7-10 were used to obtain the related values of post-elastic stiffness and characteristic strength, which are also given in Figure 7-4. The analytical model is completed with an assumption on the yield displacement.

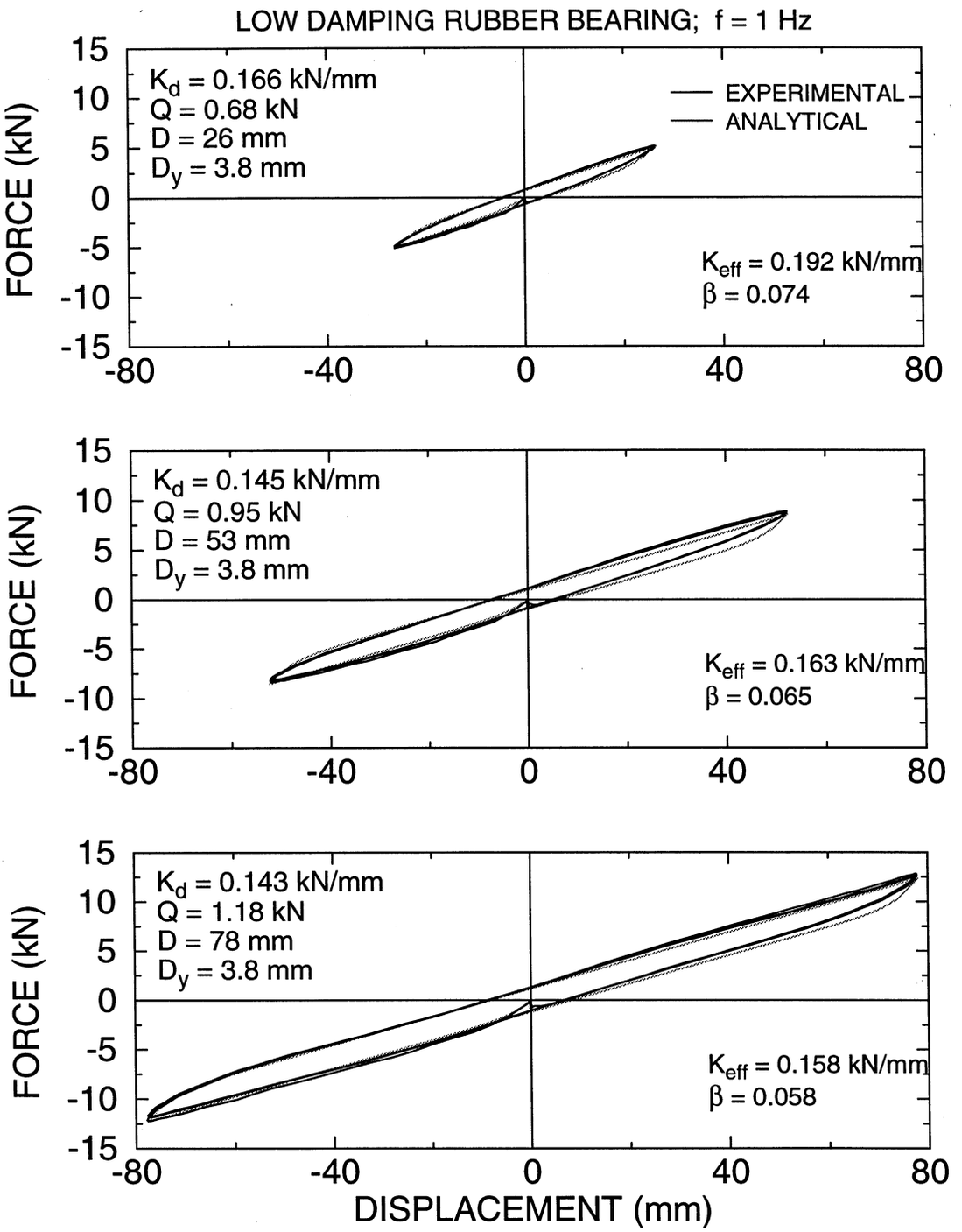

Figure 7-4: Comparison of Experimental and Analytically Constructed Hysteresis Loops of Low Damping Elastomeric Bearing

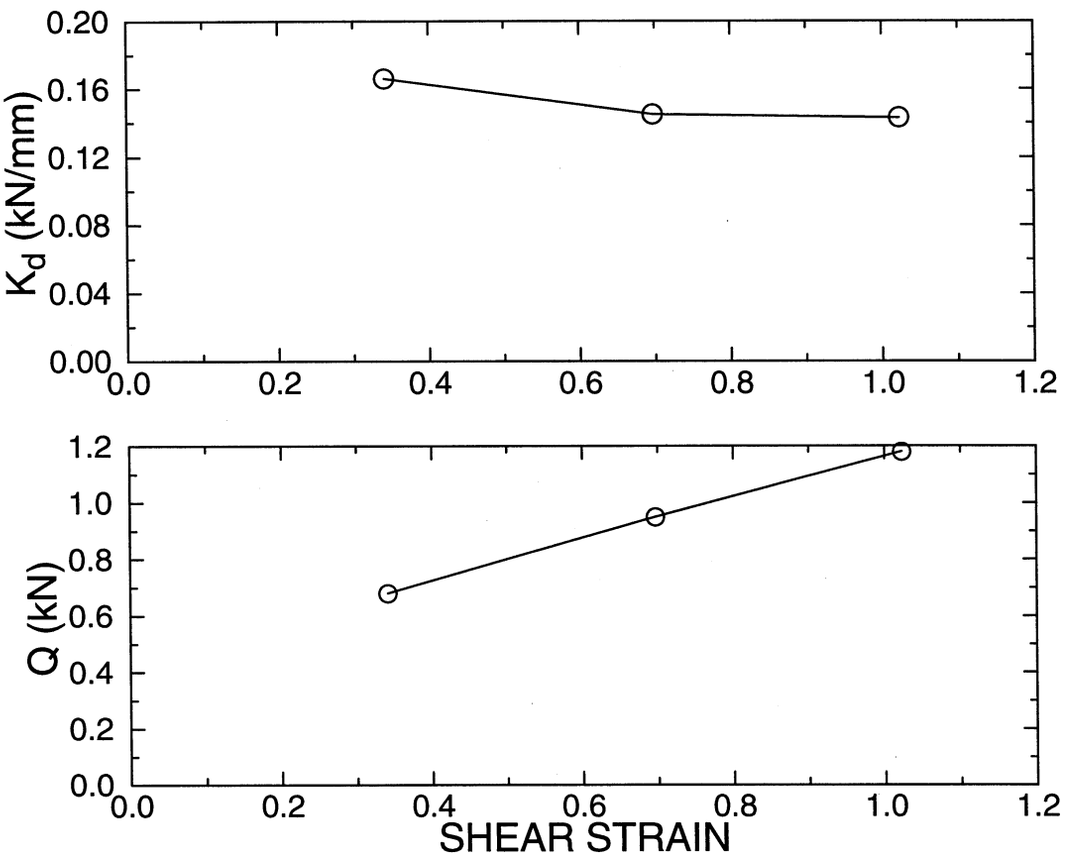

Figure 7-5: Post-elastic Stiffness and Characteristic Strength as Functions of Rubber Shear Strain

Herein we assumed that D_y is in the range of 0.05 to 0.1 times the total rubber thickness (Constantinou and Reinhorn, 1997). The hysteresis loops were analytically constructed using (7-5) and (3-15) with η=1 and are compared to the experimental ones in Figure 7-4. The prediction is very good but, of course, valid only at a specific displacement. Thus the model is expected to produce results of acceptable accuracy when the displacement is comparable to the one used in the calibration of the model.

A more accurate representation of the behavior of the bearing would require the description of the post-elastic stiffness and characteristic strength as functions of the displacement or, equivalently, the rubber shear strain γ. That is, (7-6) may be written as

$$F = K_d(\gamma)U + Q(\gamma)Z \tag{7-11}$$

where $K_d(\gamma)$ and $Q(\gamma)$ are variable of shear strain γ, as shown in Figure 7-5.

7.3.2 High Damping Elastomeric Bearings

The high damping elastomeric bearings exhibited properties that varied throughout the shake table testing program. Table 7-1 presents the sequence in which the testing of the high damping elastomeric system was conducted. The bearings were installed in the bridge model without any prior testing, that is, they exhibited during the first test unscragged properties. The effective stiffness of the bearings reduced with increasing testing and following the thirteenth test in the sequence it approximately attained the value measured in the component tests after scragging (see Section 4.3.2). Accordingly, a representative model for the behavior of the bearings for tests No. 14 and beyond in the sequence of Table 7-1 could be established on the basis of the results of components tests. This model was based on (7-5), (7-6) and (3-15) with the properties of post-elastic stiffness and characteristic strength determined by (7-9) and (7-10). Figure 7-6 presents experimental and analytically constructed loops for the tested high damping elastomeric bearing (No. 2, see Table 4-4). The calibration of the model was based on the data at frequency of 1.0 Hz and using a yield displacement D_y in the range of 0.05 to 0.1 of the total rubber thickness and a parameter η=1 (eq. 3-15). It may be seen that the model represents well the experimental results, except for the portion of the loop corresponding to the first quarter cycle. We will refer to this model as Model 2.

For the tests prior to test No. 14 in Table 7-1 the bearing exhibited a behavior which could not be established from the component testing. Rather a model was established on the basis of the properties determined in test No. H0FS001.3 with the El Centro S00E 200% input. The recorded loops for the abutment bearing were used. These loops are shown in Figure 4-7 (tests No. 3 for bearing No. 3 of batch No. 1). They correspond to a displacement of about 60 mm. Based on (7-5), (7-6) and (3-15), the parameters of this model are K_d = 0.102 kN/mm, Q = 2.72 kN, D_y = 3.8 mm and η = 1. We will refer to this model as Model 1.

Table 7-1: Sequence of Shake Table Tests Performed on High Damping Elastomeric Isolation System.

SEQUENCE NUMBER	TEST NUMBER	EXCITATION	ANALYTICAL MODEL USED
1	H0FS001.001	El CENTRO S00E 200% - 1	MODEL 1 BASED ON TEST No. H0FS001.003 K_{eff} = 0.148 kN/mm β = 0.18 K_d = 0.102 kN/mm Q = 2.72 kN D = 60 mm D_y = 3.8 mm
2	H0FS001.002	El CENTRO S00E 200% - 2	
3	H0FS001.003	El CENTRO S00E 200% - 3	
4	H0FS002.001	El CENTRO S00E H+V 200%	
5	H0FS003.001	TAFT N21E 200%	
6	H0FS004.001	TAFT N21E 400%	
7	H0FS005.001	TAFT N21E H+V 400%	
8	H0FS006.001	HACHINOHE NS 200%	
9	H0FS007.001	HACHINOHE NS 300% - 1	
10	H0FS008.001	AKITA NS 100%	
11	H0FS009.001	AKITA NS 200%	
12	H0FS010.001	PACOIMA S74W 100%	
13	H0FS011.001	PACOIMA S16E 100%	
14	H0FS001.004	El CENTRO S00E 200% - 4	MODEL 2 BASED ON COMPONENT TEST RESULTS (Figure 7-6)
15	H0FS007.002	HACHINOHE NS 300% - 2	
16	H0FS001.005	El CENTRO S00E 200% - 5	
17	H0FS012.001	El CENTRO S00E 100%	
18	H0FS013.001	El CENTRO S00E H+V 100%	
19	H0FS014.001	TAFT N21E 100%	
20	H0FS015.001	TAFT N21E H+V 100%	
21	H0FS016.001	MIYAGIKEN OKI 100%	
22	H0FS017.001	MIYAGIKEN OKI 200%	
23	H0FS018.001	MIYAGIKEN OKI 300%	
24	H0FS019.001	MIYAGIKEN OKI 500%	
25	H0FS020.001	JP LEVEL 1 GC 1 100%	
26	H0FS021.001	JP LEVEL 1 GC 2 100%	
27	H0FS022.001	JP LEVEL 1 GC 3 100%	
28	H0FS023.001	JP LEVEL 2 GC 1 100%	
29	H0FS024.001	JP LEVEL 2 GC 2 100%	
30	H0FS025.001	JP LEVEL 2 GC 3 100%	

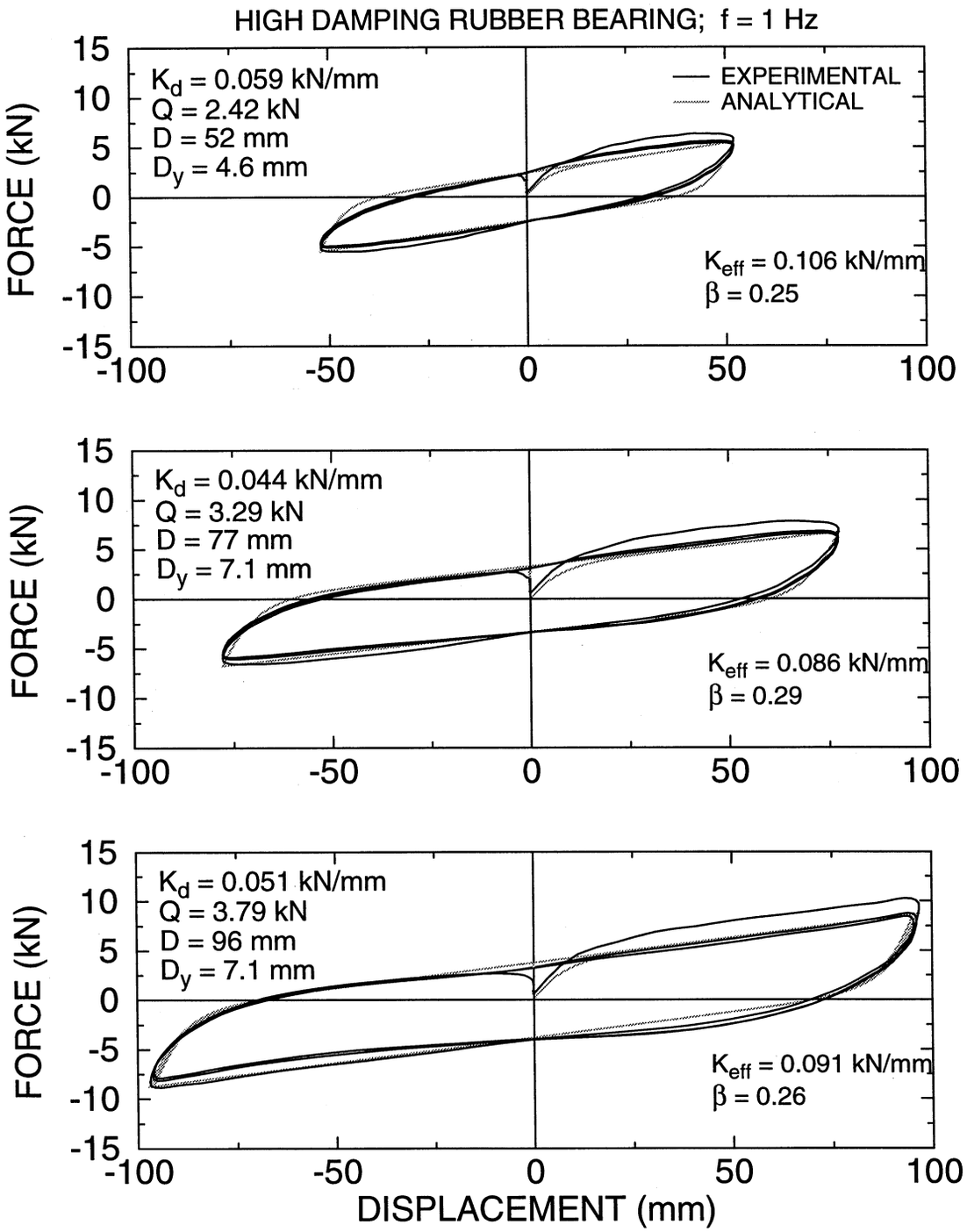

Figure 7-6: Comparison of Experimental and Analytically Constructed Hysteresis Loops of High Damping Elastomeric Bearing

7.3.3 Viscous Dampers

The viscous dampers were modeled by (4-6) and (4-7) with the parameters determined in the component tests. These parameters are shown in Figure 4-11. In the analytical model of the bridge, two dampers were placed at an angle of 45 degrees. That is, for the linear dampers the horizontal component of force in the isolation system (part of force F_{iso2} in Figure 7-2) is given by

$$F_{DH} = 2C_o\cos^2(45^o)\dot{U}_d = C_o\dot{U}_d \tag{7-12}$$

where $\dot{U}_d$ = velocity of deck with respect to the table. For the nonlinear dampers, the horizontal component of force is given by

$$F_{DH} = 2C_N\cos(45^o)\left|\dot{U}_d\cos(45^o)\right|^{\delta}\text{sign}(\dot{U}_d) \tag{7-13}$$

7.4 Comparison of Analytical and Experimental Results

The dynamic response of the isolated bridge model is described by (7-1) to (7-4). To complete the model, forces F_{iso1} and F_{iso2} need to be described. They are based on (3-15), (7-5), (7-12) and (7-13). Specifically,

(a) For the low and the high damping elastomeric system:

$$F_{iso1} = \alpha\frac{F_y}{D_y}(U_d - U_p) + (1-\alpha)F_yZ_p \tag{7-14}$$

$$F_{iso2} = \alpha\frac{F_y}{D_y}U_d + (1-\alpha)F_yZ_a \tag{7-15}$$

$$D_y\dot{Z}_p + 0.5\left|(\dot{U}_d - \dot{U}_p)\right|Z_p|Z_p|^{\eta-1} + 0.5(\dot{U}_d - \dot{U}_p)|Z_p|^{\eta} - (\dot{U}_d - \dot{U}_p) = 0 \tag{7-16}$$

$$D_y\dot{Z}_a + 0.5\left|\dot{U}_d\right|Z_a|Z_a|^{\eta-1} + 0.5\dot{U}_d|Z_a|^{\eta} - \dot{U}_d = 0 \tag{7-17}$$

(b) For the low damping elastomeric system with linear dampers:

$$F_{iso2} = \alpha\frac{F_y}{D_y}U_d + (1-\alpha)F_yZ_a + C_o\dot{U}_d \tag{7-18}$$

Moreover, equations (7-14), (7-16) and (7-17) apply.

(c) For the low damping elastomeric system with nonlinear dampers:

$$F_{iso2} = \alpha\frac{F_y}{D_y}U_d + (1-\alpha)F_yZ_a + 2C_N\cos(45^o)\left|\dot{U}_d\cos(45^o)\right|^{\delta}\text{sign}(\dot{U}_d) \tag{7-19}$$

Moreover, equations (7-14), (7-16) and (7-17) apply.

It should be noted that the same parameters in the model of the elastomeric bearings are used for both the pier and abutment locations despite the differences in their peak displacement response.

These differences were thought to have unimportant effect on the behavior of the bearings. However, depending on the level of deformation in the bearings, an appropriate model was selected among the three calibrated ones (see Figures 7-4 and 7-6) and used in the analysis. The solution of these equations was obtained by reducing them to a system of first order differential equations (variables: U_d, $\dot{U}_d$, U_p, $\dot{U}_p$, ϕ_{pc}, $\dot{\phi}_{pc}$ and Z_a and Z_p), and then numerically integrating the system by using an adaptive integration scheme with truncation error control.

The data used for the analytical model were: deck weight $m_d g = 140\ kN$, pier weight $m_p g = 8.9\ kN$, $L_p = 1.6\ m$, $h_{pc} = 413\ mm$, $h_{cm} = 98\ mm$, $I_{pc} = 38.22\ kN\ s^2\ mm$, $E_p = 200000\ MPa$, $I_p = 3.022 \times 10^{-5}$ (2 AISC TS 6x6x5/16). Based on these data, the fundamental period of each pier, in its free cantilever position, was calculated to be $0.092\ s$. This is in close agreement with the experimentally determined value of $0.096\ s$.

Damping in the pier was described by the second term in (7-4). The second mode of the pier was neglected, thus C^2_p in (7-4) was set to zero. The constant C^1_p was assigned a value equal to $0.0062\ kNs/mm$, which resulted in a damping ratio of 5-percent of critical in the fundamental mode of the free cantilever pier, which is consistent with the experimental data.

Figures 7-7 to 7-31 present comparison of experimental and analytical results on the response of the tested bridge model. The compared response quantities are:

(a) Time history of the abutment bearings,
(b) Loops of shear force versus bearing displacement at the abutment and pier locations, and
(c) Time history of pier top acceleration (the experimental acceleration is the average of the measurements by instruments 17 and 18 of Table 4-5).

Concentrating on Figures 7-7 to 7-24 which apply for the low damping elastomeric isolation system without and with viscous dampers, we observe an overall good analytical prediction of the response. In general the prediction of the peak displacement and peak isolation system force is within about 15-percent of the experimental value which is believed to be an acceptable margin of error. Specifically, the 1997 AASHTO (American Association of State Highway and Transportation Officials, 1997) contains in the Commentary C8.2.1 an indirect statement on the 15-percent acceptable range.

For the case of high damping elastomeric system, Figures 7-25 to 7-29 were based on the analytical Model 1, whereas Figures 7-30 and 7-31 were based on Model 2. In general, the analytical prediction is not as good as in the case of the other tested systems. While the displacement response is predicted (mostly overpredicted) within about a 20-percent error, there is clear evidence that the behavior of the bearings is not properly represented by the utilized bilinear hysteretic model. For example, in Figure 7-27 the bearings at the abutment side exhibit stiffening behavior at a level of displacement not observed in the component testing. The origin of this behavior is unknown. We should note that this behavior may not be characteristic of typical high damping elastomeric bearings but may rather be a manifestation of the improper curing of the bearings, the observed creep problems and the conditions of operations of the bearings due to their small scale.

Nevertheless, we should emphasize the need for the development of analytical models for elastomeric bearings which account for the phenomena of change of the mechanical properties during movement (that is, the effect of history of loading), stiffening at large displacements, recovery, etc. Currently available models (for example, Tsopelas et al., 1994b, Kikuchi and Aiken, 1997) are simply arbitrary mathematical constructions that require extensive data for calibration. The interest is in the development of mathematical models based on fundamental principles and rational mechanics.

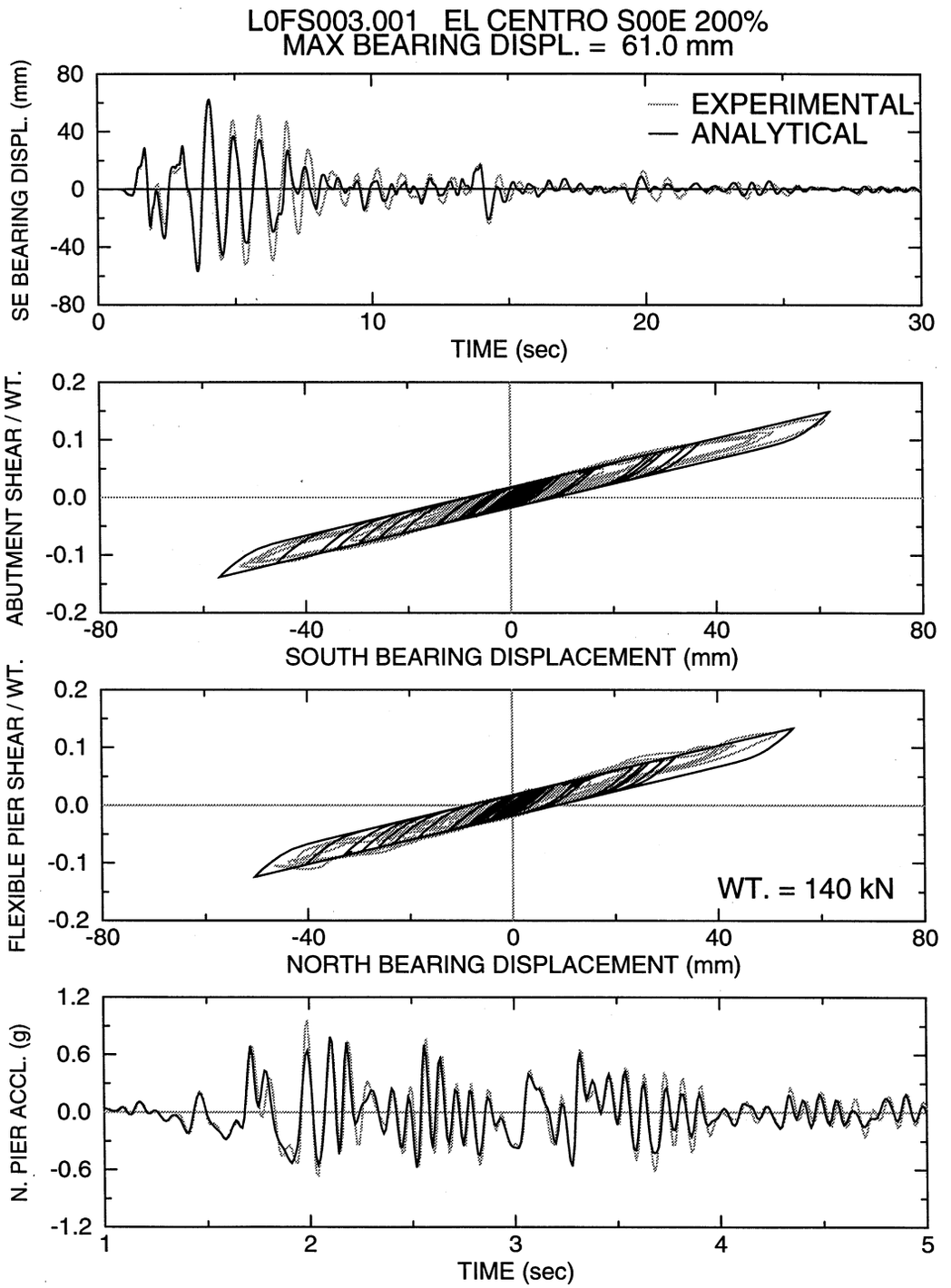

Figure 7-7: Comparison of Experimental and Analytical Results of Low Damping Elastomeric Isolation System in El Centro S00E 200% Test

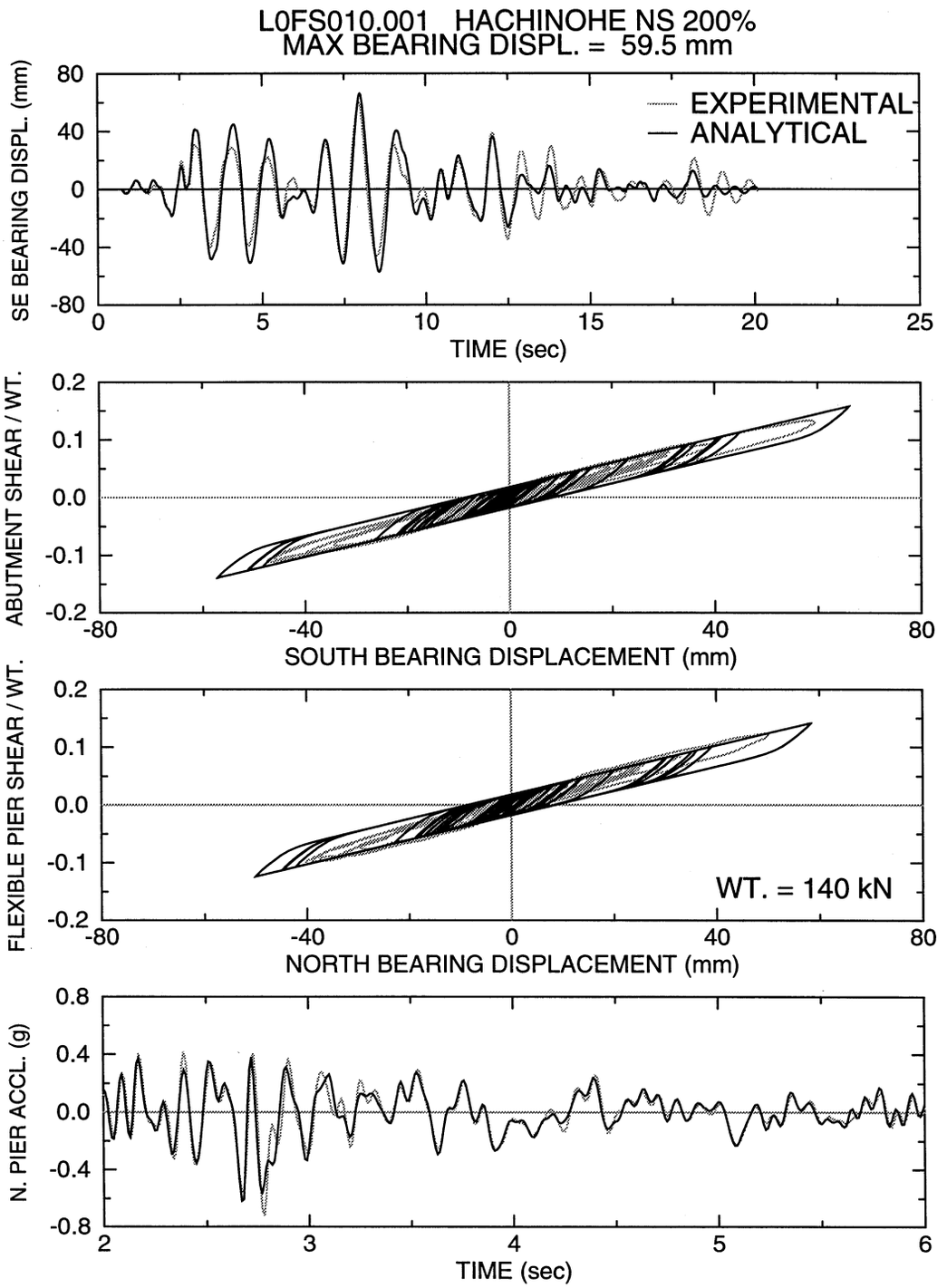

Figure 7-8: Comparison of Experimental and Analytical Results of Low Damping Elastomeric Isolation System in Hachinohe NS 200% Test

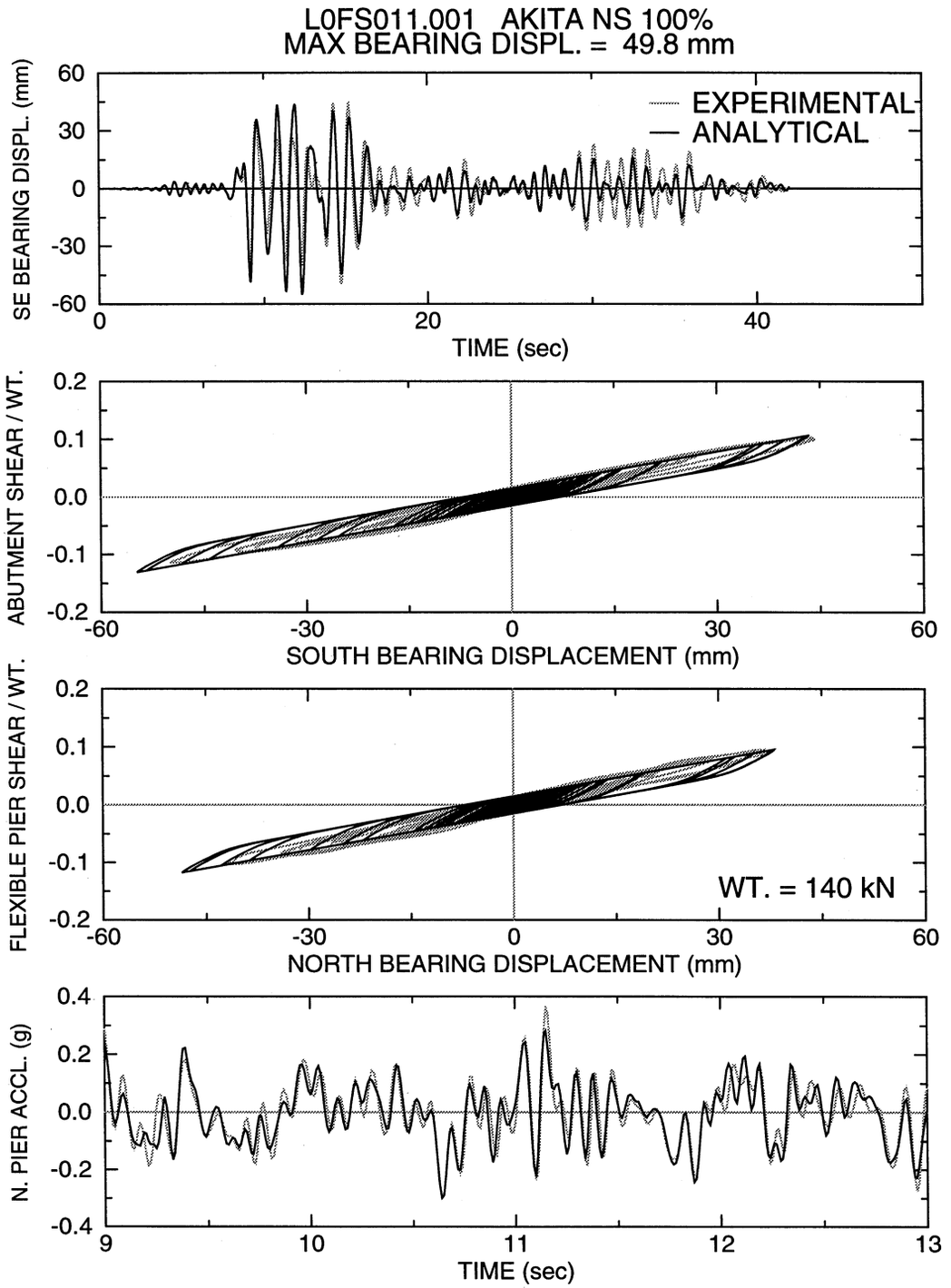

Figure 7-9: Comparison of Experimental and Analytical Results of Low Damping Elastomeric Isolation System in Akita NS 100% Test

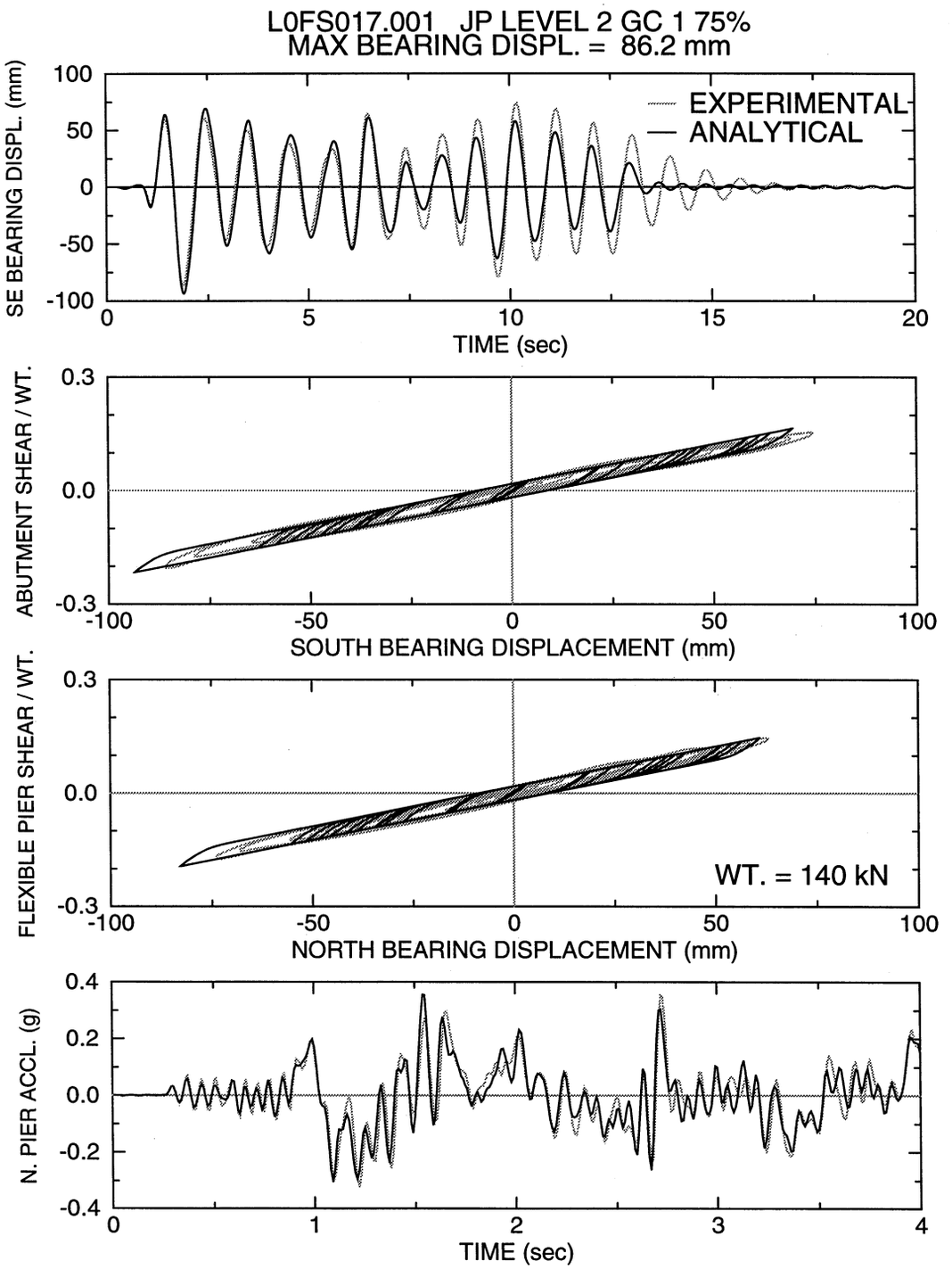

Figure 7-10: Comparison of Experimental and Analytical Results of Low Damping Elastomeric Isolation System in Japanese Level 2 GC 1 75% Test

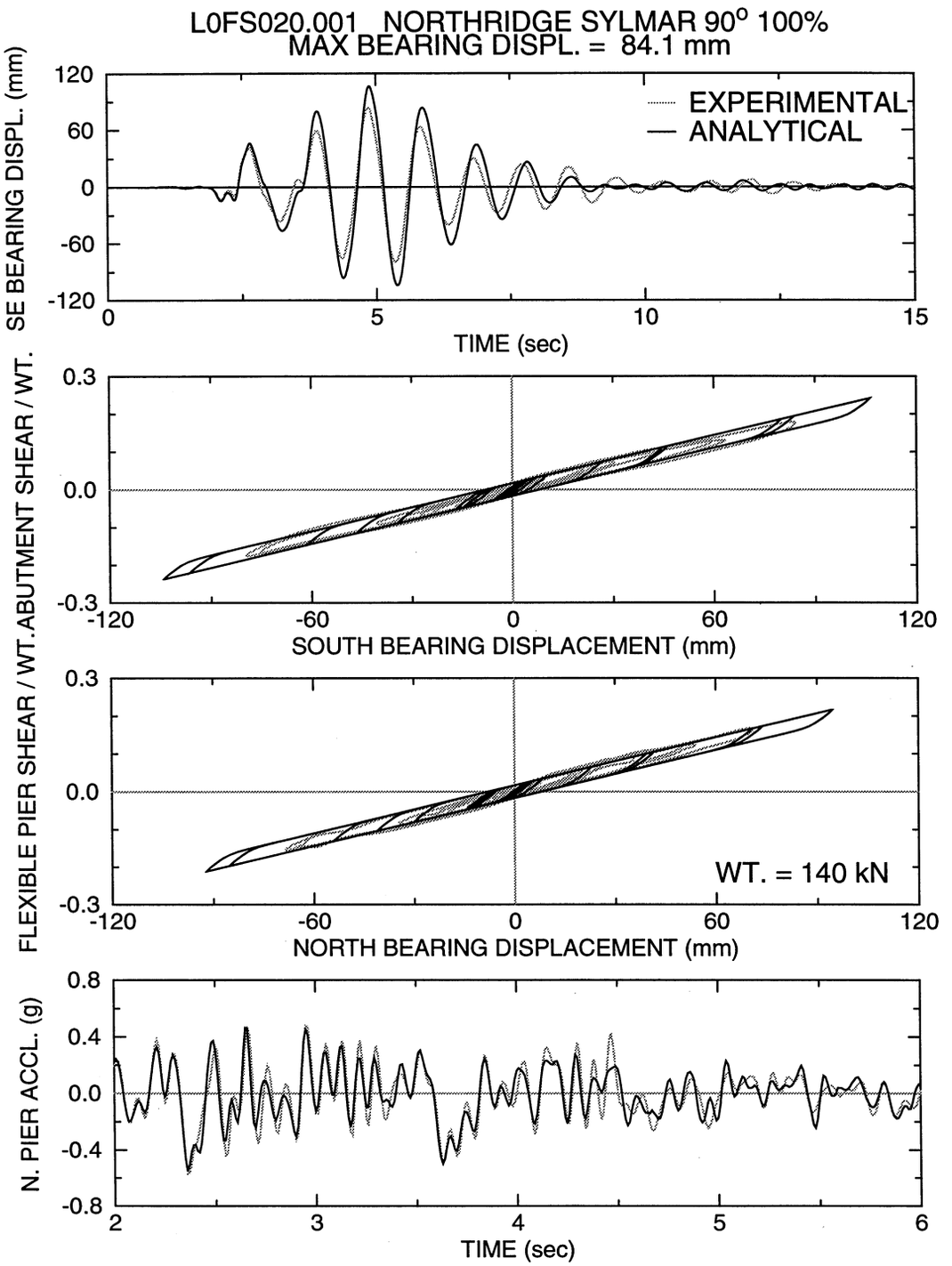

Figure 7-11: Comparison of Experimental and Analytical Results of Low Damping Elastomeric Isolation System in Northridge Sylmar 90° 100% Test

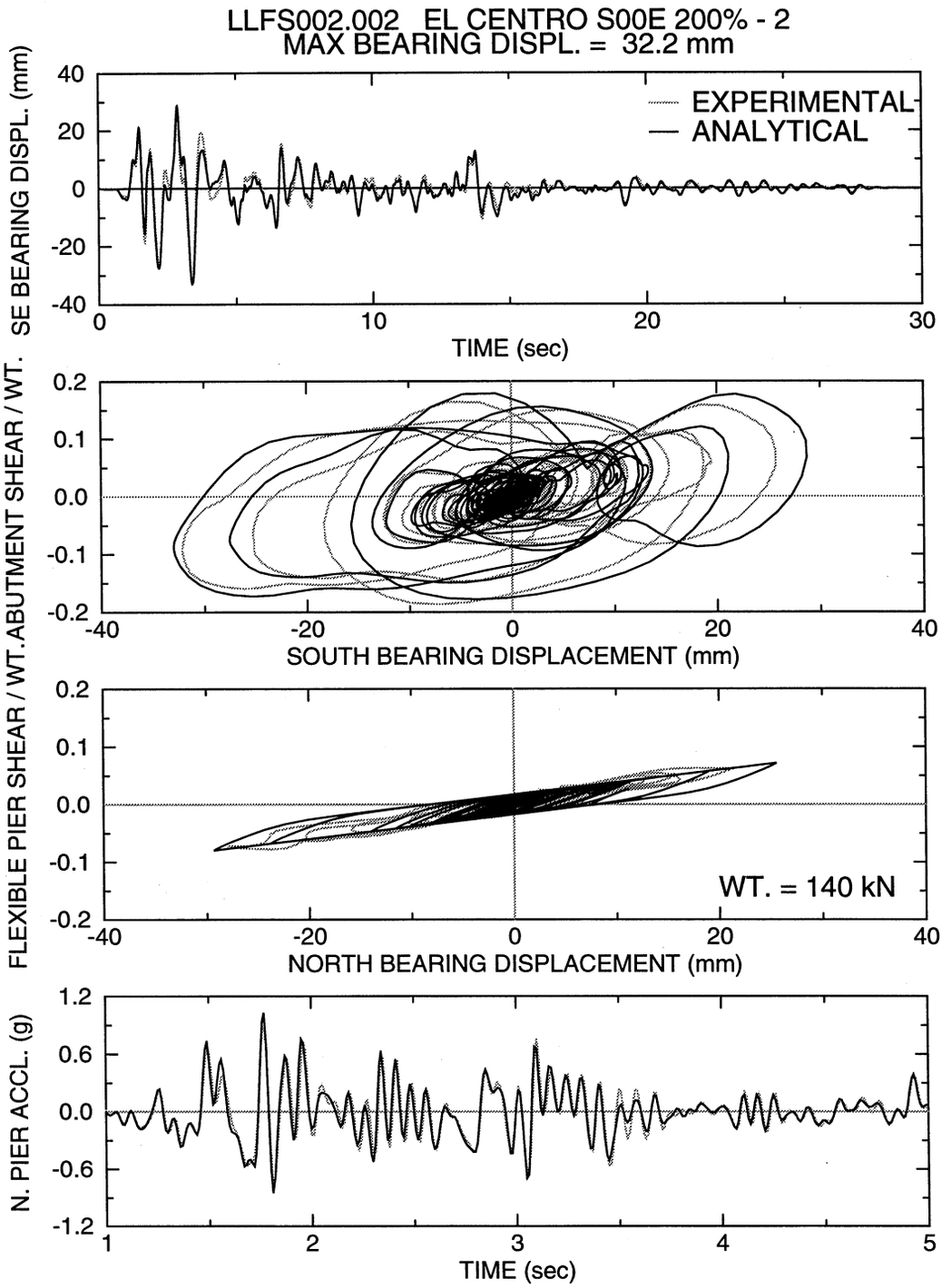

Figure 7-12: Comparison of Experimental and Analytical Results of Low Damping Elastomeric Isolation System with Linear Viscous Dampers in El Centro S00E 200% Test

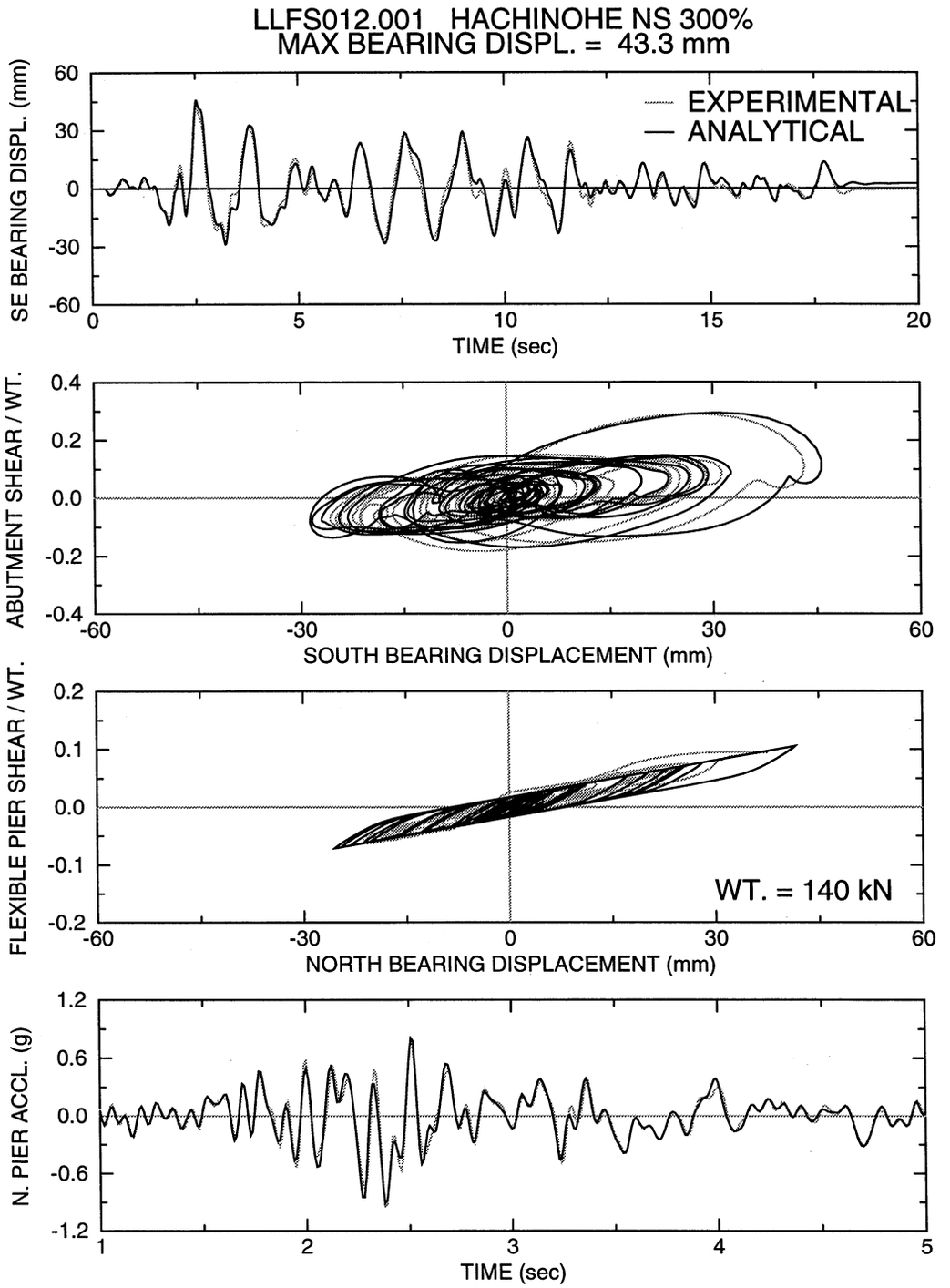

Figure 7-13: Comparison of Experimental and Analytical Results of Low Damping Elastomeric Isolation System with Linear Viscous Dampers in Hachinohe NS 300% Test

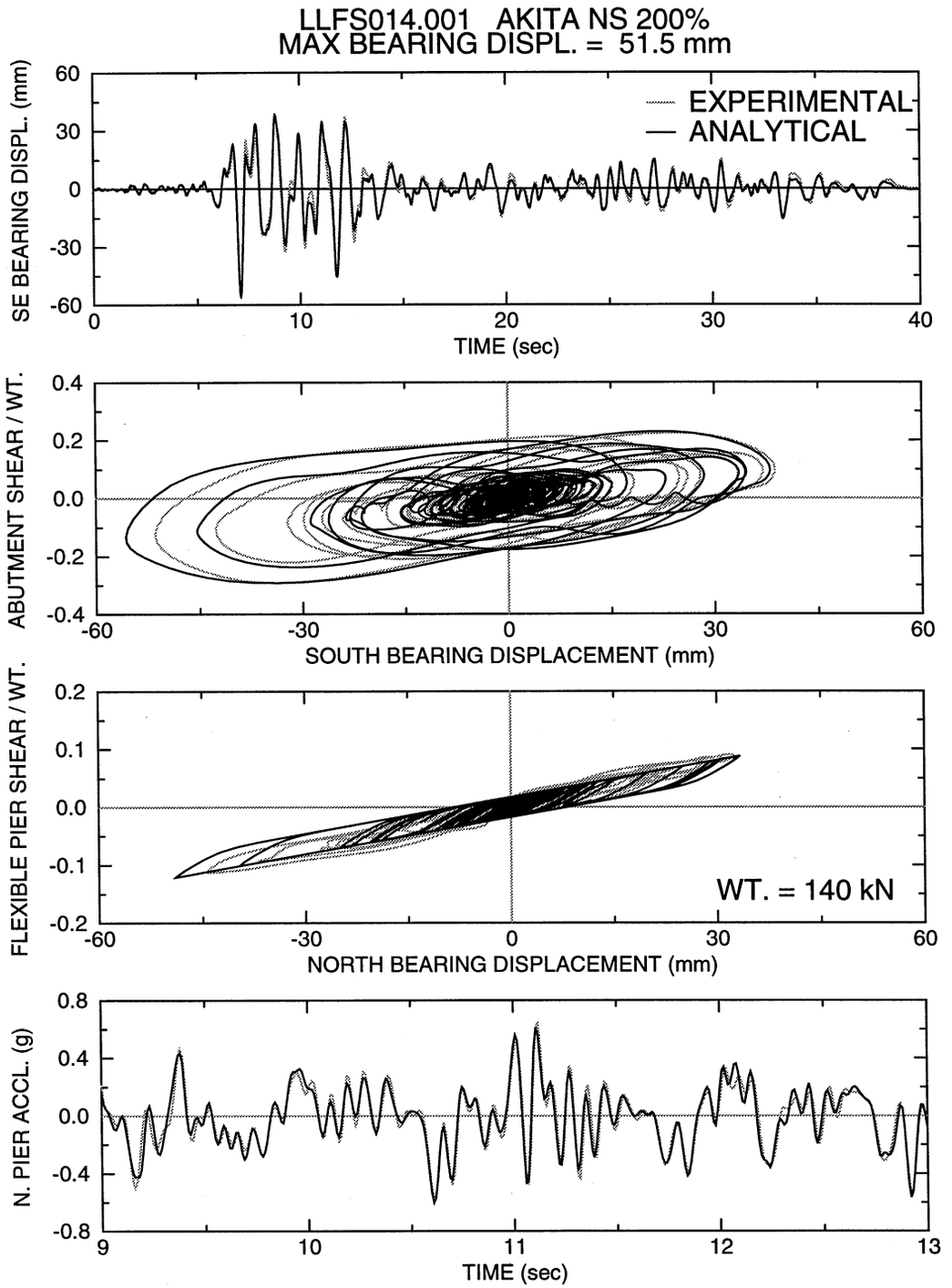

Figure 7-14: Comparison of Experimental and Analytical Results of Low Damping Elastomeric Isolation System with Linear Viscous Dampers in Akita NS 200% Test

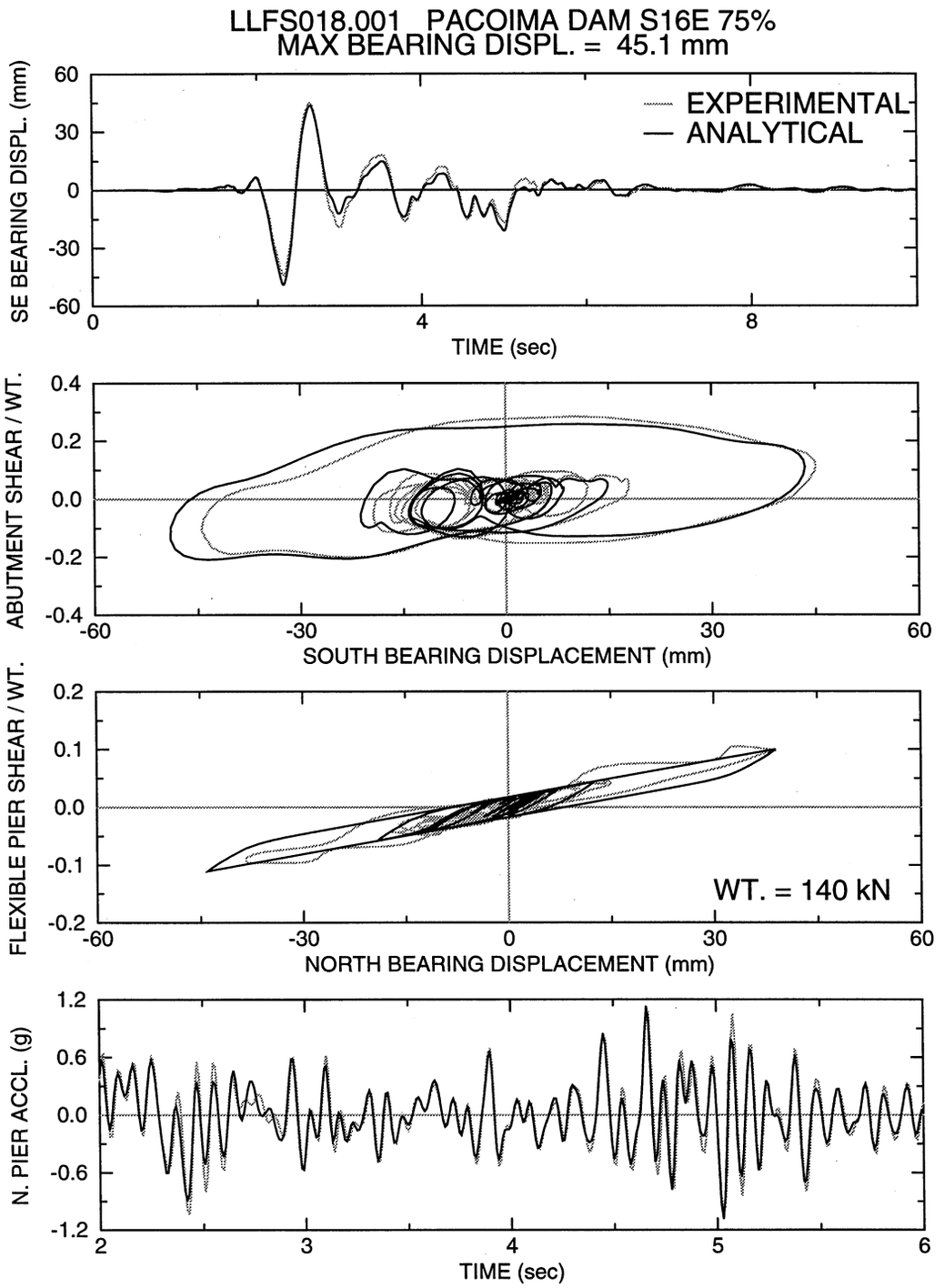

Figure 7-15: Comparison of Experimental and Analytical Results of Low Damping Elastomeric Isolation System with Linear Viscous Dampers in Pacoima Dam S16E 75% Test

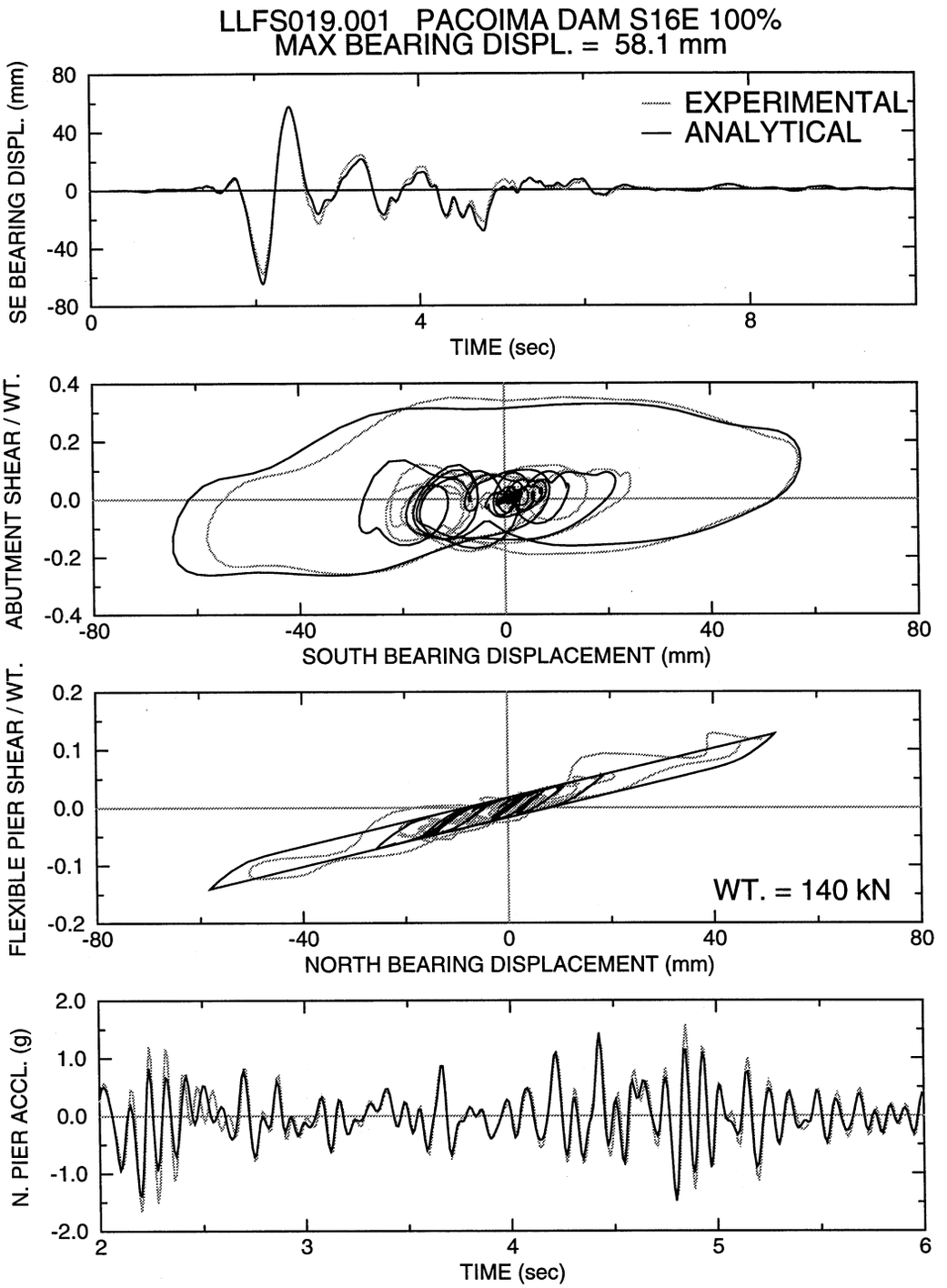

Figure 7-16: Comparison of Experimental and Analytical Results of Low Damping Elastomeric Isolation System with Linear Viscous Dampers in Pacoima Dam S16E 100% Test

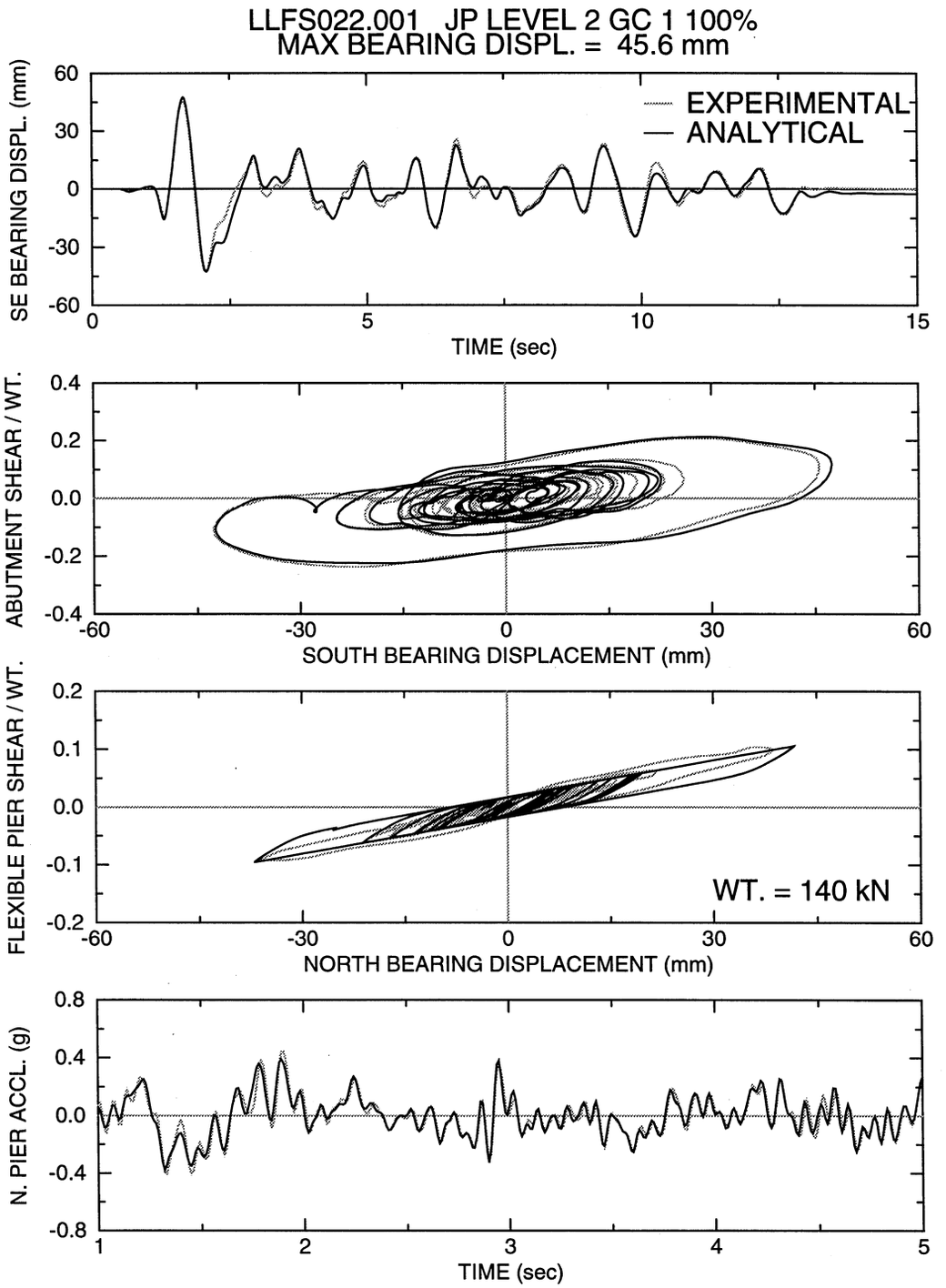

Figure 7-17: Comparison of Experimental and Analytical Results of Low Damping Elastomeric Isolation System with Linear Viscous Dampers in Japanese Level 2 GC 1 100% Test

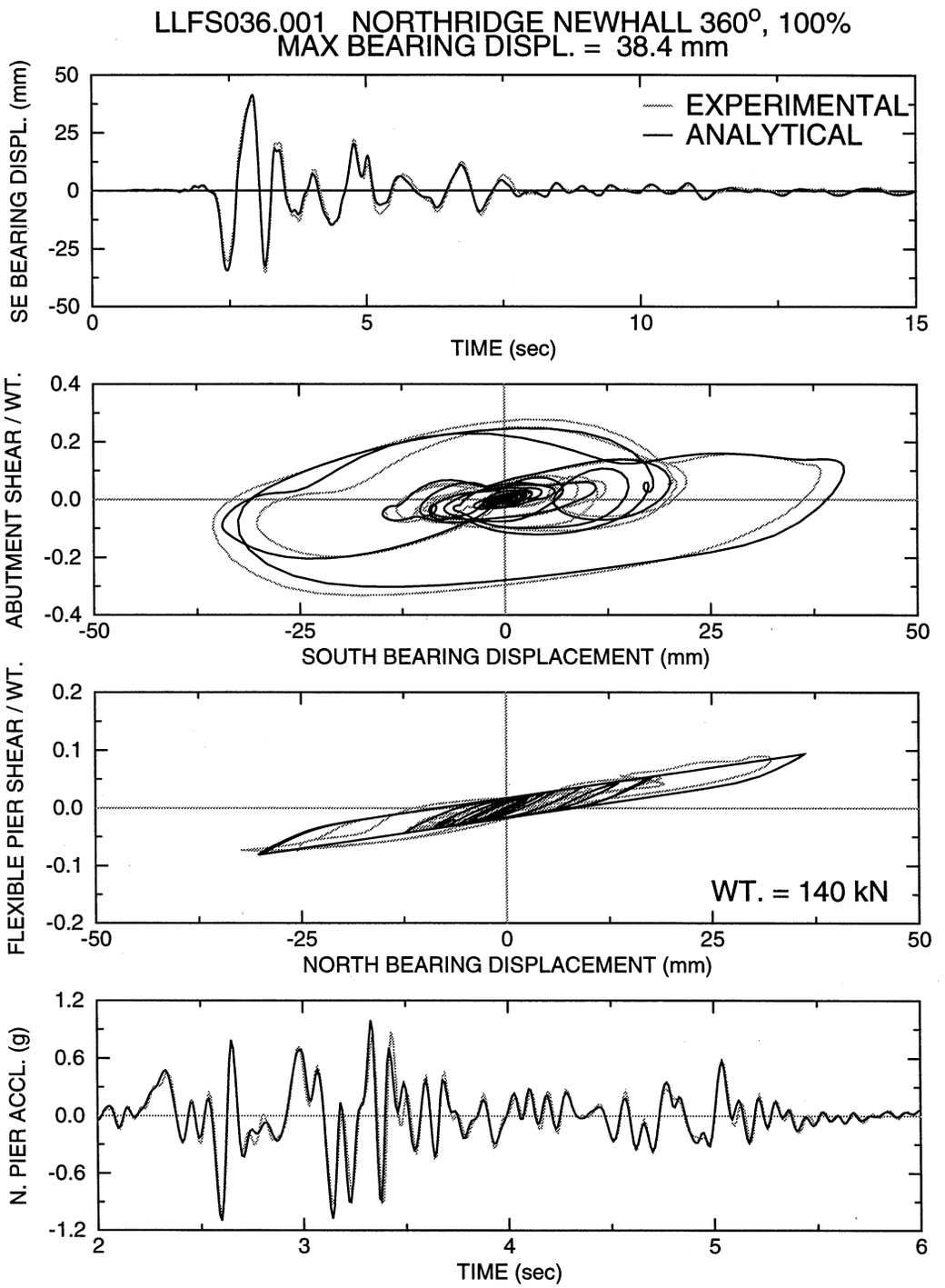

Figure 7-18: Comparison of Experimental and Analytical Results of Low Damping Elastomeric Isolation System with Linear Viscous Dampers in Northridge Newhall 360° 100% Test

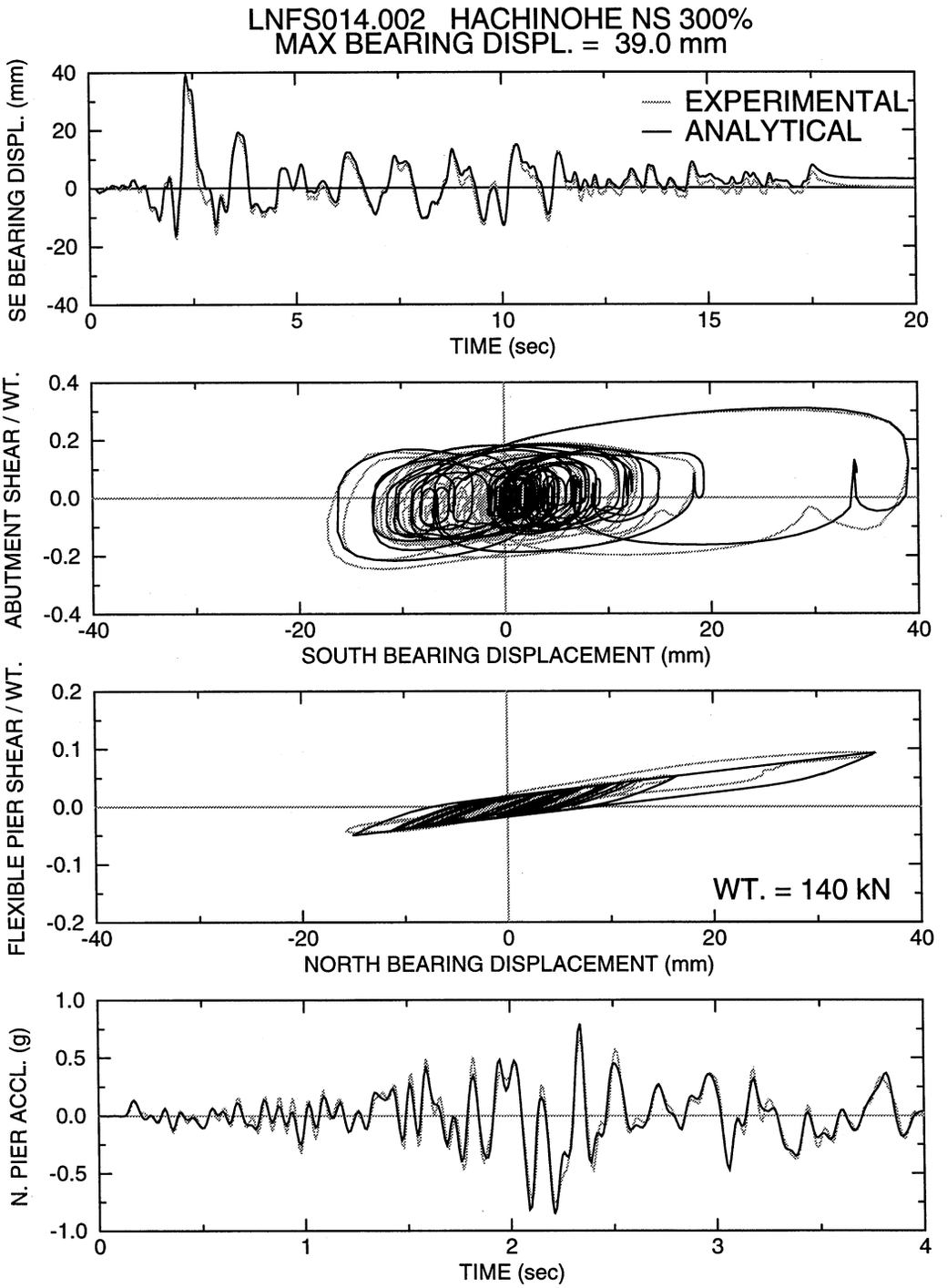

Figure 7-19: Comparison of Experimental and Analytical Results of Low Damping Elastomeric Isolation System with Nonlinear Viscous Dampers in Hachinohe NS 300% Test

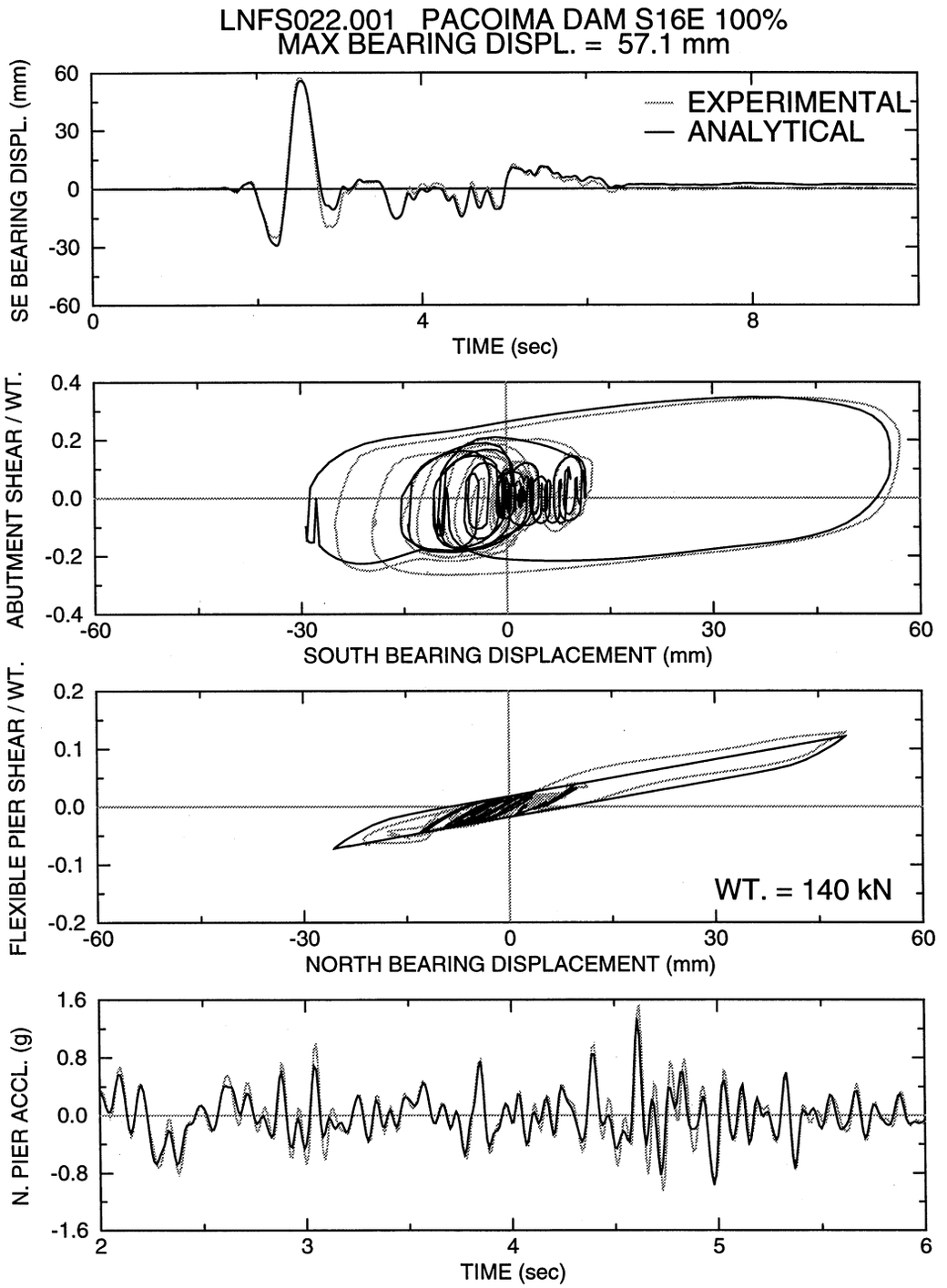

Figure 7-20: Comparison of Experimental and Analytical Results of Low Damping Elastomeric Isolation System with Nonlinear Viscous Dampers in Pacoima Dam S16E 100% Test

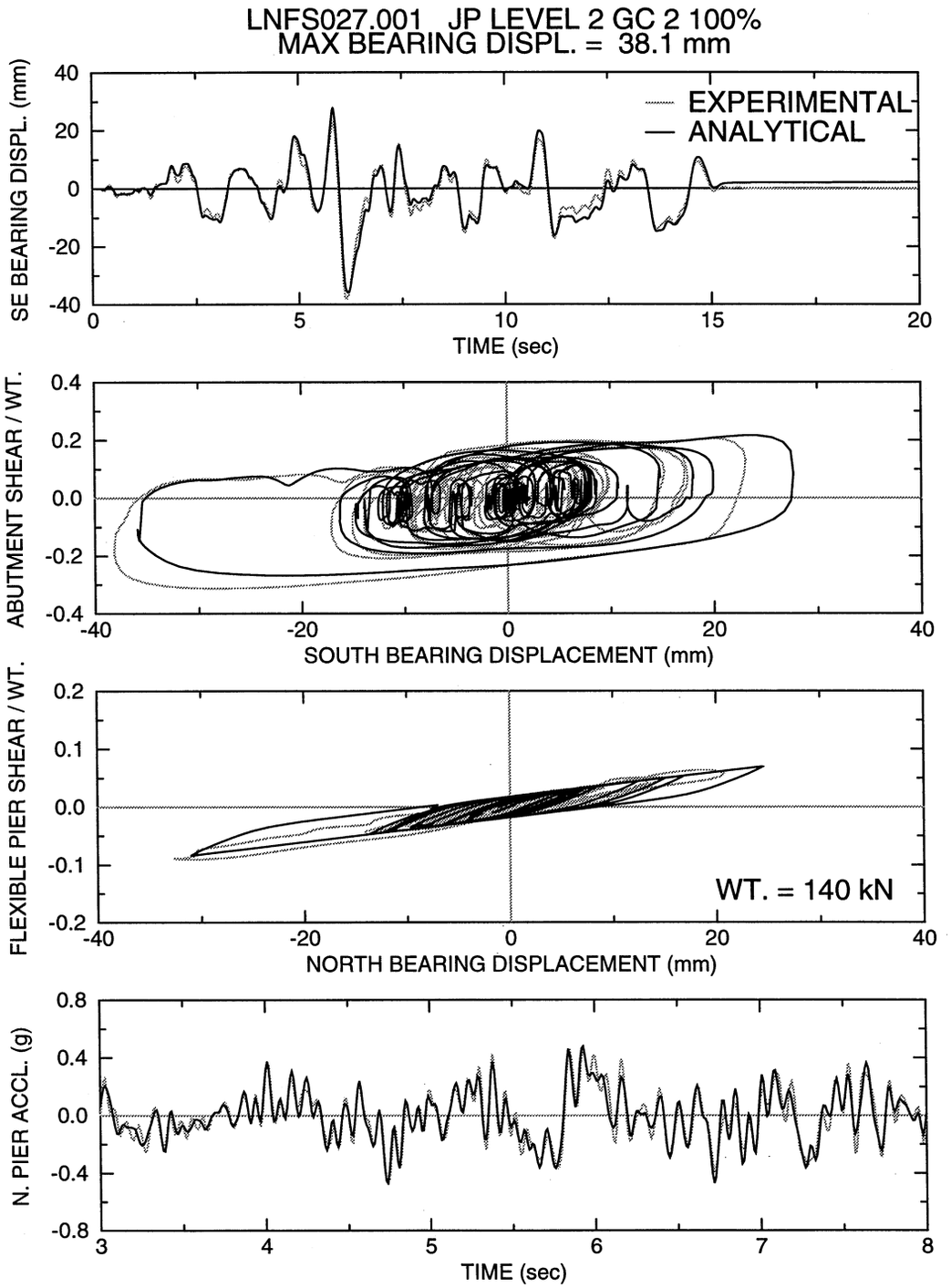

Figure 7-21: Comparison of Experimental and Analytical Results of Low Damping Elastomeric Isolation System with Nonlinear Viscous Dampers in Japanese Level 2 GC 2 100% Test

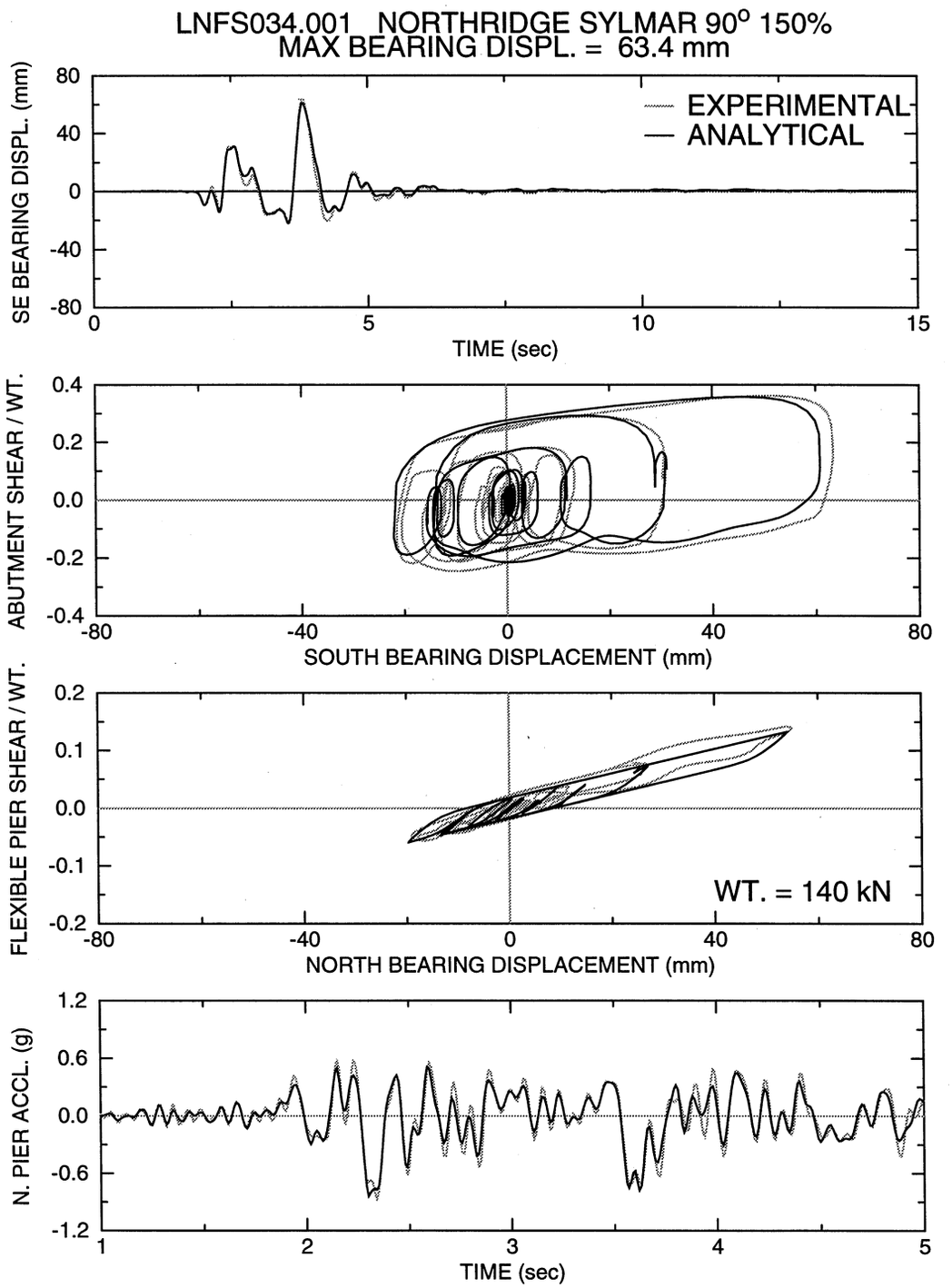

Figure 7-22: Comparison of Experimental and Analytical Results of Low Damping Elastomeric Isolation System with Nonlinear Viscous Dampers in Northridge Sylmar 90° 150% Test

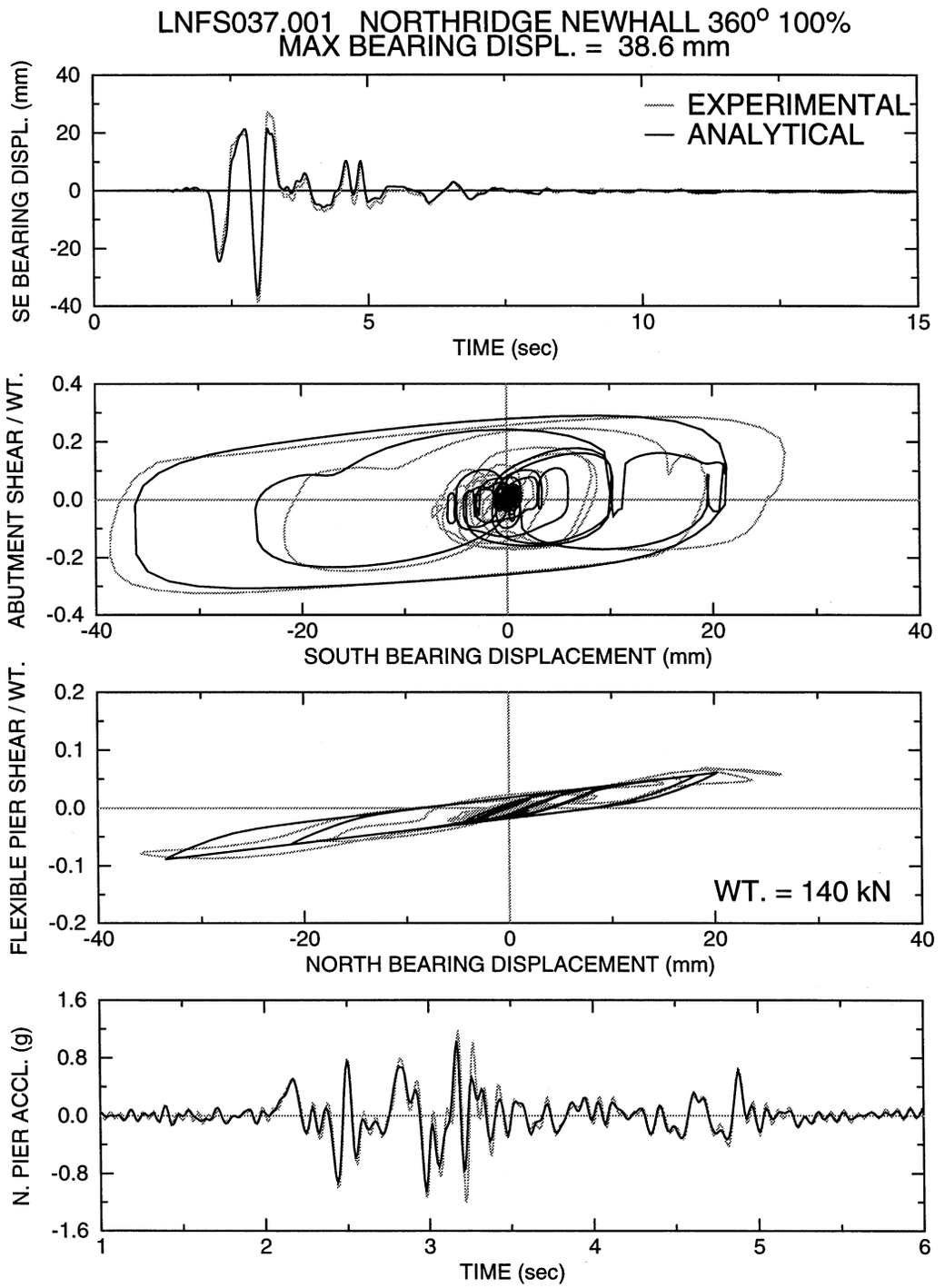

Figure 7-23: Comparison of Experimental and Analytical Results of Low Damping Elastomeric Isolation System with Nonlinear Viscous Dampers in Northridge Newhall 360° 100% Test

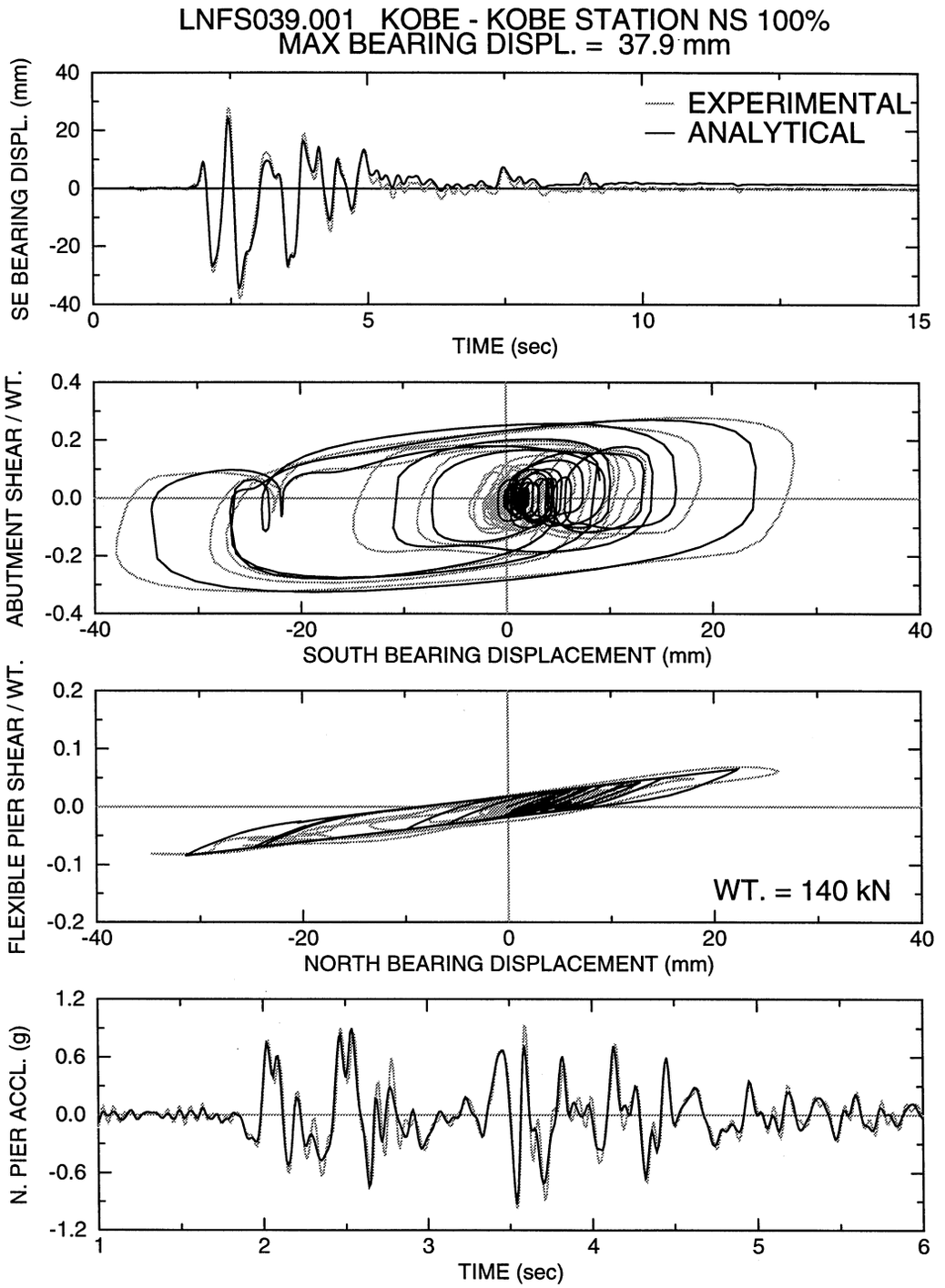

Figure 7-24: Comparison of Experimental and Analytical Results of Low Damping Elastomeric Isolation System with Nonlinear Viscous Dampers in Kobe NS 100% Test

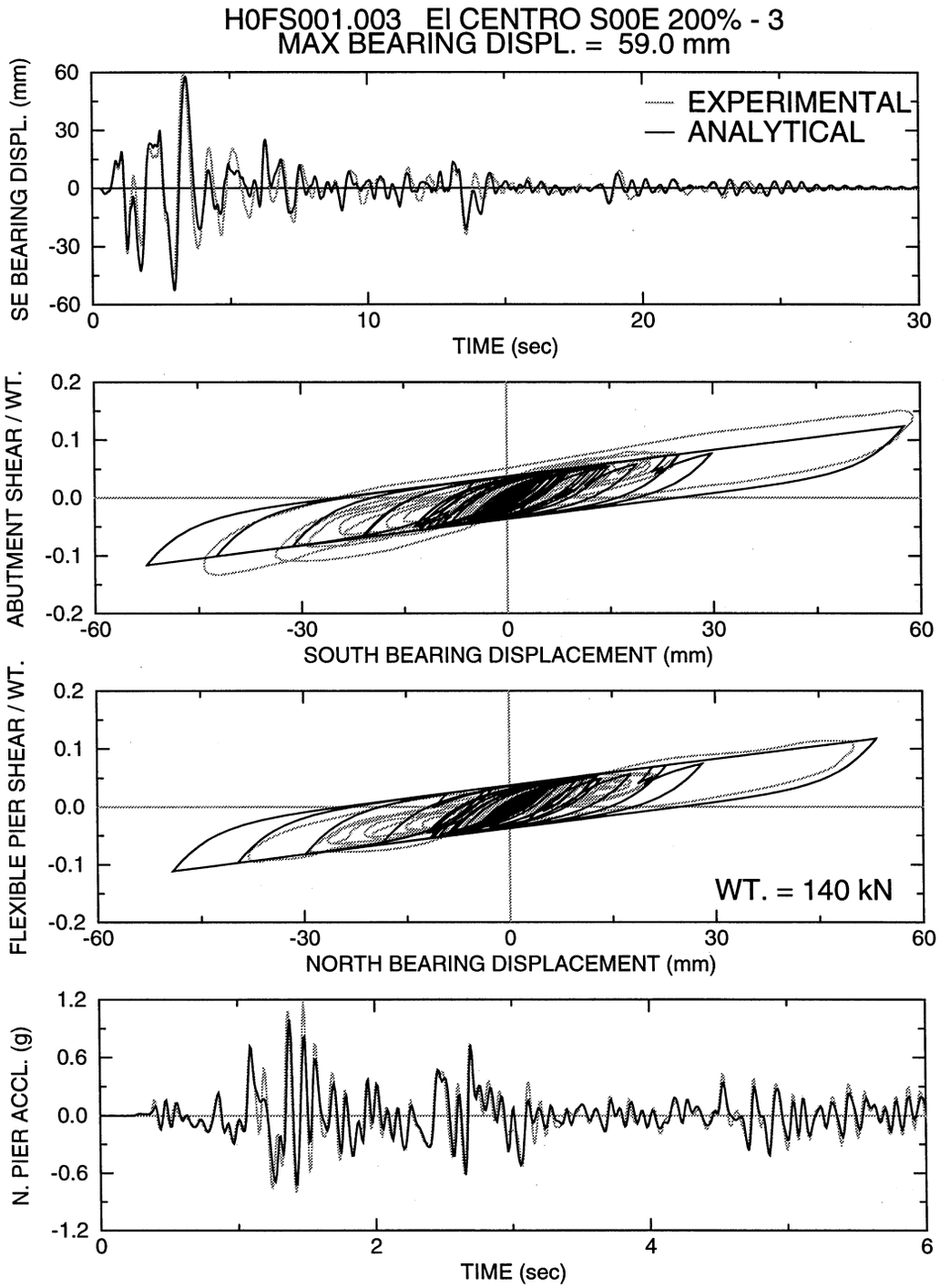

Figure 7-25: Comparison of Experimental and Analytical Results of High Damping Elastomeric Isolation System in El Centro S00E 200% Test No. 3

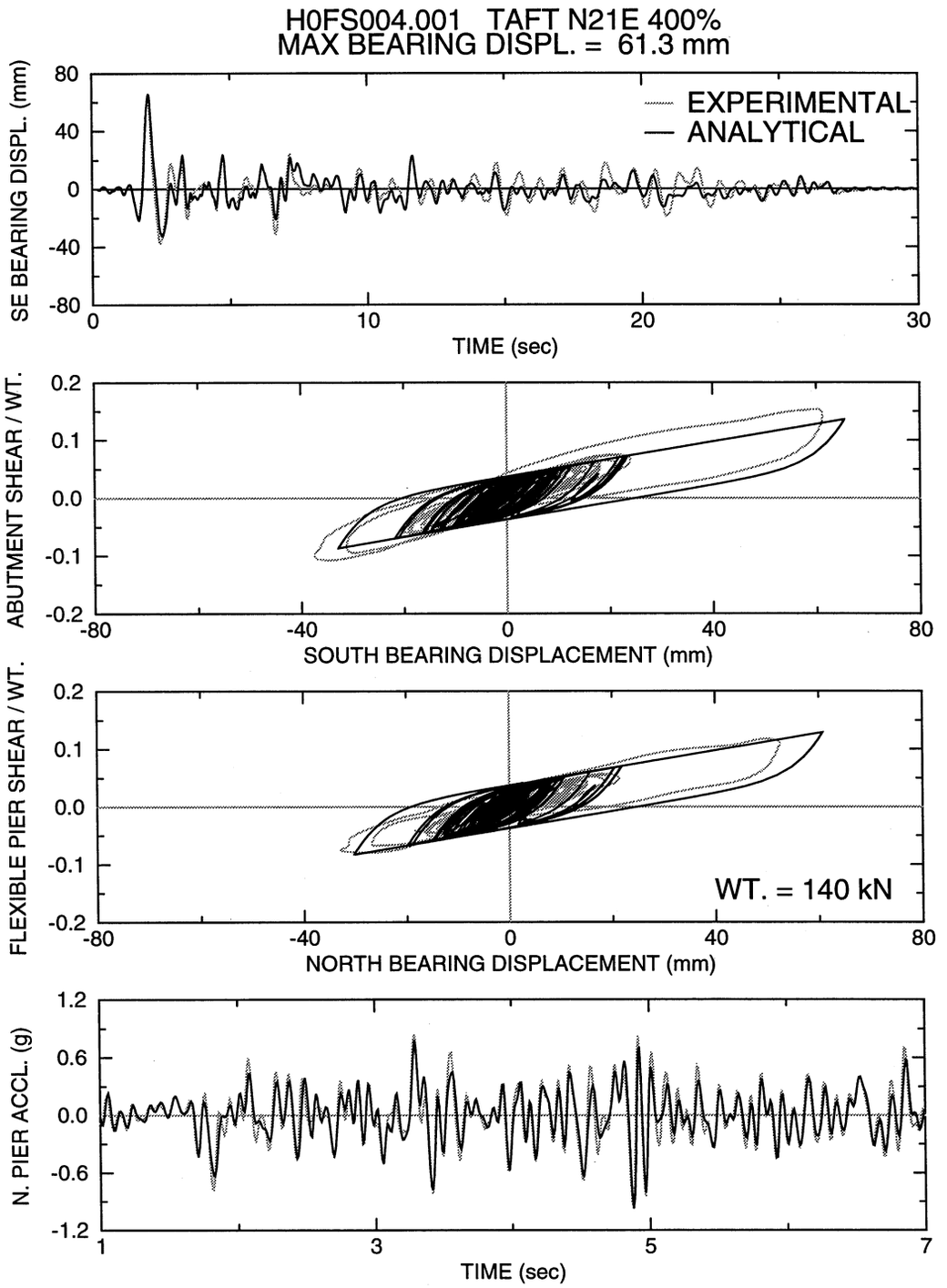

Figure 7-26: Comparison of Experimental and Analytical Results of High Damping Elastomeric Isolation System in Taft N21E 400% Test

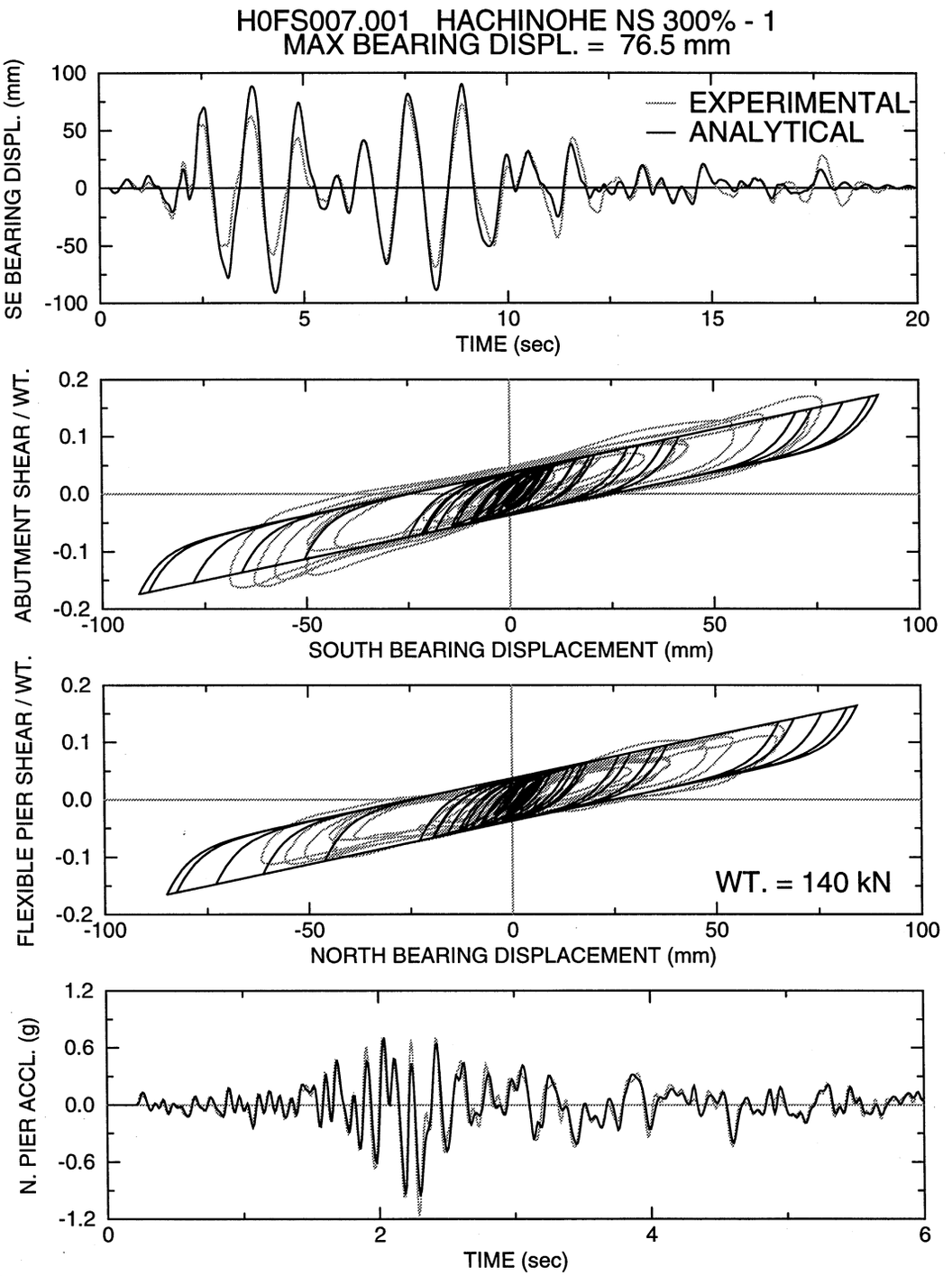

Figure 7-27: Comparison of Experimental and Analytical Results of High Damping Elastomeric Isolation System in Hachinohe NS 300% Test

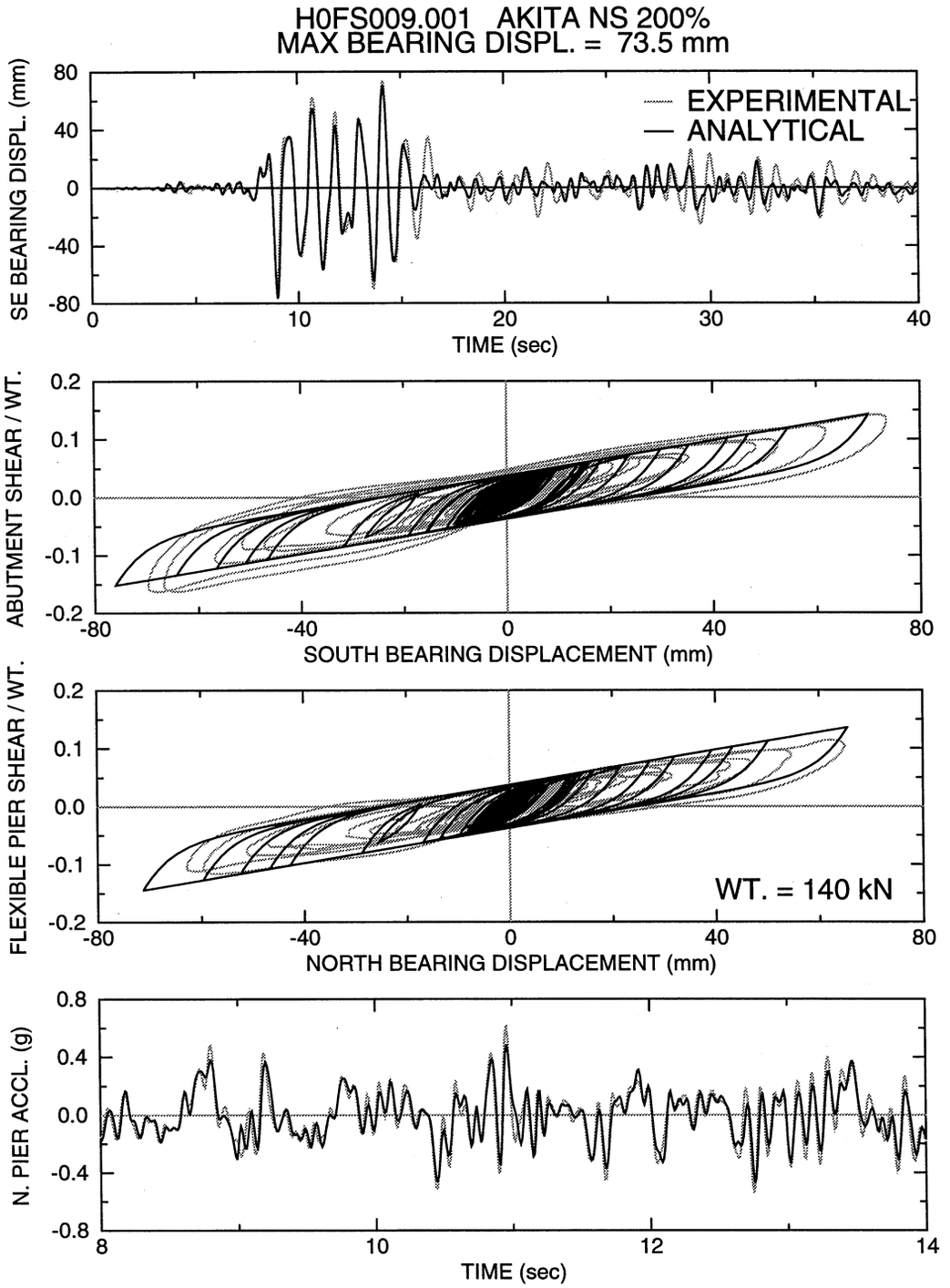

Figure 7-28: Comparison of Experimental and Analytical Results of High Damping Elastomeric Isolation System in Akita NS 200% Test

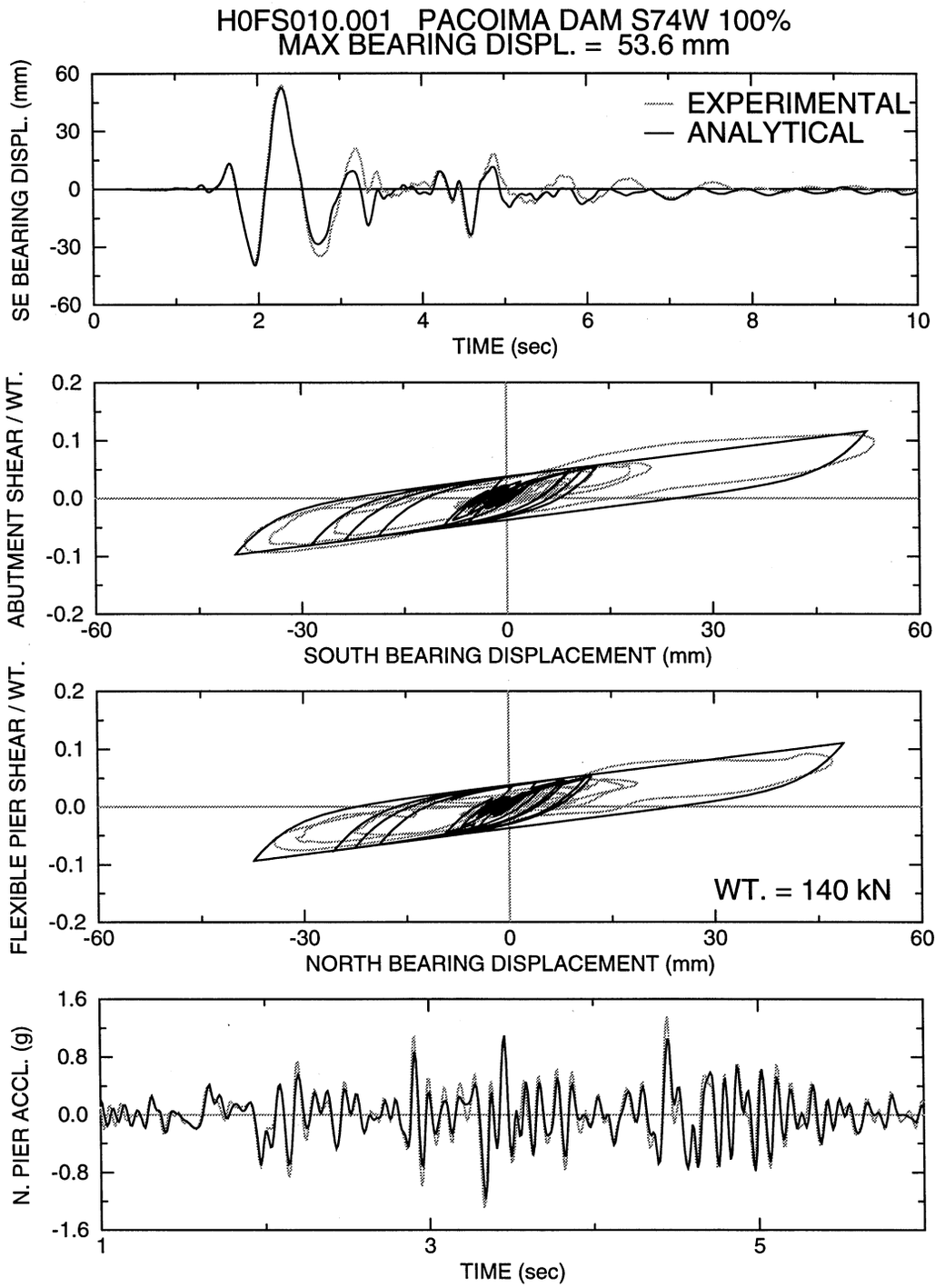

Figure 7-29: Comparison of Experimental and Analytical Results of High Damping Elastomeric Isolation System in Pacoima Dam S74W 100% Test

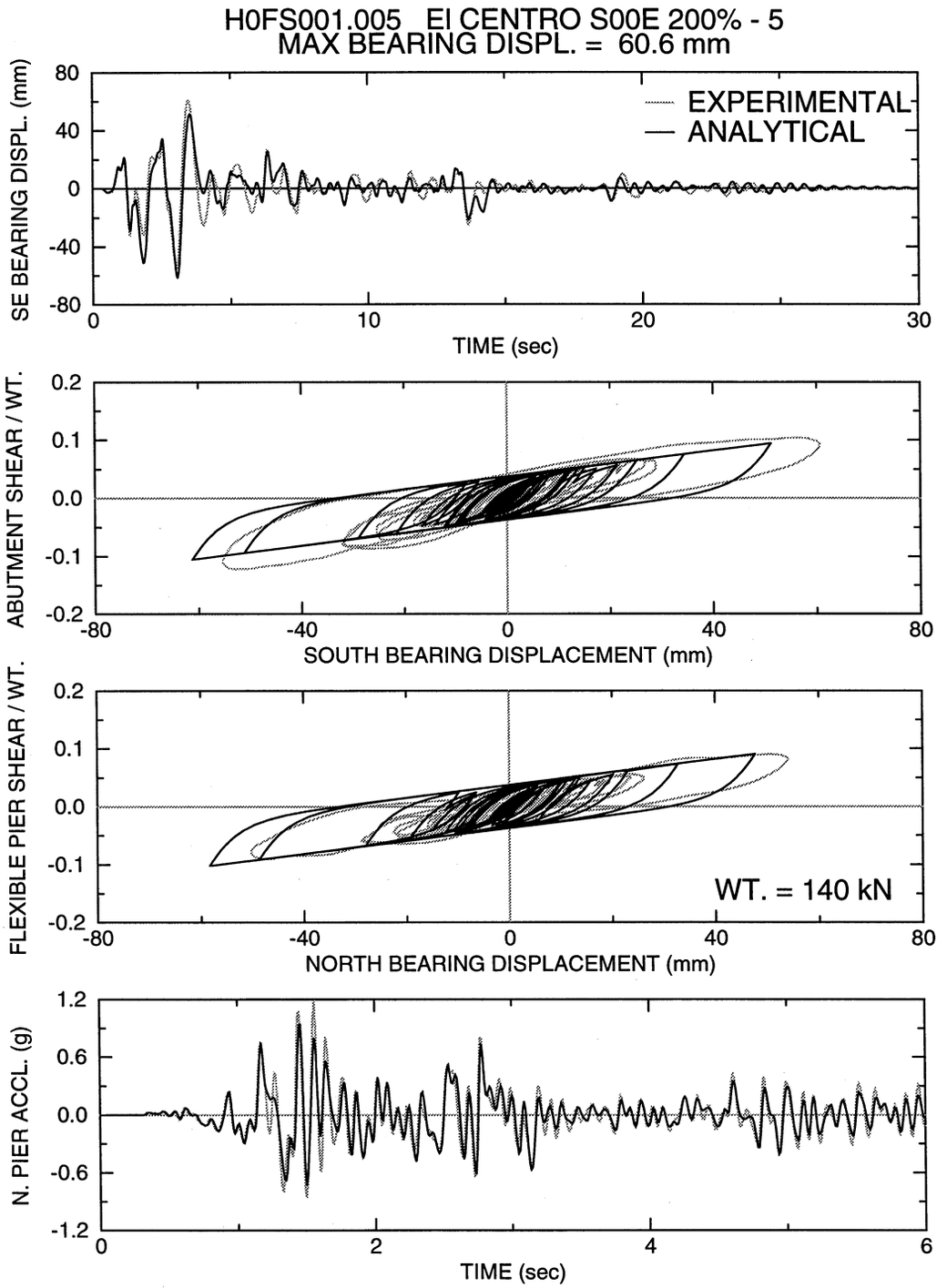

Figure 7-30: Comparison of Experimental and Analytical Results of High Damping Elastomeric Isolation System in El Centro S00E 200% Test No. 5

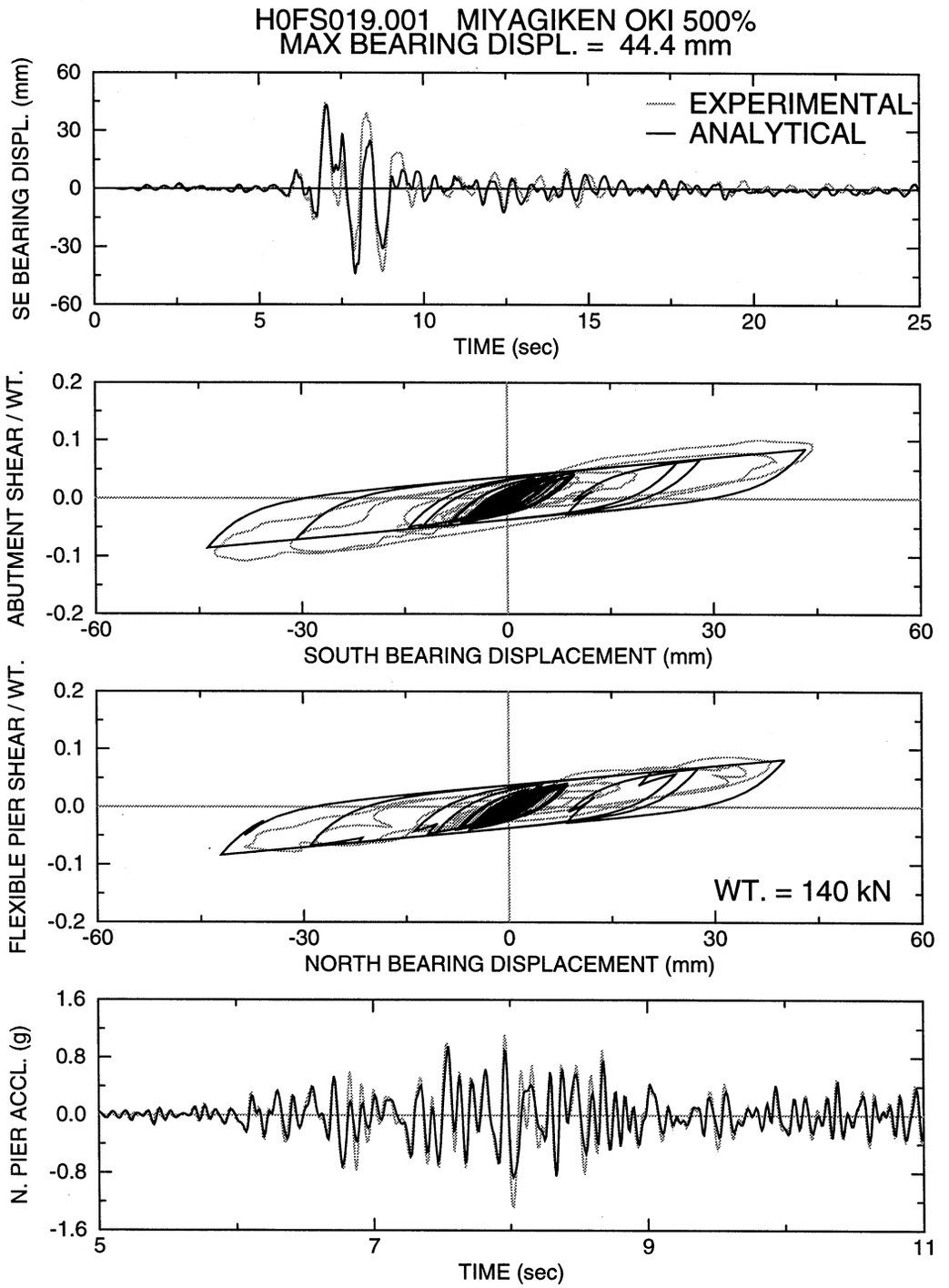

Figure 7-31: Comparison of Experimental and Analytical Results of High Damping Elastomeric Isolation System in Miyagiken Oki 500% Test

SECTION 8

CONCLUSIONS

The work described in this report consists of: (a) the design and construction of an isolator testing machine, (b) the testing and modeling of prestressed isolators, and (c) the experimental study of elastomeric and other bridge seismic isolation and energy dissipation systems.

The testing machine is now a permanent feature of the Structural Engineering and Earthquake Simulation Laboratory at the University at Buffalo. It has the capability for testing small size bearings under controlled conditions of variable axial load, lateral displacement and bearing top rotation. Moreover, the machine features an arrangement for the testing of prestressed bearings.

Prestressing represents one of a number of proposed (and some implemented) methods for preventing uplift or tension in isolation bearings. Its main advantages over other methods is that it is applicable to all types of isolation bearings and that it ensures prevention of uplift or tension regardless of the state of deformation of the bearing. In contrast, other methods are either restricted to specific types of isolators or they provide uplift restraint when the bearing displacement exceeds some preselected limit. However, prestressing of bearings requires a refined analysis, material selection and detailing. It also alters the behavior of the isolation bearings, so that the prestressing system becomes an integral part of the isolation system.

Three isolation bearings with vastly different characteristics in terms of their interaction with the prestressing system were tested. They were prestressed by the same prestressing arrangement and were subjected to similar testing in terms of histories of axial load and lateral displacement. A significant number of tests were conducted and presented in detail given that they represent the only available experimental data on prestressed isolators. The experimental results demonstrated the validity of the concept; provided an experimental evidence on the effect of prestress on the isolation system behavior and provided a basis for comparison to analytical predictions.

The prestress achieved the intended purpose in all three tested isolators by maintaining a substantial compressive load on the bearing throughout the testing. In the case of the flat sliding bearing, there was a uniform increase in the lateral force due to the initial prestress and a mild displacement-dependent increase in the lateral force due to the restoring force provided by the tendons. Similar effects were observed for the Friction Pendulum (FPS) bearing. However, substantial increases were observed in the prestressing force during lateral movement of the FPS bearing due to its geometry that results in increase in the height on lateral deformation. For the elastomeric bearing, the changes in the prestressing force as a result of lateral movement were minor due to loss in height of the bearing on lateral deformation. Moreover, the prestress had a minor effect on the mechanical properties of the elastomeric bearing.

Analytical models based on simple geometric considerations resulted in accurate prediction of the behavior of the two tested prestressed sliding bearings. In the case of the prestressed elastomeric bearing, the prediction of the tendon forces and the overall behavior of the prestressed bearing

required knowledge of the vertical movement of the bearing which itself required complex analysis of the bearing. We chose to utilize the simplest possible model of analysis of the bearing in order to maintain physical insight and ease in the calculations. The model predicted well the overall behavior of the tested prestressed bearing. However, the model did not accurately predict the excess prestress force due to the lateral bearing displacement. While the error was insignificant for practical purposes, it pointed to our incomplete understanding of the mechanics of elastomeric bearings. In this case, the errors were the result of the bearing top rotation and its effect on the vertical movement of the points of attachment of prestressing tendons. On the other hand, the analytical model could only predict the average vertical movement of the bearing.

The test results and the supporting analysis provided strong evidence for the capability of prestressing to prevent uplift or tension in isolation bearings. They also provided verified tools for the analysis of isolated structures in the presence of prestress, whether that is used for uplift or tension prevention, or for providing restoring force. It remains to test the concept within an isolated structure and provide verification of the concept.

The testing of the non-isolated bridge model without and with fluid viscous dampers provided a useful first set of experimental data on the behavior of bridges enhanced with energy dissipation devices. The addition of the damping devices caused a substantial reduction in displacement, provided relief to the vulnerable pier and caused a reduction in the total shear force transmitted to the bridge substructure. Moreover, the use of the damping devices provided for re-distribution of the reduced inertia forces from the vulnerable pier to the presumed strong abutments.

The testing of the isolated bridge configuration provided the opportunity to observe a number of interesting phenomena:

(a) The high damping elastomeric system was installed without prior testing so that the bearings exhibited unscragged properties. This was presumed to be the condition of the bearings after recovery to their initial properties following some time after the production testing. Following some testing on the shake table, the bearings were brought to their scragged condition for which the effective stiffness was less. It has been common in the past to assume that the scragged conditions prevail and that the bearings never recover. Accordingly, calculations of the displacement demands and substructure force demands were based on the scragged properties.

    A series of tests with identical seismic input was conducted and allowed for the measurement of displacements and substructure forces during the change from unscragged to scragged conditions of the bearings. The results demonstrated that the bearing displacements were only marginally affected but the substructure forces were markedly affected. Specifically, neglecting to consider the unscragged properties of the tested bearings could have resulted in underprediction of the substructure forces by about 30-percent.

    These results provide justification for the requirement in the 1997 AASHTO (American Association of State Highway and Transportation Officials, 1997) to consider the scragging/ recovery phenomenon through the use of property modification factors.

(b) The test results obtained in the testing of the elastomeric systems without added dampers provided clear evidence of the benefit provided by the high damping elastomeric bearings in reducing the displacement demand. These benefits could be assessed by the simple procedures of the 1997 AASHTO (American Association of State Highway and Transportation Officials, 1997) except for seismic inputs that (a) cause near resonance excitation of the system (such as the Mexico City type input), and (b) contain near-source high velocity shocks.

In the first case, the high damping system offered a substantially more reduction in displacement than predicted by the AASHTO procedures. However, the benefits could be assessed by equally simple procedures that are based on the theory of resonance.

In the case of the seismic input with near-source characteristics, the high damping elastomeric system did not offer any significant advantage over the comparable low damping elastomeric system. An explanation for this behavior has been provided on the basis of different initial conditions in the two systems at the instant of application of the prevailing high velocity shock in the seismic input. That is, while the two systems resist movement with different damping forces, they are at different stages of initial movement at that instance of application of the shock. The resulting displacement response may be dominated by these initial conditions and only substantial amounts of damping may have impact on the response.

(c) A comparison of results obtained in the testing of the low and the high damping elastomeric systems and of the low damping elastomeric system with added fluid dampers in motions containing near-source characteristics (specifically the Pacoima Dam S16E input) provided evidence of the significance of large damping in controlling the displacement response. The addition of dampers resulted in a near 50-percent reduction in the bearing displacement demand without an increase in the isolation system force (for example, see Figure 6-12).

Specifically, the system with linear fluid dampers was subjected to the Pacoima Dam S16E input which had prevailing near-source characteristics with peak acceleration of 1.16g and peak velocity of 679 mm/s (or 1358 mm/s in prototype scale). The bearing displacement was 58 mm (or 232 mm in prototype scale). This exceptionally low displacement demand could be achieved with a damper force having a horizontal component equal to about 25-percent of the deck weight.

(d) The testing of the low damping elastomeric system with added linear or nonlinear dampers provided several interesting results. Firstly, we note that the dampers were designed to deliver the same output force at some large velocity expected to be mobilized only in the tests with motions having strong near-source characteristics. When the two systems were tested with motions lacking near-source characteristics, the system with nonlinear dampers had, in general, a lesser displacement demand at the expense of larger isolation system force in several cases. They were also some spectacular performances of the nonlinear damper system as it can be seen, for example, in Figure 6-13 for the case of the Mexico City input.

However, the most interesting results were obtained in the case of the motions with near-source characteristics, of which a sample may be seen in Figure 6-14. The two systems

achieved large velocities, which along the damper axis exceeded the limit at which the two types of dampers delivered the same force. The two systems underwent comparable displacement responses and had comparable peak isolation system forces. However, the nonlinear dampers achieved this performance at a lesser peak damper force (for example, see Table 6-2). This demonstrates the main benefit that nonlinear dampers can offer.

The tests with motions having near-source characteristics again demonstrated the problems with high velocity ground pulses and the significance of the initial conditions as discussed earlier. Nevertheless, the test results clearly showed that for isolated bridges, large amounts of damping are needed to control displacements within strict limits in earthquakes with near-source characteristics.

(e) Tests without and with the effects of vertical ground motion showed insignificant difference in the response of the isolated bridge. This desired performance could be achieved even under conditions of substantial fluctuations of the axial bearing force, as for example can be seen in Figure 6-19.

Finally, available analytical tools for the prediction of the response of isolated structures have been shown to produce results of acceptable accuracy. Specifically, comparisons of experimental and analytically calculated responses demonstrated that the available models produce results with errors generally not exceeding the acceptable limit of about 15-percent in either the displacement or force response.

Some larger errors were observed only in the case of the high damping elastomeric system, which exhibited somehow atypical behavior. Nevertheless, it can be concluded that there is a need for the development of analytical models for elastomeric bearings which account for the phenomena of change of the mechanical properties due to the history of loading, the stiffening at large displacement, the scragging and recovery, etc. Of interest, of course, is the development of models based on fundamental principles and rational mechanics, and not the generation of arbitrary mathematical constructions which can only fit specific test data.

SECTION 9

REFERENCES

1. Al-Hussaini, T. M., Zayas, V. A. and Constantinou, M. C. (1994), "Seismic isolation of Multistory Frame Structures Using Spherical Sliding Isolation Systems," Report No. NCEER-94-007, National Center for Earthquake Engineering Research, Buffalo, NY.

2. American Association of State Highway and Transportation Officials (1997), "Guide Specifications for Seismic Isolation Design," in print.

3. Asher, J. W., Hoskere, S. N., Ewing, R. E., Mayes, R. L., Button, M. R. and Van Volkinburg, D. R. (1997), "Performance of Seismically Isolated Structures in the 1994 Northridge and 1995 Kobe Earthquakes," Proc. of Building to Last Structural Congress, Vol. 2, 1128-1132, ASCE, New York, NY.

4. Cho, D. M. and Retamal, E. (1992), "The Los Angeles County Emergency Operations Center, on High Damping Rubber Bearings to Withstand an Earthquake Bigger than the Big One," Proc. of Seminar on Seismic Isolation, Passive Energy Dissipation, and Active Control, Applied Technology Council, ATC 17-1, Vol. 1, 209-220, San Francisco, CA.

5. Chopra, A. K. (1995), "Dynamics of Structures, Theory and Applications to Earthquake Engineering," Prentice-Hall, Inc., Englewood Cliffs, NJ.

6. Computers and Structures, Inc. (1997), "SAP2000, Integrated Finite Elements Analysis and Design of Structures," Version 6.1, Berkeley, CA.

7. Constantinou, M. C. and Reinhorn, A. M. (1997), "Seismic Isolation and Control," in Computer Analysis and Design of Earthquake Resistant Structures, Advances in Earthquake Engineering, Vol. 3, Computational Mechanics Publications, Southampton, UK.

8. Constantinou, M. C., Kartoum, A., Reinhorn, A. M. and Bradford, P. (1991), "Experimental and Theoretical Study of a Sliding Isolation System for Bridges," Report No. NCEER-91-0027, National Center for Earthquake Engineering Research, Buffalo, NY.

9. Constantinou, M. C., Kartoum, A., Reinhorn, A. M. and Bradford, P. (1992a), "Sliding Isolation System for Bridges: Experimental Study," Earthquake Spectra, Vol. 8, No. 3, 321-344.

10. Constantinou, M. C., Kartoum, A. and Kelly, J. M. (1992b), "Analysis of Compression of Hollow Circular Elastomeric Bearings," Journal of Engineering Structures, 14(2), 103-111.

11. Constantinou, M. C., Mokha, A. and Reinhorn, A. M. (1990), "Teflon Bearings in Base Isolation II: Modeling," Journal of Structural Engineering, ASCE, 116(2), 455-474.

12. Constantinou, M. C., Tsopelas, P. and Kasalanati, A. (1998), "Property Modification Factors for Seismic Isolation Bearings," Final Report on Task 106-F-4.2.1(a), NCEER Highway Project, to appear as Technical Report of the National Center for Earthquake Engineering Research, Buffalo, NY.

13. Constantinou, M. C., Tsopelas, P., Kim, Y-S. and Okamoto, S. (1993), "NCEER-TAISEI Corporation Research Program on Sliding Seismic Isolation Systems for Bridges - Experimental and Analytical Study of Friction Pendulum System (FPS)," Report No. NCEER-93-0020, National Center for Earthquake Engineering Research, Buffalo, NY.

14. Feng, M. Q. and Okamoto, S. (1994), "Shaking Table Tests on Base-Isolated Bridge with Sliding System," Proceedings of the Third U.S.-Japan Workshop on Earthquake Protective Systems for Bridges, Report No. NCEER-94-0009, National Center for Earthquake Engineering Research, Buffalo, NY.

15. Griffith, M. C., Kelly, J. M, Coveney, V. A. and Koh, C. G. (1988), "Experimental Evaluation of Seismic Isolation of Medium-Rise Structures Subject to Uplift," Earthquake Engineering Research Center, Report No. UBC/EERC-88/02.

16. Griffth, M. C., Aiken, I. D. and Kelly, J. M. (1990), "Displacement Control and Uplift Restraint for Base-Isolated Structures," Journal of Structural Engineering, Vol. 116, No. 4, 1135-1148.

17. Hall, J. F., Heaton, T. H., Halling, M. W. and Wald, D. J. (1995), "Near-Source Ground Motion and its Effects on Flexible Buildings," Earthquake Spectra, Vol. 11, No. 4, 569-605.

18. Kasalanati, A. (1998), "Experimental Study of Bridge Elastomeric and Other Isolation and Energy Dissipation Systems with Emphasis on Uplift Prevention and High Velocity Near-Source Seismic Excitation," Doctoral Dissertation, State University of New York, Buffalo, NY.

19. Kawashima, K., Hasegawa, K. and Nagashima, H. (1992), "Experiment and Analysis on Seismic Response of Menshin Bridges," Proceedings from the First U.S.-Japan Workshop on Earthquake Protective Systems for Bridges, Report No. NCEER-92-0004, National Center for Earthquake Engineering Research, Buffalo, NY.

20. Kelly, J. M. (1993), "Earthquake-Resistant Design with Rubber," Springer-Verlag, New York.

21. Kelly, J. M., Buckle, I. G. and Tsai, H-C. (1986). "Earthquake Simulator Testing of a Base-Isolated Bridge Deck," Report No. UCB/EERC-85/09, Earthquake Engineering Research Center, University of California, Berkeley, California.

22. Kikuchi, M. and Aiken, I. D. (1997), "Analytical Hysteresis Model for Elastomeric Seismic Isolation Bearings," Earthquake Engineering and Structural Dynamics, Vol. 26, No. 2, 215-

231.

23. Logiadis, I. S. E. (1996), "Application of Vertical Unbonded Tensioned Prestressed Tendons in the Seismic Isolation of Structures," Dissertation, Technische Universitat Munchen (in German).

24. Nagarajaiah, S., Reinhorn, A. M. and Constantinou, M. C. (1991), "3D-BASIS: Nonlinear Dynamic Analysis of Three-dimensional Base Isolated Structures: Part II," Report No. NCEER-91-0005, National Center for Earthquake Engineering Research, Buffalo, NY.

25. Sabnis, G. M., Harris, H. G., White, R. N. and Mirza, M. S. (1983), "Structural Modeling and Experimental Techniques," Prentice-Hall, Inc., Englewood Cliffs, NJ.

26. Seleemah, A. and Constantinou, M. C. (1997), "Investigation of Seismic Response of Buildings with Linear and Nonlinear Fluid Viscous Dampers" Report No. NCEER-97-0004, National Center for Earthquake Engineering Research, Buffalo, NY.

27. Soong, T. T. and Constantinou, M. C. (editors) (1994), "Passive and Active Structural Vibration Control in Civil Engineering," CISM Course and Lectures No. 345, Springer-Verlag, Wien - New York.

28. Tsopelas, P. and Constantinou, M. C. (1994a), "NCEER-TAISEI Corporation Research Program on Sliding Seismic Isolation Systems for Bridges - Experimental and Analytical Study of Systems Consisting Sliding Bearings and Fluid Restoring Force/Damper Devices," Report No. NCEER-94-0014, National Center for Earthquake Engineering Research, Buffalo, NY.

29. Tsopelas, P. and Constantinou, M. C. (1994b), "NCEER-TAISEI Corporation Research Program on Sliding Seismic Isolation Systems for Bridges - Experimental and Analytical Study of Systems Consisting of Lubricated PTFE Sliding Bearings and Mild Steel Dampers," Report No. NCEER-94-0022, National Center for Earthquake Engineering Research, Buffalo, NY.

30. Tsopelas, P. and Constantinou, M. C. (1997), "Study of Elastoplastic Bridge Seismic Isolation System," Journal of Structural Engineering, ASCE, Vol. 123, No. 4.

31. Tsopelas, P., Constantinou, M. C., Kim, Y-S. and Okamoto, S. (1996a), "Experimental study of FPS System in Bridge Seismic Isolation," Earthquake Engineering and Structural Dynamics, Vol. 25, 65-78.

32. Tsopelas, P., Constantinou, M. C. and Reinhorn, A. M. (1994a), "3D-BASIS-ME: Computer Program for Nonlinear Dynamic Analysis of Seismically Isolated Single and Multiple Structures and Liquid Storage Tanks," Report No. NCEER-94-0010, National Center for Earthquake Engineering Research, Buffalo, NY.

33. Tsopelas, P., Okamoto, S., Constantinou, M. C., Ozaki, D. and Fujii, S. (1994b), "NCEER-TAISEI Corporation Research Program on Sliding Seismic Isolation Systems for Bridges - Experimental and Analytical Study of Systems Consisting of Sliding Bearings, Rubber Restoring Force Devices and Fluid Dampers," Report No. NCEER-94-0002, National Center for Earthquake Engineering Research, Buffalo, NY.

34. Tsopelas, P., Okamoto, S., Fujii, S. and Ozaki, D. (1996b), "Experimental Study of Bridge Seismic Sliding Isolation Systems," Journal of Engineering Structures, Vol. 18, No. 4, 301-310.

35. Wen, Y. K. (1976), "Method for Random Vibration of Hysteretic Systems," Journal of Engineering Mechanics Division, ASCE, 102(EM2), 249-263.

MULTIDISCIPLINARY CENTER FOR EARTHQUAKE ENGINEERING RESEARCH

A National Center of Excellence in Advanced Technology Applications

University at Buffalo, State University of New York
Red Jacket Quadrangle ▪ Buffalo, New York 14261-0025
Phone: 716/645-3391 ▪ Fax: 716/645-3399
E-mail: mceer@acsu.buffalo.edu ▪ WWW Site: http://mceer.buffalo.edu

University at Buffalo *The State University of New York*

ISSN 1520-295X